Investigating Electric Fields and Energy Conversion in Earth's Turbulent Magnetosheath

Harry Currell Lewis

June 2025

Imperial College London

Department of Physics

Submitted in partial fulfilment of the requirements for the degree of Doctor of Philosophy in Physics of Imperial College London and the Diploma of Imperial College London

Abstract

Turbulence plays a key role in plasma dynamics and heating throughout the Universe. Complex and unpredictable nonlinear motion leads to a transfer of energy from large to small scales, where it is dissipated into heat. In the absence of collisions, turbulence proceeds to microphysical scales where it is not known how reversible kinetic processes lead to net dissipation. Earth's magnetosheath provides an opportunity to directly probe this open question using in situ measurements. This thesis presents an investigation into the fundamental physics of turbulence using a database of magnetosheath observations by NASA's Magnetospheric Multiscale (MMS) mission. The comparative importance of different electric field contributions is studied for 60 magnetosheath intervals, revealing that how the nonlinear dynamics operate depends on both the ambient plasma conditions and the turbulence driver. The relationships uncovered provide observational constraints on turbulence theory, bounding the applicability of magnetohydrodynamic and kinetic Alfvén wave physics, with applications to other plasma regimes and simulation studies. The role of these electric field dynamics in facilitating turbulent dissipation is explored by quantifying the non-ideal energy conversion related to specific kinetic processes. It is found that energy conversion is enhanced in regions susceptible to anisotropy-driven kinetic microinstabilities, suggesting these mechanisms play a fundamental role in dissipating turbulent energy. The interpretation is that turbulence drives conditions to become locally unstable, triggering instabilities which redistribute the free energy in favour of growing wave modes. Despite these processes being reversible, the net transfer of energy is from the fields into the particles, consistent with net dissipation. Turbulence is also found to generate significantly non-Maxwellian velocity distributions, indicating that it provides additional sources of free energy whereby instabilities can thermalise the plasma.

Declaration

I declare that, except where explicitly stated otherwise and referenced, the work presented in this thesis is my own.

— *Harry C. Lewis, 2025.*

The copyright of this thesis rests with the author. Unless otherwise indicated, its contents are licensed under a Creative Commons Attribution-Non Commercial 4.0 International Licence (CC BY-NC). Under this licence, you may copy and redistribute the material in any medium or format. You may also create and distribute modified versions of the work. This is on the condition that: you credit the author and do not use it, or any derivative works, for a commercial purpose. When reusing or sharing this work, ensure you make the licence terms clear to others by naming the licence and linking to the licence text. Where a work has been adapted, you should indicate that the work has been changed and describe those changes. Please seek permission from the copyright holder for uses of this work that are not included in this licence or permitted under UK Copyright Law.

Acknowledgements

First and foremost, I am indebted to my supervisor Julia Stawarz for her unwavering support, patience, and confidence in me throughout my PhD. Without her, none of this would have been possible. I am also deeply grateful to Tim Horbury for stepping up and providing invaluable honesty, wisdom, and wit whenever I needed it. I would like to thank both my supervisors, as well as all my wonderful colleagues and collaborators from across the globe, for countless inspiring discussions. I'm also grateful to my teachers and lecturers, particularly the late Dr Khalid Obeid from Exeter College, for cultivating my desire to learn about the world and encouraging me to follow my interests above anything else.

I am profoundly grateful to my family and friends for all their love and support over the years. To Mum, Dad, Lucy, Nanny, and Grandpa, thanks for inspiring me to reach for the stars. To Lauren, thank you for your support and encouragement every single day – it has meant so much. To Harley and Zoë, thanks for sharing this journey with me – I couldn't have done it without you both and I'm so proud of what we've achieved. To Adrian, and everyone else at Imperial (old and new), thanks for the laughs, challenges, and routine (12 pm lunch, 3 pm snack – not a moment later). To Anthony, Angus, Josh, Gethin, Nick, and all my other friends from Southampton, thanks for all the fun which kept me going through lectures, exams, and COVID. To everyone mentioned here, and all my other friends from around the world, I am grateful for everything and I hope I will see considerably more of you from now on!

Finally, to Poppet, for being exceptionally fluffy and cute, if not a little bit annoying (and hungry, like, all of the time...), thanks for being a top-tier companion.

Contents

Abstract **2**

Declaration **3**

Acknowledgements **4**

List of Figures **9**

List of Tables **12**

List of Acronyms **13**

1 Introduction **15**

2 Theoretical Background **23**

2.1 Plasma Physics 23

2.1.1 Definition of a Plasma 24

2.1.2 Kinetic Theory 26

2.1.3 Magnetohydrodynamics 31

2.1.4 Generalised Ohm's Law 34

2.1.5 Diffusion and Frozen-in Flux 37

2.1.6 Collisions 39

2.2 Near-Earth Plasma Environment 42

2.2.1 Solar Wind 42

2.2.2 Earth's Magnetosphere 43

2.2.3 The Magnetosheath 46
2.3 Turbulence Theory 49
2.3.1 Turbulent Energy Spectra 49
2.3.2 Turbulent Cascade Theory 58
2.3.3 Local Structures Generated by Turbulence 63
2.3.4 Energy Conversion and Dissipation 65
2.4 Kinetic Microinstabilities 73
2.4.1 Instabilities 73
2.4.2 Quasilinear Diffusion 74
2.4.3 Anisotropy-driven Instabilities 76

3 Spacecraft Data Techniques **78**
3.1 The Magnetospheric Multiscale Mission 78
3.1.1 Science Objectives 78
3.1.2 Mission Profile 80
3.1.3 Instrumentation 83
3.2 Processing MMS Data 86
3.2.1 Resampling Time Series Data 86
3.2.2 Spintone 87
3.2.3 FPI Noise Level 87
3.2.4 Spacecraft Potential and Photoelectrons 88
3.3 Power Spectra 89
3.3.1 Power Spectral Density 89
3.3.2 Phase Scrambling 91
3.4 Multi-spacecraft Techniques 92
3.4.1 Barycentric Estimator 92
3.4.2 Checking Barycentric Estimator 94
3.5 Taylor's Hypothesis 96
3.6 Probability Density Functions 97

4 Turbulent Electric Fields Under Different Magnetosheath Conditions 99

4.1 Introduction . . . 99

4.2 Data Set and Methods . . . 102

4.2.1 Interval Selection . . . 102

4.2.2 Computing Generalised Ohm's Law . . . 105

4.2.3 Computing Power Spectra . . . 106

4.3 Dimensional Analysis . . . 107

4.3.1 Conventions . . . 108

4.3.2 Ratios Between Generalised Ohm's Law Terms . . . 109

4.3.3 Ratios of Nonlinear to Linear Contributions . . . 110

4.4 Results . . . 112

4.4.1 The Hall Scale . . . 112

4.4.2 Relative Amplitude of $\mathbf{E}_{P_e}$ and $\mathbf{E}_{Hall}$ . . . 116

4.4.3 Nonlinear and Linear $\mathbf{E}_{MHD}$ and $\mathbf{E}_{Hall}$ . . . 120

4.4.4 Nonlinear and Linear $\mathbf{E}_{P_e}$ . . . 122

4.5 Discussion . . . 125

4.5.1 The Hall Scale: Underlying Dependences . . . 125

4.5.2 Pressure vs Hall: Underlying Dependences . . . 127

4.5.3 Kinetic Alfvén Wave Predictions . . . 129

4.6 Summary . . . 131

5 Linking Turbulent Energy Conversion to Kinetic Microinstabilities 135

5.1 Introduction . . . 135

5.2 Methods . . . 140

5.2.1 Preparing the Dataset . . . 140

5.2.2 Interpretation of Anisotropy–Beta Plots . . . 143

5.3 Results . . . 145

5.3.1 $\mathbf{j} \cdot \mathbf{E}'$ on the Anisotropy–Beta Plane . . . 145

5.3.2 Parallel and Perpendicular Components of $\mathbf{j} \cdot \mathbf{E}'$ . . . 147

5.3.3 Statistics of $\mathbf{j} \cdot \mathbf{E}'$ within Enhancement Regions . . . 150

5.4 Discussion . . . 153
5.4.1 Understanding Energy Conversion Statistics . . . 153
5.4.2 Alternate Energy Conversion Signatures . . . 158
5.4.3 Validating trends on the Anisotropy–Beta Plane . . . 162
5.5 Summary . . . 164

6 Characterising Non-Maxwellianity of VDFs in Earth's Magnetosheath 167
6.1 Introduction . . . 167
6.2 Methods . . . 169
6.3 Characterising Background Non-Maxwellianity . . . 171
6.4 Non-Maxwellianity in Anisotropy–Beta Space . . . 178
6.4.1 Non-Maxwellianity . . . 178
6.4.2 Agyrotropy . . . 180
6.5 Fluctuations in the Non-Maxwellianity . . . 182
6.5.1 Fluctuating Parameters . . . 182
6.5.2 Non-Maxwellianity in an Example Interval . . . 184
6.6 Summary . . . 188

7 Conclusions 191

Bibliography 200

A Derivations 241
A.1 The Momentum Equation . . . 241
A.2 The Generalised Ohm's Law . . . 244
A.3 The Energy Equation . . . 248

B Table of Intervals 252
B.1 Chapter 4 . . . 252
B.2 Chapters 5 & 6 . . . 254

C Figure Permissions 261

List of Figures

1.1 Turbulence in *The Great Wave off Kanagawa* by Hokusai (1831) 17
1.2 Turbulence in Van Gogh's *The Starry Night* 18
1.3 Leonardo da Vinci's sketches of turbulence from his *Studies of water* . . . 19
1.4 Earth's turbulent magnetosheath 20

2.1 Helicoidal particle motion in a uniform magnetic field 27
2.2 Schematics of the three main generalised Ohm's law terms 41
2.3 Schematic of Earth's magnetosphere and surrounding environment 44
2.4 Example data from a quasi-perpendicular near-Earth environment 46
2.5 Example data from a quasi-parallel near-Earth environment 48
2.6 Example **B** power spectra in solar wind and magnetosheath 55
2.7 Example of intermittent turbulence 64
2.8 Quasilinear diffusion schematics for anisotropy-driven instabilities 75

3.1 Example orbit and multi-spacecraft formation of MMS mission 81
3.2 Power spectral density of electron and ion velocity 90
3.3 Power spectra of particle and barycentric estimator current 94
3.4 Time series of particle and barycentric estimator current 95

4.1 Schematic of electric and magnetic field power spectrum 100
4.2 Range of background parameters in Chapter 4 103
4.3 Example time series of important variables 104
4.4 Power spectra of plasma variables and Ohm's law terms 107

4.5 Ratios of spectra: E_{MHD}/E_{Hall} and $\delta u/\delta b_A$ for example interval 113
4.6 Comparison of different ways of evaluating $\delta b_A/\delta u$ in dimensional analysis 113
4.7 Trend between measured k_{Hall} and its dimensional analogue 115
4.8 Example power spectrum of δb_A, δu, and statistical uncertainty 116
4.9 Ratios of spectra: E_{P_e}/E_{Hall} and normalised $\delta P_e/\delta B$ for example interval . 117
4.10 Trend between measured E_{P_e}/E_{Hall} and the dimensional estimate 119
4.11 Example power spectrum of nonlinear/linear convective terms 120
4.12 Trend between measurements and dimensional analysis for $R_{MHD}^{NL/L}$ and $R_{Hall}^{NL/L}$ 122
4.13 Trend between measurements and dimensional analysis for $R_{P_e}^{NL/L}$ components 123
4.14 Example power spectra of components of $\mathbf{E}_{P_e}$ 124
4.15 Underlying dependencies folding into estimates of k_{Hall} 126
4.16 Underlying relationships and violation of KAW assumptions 128

5.1 Probability density plotted on the anisotropy–beta plane 141
5.2 Histograms of temperature anisotropy and parallel plasma beta 143
5.3 Energy conversion signals in anisotropy–beta space 146
5.4 Parallel and perpendicular $\mathbf{j}\cdot\mathbf{E}'$ on anisotropy–beta plane 148
5.5 Distribution of $\mathbf{j}\cdot\mathbf{E}'$ in each enhancement region 151
5.6 Distribution of $\mathbf{j}_\perp\cdot\mathbf{E}'_\perp$ and $j_\parallel E'_\parallel$ in enhancement regions 151
5.7 Distribution of $\mathbf{j}\cdot\mathbf{E}_{pl}$ on the anisotropy–beta plane 158
5.8 Example of electron firehose region structure with magnetic reconnection . 160
5.9 Phase-scrambled $\mathbf{j}\cdot\mathbf{E}'$ on the anisotropy-beta plane 161
5.10 $\mathbf{j}\cdot\mathbf{E}'$ distributed on the $\beta_\parallel(T_\perp/T_\parallel-1)$—$\beta_\parallel$ plane 163

6.1 Distribution of non-Maxwellianity against number density 170
6.2 Slices of a typical background VDF showing non-Maxwellianity (electrons) 172
6.3 Slices of a typical background VDF showing non-Maxwellianity (ions) . . . 174
6.4 Example background pitch angle distribution 176
6.5 Schematic showing suggested typical pitch angle distributions 177
6.6 Non-Maxwellianity and agyrotropy on the anisotropy–beta plane 179

6.7 Histograms of $\delta\epsilon$ against $\delta\sqrt{Q}$ and $\mathbf{j}\cdot\mathbf{E}'$ 182

6.8 Time series of non-Maxwellianity parameter 184

6.9 Time series of fluctuating $\mathbf{B}$, ϵ, and $\sqrt{Q}$ 186

6.10 Power spectral density of $\mathbf{B}$, ϵ, and $\sqrt{Q}$ 187

6.11 Scatter plot of λ_c of $\mathbf{B}$, ϵ_e, ϵ_i 188

List of Tables

2.1 Heliospheric plasma parameters 43

2.2 Table of relevant instability mechanisms 76

5.1 Dimensionless parameters for the instability growth rate thresholds 141

5.2 Statistics of $\mathbf{j} \cdot \mathbf{E}'$ distributions in each region 155

5.3 Statistics of $\mathbf{j}_\perp \cdot \mathbf{E}'_\perp$ distributions in each region 155

5.4 Statistics of $j_\parallel E'_\parallel$ distributions in each region 155

C.1 Re-used figure permissions 261

List of Acronyms

1SC Single Spacecraft.

ADP Axial Double Probe.

AFG Analogue Fluxgate.

ALPS Arbitrary Linear Plasma Solver.

ASPOC Active Spacecraft Potential Control.

DES Dual Electron Spectrometer.

DFG Digital Fluxgate.

DIS Dual Ion Spectrometer.

EDP Electric Field Double Probe.

ESA Top Hat Electrostatic Analyser.

FAC Field-aligned Coordinates.

FFT Fast Fourier Transform.

FGM Fluxgate Magnetometer.

FPI Fast Plasma Investigation.

GSE Geocentric Solar Ecliptic.

IMF Interplanetary Magnetic Field.

KAW Kinetic Alfvén Waves.

LHS Left-Hand Side.

MHD Magnetohydrodynamics.

MMS Magnetospheric Multiscale.

NASA National Aeronautics and Space Administration.

PAD Pitch Angle Distribution.

PDF Probability Density Function.

PSD Power Spectral Density.

PVI Partial Variance of Increments.

RHS Right-Hand Side.

rms Root Mean Square.

SCM Search Coil Magnetometer.

SDP Spin-plane Double Probe.

UTC Coordinated Universal Time.

VDF Velocity Distribution Function.

Chapter 1

Introduction

The behaviour of a fluid in motion is governed by the delicate balance between inertial and dissipative forces. When inertial forces prevail, the fluid enters a highly chaotic and unpredictable flow regime called *turbulence*. This flow state is characterised by circulating vortices whose interactions lead to the rapid mixing of fluid elements and a transfer of energy between fluctuations at different scales. The evolution of a turbulent system is extremely sensitive to initial and boundary conditions, rendering the dynamics impossible to reconstruct from first principles. Turbulent fluctuations are stochastic, meaning that the instantaneous configuration of a turbulent system is unlikely to resemble its average state. Consequently, turbulence must be studied by examining its statistical properties and developing phenomenological theories for how the process operates (Frisch, 1995).

Turbulence is universal phenomenon, occurring in a diverse range of systems from the quantum to the cosmological (Barenghi et al., 2014; Zhou et al., 2020). Because turbulence pervades the natural world, it has captivated artists, writers, and scientists for centuries, inspiring great works such as Hokusai's "The Great Wave off Kanagawa" (1831, Figure 1.1) and Vincent van Gogh's "The Starry Night" (1889, Figure 1.2). As a result of its ubiquity and complexity, turbulence has occupied some of the greatest minds of the last two centuries, yet many aspects of its true behaviour remain shrouded in mystery.

The first scientific investigation into turbulence was undertaken by Leonardo da Vinci in c.1510–12, who recognised that it was a flow state composed of coexisting eddies across many scales (Figure 1.3). In the 500 years since, his ideas have been mathematically formalised, but general analytical solutions for turbulence still do not exist. Leonardo noticed that turbulent water shaped the landscape, reflecting the modern appreciation that a wide-range of physical processes, from the generation of the Galactic magnetic field to the efficiency of jet engines, depend on turbulence (Barenghi et al., 2014). Being such a longstanding and ubiquitous problem, turbulence is considered by many to be "the most important unsolved problem of classical physics" (e.g. Feynman et al., 1965).

The defining characteristic of turbulence is its multiscale nature. Nonlinear interactions generate structures across several orders of magnitude in scale, ultimately leading to a cascade of energy from injection at large scales to dissipation at small scales (see Figure 1.3). This effect is amplified in inviscid fluids, which rapidly develop highly dynamic and unpredictable flow patterns. Turbulence is common in plasmas, which are conducting fluids that pervade the universe, accounting for up to 99.9 % of visible matter (Buchanan, 2016). Often referred to as the fourth state of matter, plasma consists of superheated ionised gas made up of approximately equal numbers of positive and negative charges. Its ability to carry electric currents makes plasma capable of interacting with and generating magnetic fields, which couple nonlinearly into the dynamics and further perturb the fluid motion (Biskamp, 2003). Electric fields can also exist in a plasma, driving particle acceleration and mediating energy dissipation.

In collisionless plasmas, such as many of those found in space, negligible viscosity and resistivity allows the turbulent dynamics to proceed to scales beyond the limits of a fluid description, reaching the kinetic regime where reversible microphysical processes govern the behaviour (Schekochihin et al., 2009). Turbulence is thus found in a wide range of space plasma systems, including the geospace environment (Zimbardo et al., 2010; C. H. K. Chen and Boldyrev, 2017; Rakhmanova et al., 2021), planetary magnetospheres (Saur et al., 2002; Hadid et al., 2015), the solar wind (Bruno and V. Carbone, 2013;



Figure 1.1: *The Great Wave off Kanagawa* by Hokusai (1831).

Verscharen et al., 2019), interstellar medium (Federrath, 2013; Falceta-Gonçalves et al., 2014), and accretion disks (Santos-Lima et al., 2012), to name just a few.

One outstanding question is how turbulent energy within a collisionless plasma is dissipated at small scales (Matthaeus et al., 2020). Magnetic fields are unable to do work on charged particles, so energy transfer must be mediated by electric fields. Energy conversion between the electromagnetic fluctuations and the particles can occur due to a wide variety of kinetic processes, including nonlinear processes (for example magnetic reconnection), linear processes (such as cyclotron damping and landau damping), and stochastic processes (Pezzi et al., 2021a). Once energy has been transferred to the particles, it must be thermalised by kinetic mechanisms in lieu of collisions. Kinetic processes, which are many and varied due to the inherently complex nature of particle distributions in the absence thermalisation by collisions, take free energy from the particles and redistribute it in favour of growing electromagnetic wave modes (Gary, 1993). Since these mechanisms are formally reversible, how the turbulent cascade is terminated and net dissipation into heat proceeds in the collisionless regime is a major unsolved problem.

There is a unique natural laboratory for studying collisionless plasma turbulence on our



Figure 1.2: *The Starry Night*, by Vincent Van Gogh (1889), depicts a swirling sky consistent with Kolmogorov's (1941) statistical theory of turbulence (Ma et al., 2024).

planet's doorstep. When the solar wind – a variable but persistent stream of supersonic plasma emanating from the Sun – encounters Earth's protective magnetic field, it is decelerated, heated, and compressed, forming a bow shock. The resulting region of strongly-turbulent shocked solar wind plasma ahead of Earth's magnetosphere is known as the *magnetosheath*, depicted in Figure 1.4. This region presents a valuable opportunity to study the impact of turbulence on plasma heating, energy transport, and particle acceleration (Rakhmanova et al., 2021). Since it is at the interface between the solar wind and the magnetosphere, understanding the processes occurring as a result of turbulence in the magnetosheath is potentially important for characterising the global solar wind–magnetosphere coupling (Sahraoui et al., 2020). By stirring and heating the magnetosheath, turbulence can perturb the magnetopause, impacting processes that ultimately facilitate mass and energy transport from the solar wind into the inner magnetosphere. This can drive so-called *space weather* that has potentially devastating socioeconomic ramifications (Karimabadi et al., 2014; Eastwood et al., 2017; Buzulukova and Tsurutani, 2022).

The motivations for studying turbulence in the magnetosheath are thus twofold. First,

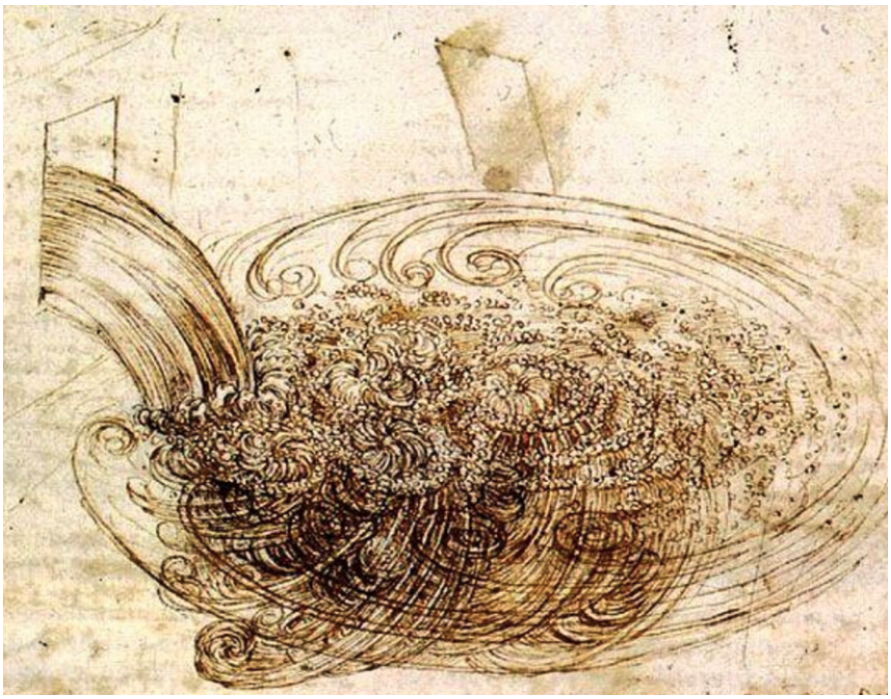


Figure 1.3: A sketch of turbulence in a water flow by Leonardo da Vinci, from his *Studies of water* (c.1510-12). Eddies and whirls of many sizes are depicted, ranging from large to small, representing what we now know as the turbulent cascade. Credit: Royal Collection Trust, reproduced from Colagrossi et al. (2021).

our understanding of the fundamental physics of turbulence is still poor – despite having known the equations which govern the behaviour of a fluid in motion for nearly two centuries (Navier, 1822; Stokes, 1845), and for a plasma for nearly a century (Alfvén, 1942; Vlasov, 1945), the inherent nonlinearities render them unsolvable. As such, how the nonlinear dynamics should behave is not certain, and how they generate structures and processes which arrange themselves self-consistently to give rise to kinetic-scale dissipation is generally unclear. It is important to identify these dissipative processes and structures because they can have tangible consequences for how the energy is partitioned. Second, since the magnetosheath represents the first link in the solar wind–geospace impact chain, it is important to understand the nature of the turbulence in this region, which is necessarily different to the pristine solar wind due to processing by the bow shock and dynamics driven within the magnetosheath itself. How the turbulent fluctuations and kinetic processes come together to heat the plasma, transport energy, and drive energetic phenomena incident on the magnetopause is a fundamental open question.

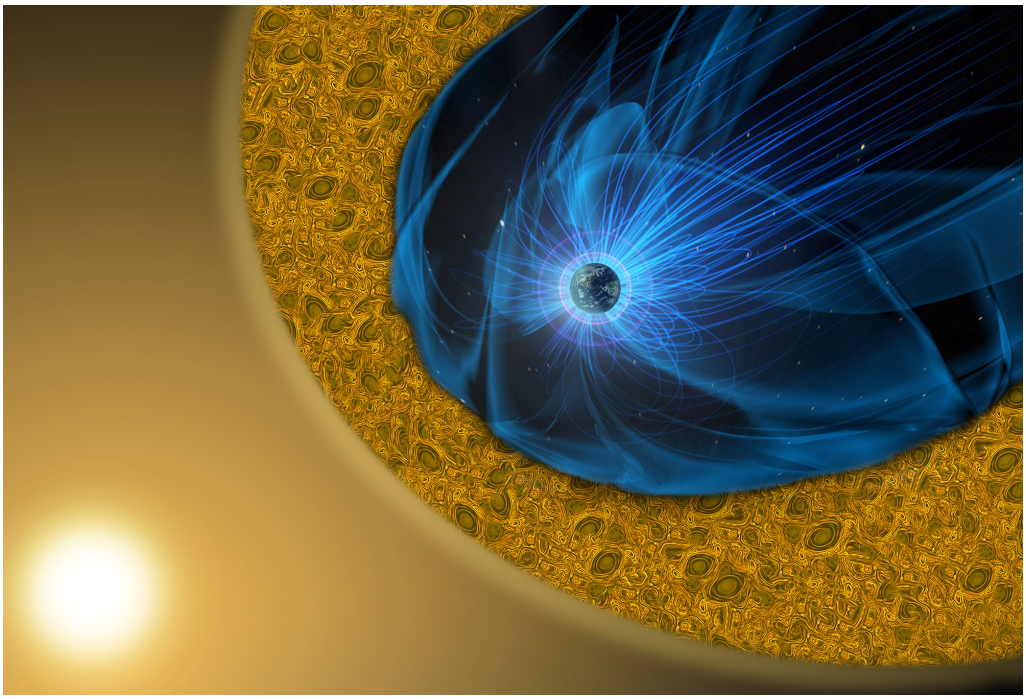


Figure 1.4: An artist's impression of Earth's turbulent magnetosheath. Credit: NASA.

A key advantage of studying turbulence in near-Earth space plasmas is the availability and high precision of in situ measurements (e.g. Horbury et al., 2012), which allow us to probe the small-scale dynamics of well-developed turbulence in these systems. In contrast, astrophysical plasmas can only be observed remotely, and laboratory plasma measurements are subject to instrumental limitations and limited ranges of scale. We are fortunate, then, to have numerous space missions making field and particle measurements throughout the heliosphere. Indeed, there is an extensive body of literature looking at turbulence in the solar wind (Coleman, 1968; Bruno and V. Carbone, 2013; Alexandrova et al., 2013; Verscharen et al., 2019); within Earth's magnetosheath, plasma sheet, and ionosphere (Rakhmanova et al., 2021; Stepanova et al., 2022); and in the magnetospheres of other planets (e.g. Vasavada and Showman, 2005; Papen et al., 2014). The wealth of in situ measurements provide an opportunity to contrast turbulence across different environments.

Of particular importance to space plasma turbulence is the Magnetospheric Multiscale (MMS) mission (Burch et al., 2016), which has provided nearly 10 years of multi-point measurements with unprecedented resolution, ushering in a new era of space plasma

turbulence research thanks to its instrumental capabilities. What sets MMS apart is that it can probe kinetic-scale particle structures and employ multi-spacecraft methods using its four identical satellite probes, facilitating in-depth studies of the turbulent dynamics and collisionless plasma phenomena occurring in the magnetosheath. These measurements are key to making progress on disentangling collisionless dissipation.

In this thesis, MMS observations of Earth's magnetosheath are used to learn about the fundamental physics of turbulence. In particular, how the electric fields within a turbulent plasma are generated by the nonlinear dynamics is explored, quantifying how the relative contribution of different electric fields arising due to the nonlinear dynamics varies as a function of the plasma conditions. Beyond this, the key open question of how collisionless processes lead to net dissipation is explored. In particular addressing how kinetic microinstabilities associated with local generation of anisotropic particle velocity distributions contribute to the dissipation process in the magnetosheath. The link between turbulence and thermalisation is investigated, with aims to reconcile the complex distributions inherent in collisionless plasmas with turbulent energy conversion and dissipation. These insights help begin to inform a broader understanding of the different regimes of turbulent behaviour across space and astrophysical plasmas. The structure of this thesis is outlined in the following.

Chapter 2 introduces the key concepts required to understand magnetosheath turbulence. The description starts with collisionless plasma physics, then the origin and salient properties of the near-Earth plasma environment, before introducing turbulence theory, and finally discussing kinetic microinstabilities.

Chapter 3 covers relevant data analysis methods, including a brief introduction to MMS instrumentation and data processing. Particular emphasis is placed on the computation of power spectral density, the estimation of spatial gradients via multi-spacecraft techniques, and Taylor's hypothesis, all crucial to undertaking turbulence studies.

Chapter 4 investigates aspects of the fundamental physics of turbulence, determining how

competing nonlinear forces in the magnetosheath behave relative to one another, and how this relative behaviour varies under different plasma conditions. The results suggest that ratios of electric field terms, and nonlinear versus linear contributions, depend both on ambient conditions and the driver of turbulence. Consequences for a variety of plasma regimes are discussed, also providing observational constraints on the assumptions going into turbulence theories.

Chapter 5 addresses the open question of collisionless dissipation by investigating the link between turbulent fluctuations and kinetic microinstabilities associated with temperature anisotropies in the plasma. The energy conversion stage of dissipation is quantified, revealing enhanced levels in local regions with unstable conditions. The findings suggest that turbulence is driving the plasma into a state under which instability mechanisms can redistribute the energy. The results have consequences for how turbulent fluctuations influence thermodynamic regulation of the magnetosheath.

The collisionless nature of the plasma means that turbulent energisation processes can lead to more complex distributions than simple anisotropic Maxwellians. Chapter 6 analyses these complex deformations to the velocity distribution function and explores their relationship with the energisation and kinetic instabilities discussed in Chapter 5. More complex distributions are found when ion populations are unstable, suggesting that not only is turbulent energy conversion triggering kinetic microinstabilities, but it is preferentially creating non-Maxwellian features as well. These results help to reconcile the coupling between non-Maxwellianity and turbulent fluctuations, representing a step toward understanding the thermalisation processes in turbulent collisionless plasmas.

Finally, Chapter 7 summarises the thesis and discusses implications for our current understanding of plasma turbulence, suggesting potential avenues for future work.

Chapter 2

Theoretical Background

2.1 Plasma Physics

Plasma is the fourth fundamental state of matter, made up of superheated gas that has become ionised to the extent that its dynamics are dominated by electromagnetic forces. Consisting mostly of ions and free electrons, plasmas are characterised by collective particle behaviour and electrical conductivity. Plasma was first discovered in laboratory experiments by Sir William Crookes (1879) which he reported on as 'radiant matter' in a lecture to the British Association for the Advancement of Science in Sheffield. The term plasma was coined by Irving Langmuir (1928) as an analogy to blood plasma when describing ionized regions in gas discharges. Over the course of the following century, the study of plasma physics has continuously expanded into a vast field, applicable to numerous physical systems from the natural to the laboratory and astrophysical. In fact, it is now known that the vast majority of baryonic matter in the Universe – from 90–99.9% – exists in the plasma state (e.g. Buchanan, 2016).

The following sections formally introduce the concept of a plasma, then outline important theoretical frameworks upon which Chapters 4–6 are based. Descriptions of plasma physics take after Baumjohann and Treumann (1996), Boyd and Sanderson (2003), and Gurnett and Bhattacharjee (2005). Since plasmas are made up of multiple particle species,

species-specific variables are hereafter denoted by a generalised subscript s, which can be specified to e for the electron species, and i for the ion species, typically taken to be protons. Throughout the thesis, unless stated otherwise, temperatures are taken in energy units (so the factor of k_B is not written down).

2.1.1 Definition of a Plasma

Plasmas are quasineutral, which means that the concentration of positive and negative free charges are approximately equal, leading to a state of macroscopic neutrality. To maintain quasineutrality, a volume element must contain sufficient particles to shield the microscopic electromagnetic fields arising from individual charges.

The Coulomb potential of each charge q,

$$\phi_C = \frac{q}{4\pi\epsilon_0 r}, \tag{2.1}$$

is shielded by other charges, resulting in an exponentially decaying Debye potential,

$$\phi_D = \frac{q}{4\pi\epsilon_0 r} \exp\left(-\frac{r}{\lambda_D}\right). \tag{2.2}$$

Here, λ_D is the Debye length, which is the characteristic length over which the Debye potential falls off by a factor of 1/Euler's number. The electron Debye length is the smallest meaningful characteristic scale in a plasma, given by

$$\lambda_D = \sqrt{\frac{\epsilon_0 T_e}{e^2 n_e}}, \tag{2.3}$$

where T_e and n_e are the electron temperature and number density, respectively. For collective shielding to occur, the physical dimension of the system, L, must greatly exceed the Debye length. This constitutes the first plasma criterion,

$$\boxed{\lambda_D \ll L.} \tag{2.4}$$

For shielding to be effective, there must be sufficient particles within a sphere of radius λ_D, given by the plasma parameter Λ

$$\boxed{\Lambda = n_e \lambda_D^3 \gg 1,} \tag{2.5}$$

which constitutes the second plasma criterion. This criterion means that the mean potential energy of a particle due to its nearest neighbour must be much smaller than its mean energy $k_B T_e$ (or T_e in energy units, as used hereafter). If the first and second criteria are satisfied, we observe collective plasma behaviour.

If an external force is applied to a fully ionised plasma which leads to a local reduction in electron number density, electrons will be accelerated to maintain quasineutrality. Such a situation causes an oscillation of the electrons with respect to the ions, known as a Langmuir wave, in which the electrostatic force acts as the restoring force for fast collective electron oscillations. These oscillations occur at the plasma frequency ω_{pe},

$$\omega_{pe} = \sqrt{\frac{n_e e^2}{m_e \epsilon_0}}. \tag{2.6}$$

If the plasma is not fully ionised, collisions with neutrals can inhibit the collective plasma behaviour. If τ_n is the average time between electron–neutral collisions, then for the electrons to be unaffected by collisions the plasma oscillations must occur much more rapidly than τ_n, such that

$$\boxed{\omega_{pe} \tau_n \gg 1.} \tag{2.7}$$

This is the third plasma criterion. When satisfied, this condition means that electromagnetic effects will dominate over ordinary kinetic gas processes.

Additionally, electromagnetic waves are unable to propagate through a plasma at frequencies $\lesssim \omega_{pe}$ because the Debye shielding by free charges serves to exponentially reduce the wave amplitude. The exponential decay length over which this shielding occurs is given

by the inertial length for a given species s,

$$d_s = \frac{v_{A,s}}{|\Omega_s|} = \frac{c}{\omega_{ps}}, \tag{2.8}$$

where

$$v_{A,s} = \frac{B_0}{\sqrt{n_0 m_s}} \tag{2.9}$$

is the Alfvén speed, $B_0 = |\langle \mathbf{B} \rangle|$ is the background magnetic field strength, n_0 is the background number density, Ω_s is the gyrofrequency (see Section 2.1.2), c is the speed of light in a vacuum, and ω_{ps} is the plasma frequency. The Alfvén speed represents the fastest speed at which magnetic signals can propagate through a plasma – an important plasma parameter in the Magnetohydrodynamics (MHD) description (see Section 2.1.3). The Alfvén speed of the ions is much lower than the electrons, since the greater inertia of the ions slows down the restoring force (magnetic tension – see Section 5.1) of the wave.

2.1.2 Kinetic Theory

Field Equations

Electromagnetic fields influence the motion of charged particles, which in turn give rise to the fields via Maxwell's equations,

$$\nabla \cdot \mathbf{E} = \frac{\rho}{\epsilon_0}, \tag{2.10}$$

$$\nabla \cdot \mathbf{B} = 0, \tag{2.11}$$

$$\nabla \times \mathbf{E} = -\frac{\partial \mathbf{B}}{\partial t}, \tag{2.12}$$

$$\nabla \times \mathbf{B} = \mu_0 \mathbf{j} + \epsilon_0 \mu_0 \frac{\partial \mathbf{E}}{\partial t}, \tag{2.13}$$

where $\mathbf{B}$ is the magnetic field, and $\mathbf{E}$ is the electric field. The first expression shows that electric space charge density, $\rho = e(n_i - n_e)$, is the source of electric fields. The second expression indicates that there are no sources or sinks of magnetic field (no 'monopoles'), so all magnetic field lines are closed. The third and fourth equation show that the electric

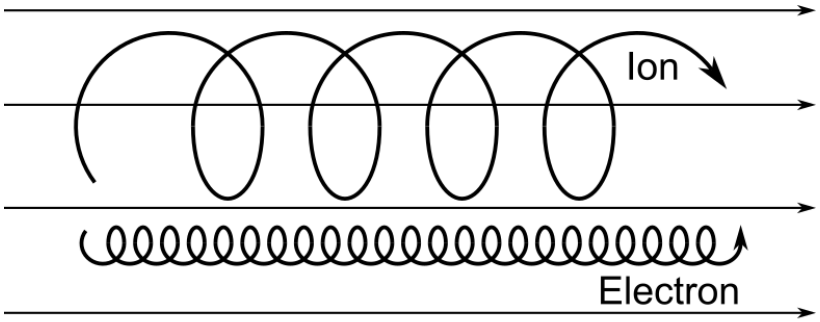


Figure 2.1: Helicoidal motion of charged particles moving along a uniform magnetic field. Gyro-orbits are not to scale. After Baumjohann and Treumann (1996).

and magnetic fields are coupled by their spatiotemporal variations, although for negligible fast electric field fluctuations the magnetic field structure is generated by current density $\mathbf{j} = e(n_i\mathbf{v}_i - n_e\mathbf{v}_e)$.

Single Particle Motion

Before considering collective behaviour, it is useful to discuss the motion of individual charges within a plasma. The velocity $\mathbf{v}$ of a particle will respond to electromagnetic forcing in accordance with the Lorentz equation,

$$m_s \frac{d\mathbf{v}}{dt} = q_s \left(\mathbf{E} + \mathbf{v} \times \mathbf{B}\right), \tag{2.14}$$

where m_s and q_s are the mass and charge of species s. Charged particles will undergo gyromotion around magnetic field lines, circulating at the gyrofrequency,

$$\Omega_s = \frac{q_s B}{m_s}, \tag{2.15}$$

where $B = |\mathbf{B}|$ is the magnitude of $\mathbf{B}$. The radius of this motion is the gyroradius,

$$\rho_s = \frac{v_{\perp,s}}{\Omega_s}, \tag{2.16}$$

where $v_\perp$ is the component of particle velocity perpendicular to the magnetic field. The motion of charged particles along a uniform $\mathbf{B}$ is illustrated in Figure 2.1.

Particle Drifts

In the presence of an electric field, the guiding center (the center of the gyrating orbit) can itself undergo drift motion. In an electrostatic electric field, the guiding center is subject to the $E \times B$ *drift*, given by

$$\mathbf{v}_E = \frac{\mathbf{E} \times \mathbf{B}}{B^2}. \tag{2.17}$$

This drift is independent of the particle mass and charge, so electron and ions move in the same direction. As such, this drift does not cause a current. It is also related to the Lorentz transformation, as for a free particle $\mathbf{E} = -\mathbf{v} \times \mathbf{B}$. In the case of a slowly varying electric field, an additional drift component known as the *polarisation drift* affects the guiding center, given by

$$\mathbf{v}_P = \frac{1}{\Omega_s B} \frac{d\mathbf{E}_\perp}{dt}. \tag{2.18}$$

In this case, the drift velocity depends on the charge and mass of the particles, and is directed along the perpendicular component of the electric field (in opposite directions for ions and electrons). This leads to a polarisation current which is mostly carried by the plasma since $m_i \gg m_e$.

In addition to the aforementioned electric drifts, there are several drift processes caused by weak variations in the magnetic field. Within a magnetic gradient ∇B the gyroradius of the particle orbits will be larger in the part of the orbit with stronger magnetic field strength, and vice versa. This leads ions and electrons to drift in opposite directions with the velocity

$$\mathbf{v}_\nabla = \frac{m v_\perp^2}{2qB^3}(\mathbf{B} \times \nabla B). \tag{2.19}$$

As well as linear gradients, curvature in the magnetic field can cause a drift motion due to the centrifugal force experienced by particles due to their parallel velocity. In terms of the local radius of curvature, $\mathbf{R}_c$, the *curvature drift* is given by

$$\mathbf{v}_R = \frac{m_s v_\parallel^2}{q_s} \frac{\mathbf{R}_c \times \mathbf{B}}{R_c^2 B^2}. \tag{2.20}$$

This drift motion is perpendicular to the magnetic field and its local curvature, and is proportional to the parallel particle energy $\frac{1}{2}m_s v_\parallel^2$. Overall, the drift caused by a generalised force $\mathbf{F}$ is given by

$$\mathbf{v}_F = \frac{1}{\Omega_s}\left(\frac{\mathbf{F}}{m_s} \times \frac{\mathbf{B}}{B}\right), \tag{2.21}$$

so that by choosing an appropriate force term the particle drifts can all be described.

Exact Phase Space Density

The most complete description of a plasma constitutes an N-body problem, where the position and velocity of every particle must be known. Only with this information is it possible to solve the equations of motion which specify the trajectories individual particles follow in response to microscopic fields. The position and velocity of every particle can be represented in a 6D coordinate system called the phase space, which has the axes $(\mathbf{x}, \mathbf{v})$. The exact number density of a single j-th particle at time t is

$$\mathcal{F}_j\left(\mathbf{x}, \mathbf{v}, t\right) = \delta(\mathbf{x} - \mathbf{x}_j(t))\delta(\mathbf{v} - \mathbf{v}_j(t)), \tag{2.22}$$

where

$$\delta(\mathbf{x} - \mathbf{x}_j(t)) = \delta(x - x_j)\delta(y - y_j)\delta(z - z_j), \tag{2.23}$$

$$\delta(\mathbf{v} - \mathbf{v}_j(t)) = \delta(v_x - v_{x,j})\delta(v_y - v_{y,j})\delta(v_z - v_{z,j}), \tag{2.24}$$

are three-dimensional Dirac delta functions in position and velocity space. The total exact number density is given by the sum over Equation 2.22.

The Distribution Function

Unfortunately, considering the evolution of exact phase space density under the influence of microscopic electromagnetic fields becomes intractable for even a small number of particles, let alone sufficient numbers to validate the second plasma criterion (Equation 2.5). In systems with large numbers of particles, it becomes convenient to smooth out

phase space by defining the average number density of particles in a small phase space volume $d^3x\, d^3v$. The total number of particles in the system N is then defined as

$$N = \int_{-\infty}^{\infty} f(\mathbf{x}, \mathbf{v}, t)\, d^3x\, d^3v, \tag{2.25}$$

where $f(\mathbf{x}, \mathbf{v}, t)$ is termed the distribution function. If the plasma is made up of multiple species, it is necessary to define a distribution function of each species s.

The equation which describes the evolution of the distribution function in response to macroscopic fields and interparticle collisions is called the Boltzmann equation (after Boltzmann, 1896), given by

$$\frac{df_s}{dt} \equiv \frac{\partial f_s}{\partial t} + \mathbf{v} \cdot \nabla_{\mathbf{x}} f_s + \frac{q_s}{m_s} (\mathbf{E} + \mathbf{v} \times \mathbf{B}) \cdot \nabla_{\mathbf{v}} f_s = \frac{\delta_c f_s}{\delta t}, \tag{2.26}$$

where $\delta_c f_s / \delta t$ is the collision operator. In most space plasmas, collisions are negligible compared to long-range collective forces (e.g. Verscharen et al., 2019, see Section 2.1.6), so the collision operator goes to zero and we get the Vlasov equation (after Vlasov, 1945),

$$\frac{df_s}{dt} \equiv \frac{\partial f_s}{\partial t} + \mathbf{v} \cdot \nabla_{\mathbf{x}} f_s + \frac{q_s}{m_s} (\mathbf{E} + \mathbf{v} \times \mathbf{B}) \cdot \nabla_{\mathbf{v}} f_s = 0. \tag{2.27}$$

Macroscopic Quantities

Assessing the full distribution function reveals information about the whole of 6D phase space, but often it is useful to measure macroscopic quantities, such as density, bulk flow velocity, average temperature, etc. These quantities depend only on space and time, so we need to integrate over velocity space to obtain them. Such integrals must be weighted by $f(\mathbf{x}, \mathbf{v}, t)$, multiplied by the outer (dyadic) product of the velocity $\mathbf{v}$ raised to the i-th power. These integrals are called velocity moments, where the i-th $= 0, 1, 2, 3$ velocity moments correspond to useful macroscopic quantities,

$$\text{number density, } n_s = \int_V f_s(\mathbf{v})\, d^3v, \tag{2.28}$$

$$\text{bulk velocity, } \mathbf{v}_s = \frac{1}{n_s}\int_V \mathbf{v} f_s(\mathbf{v})\, d^3v, \tag{2.29}$$

$$\text{pressure tensor, } \mathbf{P}_s = m_s \int_V (\mathbf{v}-\mathbf{v}_s)(\mathbf{v}-\mathbf{v}_s) f_s(\mathbf{v})\, d^3v, \tag{2.30}$$

$$\text{heat flux vector, } \mathbf{q}_s = \frac{m_s}{2}\int_V (\mathbf{v}-\mathbf{v}_s)\cdot(\mathbf{v}-\mathbf{v}_s)(\mathbf{v}-\mathbf{v}_s) f_s(\mathbf{v})\, d^3v. \tag{2.31}$$

The number density n_s is the number of particles from species s per unit volume. The bulk velocity $\mathbf{v}_s$ is the average velocity of the bulk flow. The pressure tensor $\mathbf{P}_s = [P_{s,ij}]$ is the rate of momentum transfer in direction i across surface j in the frame of reference moving with the bulk velocity. The heat flux vector $\mathbf{q}_s$, which is the trace of the heat flux tensor $\mathbf{Q}_s$, corresponds to the transfer of heat in a direction which need not be aligned with the bulk velocity.

The pressure tensor can be expressed as $n_s\mathbf{T}_s$, where $\mathbf{T}_s$ is the kinetic temperature of the distribution. As we will see later, collisionless plasmas are rarely in a state of thermodynamic equilibrium, so this temperature does not correspond to a thermodynamic temperature in the traditional sense. The isotropic temperature T_s is given by the trace $\mathrm{Tr}[\mathbf{T}_s]/3$, under the assumption that off-diagonal components are negligible. In an anisotropic plasma, the temperatures parallel and perpendicular to the magnetic field are defined as

$$T_{s,\parallel} = \mathbf{b}^T\mathbf{T}_s\mathbf{b}, \tag{2.32}$$

$$T_{s,\perp} = (\mathrm{Tr}[\mathbf{T}_s] - T_{s,\parallel})/2, \tag{2.33}$$

where $\mathbf{b} = \mathbf{B}/|\mathbf{B}|$ is the local magnetic field unit vector. It is usually the case that off-diagonal components are negligible, and the temperature is symmetric with respect to the perpendicular directions. When this does not hold, the distribution is said to be agyrotropic.

2.1.3 Magnetohydrodynamics

Magnetohydrodynamics (MHD) (Alfvén, 1942) is a hydrodynamic theory which treats the plasma as an electrically charged fluid responding to external and internal magnetic

fields. The system is highly complex because when the charged fluid responds to external fields it generates further fields by nature of its motion. The generalisation of this theory is the multi-fluid theory of plasmas, of which ideal MHD is a simplifying approximation where the plasma is treated as a single set of mass-weighted fluid variables. To explain the work presented in this thesis, it is necessary to introduce some elements of both ideal MHD as well as multi-fluid theory.

The Moment Equations

In many plasma physics systems, we are more interested in the macroscopic quantities than the full distribution function. In this case, a system of equations called the moment equations can be used. These equations are obtained (for a collisionless plasma) by taking velocity moments of the Vlasov equation (Equation 2.27).

The zeroth moment equation,

$$\frac{\partial n_s}{\partial t} + \nabla \cdot (n_s \mathbf{v}_s) = 0, \tag{2.34}$$

is simply the mass continuity equation. Multiplying by the charge q_s and summing over all species yields the charge continuity equation. The first moment equation (which is derived fully in Appendix A.1),

$$\frac{\partial}{\partial t}(m_s n_s \mathbf{v}_s) + \nabla \cdot (m_s n_s \mathbf{v}_s \mathbf{v}_s) = q_s n_s (\mathbf{E} + \mathbf{v}_s \times \mathbf{B}) - \nabla \cdot \mathbf{P}_s, \tag{2.35}$$

is called the momentum equation (or the momentum density conservation equation), which corresponds to Newton's second law. The trace of the second moment equation (which is derived fully in Appendix A.3),

$$\frac{\partial}{\partial t}\left[\frac{1}{2} m_s n_s v_s^2 + \frac{3p_s}{2}\right] + \nabla \cdot \left[\frac{1}{2} m_s n_s v_s^2 \mathbf{v}_s + \frac{3p_s \mathbf{v}_s}{2} + \mathbf{v}_s \cdot \mathbf{P}_s + \mathbf{q}_s\right] - \mathbf{E} \cdot \mathbf{j}_s = 0, \tag{2.36}$$

gives the energy equation, which states the conservation of energy for species s. The total energy conversion, $\mathbf{j} \cdot \mathbf{E} = \sum_s \mathbf{j}_s \cdot \mathbf{E}$, is a useful quantity which encapsulates the

reversible (for a collisionless plasma) conversion of energy between electromagnetic fields and particles. The $\mathbf{j} \cdot \mathbf{E}$ term, and decompositions based on different components of the electric field, is a key measure of energy conversion which will be used throughout this thesis, particularly in Chapter 5 (see also Section 2.3.4).

The Closure Problem

The precise reasons for the introduction of Equations 2.35 and 2.36 will become clear in subsequent sections, however it is worth briefly mentioning a consequence of their form which is central to the difficulty of analytically describing the evolution of plasmas. This problem is called the closure problem, which makes it impossible to close the system of moment equations without specifying an equation of state or solving an infinite number of equations.

This problem arises due to the $\mathbf{v} \cdot \nabla f_s$ term in the Vlasov equation, which couples the i-th moment of the Vlasov equation to the $(i+1)$-th moment of the velocity distribution. As such, the number of unknown moments always exceeds the number of equations. There isn't a formal way to determine the relationship between the $(i+1)$-th and i-th moment, however the external imposition of an equation of state relating $\mathbf{P}_s$ to n_s is most commonly employed method of closing the problem analytically. However, this approach is more successful in a collisional plasma (which is closer to thermodynamic equilibrium), than a collisionless one. Additionally, the closure problem can be avoided in observational studies by using a measured variable – usually $\mathbf{P}_s$ – to close the system.

Single-Fluid Theory

In single-fluid theory, we treat the plasma as a conducting fluid supporting electromagnetic fields and currents. This treatment leads to the MHD equations of a plasma, which can be derived using the following single-fluid variables:

$$\text{charge density, } \rho = e(n_i - n_e) \approx 0 \text{ due to quasineutrality,} \tag{2.37}$$

$$\text{current density, } \mathbf{j} = e(n_i \mathbf{v}_i - n_e \mathbf{v}_e), \tag{2.38}$$

$$\text{single-fluid number density, } n = \frac{m_e n_e + m_i n_i}{m_e + m_i}, \tag{2.39}$$

$$\text{single-fluid mass, } m = m_e + m_i = m_i \left(1 + \frac{m_e}{m_i}\right), \tag{2.40}$$

$$\text{single-fluid velocity, } \mathbf{u} = \frac{m_i n_i \mathbf{v}_i + m_e n_e \mathbf{v}_e}{m_e n_e + m_i n_i}. \tag{2.41}$$

From these variables, one obtains the MHD continuity equation by multiplying Equation 2.34 by m_i for the ions and m_e for the electrons, summing the resulting equations, and simplifying as

$$\frac{\partial n}{\partial t} + \nabla \cdot (n\mathbf{u}) = 0. \tag{2.42}$$

Obtaining the MHD momentum conservation equation is more involved due to the nonlinear terms. The process involves taking the multi-species momentum equations (Equation 2.35), multiplying the electron equation by m_i and the ion equation by m_e, adding the equations, making use of the definitions of $\mathbf{P} = \mathbf{P}_e + \mathbf{P}_i$, ρ, $\mathbf{j}$, and finally invoking $n_e \approx n_i$ and $m_e \ll m_i$, resulting in

$$\frac{\partial (nm\mathbf{u})}{\partial t} + \nabla \cdot (nm\mathbf{u}\mathbf{u}) = -\nabla \cdot \mathbf{P} + \rho\mathbf{E} + \mathbf{j} \times \mathbf{B}, \tag{2.43}$$

where $\rho\mathbf{E} \approx 0$ due to quasineutrality.

2.1.4 Generalised Ohm's Law

Equation 2.43 introduced the current density as a new variable, so since the plasma is a conducting medium, an expression describing the evolution of $\mathbf{j}$ in response to the electric field $\mathbf{E}$ is required to close the system. This equation is known as generalised Ohm's law. The equation is obtained by subtracting the two-fluid momentum equations (2.35); a full derivation is provided in Appendix A.2.

The full expression for generalised Ohm's law in a collisionless plasma is

$$\mathbf{E} = \underbrace{-\mathbf{u}\times\mathbf{B}}_{\mathbf{E}_{MHD}} + \underbrace{\frac{1}{ne}\mathbf{j}\times\mathbf{B}}_{\mathbf{E}_{Hall}} - \underbrace{\frac{1}{ne}\nabla\cdot\mathbf{P}_e}_{\mathbf{E}_{P_e}} + \underbrace{\frac{m_e}{ne^2}\left[\nabla\cdot\left(\mathbf{uj}+\mathbf{ju}-\frac{\mathbf{jj}}{ne}\right)+\frac{\partial\mathbf{j}}{\partial t}\right]}_{\mathbf{E}_{inertia}} + \underbrace{\sum_{\ell=1}^{\infty}\left(-\frac{m_e}{m_i}\right)^{\ell}\mathcal{M}_\ell}_{\mathbf{E}_{\delta m_e}}, \tag{2.44}$$

where underbraces denote the short-hand names of each term, and where the finite electron mass corrections ($\mathbf{E}_{\delta m_e}$) are defined using (e.g. Stawarz et al., 2021)

$$\mathcal{M}_\ell = \frac{2}{ne}\mathbf{j}\times\mathbf{B} - \frac{1}{ne}\nabla\cdot\mathbf{P} + \frac{m_e}{ne^2}\left[\nabla\cdot\left(\mathbf{uj}+\mathbf{ju}-(1+2\ell)\frac{\mathbf{jj}}{ne}\right)+\frac{\partial\mathbf{j}}{\partial t}\right]. \tag{2.45}$$

There are many terms in Equation 2.44, which amount to successive corrections to the Lorentz force acting upon the mass-weighted single fluid plasma motion, because of the absence of electrical resistivity, $\eta = m_e\nu_c/ne^2$, where ν_c is the collision frequency. If $\eta \neq 0$ then this leads to an electric field, $\mathbf{E}_\eta = \eta\mathbf{j}$, which can dominate $\mathbf{E}$, allowing field-particle interactions to heat the plasma at the expense of electromagnetic energy. The MHD description provided in this thesis is 'ideal', referring to the $\eta = 0$ case, so that the resistive term in generalised Ohm's law, $\mathbf{E}_\eta = \eta\mathbf{j}$ is equal to zero. This assumption is justified for near-Earth space plasmas, which are all collisionless (i.e. $\nu_c \approx 0$, see Sections 2.1.6 & 2.2), so collisional effects such as kinematic viscosity and electrical resistivity can be ignored.

Figure 2.2 illustrates the basic mechanism behind the first three terms on the right hand side of Equation 2.44. The MHD term ($\mathbf{E}_{MHD}$) is associated with the magnetic field being frozen into the plasma flow $\mathbf{u}$ at large scales (see Section 2.1.5); indeed, for an ideal MHD plasma, $\mathbf{E} = \mathbf{E}_{MHD} = -\mathbf{u}\times\mathbf{B}$. In Figure 2.2, the electric field arises to account for the deflection of positive and negative charges in opposite directions when moving through the magnetic field. The resultant electric field is directed from positive to negative charges.

The Hall term ($\mathbf{E}_{Hall}$) arises due to differential motion between ions and electrons, which can give rise to electric fields transverse to the current and magnetic field even for a collisionless plasma. Figure 2.2 shows the simple case of positive charges moving relative

to stationary negative charges. The positive charges are deflected, setting up an electric field directed to oppose the charge separation. $\mathbf{E}_{Hall}$ typically becomes important around the ion gyroradius, as below these scales the ion fluid is decoupled from the bulk flow.

The electron pressure term ($\mathbf{E}_{P_e}$) is an ambipolar electric field arising from the thermal motions of the particles, specifically due to a spatial gradient leading to a flux of momentum density from one region to another. This is illustrated in Figure 2.2, which shows that particles will be exchanged from an area of higher pressure to an area of lower pressure, setting up an electric field which acts to oppose this change.

The inertia term ($\mathbf{E}_{inertia}$) comes from the finite inertia of the electrons, preventing them from instantly responding to driving by $\mathbf{E}$. The finite-m_e correction term $\mathbf{E}_{\delta m_e}$, which comes from the Taylor expansion for small electron mass when writing the equations in terms of single-fluid variables, is observed and expected to be negligibly small (Stawarz et al., 2021, see also Chapter 4).

The combination of pressure and inertia electric fields is referred to as the non-ideal electric field,

$$\mathbf{E}' = \mathbf{E} + \mathbf{v}_e \times \mathbf{B} = \mathbf{E}_{P_e} + \mathbf{E}_{inertia}, \tag{2.46}$$

which is the contribution to $\mathbf{E}$ capable of decoupling the motion of electrons from the magnetic field. The parallel component of $\mathbf{E}'$ is important because it can lead to acceleration along magnetic field lines, a key part of the mechanisms behind particle energisation and heating. The concept of the non-ideal electric field will be drawn upon heavily in the work chapters of this thesis, particularly through $\mathbf{j}\cdot\mathbf{E}'$ as the mediator of non-ideal energy conversion (energy conversion between the fields and particles coming from sources other than convection).

2.1.5 Diffusion and Frozen-in Flux

The Induction Equation

The general induction law of MHD comes from inserting the electric field from generalised Ohm's law (Equation 2.44) into Faraday's law (Equation 2.12),

$$\frac{\partial \mathbf{B}}{\partial t} = \nabla \times \left(\mathbf{u} \times \mathbf{B} - \frac{1}{ne}\mathbf{j} \times \mathbf{B} + \frac{1}{ne}\nabla \cdot \mathbf{P}_e - \frac{m_e}{ne^2}\left[\nabla \cdot \left(\mathbf{uj} + \mathbf{ju} - \frac{\mathbf{jj}}{ne} \right) + \frac{\partial \mathbf{j}}{\partial t} \right] \right), \quad (2.47)$$

where finite-m_e corrections have been neglected. Equation 2.47 can be expressed as

$$\frac{\partial \mathbf{B}}{\partial t} = \nabla \times (\mathbf{u} \times \mathbf{B}) - \frac{1}{ne}\nabla \times (\mathbf{j} \times \mathbf{B}) - \nabla \times \mathbf{E}', \quad (2.48)$$

where the first term on the right hand side represents the magnetic field being 'frozen-in' to the plasma flow via the ideal MHD electric field (meaning magnetic flux through an arbitrary surface moving with $\mathbf{u}$ remains constant). The second term represents the decoupling of the magnetic field from $\mathbf{u}$ due to the Hall electric field (but the magnetic field remains frozen-in to the electron flow). The final term represents the effect of the non-ideal electric field in allowing the magnetic field to decouple from the electron velocity, enabling, for example, magnetic reconnection. The significance of this equation is that the balance between the terms indicates whether $\mathbf{B}$ is convected with the flow or whether it is able to decouple from the fluid motion and diffuse across the flow. The importance of the non-MHD electric fields as a function of scale will be explored in Chapter 4, with consequences for the dynamics of the system, and their impact via $\mathbf{j} \cdot \mathbf{E}'$ (see Equation 2.36; Section 2.1.4), in Chapters 5 & 6.

Magnetic Pressure

When variations are slow enough to neglect the displacement current in the plasma, the Lorentz force in the MHD momentum equation (Equation 2.43) can be rewritten using

the Ampère-Maxwell law (Equation 2.13) as

$$\mathbf{j} \times \mathbf{B} = -\frac{1}{\mu_0}\mathbf{B} \times (\nabla \times \mathbf{B}), \tag{2.49}$$

which introduces the MHD magnetic tension force. This force appears when re-arranging Equation 2.49 using the vector identity

$$\mathbf{B} \times (\nabla \times \mathbf{B}) = \frac{1}{2}\nabla(\mathbf{B} \cdot \mathbf{B}) - (\mathbf{B} \cdot \nabla)\mathbf{B}, \tag{2.50}$$

giving

$$\mathbf{j} \times \mathbf{B} = -\nabla\left(\frac{B^2}{2\mu_0}\right) + \frac{1}{\mu_0}(\mathbf{B} \cdot \nabla)\mathbf{B}. \tag{2.51}$$

The first term in Equation 2.51 corresponds to the gradient of magnetic pressure p_B, a pressure term which contributes along with the thermal pressure to the total pressure,

$$p_{total} = p_{th} + p_B, \tag{2.52}$$

where $p_{th,s}$ is typically taken as $n_s T_s$. The second term can be expressed as the divergence of the magnetic stress tensor, $\nabla \cdot (\mathbf{BB})/\mu_0$, a term which leads to tensional and torsional forces on the plasma.

The Plasma Beta

A useful parameter is the plasma beta, which is defined as the ratio of thermal to magnetic pressure,

$$\beta = \frac{p_{th}}{B^2/2\mu_0}. \tag{2.53}$$

This parameter encodes whether the fluid or the frozen-in magnetic field controls motion; when $\beta > 1$, the MHD fluid dynamics drive the system; when $\beta < 1$ magnetic forces dominate. Space plasma systems are generally referred to as low-beta for $\beta \ll 1$ and high-beta for $\beta \gtrsim 1$, including $\beta \approx 1$.

For a multi-species fluid, one can define separate β_s for individual species based on their

thermal pressure. The total β is then the sum over all β_s. For example, in the electron-ion case, the total $\beta = \beta_e + \beta_i$. Additionally, parallel and perpendicular β_s can be defined based on the pressure components $p_\parallel$ and $p_\perp$.

2.1.6 Collisions

The description of plasma physics in this chapter has been for collisionless regimes, where system dynamics occur over length scales equivalent to or smaller than those over which Coulomb interactions are able to thermalise VDFs. As such, collisionless plasma dynamics take place throughout all of phase space (Pezzi et al., 2021a), requiring a kinetic treatment of reversible microphysical processes to understand problems such as energy dissipation (e.g. Gary, 1993; Verscharen et al., 2019; Verscharen et al., 2022, some elements of which will be introduced in Section 2.4). Additionally, while interspecies collisions remain rare, sharp velocity space gradients found in strongly distorted VDFs may be able to activate intraspecies collision operators (Schekochihin et al., 2009; Pezzi et al., 2021a, and references therein).

The mean free path, $\lambda_{\rm mfp}$, encodes the characteristic distance between subsequent collisions. In a fully-ionised collisional plasma, $\lambda_{\rm mfp}$ is very long, $\gg \lambda_D$ (Baumjohann and Treumann, 1996). In collisionless plasmas, the viscous (i.e. related to momentum exchange between particles of the same species) mean free path is a ratio of the parallel thermal velocity to the intraspecies collision frequency (Howes, 2024),

$$\lambda_{\rm mfp,s} = \frac{v_{th\parallel,s}}{\nu_{ss}}, \tag{2.54}$$

where

$$v_{th\parallel,s} = \sqrt{\frac{2T_{s,\parallel}}{m_s}} \tag{2.55}$$

is the parallel thermal speed, and the collision frequency is

$$\nu_{ss} = \frac{e^4 n_s \ln\Lambda}{(4\pi\epsilon_0)^2 m_s^{1/2} T_{s,\parallel}^{3/2}}, \tag{2.56}$$

where Λ is the plasma parameter, given by Equation 2.5.

For interspecies collisions, which exchange momentum between ions and electrons and are as such related to the electrical resistivity, the following relations can be used (Boyd and Sanderson, 2003)

$$\nu_{ei} \sim \nu_{ee}, \tag{2.57}$$

$$\nu_{ie} \sim \frac{m_e}{m_i}\left(\frac{T_{e,\parallel}}{T_{i,\parallel}}\right)^{3/2}\nu_{ee} \sim \sqrt{\frac{m_e}{m_i}}\nu_{ii}. \tag{2.58}$$

Due to their mass ratio, to exchange equal and opposite momentum the ions will experience small-angle scattering (amounting to a random walk in velocity space) whereas the electrons undergo large-angle deflections, hence

$$\nu_{ee} \sim \nu_{ei} \gg \nu_{ii} \sim \sqrt{\frac{m_e}{m_i}}\nu_{ei} \gg \nu_{ie} \sim \frac{m_e}{m_i}\nu_{ei}. \tag{2.59}$$

These inequalities demonstrate that electron–electron collisions are as frequent as electron–ion, which are much more common than ion–ion, which in turn are much faster than the time it takes for ions to be affected by collisions with electrons.

Many space plasmas are considered collisionless because they are hot and rarefied, leading to very small ν and thus very large λ_{mfp}. This will be quantified in Section 2.2, but λ_{mfp} can range from comparable to several orders of magnitude larger than the system size.

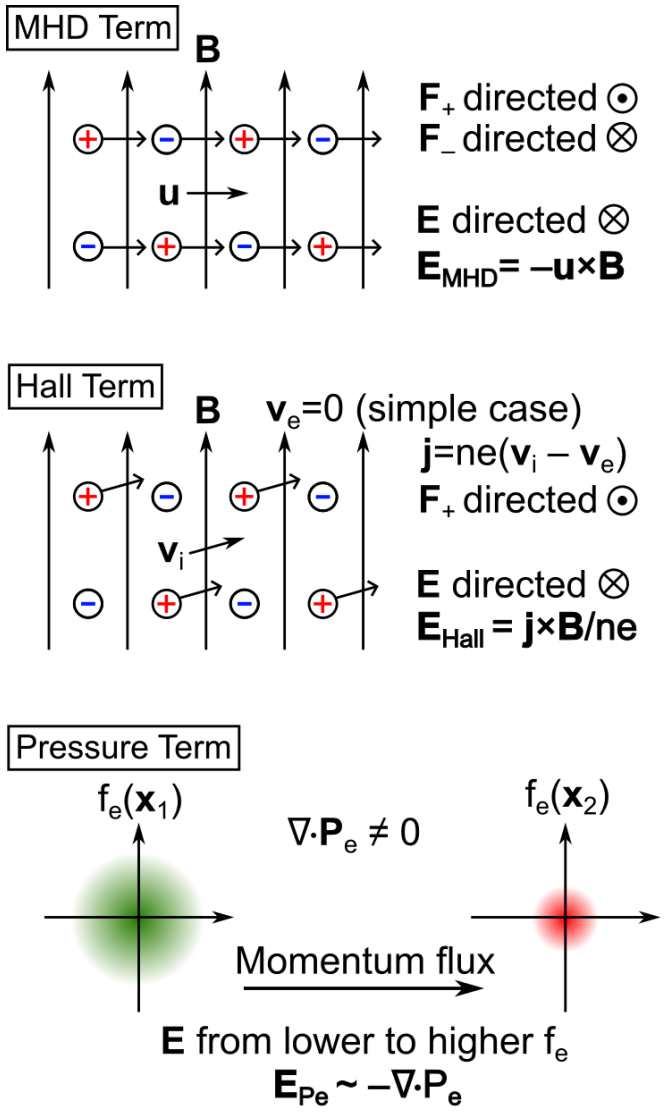


Figure 2.2: Schematics illustrating the mechanisms behind each of the principal generalised Ohm's law terms (Equation 2.44). $\mathbf{F}_+$ and $\mathbf{F}_-$ represent the force on the positive and negative charges, respectively, and $\mathbf{x}$ represents a spatial position. The MHD term shows that an electric field is set up to oppose the separation of moving positive and negative charges as they are deflected in a uniform magnetic field. The Hall term shows a simple example where the ions move relative to the electrons, the electric field accounting for their displacement due to the magnetic field. The pressure term arises from a flux of momentum from one spatial location to another, the electric field coming from the growing spatial charge imbalance.

2.2 Near-Earth Plasma Environment

The interaction between the solar wind – a dynamic, but persistent, stream of plasma emanating from the Sun – and Earth's protective magnetic field gives rise to a highly variable, structured system in the near-Earth environment. The key regions of this interaction are presented in Figure 2.3, and will be introduced in the following sections.

2.2.1 Solar Wind

The solar wind is a magnetised plasma outflow originating in the solar corona (the outermost layer of the Sun's atmosphere) and propagating approximately radially throughout the heliosphere. The history of solar wind research is rich, beginning with recognition of a link between solar activity and changes to Earth's magnetic field (Sabine, 1851; Sabine, 1852; Hodgson, 1859; Stewart, 1861). The first connection between these observations and the idea of a stream of 'corpuscular radiation' came later (Eddington, 1910; Birkeland, 1914; Chapman, 1917), where the idea was developed to explain observations of comet tails (see Verscharen et al., 2019, for a more detailed review). It was only when Parker (1958) demonstrated that a hot solar corona is not in hydrostatic equilibrium, but rather accelerated to supersonic speeds by the pressure gradient force, that the 'solar wind' was first formally predicted, promptly being measured by spacecraft a few years later (Gringauz et al., 1960; Neugebauer and Snyder, 1962). Parker's model forms the cornerstone of solar wind predictions and explanations ever since, yet there are several unsolved problems which remain unsolved, such as the mechanism behind coronal heating and acceleration (Verscharen et al., 2019; Sahraoui et al., 2020).

The solar wind is composed of radially streaming electrons and protons, with small populations of α-particles and heavy ions. Beyond around 10 R_{Sun} the radial velocity is approximately constant, and density falls off as about $n \propto r^{-2}$ (with slight deviations due to deceleration of α-particles, see e.g. Verscharen et al., 2019). The Interplanetary Magnetic Field (IMF) is frozen into the streaming solar wind plasma, which drags it out into a spiral shape in the plane of the ecliptic (Parker, 1958) due to the Sun's rotation. At 1 AU

Symbol	Corona[(1)]	Solar Wind[(1)]	Magnetosheath[(2)]	Definition
n	10^6 cm^{-3}	3 cm^{-3}	10 cm^{-3}	Number density
T	10^6 K	10^5 K	10^5—10^6 K	Temperature
B	10^5 nT	3 nT	10 nT	Magnetic field strength
u	N/A	300—800 km/s	200 km/s	Bulk flow speed
L	100 Mm	1 AU	10 R_E	System size
λ_{mfp}	10^{-4} AU	3 AU[(3)]	0.4 AU[(3)]	Mean free path
d_i	0.2 km	140 km	50 km	Ion inertial length
ρ_i	0.01 km	160 km	160 km	Ion gyroradius
d_e	5 m	3 km	1 km	Electron inertial length
ρ_e	30 cm	2 km	2 km	Electron gyroradius
β_i	$\ll 1$	~ 1	~ 10	Ion beta
β_e	$\ll 1$	~ 1	~ 1	Electron beta

Table 2.1: Typical values for a variety of important plasma parameters throughout the heliosphere. Sources of data are [(1)]Verscharen et al. (2019), [(2)]Chapter 4, and [(3)]Stawarz and Genestreti (2023). Quoted solar wind parameters are for 1 AU. Bulk speed in the corona is omitted as the solar wind is still being accelerated. λ_{mfp} depends on the type of collision (see Section 2.1.6) – values here are for the protons. For an in-depth study of solar wind plasma parameters as a function of heliocentric distance, solar cycle, and other variables, see Maruca et al. (2023).

the angle between the solar wind and IMF is around 45°, and this value asymptotes to 90° in the outer heliosphere. More details on the heliospheric magnetic field can be found in the review by Owens and Forsyth (2013). Solar wind streams are usually categorised into the slow wind (300–500 km/s) and fast wind (500–800 km/s), as well as eruptive transient events such as coronal mass ejections. The solar wind is weakly collisional, as $\lambda_{mfp} \sim L$ (especially in the outer heliosphere), and can be reasonably understood by incompressible MHD theory over large scales ($\nabla \cdot \mathbf{u} = 0$, see e.g. Grappin et al., 1990; Marsch and Tu, 1990, see also Section 2.3.2). A table of typical parameters is presented in Table 2.1, which is complemented by the reviews by Verscharen et al. (2019) and Maruca et al. (2023) for the solar wind.

2.2.2 Earth's Magnetosphere

Earth's intrinsic magnetic field arises from the convective motion of molten iron and nickel in the outer core. Any magnetic field lines that are ultimately connected to the Earth form part of a complex geomagnetic system called the magnetosphere. This magnetic field

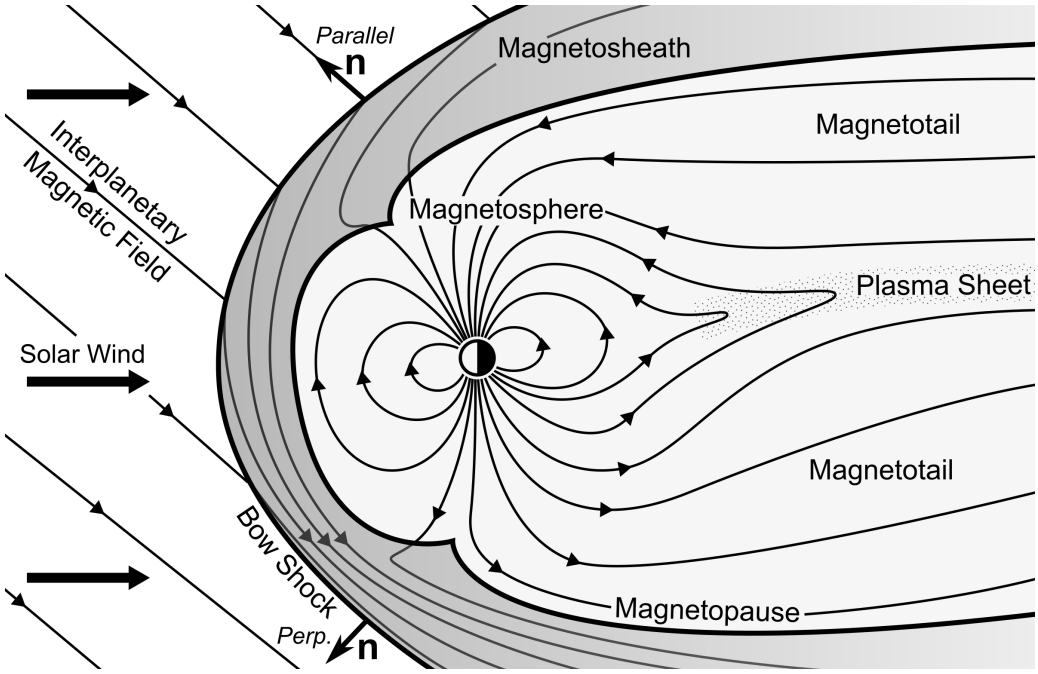


Figure 2.3: Earth's magnetosphere, showing the interface with an oblique Interplanetary Magnetic Field (IMF) (carried by the solar wind). 'Parallel' and 'Perp.' areas of the bow shock refer to the angle between the shock normal **n** and the incoming IMF. The IMF angle in the GSE X-Z plane of $\approx 135^\circ$ is rather extreme, but chosen to clearly illustrate the shock geometry. Inspired by Baumjohann and Treumann (1996).

dominates the near-Earth region of space, where it hosts numerous current systems and plasma populations. The structure of the magnetosphere is outlined in 2.3. The internal dynamo gives rise to a nearly-dipolar magnetic field, which is compressed on the dayside by the solar wind (since frozen-in plasmas cannot mix, see Sections 2.1.5 and 2.2.3) and drawn-out on the nightside into a long 'magnetotail'. Between the oppositely-directed lobes of the magnetotail is the plasma sheet, a site of magnetic reconnection. The inner structure of the magnetosphere and its connection to the surface via the ionosphere is a rich subject in itself (see Baumjohann and Treumann, 1996, for an introduction to these regions).

The interface between the magnetosphere and the IMF is called the magnetopause. This boundary moves toward and away from the Earth depending on the balance between dynamic pressure from the variable solar wind and magnetic pressure of the magnetosphere itself. Assuming the magnetospheric field is dipolar, the magnetic field strength at 0°

magnetic latitude is

$$B = \frac{\mu_0}{4\pi}\frac{M_E}{r^3}, \tag{2.60}$$

where M_E is Earth's dipole moment, $M_E = 8.05 \times 10^{22}$ Am^2. The magnetopause stand-off distance R_{mp} can be estimated by equating the solar wind dynamic pressure with the magnetic pressure from Earth's magnetic field,

$$n_{sw} m_i v_{sw}^2 = \frac{\left(2B(R_{mp})\right)^2}{2\mu_0} = \frac{\mu_0}{8\pi^2}\frac{M_E^2}{R_{mp}^6}, \tag{2.61}$$

where the factor of 2 comes from currents running along the magnetopause increasing the magnetospheric magnetic field to twice that of a dipole (Lopez and Gonzalez, 2017). Equation 2.61 can be solved for R_{mp} as

$$R_{mp} = \left(\frac{\mu_0 M_E^2}{8\pi^2 n_{sw} m_i v_{sw}^2}\right)^{1/6}. \tag{2.62}$$

Under steady solar wind conditions, $R_{mp} \approx 10$ R$_E$, and this value isn't particularly sensitive to solar wind dynamic pressure due to the sixth root (Baumjohann and Treumann, 1996).

The dayside magnetopause is a site of magnetosphere–IMF coupling, where magnetic reconnection and the Kelvin-Helmholtz instability (a fluid shear effect) are able to inject solar wind plasma into the magnetosphere (see, e.g. Johnson et al., 2014; Hesse and Cassak, 2020; H. Zhang et al., 2022). Dayside magnetic reconnection is favoured in southward (i.e. directed from above to below the ecliptic) IMF conditions due to the large magnetic shear between the solar wind and Earth's magnetic field, whereas under northward IMF other processes may become important (Kavosi and Raeder, 2015).

The magnetosphere is depicted in southward IMF conditions in Figure 2.3, where reconnection would be favoured at the subsolar (directly facing the Sun) point. Newly injected plasma circulates around the magnetosphere, convecting from the dayside to the nightside via a drift mechanism known as the Dungey cycle (Dungey, 1961). On the nightside, reconnection can occur at the plasma sheet, leading to plasma exhausts which reach the

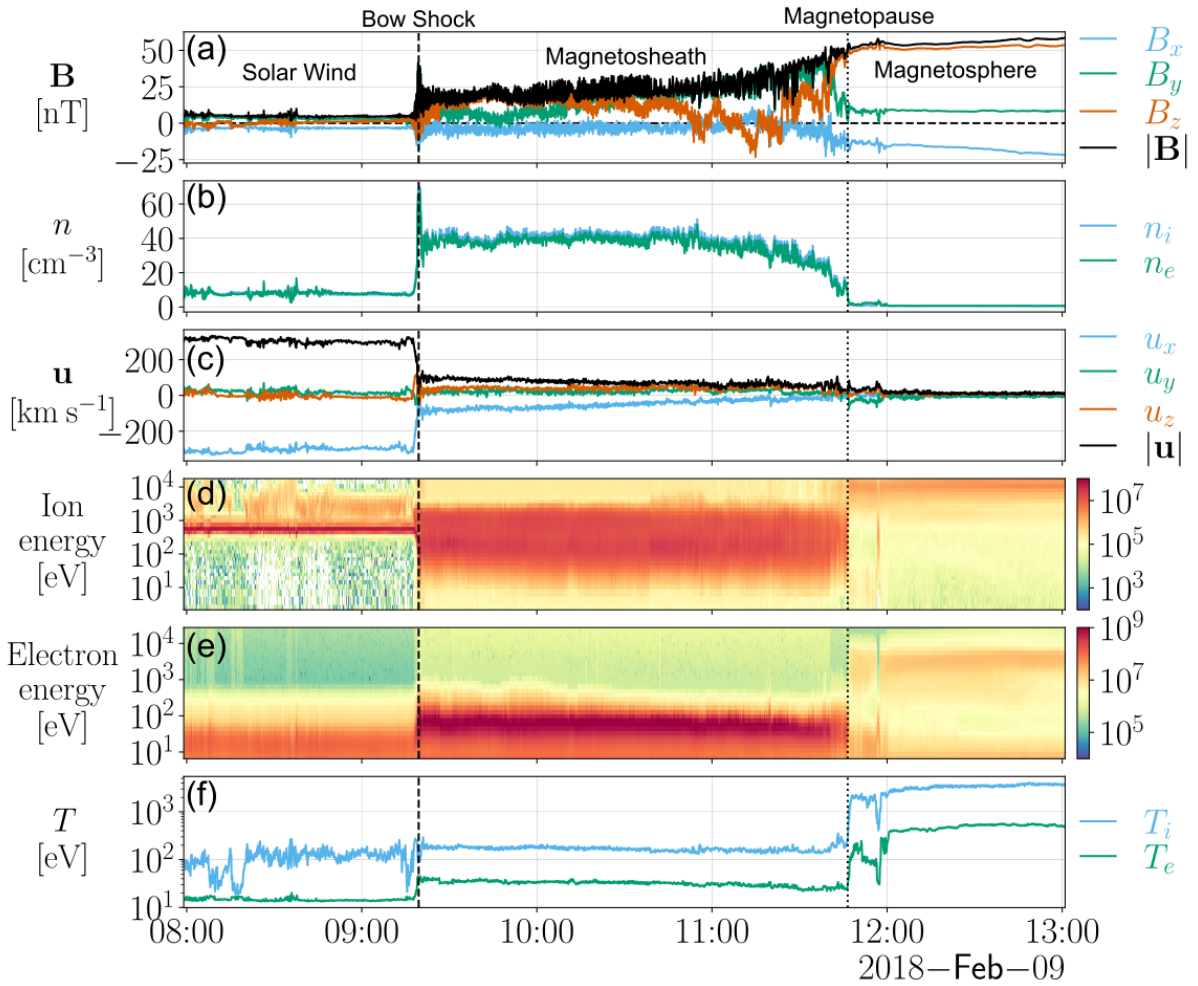


Figure 2.4: Example of spacecraft measurements passing from the solar wind, through the magnetosheath, into the magnetosphere during quasi-perpendicular conditions ($\theta_{Bn} \approx 57°$ based on magnetic coplanarity). Measurements by MMS (see Section 3.1) on 2018-02-09 from 08:00:00 to 12:45:00 UTC. Panels display: (a) the vector magnetic field; (b) the number density; (c) the MHD bulk velocity (Equation 2.41); (d) the omnidirectional ion energy spectrum; (e) the omnidirectional electron energy spectrum; (f) the temperature, which is not well-measured in the solar wind or magnetosphere due to low density. Colour-axis units in panels (d) & (e) are keV/(cm^2 s sr keV). The vertical dashed line represents the approximate location of the bow shock, and the vertical dotted line represents the approximate location of the magnetopause. Vectors are in GSE coordinates.

inner regions of the magnetosphere and cause space weather with potentially wide-ranging socioeconomic impacts (e.g. Eastwood et al., 2017; Buzulukova and Tsurutani, 2022).

2.2.3 The Magnetosheath

When a supersonic flow encounters an obstacle it is decelerated and deflected, causing a bow shock. Since the solar wind is unable to directly penetrate into the magnetosphere,

it slows from supersonic to subsonic flow within a narrow region upstream of the magnetopause known as the magnetosheath (Baumjohann and Treumann, 1996). The shocked plasma which makes up the magnetosheath is slower, hotter, and more compressed than the solar wind, as shown in Table 2.1, and it is host to enhanced fluctuation amplitudes, large variations in plasma parameters, and a variety of plasma structures. Understanding dynamics in the magnetosheath is key to characterising magnetosphere–solar wind coupling (e.g. Sahraoui et al., 2020).

The local conditions of the magnetosheath depend heavily on upstream properties, particularly the angle θ_{Bn} (0–90°) between the IMF and the normal to the bow shock (e.g Greenstadt, 1972). When $\theta_{Bn} < 45°$ the shock is referred to as quasi-parallel, otherwise it is quasi-perpendicular. Magnetosheath properties downstream of these shock configurations are quite variable, in particular the nature of the turbulence (which will be further discussed in Section 2.3). Quasi-parallel regions typically have a more turbulent upstream ('foreshock'), whereas quasi-perpendicular shocks have a more clearly defined transition region due to rapid deceleration of the solar wind plasma (Johlander et al., 2018).

An example of how the plasma conditions change between the solar wind, magnetosheath, and magnetosphere is shown in Figure 2.4. In this transit of a quasi-perpendicular region, it is demonstrated that the magnetosheath plasma is compressed, decelerated, and heated, with enhanced magnetic field strength and strong fluctuations. Inspection of panels 2.4 (d) & 2.4 (e) shows the vastly different energy spectrum in each region, where the solar wind ions exhibit a strong beam with a weaker secondary beam corresponding to the alpha particles, and the electrons have lower temperature. In the magnetosheath, both populations are strongly heated, and in the magnetosphere the density has significantly dropped but the ion energies are above the instrumental limit.

Alternatively, an example with quasi-parallel conditions is shown in Figure 2.5. Here, the bow shock boundary is far less well-defined, with significant structure making up the 'foreshock' regions. Fluctuation amplitudes in the magnetosheath are much larger, and the boundary with the magnetopause is also quite poorly defined. Around the bow shock

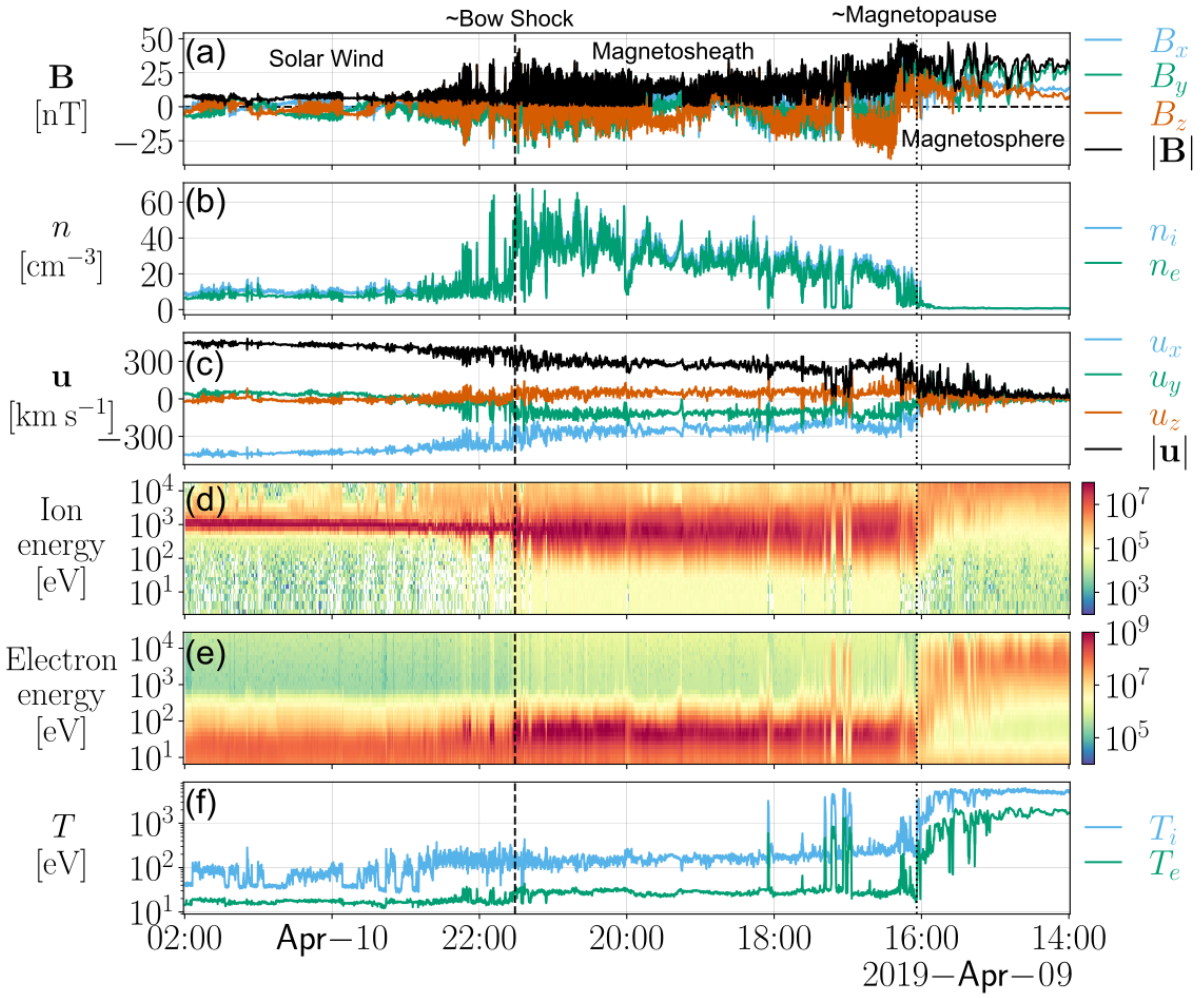


Figure 2.5: Example of spacecraft measurements passing from the solar wind, through the magnetosheath, into the magnetosphere during quasi-parallel conditions ($\theta_{Bn} \approx 27°$ based on magnetic coplanarity). Measurements by MMS (see Section 3.1) on 2019-04-09/14:00:00 to 2019-04-10/02:00:00 UTC – note that the time axis is reversed for comparison to Figure 2.4. Panels display: (a) the vector magnetic field; (b) the number density; (c) the MHD bulk velocity (Equation 2.41); (d) the omnidirectional ion energy spectrum; (e) the omnidirectional electron energy spectrum; (f) the temperature, which is not well-measured in the solar wind or magnetosphere due to low density. Colour-axis units in panels (d) & (e) are keV/(cm^2 s sr keV). The vertical dashed line represents the approximate location of the bow shock, and the vertical dotted line represents the approximate location of the magnetopause. Vectors are in GSE coordinates.

and magnetopause there are several crossings in and out of the magnetosheath. It is carefully-selected quasi-parallel intervals which will make up the bulk of the observations used in this thesis, due to the strong fluctuation amplitudes.

In situ observations of the magnetosheath are favourable for studies of turbulence and small-scale behaviour because of the high signal-to-noise ratio compared to the solar wind (e.g. Sahraoui et al., 2013). Data from this so-called 'natural laboratory' will be used

throughout this thesis, as outlined in Chapter 3 and the studies in Chapters 4–6. Before then, it is necessary to introduce some key concepts of plasma turbulence in the following Sections.

2.3 Turbulence Theory

Turbulence is a fundamental fluid phenomenon which transfers fluctuation energy between different scales. This transfer usually takes energy from large driving scales where it is injected, through an 'inertial range' where it is conserved, into small scales where dissipation converts it irreversibly to heat (e.g. Frisch, 1995; Schekochihin et al., 2009; Bruno and V. Carbone, 2013; Verscharen et al., 2019). In plasmas, turbulent fluctuations include perturbations to the electromagnetic fields as well as the velocity, which due to their coupling strongly influence the dynamics. In collisionless plasmas, the absence of viscosity and electrical resistivity means that there is negligible damping of fluctuations, allowing the turbulence to reach far smaller scales than in the hydrodynamic case. At these kinetic scales (below d_i for $\beta_i \leq 1$ or ρ_i for $\beta_i \geq 1$), reversible kinetic processes take over the dynamics. Understanding how energy is dissipated through these kinetic processes in the collisionless regime remains a major unsolved problem in plasma physics (e.g. Kiyani et al., 2015; Matthaeus et al., 2020). In this section, the phenomenology of MHD turbulence is introduced, before addressing the changes the process undergoes as it the transition to kinetic scales.

2.3.1 Turbulent Energy Spectra

The turbulent cascade is the name given to the net transfer of energy from larger to smaller scales. The phenomenological picture of turbulence is that it occurs as a result of local nonlinear interactions between similarly-sized eddies, generating new smaller eddies which likewise interact nonlinearly with their neighbours to produce yet smaller eddies, and so on until dissipation (e.g. Verscharen et al., 2019). The earliest attempts to formulate a theory of turbulence in hydrodynamics used this principle, as famously summarised by

Richardson (1922) in a rhyming verse:

> Big whirls have little whirls that feed on their velocity,
> and little whirls have lesser whirls, and so on to viscosity.[1]

This idea of a turbulent cascade has been continuously developed and refined to the present day. Turbulence theories typically make predictions for the shape of the energy spectrum, $E(k)$, in the inertial range. The energy spectrum in this range usually follows a power law, $E(k) \sim k^{-\alpha}$, where α is the spectral index. The spectral index contains information about the mechanism leading to the cascade of fluctuation energy from larger to smaller scales.

Kolmogorov Turbulence

The first statistical theory of hydrodynamic turbulence was developed by Kolmogorov (1941a, 1941b). Using dimensional analysis and assuming the inertial range is homogenous, isotropic, scale-invariant, and local in scale, a constant energy transfer rate as a function of scale is defined as

$$\epsilon \sim \delta u_l^2 / \tau_{nl}, \tag{2.63}$$

where δu_l is the velocity fluctuation across an eddy of size l, and $\tau_{nl} \sim l/\delta u_l$ is the characteristic eddy turnover time (the nonlinear time). Substituting and rearranging gives

$$\delta u_l \sim (\epsilon l)^{1/3}. \tag{2.64}$$

Relating scale to wavenumber via $k \sim 1/l$ and noting that only fluctuations at scales smaller than l contribute to the energy at scale l, the fluctuation energy in each wavenum-

[1] Richardson's verse was a play on two lines of an 1872 poem by De Morgan (1915):
> Great fleas have little fleas upon their backs to bite 'em,
> And little fleas have lesser fleas, and so *ad infinitum*.

which was itself based on part of a 1733 satirical poem on the role of poets in society by Swift (1734):
> So, Nat'ralists observe, a Flea Hath smaller Fleas that on him prey,
> And these have smaller yet to bite 'em, And so proceed *ad infinitum*.

ber band, $E(k)dk$, can be integrated to give the total fluctuation energy spectrum,

$$\int_k^\infty E(k')dk' \sim E(k)k \sim \delta u_l^2 \sim (\epsilon l)^{2/3}, \tag{2.65}$$

$$E(k) \sim \epsilon^{2/3} k^{-5/3}. \tag{2.66}$$

This power law in k is frequently observed in the inertial range of turbulent plasmas, for example in the solar wind (e.g. Coleman, 1968; Kiyani et al., 2015; Verscharen et al., 2019).

Alfvénic Turbulence

Iroshnikov (1964) and Kraichnan (1965) independently developed a theory of Kolmogorov-style turbulence that could be applied to MHD. This model of so-called Alfvénic turbulence treats fluctuations as counterpropagating Alfvén waves directed along the mean **B** direction. These wave packets have parallel extent $l_\parallel$ and perpendicular extent $l_\perp$, and it is assumed that interactions between fluctuations are local in scale. Dimensional analysis is no longer sufficient to describe the cascade time as there are two physical timescales, the nonlinear turnover time $\tau_{nl}(l) \sim l/\delta u_l$ and the Alfvén time $\tau_A(l) \sim l_\parallel/v_A$ (Schekochihin and Cowley, 2007). Nonlinear interactions between counterpropagating wavepackets either increases or decreases the fluctuation amplitudes, by

$$\Delta\delta u_l \sim \frac{\delta u_l^2}{l}\tau_A \sim \delta u_l \frac{\tau_A}{\tau_{nl}} \tag{2.67}$$

during the time it takes for the wavepackets to propagate through one another. The turbulence is taken to be weak, such that many interactions are required to significantly alter the fluctuations ($\tau_A \ll \tau_{nl} \Leftrightarrow \Delta\delta u_l \ll \delta u_l$).

The number of interactions in a time t is $N = t/\tau_A$, and the total fractional change in amplitude is $\sqrt{\tau_A t/\tau_{nl}^2}$. The cascade time τ_l can then be defined as the time taken for

$\sqrt{\tau_A t/\tau_{nl}^2} = 1$, such that δu_l is changed by a considerable fraction of itself:

$$\tau_l \sim \frac{\tau_{nl}^2}{\tau_A} \sim \frac{l^2 v_A}{\delta u_l^2 l_\parallel}. \tag{2.68}$$

Recalling that $\epsilon \sim \delta u_l^2/\tau_l$ and taking $l_\parallel/l \sim 1$ because of isotropy, then rearranging, and substituting as

$$\delta u_l^2 \sim (\epsilon l v_A)^{1/2}, \tag{2.69}$$

the expression for the energy spectrum is found to be

$$E(k) \sim (\epsilon v_A)^{1/2} k^{-3/2}. \tag{2.70}$$

The spectral index here is lower than in Kolmogorov turbulence due to the reduction of the cascade rate by the ratio τ_A/τ_{nl}.

Anisotropic Turbulence and Critical Balance

Alfvénic turbulence was the accepted model of solar wind turbulence until a growing number of results from observational studies were found to be inconsistent with the assumption of isotropy (e.g. Matthaeus et al., 1991). Naturally, one would expect $k_\parallel \ll k_\perp$ in a strong magnetic field, as frozen-in magnetic field can be moved laterally quite freely but resists bending (Schekochihin, 2022).

To exemplify this, consider counterpropagating Alfvén waves $\mathbf{k}_1$ and $\mathbf{k}_2$ that form $\mathbf{k}_3$, whose wavevectors $\mathbf{k}$ and frequencies $\omega^\pm(\mathbf{k}) = \pm k_\parallel v_A$ must satisfy the resonance conditions (see e.g. Galtier et al., 2000; Schekochihin and Cowley, 2007)

$$\mathbf{k}_1 + \mathbf{k}_2 = \mathbf{k}_3 \qquad \Rightarrow \qquad k_{\parallel 1} + k_{\parallel 2} = k_{\parallel 3}, \tag{2.71}$$

$$\omega^\pm(\mathbf{k}_1) + \omega^\mp(\mathbf{k}_2) = \omega^\pm(\mathbf{k}_3) \qquad \Rightarrow \qquad k_{\parallel 1} - k_{\parallel 2} = k_{\parallel 3}. \tag{2.72}$$

These conditions are satisfied only if one incoming wave has $k_\parallel = 0$ and the other wave has $k_\parallel$ unchanged after the interaction. This means the weak turbulent cascade can only

develop in $k_\perp$, thus $k_\perp \gg k_\parallel$. In the limit of weak turbulence, the spectrum can be found to be $E(k_\perp) \sim (\epsilon k_\parallel)^{1/2} k_\perp^{-2}$ (Goldreich and Sridhar, 1997), however because it is assumed that $\tau_A \ll \tau_{nl}$, increasing $k_\perp$ will eventually lead to $\chi = \tau_A/\tau_{nl} \to 1$, which is in violation of the weak turbulence conditions.

Goldreich and Sridhar (1995) proposed that in strong turbulence $\tau_A \sim \tau_{nl}$ is satisfied scale-by-scale, giving $k_\perp/k_\parallel \sim \delta u_l/v_A$ – a property known as critical balance. When $\chi < 1$, weak turbulence theory causes $\chi \to 1$, but it is argued that $\chi > 1$ will not occur because parallel Alfvénic fluctuations will become uncorrelated if the eddy turnover time is faster than the time it takes for the interaction between Alfvénic wave packets to take place. Taking $\tau_l \approx \tau_A \approx \tau_{nl}$ and assuming constant ϵ gives

$$\tau_l = k_\parallel v_A = k_\perp \delta u_l, \tag{2.73}$$

$$k_\parallel \sim v_A^{-1} k_\perp \delta u_l \sim v_A^{-1} k_\perp \left(\frac{\epsilon}{k_\perp}\right)^{1/3} \sim v_A^{-1} \epsilon^{1/3} k_\perp^{2/3}. \tag{2.74}$$

The final term in Equation 2.74 shows that wavevector anisotropy increases as the turbulence cascades to smaller scales, as

$$\frac{k_\perp}{k_\parallel} \sim k_\perp^{1/3}. \tag{2.75}$$

By integrating the 2D energy spectrum over wavenumber, the 1D 'reduced' spectra are found to be $E(k_\perp) \sim k_\perp^{-5/3}$ and $E(k_\parallel) \sim k_\parallel^{-2}$. A direct result of the critical balance condition is that the parallel spectral index is steeper – due to parallel decorrelation caused by the perpendicular cascade. In essence, critical balance can be thought of as an application of linear wave physics to strongly turbulent plasmas (Shestov et al., 2022). The critical balance conjecture is consistent with several observational results for the solar wind (e.g. Horbury et al., 2008; C. H. K. Chen, 2016), and it is established that there is scale-dependent anisotropy, however whether the solar wind always agrees with the $k_\perp^{-5/3}$ spectral scaling is still somewhat unclear (Schekochihin, 2022).

As such, critical balance theory is still developing. Critical balance has also been extended to collisional turbulence, in which it still applies (Terry, 2018). Shestov et al. (2022) point out that there are several ongoing problems in critically-balanced turbulence, such as explaining nonlocal effects found in Alfvén wave collisions (Beresnyak and Lazarian, 2008), and incorporating the role of plasma compressibility (Magyar et al., 2019).

Dynamic Alignment

A further revision of Goldreich-Sridhar (1995) critical balance comes from Boldyrev (2006), called (scale-dependent) dynamic alignment. As put by Chandran et al. (2015), dynamic alignment describes the increasingly parallel configuration into which two advecting Aflvén wavepackets shear. In other words, that magnetic and velocity fluctuations tend towards maximal alignment while still supporting a constant energy cascade flux (if they were completely aligned, no nonlinear interactions would be taking place so there would be no energy cascade) (Schekochihin, 2022). Boldyrev (2006) suggests that misalignment occurs in the parallel direction because the local field direction can only be defined within a small angle. The alignment angle is scale dependent ($\theta_{ub} \sim k_\perp^{-1/4}$), leading to a perpendicular energy spectrum of $E(k_\perp) \sim k_\perp^{-3/2}$ – equivalent to if Kraichnan (1965) had used their dimensional argument for only the perpendicular spectrum. However, dynamic alignment is not a universally accepted hypothesis, subject to its own share of controversy (more so than critical balance, in fact). Numerical evidence in favour of Boldyrev (2006) has been contested due to spectral observations inconsistent with dynamic alignment in the solar wind (see C. H. K. Chen, 2016; Schekochihin, 2022, and references therein).

Spectral Laws in the Solar Wind and Magnetosheath

To highlight typical behaviour and common variations it is useful to now show examples of magnetic energy spectra in the solar wind and magnetosheath. Figure 2.6 compiles three examples from Sahraoui et al. (2020), who undertook a review of properties of turbulence in the solar wind at 1 AU and the magnetosheath. Figure 2.6 (a) gives a solar

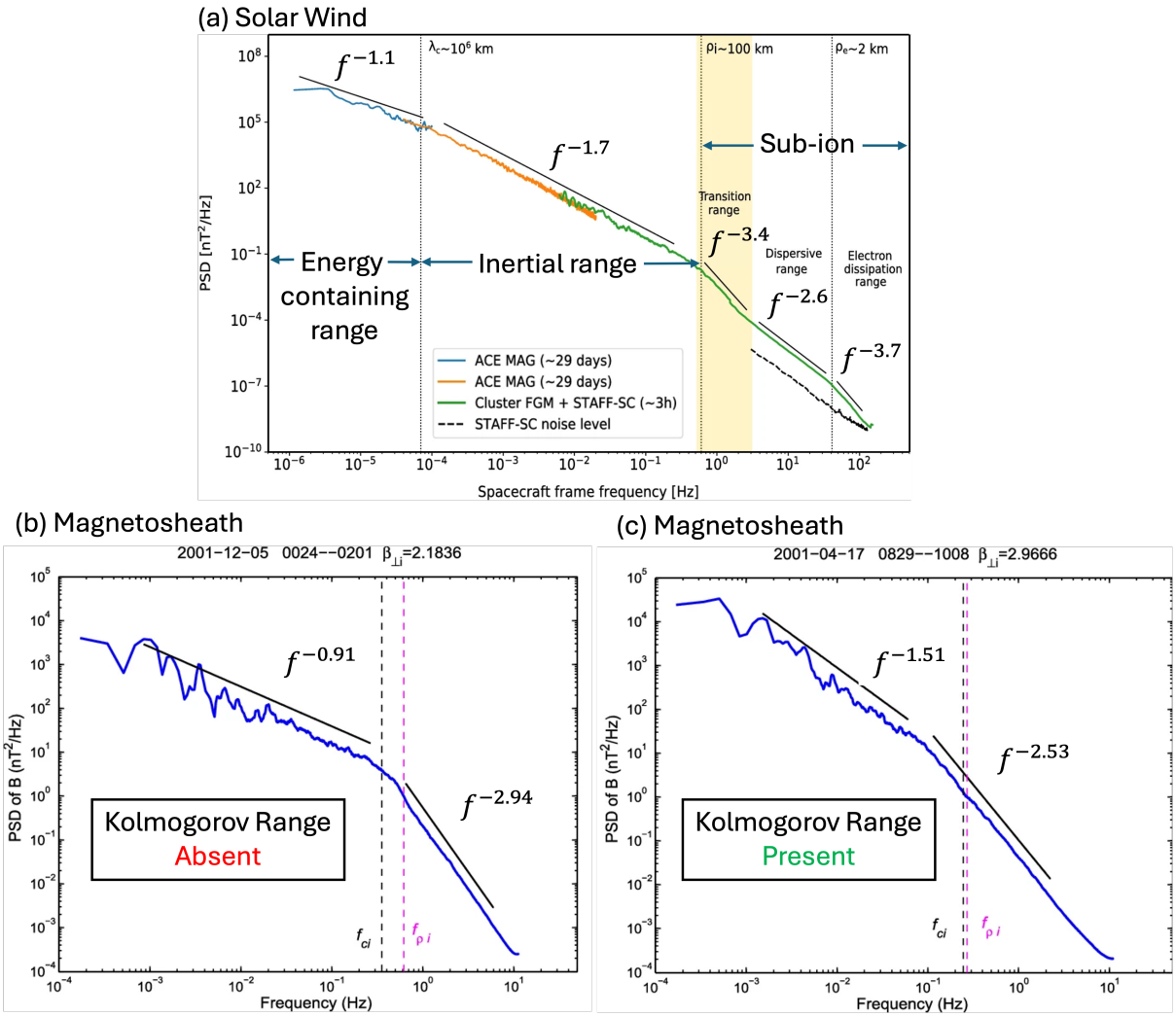


Figure 2.6: Power spectrum of magnetic field fluctuations measured in (a) the solar wind and (b, c) the magnetosheath, illustrating the differences between spectral laws in the different regions. Vertical dashed lines denote the magnetic correlation length (λ_c, see Section 2.3.2), ion/electron gyroradius ($\rho_{i/e}$, $f_{\rho i}$), ion gyrofrequency (f_{ci}). Adapted from Sahraoui et al. (2020) Figures 3 & 4.

wind power spectrum in frequency-space (because spacecraft measure time series, see Section 3.5), where a clear inertial range $\sim f^{-5/3}$ exists between the correlation scale (see Section 2.3.2) and the ion scales. Below ρ_i, there are several sub-ranges as kinetic effects successively take effect. After the transition range, the dispersive range (also called the dissipative range) features a scaling law $\sim f^{-8/3}$, in line with other studies (e.g. Kiyani et al., 2015). Finally, at sub-electron scales a further steepening in the spectrum corresponds to electron dynamics decoupling from the magnetic field.

Studies of magnetosheath scaling relations are fewer and further between, as the dy-

namics are a combination of solar wind turbulence processed by the bow shock and new dynamics generated within the magnetosheath (Huang et al., 2017; Sahraoui et al., 2020; Rakhmanova et al., 2021). Being confined by the bow shock and magnetopause, large-scale turbulent dynamics are expected to depend on upstream solar wind forcing, location within the magnetosheath, and quasi-parallel/quasi-perpendicular shock geometry (e.g. Karimabadi et al., 2014). For example, fluctuations behind the quasi-parallel bow shock have 2–3 times higher amplitude than in quasi-perpendicular regions (Rakhmanova et al., 2021). It is also argued that the bow shock destroys existing solar wind correlations, which must then re-develop, corroborated by Breuillard et al. (2018) who report an $\sim f^{-1}$ scaling behind the bow shock.

In contrast with solar wind observations at 1 AU, it has been found that a significant fraction of observed magnetosheath spectra do not exhibit a Kolmogorov inertial range $\sim f^{-5/3}$ (Huang et al., 2017; Sahraoui et al., 2020), for example in Figure 2.6 (b). This is attributed to location within the magnetosheath – spectra showing a well-developed inertial range are measured away from the bow shock in the quasi-parallel flanks, such as in Figure 2.6 (c) (Alexandrova et al., 2008; Huang et al., 2017), but not behind the quasi-perpendicular bow shock (Shevyrev et al., 2006; Breuillard et al., 2018). In agreement with other magnetosheath studies, Yordanova et al. (2020) and Rakhmanova et al. (2021) demonstrated the presence of an inertial range in quasi-parallel regions, with non-Kolmogorov scalings (and a spectral bump around ion scales) in quasi-perpendicular regions.

At kinetic scales, which are much smaller than the system size, the spectra appear not to be dependent on location within the magnetosheath. The slope in the dispersive range is reminiscent of the solar wind case, which is surprising when the difference between plasma parameters in the two systems is considered. Indeed, Sahraoui et al. (2020) suspect that this indicates that there is not a statistical dependence of turbulence scaling on local plasma conditions, a result confirmed by a lack of correlation between spectral index and these parameters (Sahraoui et al., 2013; Huang et al., 2014). Moreover, in a case study on

magnetosheath turbulence associated with different instabilities, Breuillard et al. (2016) found that dominating mirror instability enhanced the parallel spectrum, whereas the opposite case was true in dominating Alfvén ion cyclotron instability (see Section 2.4 for a brief overview of instabilities) – the authors noted that in the absence of instabilities, the magnetic spectrum was isotropic. The difference in spectral slopes when instabilities are present may indicate a difference in dissipation mechanism. Finally, in the electron dissipation range, slopes are found to be much steeper than in the solar wind, which is suspected to be due to suboptimal signal-to-noise ratios in solar wind measurements (Huang et al., 2014).

Overall, the relationship between upstream conditions, the bow shock, and magnetosheath turbulence throughout the region are still being actively explored.

Kinetic Turbulence

In the absence of collisions to terminate the turbulent cascade at fluid scales, turbulence can proceed into the sub-ion regime where the (ideal) MHD model breaks down. At these scales, the Hall term and non-ideal electric fields from generalised Ohm's law (Equation 2.44) become important to the dynamics. These terms factor into the second and third terms of the right-hand side of the induction equation (Equation 2.48). If the Hall term is assumed to dominate the dynamics (the extent to which this is true is evaluated in Chapter 4), the Strong Hall MHD model becomes relevant (Biskamp et al., 1999, also known as the electron MHD model). In this model, $\mathbf{B}$ contains most of the fluctuation energy, and a steeper power law of $\sim k^{-7/3}$ emerges due to the extra derivative in $\mathbf{B}$ (Stawarz et al., 2024). However, there are varied observations of power law scalings in the magnetosheath, representing the inherent complexity of trying to understand how small-scale turbulence operates in this region.

Several other models have been proposed to explain observations, some of which take a critical balance approach invoking kinetic-scale wave modes, such as kinetic Alfvén waves (Boldyrev and Perez, 2012), inertial kinetic Alfvén waves (C. H. K. Chen and Boldyrev,

2017), and whistler waves (Narita and Gary, 2010; Boldyrev et al., 2013). Slightly steeper spectra around $\sim k^{-2.8}$ are sometimes observed in spacecraft observations (e.g. Alexandrova et al., 2009; C. H. K. Chen et al., 2010; Salem et al., 2012), which may be because in reality turbulence is not as space-filling and self-similar as assumed in most theories (see discussion in Stawarz et al., 2024). Several studies have also reported an exponential turnover in the power spectrum at electron scales, particularly in the solar wind (Alexandrova et al., 2009; Alexandrova et al., 2012; Alexandrova et al., 2013; Roberts et al., 2017; Alexandrova et al., 2021), although the applicability of these findings to magnetosheath turbulence is still a matter of active research (Sahraoui et al., 2020; Rakhmanova et al., 2024). Discerning the exponential spectrum from the power-law behaviour is difficult in the solar wind due to instrumental limitations (Sahraoui et al., 2013; F. Carbone et al., 2021). It is also difficult to study electron scales in the magnetosheath due to reformation of the turbulence by the bow shock (Rakhmanova et al., 2021) and the wide variety of small-scale processes which can modify the behaviour of turbulence in the kinetic regime (Chiappetta et al., 2023).

Overall, our understanding of how turbulence operates in the kinetic regime is still poor. Chapter 4 addresses several aspects of this problem, providing observational constraints on the relative importance of different nonlinear forces as a function of scale, turbulent driver, and varying plasma conditions.

2.3.2 Turbulent Cascade Theory

As a formal introduction to turbulent cascade theory, it is helpful to discuss incompressible MHD turbulence (where $\nabla \cdot \mathbf{u} = 0$ and therefore $\nabla n = 0$ throughout the medium). Additional complexities are introduced by compressible and kinetic effects (both of which are relevant to the work presented in this thesis), however incompressible MHD is sufficient to describe the core concepts. The following description follows after Frisch (1995), Biskamp (2003), Bruno and V. Carbone (2013), Schekochihin (2022), and Stawarz et al. (2024).

To start, it can be helpful to break down plasma and electromagnetic variables $\mathcal{Q}(\mathbf{x}, t)$ into their background $\mathcal{Q}_0$ and fluctuation $\delta\mathcal{Q}(\mathbf{x}, t)$ components, such that $\mathcal{Q}(\mathbf{x}, t) = \mathcal{Q}_0 + \delta\mathcal{Q}(\mathbf{x}, t)$ (e.g. Stawarz et al., 2024). So treating the MHD momentum equation (Equation 2.35) leads to

$$\frac{\partial \mathbf{u}}{\partial t} = -\nabla \cdot (\mathbf{u}\mathbf{u}) - \frac{\nabla p}{\rho} + \frac{\mathbf{j} \times \mathbf{B}}{\rho}, \tag{2.76}$$

where p is the trace particle pressure, $\mathbf{u}$ is the single fluid velocity translated into the $\mathbf{u}_0 = 0$ frame, and $\rho = \rho_0 = n_0 m$ is the mass density (which is spatiotemporally uniform). Employing the vector identity $\nabla \cdot (\mathbf{x}\mathbf{x}) = (\mathbf{x} \cdot \nabla)\mathbf{x} + \mathbf{x}(\nabla \cdot \mathbf{x})$, Equation 2.76 can be expressed as

$$\frac{\partial \delta\mathbf{u}}{\partial t} = \underbrace{\frac{(\nabla \times \delta\mathbf{B}) \times \mathbf{B}_0}{\mu_0 \rho_0} - \frac{\nabla \delta p}{\rho_0}}_{Linear} \underbrace{- \delta\mathbf{u} \cdot \nabla \delta\mathbf{u} + \frac{(\nabla \times \delta\mathbf{B}) \times \delta\mathbf{B}}{\mu_0 \rho_0}}_{Nonlinear}. \tag{2.77}$$

Similarly, the induction equation (Equation 2.48) can be expressed as

$$\frac{\partial \delta\mathbf{B}}{\partial t} = \underbrace{\nabla \times (\delta\mathbf{u} \times \mathbf{B}_0)}_{Linear} + \underbrace{\nabla \times (\delta\mathbf{u} \times \delta\mathbf{B})}_{Nonlinear}. \tag{2.78}$$

Finally, by taking the divergence of Equation 2.76 the incompressibility condition ($\nabla \cdot \delta\mathbf{u} = 0$) becomes

$$\nabla^2 \delta p = \underbrace{\nabla \cdot \left(\frac{(\nabla \times \delta\mathbf{B}) \times \mathbf{B}_0}{\mu_0} \right)}_{Linear} \underbrace{- \nabla \cdot \left(\rho_0 \delta\mathbf{u} \cdot \nabla \delta\mathbf{u} - \frac{(\nabla \times \delta\mathbf{B}) \times \delta\mathbf{B}}{\mu_0} \right)}_{Nonlinear}. \tag{2.79}$$

In Equations 2.77–2.79, the terms are split into linear and nonlinear components, containing single and multiple fluctuating variables, respectively. Linear terms give rise to wave modes, whereas nonlinear terms are responsible for the turbulent dynamics. The overall dynamics are a combination of both types of term, and as seen in Section 2.3.1 it is necessary to consider the balance of both when developing a theoretical description of turbulence. This information is encoded in a generalised χ parameter,

$$\chi = \frac{\tau_l}{\tau_{nl}}. \tag{2.80}$$

Typically $\chi > 1$ in the solar wind (Matthaeus et al., 2014), however it will be shown in Chapter 4 that this ratio varies from $\chi < 1$ to $\chi > 1$ in the magnetosheath. There is a distinction between defining global $\mathbf{B}_0$ and local or scale-dependent versions (which can be used for small fluctuations which experience locally averaged $\mathbf{B}$, e.g. C. H. K. Chen, 2016). Local $\mathbf{B}_0$ is subject to random variations to the reference frame (Matthaeus et al., 2012), so additional care must be taken when fluctuations with respect to a local background are used.

In collisional MHD, two further parameters would usually have been defined – the Reynolds number $Re = lu_0/\nu$ (where ν is the viscosity), and the magnetic Reynolds number $Re_M = lu_0/\eta$ (where η is the resistivity). Re encodes the delicate balance between inertial and viscous forces: when small, velocity fluctuations can complicate and distort the plasma; when large, fluctuations are damped out as a result of viscosity. Similarly, Re_M characterises the ratio of magnetic induction to resistive diffusion. However, since the plasmas considered in this thesis are collisionless (see Sections 2.1.6 & 2.2), ν and η tend towards zero, leading to highly turbulent systems with little damping. Howes (2024) give a helpful review of the alternative parameters which describe the nature of collisionless turbulence.

Turbulence theories typically aim to describe statistical properties of turbulence, due to the complex and distorted nature of its fluctuations which occur over a broad range of physical scales. One way of probing turbulence is via the autocorrelation tensor,

$$\mathbb{R}_{ij}^{\mathbf{g}}(\mathbf{x}, \boldsymbol{\ell}) = \langle \delta g_i(\mathbf{x} + \boldsymbol{\ell})\, \delta g_j(\mathbf{x}) \rangle, \tag{2.81}$$

where $\langle \ldots \rangle$ represents a spatial average, equivalent to an ensemble average if the turbulence is homogeneous. $\mathbb{R}_{ij}^{\mathbf{g}}$ contains the correlation coefficient between components of an arbitrary quantity $\mathbf{g}(\mathbf{x})$ as a function of the physical-space 'lag' $\boldsymbol{\ell}$. The trace of $\mathbb{R}_{ij}^{\mathbf{g}}$ gives the correlation function of fluctuation energy,

$$\mathcal{R}^{\mathbf{g}}(\mathbf{x}, \boldsymbol{\ell}) = \langle \delta \mathbf{g}(\mathbf{x} + \boldsymbol{\ell}) \cdot \delta \mathbf{g}(\mathbf{x}) \rangle, \tag{2.82}$$

which is essentially a measure of how correlated fluctuations are at different points in the flow. As $\boldsymbol{\ell} \to \infty$ the value of the correlation function should go to zero. A commonly-used measure used to characterise the scale associated with $\delta\mathbf{g}$ is the correlation length, defined as

$$\lambda_{c,\mathbf{g}} = \frac{1}{\mathcal{R}^{\mathbf{g}}(0)} \int_0^\infty \mathcal{R}^{\mathbf{g}}(\boldsymbol{\ell})\, d\ell, \tag{2.83}$$

which represents the characteristic decorrelation scale for fluctuations $\delta\mathbf{g}$ (or, alternatively, the largest scale of correlated turbulent fluctuations). Another statistical quantity related to $\mathcal{R}^{\mathbf{g}}(\boldsymbol{\ell})$ is the 2nd-order structure function,

$$\mathcal{S}_2^{\mathbf{g}}(\mathbf{x}, \boldsymbol{\ell}) = \langle |\Delta\mathbf{g}(\mathbf{x}, \boldsymbol{\ell})|^2 \rangle = \langle |\mathbf{g}(\mathbf{x} + \boldsymbol{\ell}) - \mathbf{g}(\mathbf{x})|^2 \rangle, \tag{2.84}$$

which is employed in the original Kolmogorov (1941a, 1941b) statistical descriptions of turbulence. If fluctuations are statistically homogeneous, the relationship between $\mathcal{S}_2^{\mathbf{g}}(\boldsymbol{\ell})$ and $\mathcal{R}^{\mathbf{g}}(\boldsymbol{\ell})$ is (Biskamp, 2003)

$$\mathcal{S}_2^{\mathbf{g}}(\boldsymbol{\ell}) = 2\mathcal{R}^{\mathbf{g}}(0) - 2\mathcal{R}^{\mathbf{g}}(\boldsymbol{\ell}). \tag{2.85}$$

With the tools introduced in Equations 2.81–2.85, the incompressible MHD equations 2.77–2.79 can be written in terms of the 2nd-order structure function of the kinetic ($\mathbf{u}$) plus magnetic ($\mathbf{b}_A$, where $\mathbf{b}_A = \mathbf{B}/\sqrt{\mu_0\rho}$ is the magnetic field in Alfvén units) fluctuation energy,

$$\mathcal{S}_2(\boldsymbol{\ell}) = \mathcal{S}_2^{\mathbf{u}}(\boldsymbol{\ell}) + \mathcal{S}_2^{\mathbf{b}_A}(\boldsymbol{\ell}), \tag{2.86}$$

$$\mathcal{R}(\boldsymbol{\ell}) = \mathcal{R}^{\mathbf{u}}(\boldsymbol{\ell}) + \mathcal{R}^{\mathbf{b}_A}(\boldsymbol{\ell}). \tag{2.87}$$

Assuming fluctuations are statistically homogeneous, $\mathrm{S}_2(\boldsymbol{\ell})$ evolves in time as (Politano and Pouquet, 1998b; Adhikari et al., 2023b)

$$\frac{\partial \mathcal{S}_2(\boldsymbol{\ell})}{\partial t} = \mathcal{P}(\boldsymbol{\ell}) - \frac{\partial}{\partial \boldsymbol{\ell}} \cdot \mathbf{Y}(\boldsymbol{\ell}) + 2\mathcal{D}(\boldsymbol{\ell}) - 4\epsilon. \tag{2.88}$$

In systems with high enough *Re* (or equivalent collisionless analogue), each of the terms in Equation 2.88 should dominate at different scales (Pecora et al., 2023). The terms are as follows: $\mathcal{P}(\boldsymbol{\ell})$ represents the injection of fluctuation energy at large scales; $\mathbf{Y}(\boldsymbol{\ell})$ is a mixed 3rd-order structure function containing the nonlinear terms,

$$\mathbf{Y}(\boldsymbol{\ell}) = \langle \Delta\mathbf{u}(\boldsymbol{\ell}) |\Delta\mathbf{u}(\boldsymbol{\ell})|^2 + \Delta\mathbf{u}(\boldsymbol{\ell}) |\Delta\mathbf{b}_A(\boldsymbol{\ell})|^2 - 2\Delta\mathbf{b}_A(\boldsymbol{\ell}) [\Delta\mathbf{u}(\boldsymbol{\ell}) \cdot \Delta\mathbf{b}_A(\boldsymbol{\ell})] \rangle; \quad (2.89)$$

$\mathcal{D}(\boldsymbol{\ell})$ is the dissipation due to viscosity and resistivity, given in a collisional plasma by

$$\mathcal{D}(\boldsymbol{\ell}) = \nu \frac{\partial^2}{\partial \boldsymbol{\ell}^2} \mathcal{S}_2^{\mathbf{u}}(\boldsymbol{\ell}) + \frac{\eta}{\mu_0} \frac{\partial^2}{\partial \boldsymbol{\ell}^2} \mathcal{S}_2^{\mathbf{b}_A}(\boldsymbol{\ell}); \quad (2.90)$$

and ϵ is the average energy dissipation rate. Naturally, $\mathcal{D}(\boldsymbol{\ell}) \to 0$ in collisionless systems, although recent work has provided some non-collisional proxies for this term (Pezzi et al., 2021a; Pezzi et al., 2021b; Yang et al., 2022; Yang et al., 2024). $\mathbf{Y}(\boldsymbol{\ell})$, termed the 'Yaglom flux' by some in analogy with its hydrodynamic counterpart (Yaglom, 1949), contains an energy term from kinetic and magnetic energies coupled into velocity shears, and a cross-helicity term from correlated $\delta\mathbf{u}$ and $\delta\mathbf{b}_A$ coupled with magnetic gradients (Marino and Sorriso-Valvo, 2023). In the case of purely Alfvénic fluctuations, the two terms in $\mathbf{Y}(\boldsymbol{\ell})$ cancel out and the cross-scale energy cascade ceases. $\mathbf{Y}(\boldsymbol{\ell})$ introduces a closure problem, whereby the equation for the 2nd-order structure function (Equation 2.88) depends on the 3rd-order structure function, the evolution of which will depend on the 4th-order structure function, and so on. This represents a key difficulty in the development of complete turbulence theories.

In the range of scales where $\mathbf{Y}(\boldsymbol{\ell})$ dominates the steady-state case of Equation 2.88 (the aforementioned inertial range), one of the few exact results in MHD turbulence emerges (Politano and Pouquet, 1998a; Politano and Pouquet, 1998b; Marino and Sorriso-Valvo, 2023)

$$\frac{\partial}{\partial \boldsymbol{\ell}} \cdot \mathbf{Y}(\boldsymbol{\ell}) = -4\epsilon. \quad (2.91)$$

Equation 2.91 encapsulates the important role played by the nonlinear dynamics in facil-

itating the cascade of turbulent energy from driving scales to dissipation scales. In the absence of significant nonlinearities, turbulence would be unable to fully develop and no cross-scale transport would occur.

This section has focused on describing turbulent cascade theory through the lens of homogeneous incompressible MHD theory. However, several extensions have been studied which, while unnecessary to elucidate the core concepts of turbulence theory as is the aim of this section, are nonetheless noteworthy. Examples include consideration of background velocity shears (Wan et al., 2009; Stawarz et al., 2011), compressibility (i.e. $\nabla \cdot \delta\mathbf{u} \neq 0$, Banerjee and Galtier, 2013), the Hall effect (Galtier, 2008; Hellinger et al., 2018; Ferrand et al., 2019; Hellinger et al., 2021; Ferrand et al., 2021), compressible Hall physics (Andrés et al., 2018), and kinetic particle-in-cell simulations (Marino and Sorriso-Valvo, 2023).

2.3.3 Local Structures Generated by Turbulence

While the spatial configuration of a turbulent system could be reconstructed as a superposition of wave modes, these are far from random and uncorrelated. Instead, there are preferential phase correlations between modes at different scales which are generated by the nonlinear dynamics, giving rise to 'coherent' structures (e.g. Stawarz et al., 2024). In turbulent magnetic fields, localised coherent structures form current sheets, magnetic shears, and other complex filamentary and vortical structures (Greco et al., 2009; Matthaeus et al., 2015). Specifically, the Probability Density Function (PDF) of $\Delta\mathbf{B}$ and $\Delta\mathbf{u}$ exhibits enhanced tails, indicating that sharp gradients occur more often than expected for a normal distribution – these bursty patches of turbulence are referred to as intermittency (Verscharen et al., 2019).

Intermittency can be identified by the Partial Variance of Increments (PVI) diagnostic (Greco et al., 2008),

$$\mathrm{PVI} = \frac{|\Delta\mathbf{B}(\mathbf{x}, \boldsymbol{\ell})|}{\sqrt{\langle|\Delta\mathbf{B}(\mathbf{x}, \boldsymbol{\ell})|^2\rangle}}, \tag{2.92}$$

which may be equivalently expressed in terms of time lag increments $\Delta\mathbf{B}(t, \tau)$ via Taylor's hypothesis (see Section 3.5) for time series measurements of $\mathbf{B}(t)$ (Greco et al., 2018).

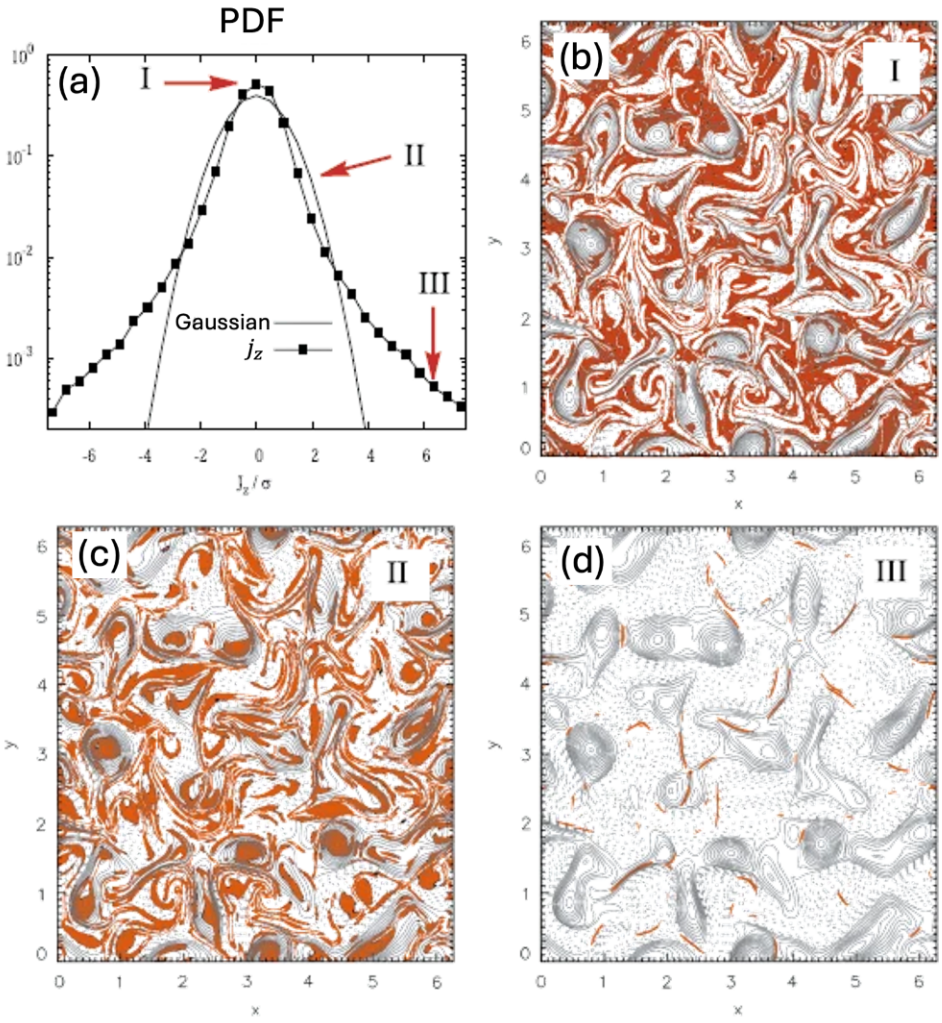


Figure 2.7: Example of intermittent turbulence from a 2D MHD simulation. (a) The PDF of out-of-plane current density j_z compared to a reference Gaussian. Panels (b)–(d) show magnetic field lines, coloured red where contributions come from region I–III of the PDF, respectively. Adapted from Greco et al. (2018).

Large PVI values occur in the presence of coherent structures, which are thought to give rise to intermittency (Verscharen et al., 2019). An example of intermittency in a 2D MHD turbulence simulation is shown in Figure 2.7. The generation of sharp magnetic gradients (i.e. strong j_z) related to the super-Gaussian tails (III) of the PDF leads to coherent filamentary structures, such as current sheets, which survive longer than the surrounding turbulence. Within these strong gradients the ideal MHD approximation can be violated, leading to magnetic diffusion and non-ideal electric fields.

Intermittency is observed in the solar wind, the bow shock, and the magnetosheath (e.g. Greco et al., 2009; V. Carbone, 2012; Karimabadi et al., 2013; Matthaeus et al., 2015;

Chasapis et al., 2018a; Plank and I. L. Gingell, 2023). Coherent structures are often host to increased plasma heating and non-Maxwellian features in the VDF (Osman et al., 2011; Wan et al., 2012; Karimabadi et al., 2013; Wu et al., 2013; Wan et al., 2015; Parashar and Matthaeus, 2016; Yang et al., 2017a). The link between intermittent turbulence, energy conversion, and non-Maxwellianity is still an unresolved question (e.g. Verscharen et al., 2019; Parashar and Gary, 2019; Perri et al., 2020; Bandyopadhyay et al., 2021; Pezzi et al., 2021a; Graham et al., 2021), which will be explored in Chapters 5 and 6.

2.3.4 Energy Conversion and Dissipation

Turbulent Electric Fields

Electric fields play a key role in turbulent processes as magnetic fields are unable to do work on charged particles. Electric fields enable interactions between the electromagnetic field and the particles by coupling magnetic and velocity field fluctuations via the Lorentz force, mediating energy transfer between the two through a nonzero $\mathbf{j} \cdot \mathbf{E}$ (Stawarz et al., 2021, see also Sections 2.1.3–2.1.4). As such, below the MHD scales $\mathbf{E}$ plays an important role in the dynamics (e.g. Vörös et al., 2019). It has been observed that the power spectrum of $\mathbf{E}$ is steeper in the MHD inertial range and then flattens at sub-ion scales (Li et al., 2020, see also Chapter 4). The diverging power laws of $\mathbf{E}$ and $\mathbf{B}$ spectra at sub-ion scales is attributed to the dominance of $\mathbf{E}_{Hall}$ in this range, introducing an extra factor k from the power spectrum of the curl in $\mathbf{j} = (\nabla \times \mathbf{B})/\mu_0$ (Matteini et al., 2016; Stawarz et al., 2021).

Learning about the turbulent electric field is crucial to understand the dynamics at different scales. Unfortunately, electric field measurements are prone to poor signal-to-noise ratios, particularly due to contamination from the spacecraft environment, which means sub-ion scale studies aren't reliably achievable in the solar wind (Bale et al., 2005; Matteini et al., 2016). Fortunately, strong fluctuations in $\mathbf{E}$ make the magnetosheath an ideal laboratory to study the cross-scale nature of electric field fluctuations, both in the ambient magnetosheath as well as localised coherent structures. While it is difficult

to measure generalised Ohm's law due to the spatial gradient terms and high particle-instrument frequencies needed to probe sub-ion scales, this feat can be accomplished in the magnetosheath thanks to high-resolution multipoint measurements from NASA's Magnetospheric Multiscale (MMS) mission (Burch et al., 2016, see Section 3.1).

Comparative analyses of the terms in generalised Ohm's law, which have been performed using multi-spacecraft measurements in turbulence and reconnection studies (e.g. André et al., 2004; Khotyaintsev et al., 2006; Torbert et al., 2016b; Genestreti et al., 2018; Stawarz et al., 2021), reveal a complex interplay between the different terms, the turbulence, and plasma parameters, all of which will be the subject of Chapter 4. It has been shown that non-ideal terms in generalised Ohm's law (see Section 2.1.4), $\mathbf{E}_{P_e}$ and $\mathbf{E}_{inertia}$, mediate energy conversion inside electron diffusion regions via $\mathbf{j}\cdot\mathbf{E}'$ (Torbert et al., 2016b; Genestreti et al., 2018; Vörös et al., 2019), highlighting the importance of studying the non-MHD electric field components to characterise the energetics in kinetic-scale processes.

When considering generalised Ohm's law in the context of turbulent plasmas, writing out the equations for the Fourier transform of the spatial electric field, denoted $\widetilde{\mathbf{E}}(\mathbf{k})$, reveals why the cross-scale behaviour of the electric field is so complex. Considering $\mathbf{E}_{MHD}$,

$$\widetilde{\mathbf{E}}_{MHD}\left(\mathbf{k}\right) = \int_{-\infty}^{\infty}\int_{-\infty}^{\infty} -\widetilde{\mathbf{u}}(\mathbf{k}_1)\times\widetilde{\mathbf{B}}(\mathbf{k}_2)\,\delta(\mathbf{k}_1+\mathbf{k}_2-\mathbf{k})\,dk_1\,dk_2, \tag{2.93}$$

where the convolution theorem has been used. The same process can be applied to $\mathbf{E}_{Hall}$, where an extra factor of $\mathbf{k}$ comes from the Fourier transform of ∇ when expressing $\mathbf{j} = \nabla\times\mathbf{B}/\mu_0$,

$$\widetilde{\mathbf{E}}_{Hall}\left(\mathbf{k}\right) = \frac{1}{ne}\int_{-\infty}^{\infty}\int_{-\infty}^{\infty} \frac{i\mathbf{k}\times\widetilde{\mathbf{B}}(\mathbf{k}_1)}{\mu_0}\times\widetilde{\mathbf{B}}(\mathbf{k}_2)\,\delta(\mathbf{k}_1+\mathbf{k}_2-\mathbf{k})\,dk_1\,dk_2, \tag{2.94}$$

where, for illustrative purposes, it has been assumed that $n = n_0$ in the $1/ne$ prefactor. If this is not the case, a further convolution arises from fluctuations in n.

The Fourier transform of $\widetilde{\mathbf{E}}_{P_e}$ may be expressed as

$$\widetilde{\mathbf{E}}_{P_e}(\mathbf{k}) = \frac{-1}{ne}\int_{-\infty}^{\infty}\int_{-\infty}^{\infty} i\mathbf{k}\cdot\left[\widetilde{n}_e(\mathbf{k}_1)\,\widetilde{\mathbf{T}}_e(\mathbf{k}_2)\,\delta(\mathbf{k}_1+\mathbf{k}_2-\mathbf{k})\right]\,dk_1\,dk_2, \tag{2.95}$$

where the electron pressure has been decomposed into $\mathbf{P}_e = n_e\mathbf{T}_e$. By nature of the convolutions in Equations 2.93–2.95, there are, in principle, contributions to the dynamics that generate each $\widetilde{\mathbf{E}}(\mathbf{k})$ from all other k, encoding key information about the nature of the nonlinear interactions in the turbulent environment. Turbulence theories are built on assumptions about how these convolutions behave, which is not a priori obvious. In Chapter 4, the unique measurements from MMS are employed to directly measure these convolutions in Earth's magnetosheath and probe how the nonlinear dynamics behave.

Investigating how the balance of electric field terms changes as a function of scale improves understanding of which physical effects are dominating the turbulent energy transfer at different scales, enhancing our understanding of the turbulent energy cascade process and its implications for particle acceleration and energisation. This subject will be explored thoroughly in Chapter 4, in terms of electric field contributions, and Chapters 5–6, in terms of energy conversion as a result of the non-ideal electric field and the kinetic mechanisms with which it couples.

Turbulent Dissipation

One of the crucial open questions in collisionless plasma turbulence is determining which mechanisms are responsible for dissipating energy at small scales? It is unknown which of the wide variety of kinetic plasma processes are responsible for turbulent dissipation, why these processes are occurring, and how they are distributed within the turbulent environment. Further, it is unknown how the energy is partitioned between the electrons and ions, and how it is distributed in velocity space. Finally, it is not clear whether the mechanisms responsible for dissipation and their distribution throughout the turbulent environment are the same in every situation, or whether it varies depending on the ambient plasma conditions and the drivers of the turbulence.

As established in previous sections, the absence of collisional viscosity and resistivity means that the turbulent cascade reaches sub-fluid scales, where kinetic physics controls the dynamics and eventual dissipation into heat. Without a singular process which terminates the cascade at small scales, a variety of dissipation proxies have been suggested in attempts to solve this problem. Attempts to explain dissipation have often focused on specific wave modes and instabilities, on individual mechanisms such as magnetic reconnection, phase mixing, or stochastic heating, or on investigating different energy channels within a plasma (Matthaeus et al., 2020). Pezzi et al. (2021a) split the wide variety of dissipation proxies into two classes: 'energy-based', which treats dissipation as a transfer between energy modes in a fluid-like description; and 'VDF-based', which aim to directly quantify deviations from VDF equilibrium.

In the energy-based dissipation formalism, much recent work has focused on the channels by which energy can be transferred between different forms, mediated by $\mathbf{j} \cdot \mathbf{E}$ and the pressure–strain interaction $(\mathbf{P}_s \cdot \nabla) \cdot \mathbf{v}_s$ (e.g. Del Sarto et al., 2016; Yang et al., 2017b; Yang et al., 2017a; Chasapis et al., 2018b; Pezzi et al., 2019; Matthaeus et al., 2020; Pezzi et al., 2021a; Yang et al., 2022). These studies focus on the statistical movement of energy between forms through exchange terms, rather than individual physical structures or processes giving rise to the energy conversion. The electromagnetic energy density is given by

$$\mathcal{E}^m(\mathbf{x}, t) = \frac{1}{2}\left(\varepsilon_0 \mathbf{E}^2(\mathbf{x}, t) + \frac{1}{\mu_0}\mathbf{B}^2(\mathbf{x}, t)\right), \tag{2.96}$$

and the particle kinetic energy density is given by

$$\mathcal{E}_s(\mathbf{x}, t) = \frac{1}{2} m_s \int v^2 f_s(\mathbf{x}, \mathbf{v}, t)\, d^3v. \tag{2.97}$$

$\mathcal{E}_s$ can be broken up into fluid flow kinetic energy density $\mathcal{E}_s^f$ and internal energy density $\mathcal{E}_s^{th}$, which are defined as

$$\mathcal{E}_s^f(\mathbf{x}, t) = \frac{1}{2} m_s n_s |\mathbf{v}_s|^2, \tag{2.98}$$

$$\mathcal{E}_s^{th} = \frac{1}{2} m_s \int (\mathbf{v} - \mathbf{v}_s)^2 f_s(\mathbf{x}, \mathbf{v}, t)\, d^3v, \tag{2.99}$$

respectively. The role of $\mathbf{j} \cdot \mathbf{E}$ and pressure–strain in energy transfer becomes apparent when writing out the equations for time evolution of the different energy densities, given by

$$\frac{\partial \mathcal{E}_s^f}{\partial t} + \nabla \cdot (\mathcal{E}_s^f \mathbf{v}_s) + \nabla \cdot (\mathbf{P}_s \cdot \mathbf{v}_s) = (\mathbf{P}_s \cdot \nabla) \cdot \mathbf{v}_s + \mathbf{j}_s \cdot \mathbf{E}, \tag{2.100}$$

$$\frac{\partial \mathcal{E}_s^{th}}{\partial t} + \nabla \cdot (\mathcal{E}_s^{th} \mathbf{v}_s) + \nabla \cdot \mathbf{q}_s = -(\mathbf{P}_s \cdot \nabla) \cdot \mathbf{v}_s, \tag{2.101}$$

$$\frac{\partial \mathcal{E}^m}{\partial t} + \frac{1}{\mu_0} \nabla \cdot (\mathbf{E} \times \mathbf{B}) = -\mathbf{j} \cdot \mathbf{E}. \tag{2.102}$$

Noting that $\mathbf{j} \cdot \mathbf{E}$ and pressure–strain both appear in two equations, their role as exchange terms is apparent: positive $\mathbf{j} \cdot \mathbf{E}$ removes energy from $\mathcal{E}^m$ in favour of $\mathcal{E}^f$; positive $(\mathbf{P}_s \cdot \nabla) \cdot \mathbf{v}_s$ transfers energy from the bulk flow to random internal motions. The $(\mathbf{P}_s \cdot \nabla) \cdot \mathbf{v}_s$ term is commonly decomposed into $P_s \theta_s$ (called P–θ_s) and $\mathbf{\Pi}_s : \boldsymbol{\mathcal{D}}_s$ (called Pi–D_s), which correspond to plasma expansion and compression, and the work per unit volume done by flow shear, respectively.

Neither $\mathbf{j} \cdot \mathbf{E}$ or pressure–strain is sign-definite (Matthaeus et al., 2020), instead the net transfer of energy is expected to be from the electromagnetic field into the particles to facilitate dissipation of turbulent fluctuations. For this reason – and the difficulty in measuring spatial gradients of the particle moments (Adhikari et al., 2023a) – observational studies often choose to remain agnostic to the ultimate partition of particle energy density into $\mathcal{E}^f$ and $\mathcal{E}^{th}$. Instead, the critical aspect of dissipation is treated as the transfer of energy between electromagnetic fluctuations and bulk particle energy, via $\mathbf{j} \cdot \mathbf{E}$, which is the scheme adopted in Chapters 5 & 6 in line with many works on magnetic reconnection (e.g Birn and Hesse, 2005; Zenitani et al., 2011b; Phan et al., 2018) and turbulence (e.g. Wan et al., 2015; Vörös et al., 2019).

For VDF-based dissipation proxies, the key idea is to quantify non-equilibrium features in the VDF. These features are observed to be significant at sites of intense current sheets, vortices, and other coherent structures where dissipation is thought to occur (Osman et al., 2011; Servidio et al., 2012; Matthaeus et al., 2012; Parashar and Matthaeus, 2016). To capture non-equilibrium features without visually inspecting entire distribution functions,

various non-Maxwellianity parameters have been proposed. Many non-Maxwellianity parameters are based on changes in kinetic entropy density (e.g. Liang et al., 2020),

$$s_s = -k_B \int f_s \ln f_s \, d^3v. \tag{2.103}$$

Using this principle, Kaufmann and Paterson (2009) propose a measure of non-Maxwellianity as

$$\bar{M}_{KP,s} = \frac{s_M - s_s}{\frac{3}{2} k_B n_s}, \tag{2.104}$$

where s_M is the entropy density of the equivalent Maxwellian distribution. Liang et al. (2020) propose a renormalisation of $\bar{M}_{KP,s}$ to prevent problems at extreme temperatures. The renormalisation can be expressed as

$$\bar{M}_s = \frac{\bar{M}_{KP,s}}{\left(1 + \ln \frac{2\pi T_s}{m_s (\Delta^3 v)^{3/2}}\right)}. \tag{2.105}$$

This scheme involves course-graining phase space into cells of hypervolume $\Delta^3 r \Delta^3 v$, where $\Delta^3 r$ is a spatial volume and $\Delta^3 v$ is the volume of a cell in velocity space. The velocity space grid scale is encoded into the renormalised parameter to account for the sharp, delta functions of structures as $T \to 0$ and for the breakdown of statistical physics descriptions as $T \to \infty$. $\bar{M}_s$ thus provides a dimensionless non-Maxwellianity measure which is 0 for a Maxwellian, and is always non-negative so long as appropriate $\Delta^3 v$ is chosen.

Other attempts to quantify non-Maxwellianity involve integrating over velocity space the difference between a measured distribution and a model Maxwellian with the same density, bulk velocity, and temperature. Greco et al. (2012) define their non-Maxwellianity parameter as

$$\varepsilon_s = \frac{1}{n_s} \sqrt{\int (f_s - g_s)^2 \, d^3v}, \tag{2.106}$$

where g_s is the model Maxwellian. This quantity is linked to the enstrophy of the plasma as $\Omega_s = (\varepsilon_s n_s)^2$ (Servidio et al., 2017), which is also related to the free energy in some plasma models (e.g. Schekochihin et al., 2008). Pezzi et al. (2021a) propose a slight

modification to ε_s, renormalising it to

$$\xi_s = \varepsilon_s v_{th,s}^{3/2}, \tag{2.107}$$

where $v_{th,s} = \sqrt{T_s/m_s}$ is the local thermal speed, as ε_s has dimensions of $v^{-3/2}$.

Unfortunately, the Greco et al. (2012) non-Maxwellianity parameter is problematic to use on a collection of different intervals as the parameter is sensitive to large changes in density. Instead, Graham et al. (2021) define the non-bi-Maxwellianity (hereafter non-Maxwellianity for brevity) ϵ_s as the absolute difference between f_s and a model bi-Maxwellian g_s with the same velocity moments, integrated in velocity space as

$$\epsilon_s = \frac{1}{2n_s} \int_{v,\theta,\phi} |f_s - g_s| v^2 \sin\theta dv d\theta d\phi, \tag{2.108}$$

where

$$g_s = \frac{n_s}{\pi^{3/2} v_{s,\parallel}^3} \frac{T_{s,\parallel}}{T_{s,\perp}} \exp\left(-\frac{(v_\parallel - V_\parallel)^2}{v_{s,\parallel}^2} - \frac{(v_{\perp,1} - V_\perp)^2 + v_{\perp,2}^2}{v_{s,\parallel}^2 (T_{s,\perp}/T_{s,\parallel})} \right) \tag{2.109}$$

is the model bi-Maxwellian, $V_{\parallel/\perp}$ are the bulk velocity parallel/perpendicular to $\mathbf{B}$, velocity space coordinates $(v_\parallel, v_{\perp,1}, v_{\perp,2})$ are parallel to $(\mathbf{B}, \mathbf{V}_\perp, \mathbf{B} \times \mathbf{V}_\perp)$, respectively, and

$$v_{s,\parallel} = \sqrt{\frac{2T_{s,\parallel}}{m_s}} \tag{2.110}$$

is the parallel thermal speed. ϵ ranges from 0 (perfect bi-Maxwellian) to 1 (no overlap between g_s and f_s). The Graham et al. (2021) definition of ϵ is dimensionless, which is preferable to enstrophy-related measures such as defined by Greco et al. (2012), as the former do not pick up large changes in density. Another benefit of the chosen method is that g_s is defined by a drifting bi-Maxwellian, so temperature anisotropies are not captured by ϵ, and large bulk velocities will be accounted for.

It is often helpful to know how asymmetric the VDF is around the local magnetic field direction, deviations from which are termed 'agyrotropy'. Since g_s is cylindrically symmetric in the direction perpendicular to $\mathbf{B}$ (i.e. $T_{\perp,1} = T_{\perp,2}$), agyrotropic features in the

observed distribution will be captured by ϵ. To isolate the part of non-Maxwellianity coming from agyrotropy, one can use the agyrotropy measure $\sqrt{Q}$ (Swisdak, 2016), given by

$$\sqrt{Q} = \left(1 - \frac{4I_2}{(I_1 - P_\parallel)(I_1 + 3P_\parallel)}\right)^{1/2}, \tag{2.111}$$

where the parallel pressure $P_\parallel$, the trace I_1, and the sum of principal minors I_2, are defined for a pressure tensor $\mathbf{P}$ in arbitrary coordinates (x, y, z) by

$$P_\parallel = \hat{\mathbf{b}} \cdot \mathbf{P} \cdot \hat{\mathbf{b}} = b_x^2 P_{xx} + b_y^2 P_{yy} + b_z^2 P_{zz} + 2(b_x b_y P_{xy} + b_x b_z P_{xz} + b_y b_z P_{yz}), \tag{2.112}$$

$$I_1 = \mathrm{Tr}[\mathbf{P}] = P_{xx} + P_{yy} + P_{zz}, \tag{2.113}$$

$$I_2 = P_{xx}P_{yy} + P_{xx}P_{zz} + P_{yy}P_{zz} - (P_{xy}P_{yx} + P_{xz}P_{zx} + P_{yz}P_{zy}), \tag{2.114}$$

respectively, where $\hat{\mathbf{b}} = \mathbf{B}/|\mathbf{B}|$ is the local magnetic field direction. $\sqrt{Q}$ ranges from 0 to 1, where 0 represents gyrotropy and 1 corresponds to maximal agyrotropy. A maximally agyrotropic pressure tensor will be given by

$$\mathbf{P} = \begin{pmatrix} x & \sqrt{x} & \sqrt{x} \\ \sqrt{x} & 1 & 1 \\ \sqrt{x} & 1 & 1 \end{pmatrix}, \tag{2.115}$$

with eigenvalues are 0, 0, $x+2$ for any $x \geq 0$. The $\sqrt{Q} = 1$ tensor takes this form because a small perturbation which increases any of the off-diagonal components will drive one of the eigenvalues to be negative, which would result in a tensor which is not real and symmetric (and as such, not a physically meaningful pressure moment of the VDF).

One additional way of investigating dissipation, which is worthy of mention but not used for the large statistical studies in this thesis, is the field-particle correlation technique (e.g. Klein and Howes, 2016). This method explores correlations between the electric field and the particle distribution function via the term proportional to $(\mathbf{E} + \mathbf{v} \times \mathbf{B}) \cdot \nabla_{\mathbf{v}} f_s$ in the Vlasov equation (Equation 2.27). By diagnosing the energy transfer at each point in phase space, the distribution of energy transfer in velocity space can be determined,

producing a unique velocity-space signature of the mechanism mediating the process. Since each collisionless mechanism is likely to have a different characteristic, the field-particle correlation technique can be used to explore the resonant interactions underlying energy transfer. However, due to the inherent complexity of investigating individual structures in VDFs, it is not feasible to use this method in a statistical study.

Both ϵ and $\sqrt{Q}$ will be investigated in Chapter 6 to probe the link between non-Maxwellian features and turbulence. At this point, it is critical to note that the two classes of dissipation proxies are not uncorrelated – distortion of the VDF occurs as a result of energy transfer and vice versa (Pezzi et al., 2021a). Different dissipation measures are found to be regionally correlated, i.e. they are enhanced in similar spatial regions, but generally not point-to-point correlated (Yang et al., 2019; Matthaeus et al., 2020). Dissipation in collisionless turbulence remains an active area of research (oftentimes hotly debated), which is a key theme underlying the motivation behind work presented in this thesis.

2.4 Kinetic Microinstabilities

2.4.1 Instabilities

As discussed in Section 2.3, the physical mechanisms which give rise to dissipation in collisionless plasmas are still poorly understood. Additionally, in the absence of collisions the VDF can deviate significantly from equilibrium, introducing wave–particle interactions that reduce the free energy of the system (Schekochihin et al., 2009; Verscharen et al., 2019). Since the magnetosheath is host to strong electromagnetic fluctuations and non-Maxwellian VDFs (e.g. Perri et al., 2020; Graham et al., 2021), understanding wave–particle interactions helps elucidate thermodynamic regulation in this highly dynamic region of near-Earth space plasma.

Kinetic microinstabilities are a class of wave–particle interactions which are frequently called upon in Chapters 5 & 6. These processes act to reduce non-Maxwellian features in the VDF by redistributing free energy in favour of growing wave modes. In this

section, the basic principles of kinetic microinstabilities are laid out to give context to the results in Chapters 5 & 6. These mechanisms are used only as a tool to probe the thermodynamic regulation of the magnetosheath, rather than the individual instability mechanisms themselves being the focus of in-depth investigation, which is reflected in the description provided here.

Turbulence is dominated by a local cascade, whereas wave–particle instabilities are able to directly inject energy at small scales by generating kinetic-scale electric and/or magnetic fluctuations (Verscharen et al., 2019). This leads to an effective viscosity when particles scatter on the small-scale field fluctuations, influencing the large-scale plasma behaviour. When the VDF meets the conditions for an instability, wave mode amplitude A grows exponentially with time, as

$$A(\mathbf{x}, t) \propto e^{\gamma t}, \tag{2.116}$$

where $\gamma > 0$ is the growth rate of the instability. When the instability is growing the wave mode, free energy in the VDF is used to drive the system closer to local thermodynamic equilibrium. Then, when the conditions are no longer satisfied, γ falls and the system tends towards marginal stability.

2.4.2 Quasilinear Diffusion

The effect of resonant interactions between waves and particles on the VDF is described by quasilinear diffusion (Gary, 1993; Marsch, 2006; Verscharen et al., 2019). Particles can partake in resonant interactions when their parallel speed is equal to the resonance phase speed of a wave mode,

$$v_{ph} = \frac{\omega_r - n\Omega_s}{k_\parallel}, \tag{2.117}$$

where ω_r is the real frequency of the wave mode, n is a signed integer, and $k_\parallel$ is the wavevector component parallel to the background magnetic field. When $n = 0$ the diffusion mechanism corresponds to Landau damping, and when $n \neq 0$ it is cyclotron damping.

During quasilinear diffusion, particles diffuse in the direction which leads from higher to

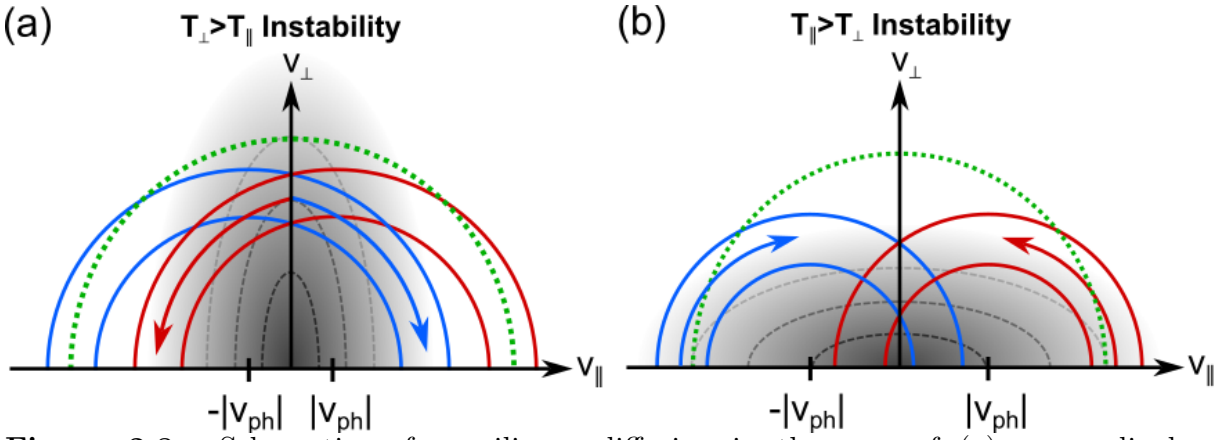


Figure 2.8: Schematics of quasilinear diffusion in the case of (a) perpendicular-anisotropic, and (b) parallel-anisotropic distributions. The grey gradient and dashed lines represent isodensity contours of the anisotropic distribution functions. The solid semicircles show paths of conserved particle kinetic energy in the frame moving with resonant waves at parallel phase speed $|v_{ph}|$ (blue) and $-|v_{ph}|$ (red). The arrows represent the quasilinear diffusive flux of cyclotron-resonant particles. The dotted green line corresponds to $v_\parallel^2 + v_\perp^2 =$ constant. Based on Verscharen et al. (2019, 2022).

lower phase space density, along semi-circles defined by

$$\left(v_\parallel - \frac{\omega_r}{k_\parallel}\right)^2 + v_\perp^2 = \text{constant}, \tag{2.118}$$

i.e. energy in the frame moving with v_{ph} is conserved. Energy which is gained or lost by the particles (corresponding to a positive/negative change in $v_\parallel^2 + v_\perp^2$) is transferred from or to the wave via the resonance at $k_\parallel$ and ω_r (Verscharen et al., 2019).

The quasilinear diffusion mechanism is illustrated in Figure 2.8 for anisotropy-driven instabilities, where cyclotron damping drives a VDF with $T_\perp \neq T_\parallel$ closer to local thermodynamic equilibrium. Figure 2.8 (a) shows how a VDF with perpendicular-dominated anisotropy will evolve due to quasilinear diffusion. Particles with $v_\parallel < 0$ resonate with oppositely directed wave modes, diffusing tangent to the red semi-circles from greater to smaller $f(v_\parallel, v_\perp)$. This reduces $v_\parallel^2 + v_\perp^2$, as the particles have moved inwards, further from the line of constant kinetic energy (green). Particles with $v_\parallel > 0$ likewise interact with resonant waves at parallel phase speed $-|v_{ph}|$, reducing their kinetic energy as well. The overall effect is to redistribute excess phase space density from large to small $v_\perp$, isotropising the distribution. The comparable case of parallel-dominated temperature anisotropy

Name	Instability	Driver	Driven Scale
Ion cyclotron	$T_{i,\perp}/T_{i,\parallel} > 1$	Kinetic	Micro
Ion mirror	$T_{i,\perp}/T_{i,\parallel} > 1$	Kinetic	Macro
Parallel ion firehose	$T_{i,\perp}/T_{i,\parallel} < 1$	Kinetic	Micro
Oblique ion firehose	$T_{i,\perp}/T_{i,\parallel} < 1$	Kinetic	Micro
Parallel electron firehose	$T_{e,\perp}/T_{e,\parallel} > 1$	Kinetic	Micro
Oblique electron firehose	$T_{e,\perp}/T_{e,\parallel} > 1$	Configuration	Micro
Electron whistler	$T_{e,\perp}/T_{e,\parallel} < 1$	Kinetic	Micro

Table 2.2: Table of relevant instability mechanisms. After Verscharen et al. (2019).

is shown in Figure 2.8 (b), where particles with $v_\parallel \gg 0$ resonate with resonant waves at $|v_{ph}|$, diffusing down the phase space density gradient and reducing their kinetic energy. The same happens for particles with $v_\parallel \ll 0$ and waves at $-|v_{ph}|$. The resultant change to the distribution function acts to reduce $T_\parallel$ and increase $T_\perp$ towards isotropy. Thus, in both Figures 2.8 (a) & (b), free energy in the VDF is removed from the particles to grow wave modes.

2.4.3 Anisotropy-driven Instabilities

Wave–particle instabilities are usually classified based on the spatial scale of the driven unstable modes (macro/micro, e.g. Treumann and Baumjohann, 1997) or the driving mechanism (configuration/kinetic; Verscharen et al., 2019). In the former classification, macroinstabilities and microinstabilities refer to wave modes driven at scales much larger than, or comparable to, the kinetic scales, respectively. In the latter classification, configuration instabilities are those which occur due to deviations of macroscopic quantities from equilibrium, whereas kinetic instabilities arise due to resonances involving non-Maxwellian VDFs. A table of properties for the instabilities discussed in Chapters 5 & 6 is given in Table 2.2. These mechanisms are all temperature anisotropy-driven, as this class of instability can be investigated conveniently on the plane of temperature anisotropy and parallel beta (see Section 5.1).

Throughout this thesis, the instability mechanisms are collectively referred to as kinetic microinstabilities, however there is some nuance to this description in the case of the ion

mirror and oblique electron firehose instabilities, as shown in Table 2.2. Furthermore, the parallel electron firehose instability is neglected due to the lower instability threshold of the oblique electron firehose (e.g. Cozzani et al., 2023), the latter of which is hereafter termed the electron firehose instability for brevity. For further information about these instability mechanisms and a variety of others, see the textbook by Gary (1993), and the review papers by Verscharen et al. (2019, 2022).

Chapter 3

Spacecraft Data Techniques

3.1 The Magnetospheric Multiscale Mission

Magnetospheric Multiscale (MMS) is a NASA space mission launched on 13 March 2015, consisting of four spacecraft probes containing identical instrument suites. The mission is designed to investigate magnetic reconnection and explore aspects of turbulence and particle energisation (Burch et al., 2016). Its instrumental resolution is unprecedented, which, in conjunction with high spatial resolution multi-spacecraft capabilities, has unleashed a new era of in situ space plasma research. In this section, the mission objectives, profile, and instruments are introduced. Subsequent sections discuss the techniques employed to clean up and process MMS data to take advantage of its scientific capabilities.

3.1.1 Science Objectives

In the mission overview, Burch et al. (2016) state three specific objectives to be addressed in priority order:

1. Determine the role played by electron inertial effects and turbulent dissipation in driving magnetic reconnection in the electron diffusion region.

2. Determine the rate of magnetic reconnection and the parameters that control it.

3. Determine the role played by ion inertial effects in the physics of magnetic reconnection.

The studies made possible by MMS have significantly advanced our understanding of how magnetospheric dynamics is driven by the solar wind, elucidated how kinetic plasma physics operates in a collisionless regime, and led to the discovery of new dissipation processes such as electron-only magnetic reconnection. As of March 2025 there are over 1500 publications indexed in the Google Scholar MMS collection[1], quantifying this mission's invaluable contribution to the field.

Beyond its primary objective of unravelling the mysteries of magnetic reconnection, MMS is capable of being used to undertake detailed studies into turbulence. With its high instrumental resolution and multi-point measurements, MMS is able to investigate kinetic-scale processes such as energy transfer (e.g. Chasapis et al., 2018a; Chasapis et al., 2018b; Vörös et al., 2019; Pecora et al., 2023) and dissipation of turbulent energy (e.g. Chasapis et al., 2018b; Matthaeus et al., 2020; Bandyopadhyay et al., 2021; Roy et al., 2022). Since how dissipation operates in the absence of collisions is a critical unsolved problem, the extensive MMS dataset represents a unique toolset to explore this unknown aspect of turbulence.

Because MMS consists of four spacecraft orbiting in a tetrahedral formation with a small separation between the spacecraft, accurate estimates of 3D spatial gradients can be obtained from the data (see Section 3.4.1), which are key to probing the turbulent dynamics. In Chapter 4, this capability will be used to directly measure the contributions to the electric field from the individual terms in generalised Ohm's law (Equation 2.44), providing observational constraints on the nature of the turbulent dynamics and turbulent energy dissipation. While this feat could be achieved by the four-spacecraft Cluster mission (Escoubet et al., 2001; Matteini et al., 2016), MMS can resolve the terms down to sub-ion scales (which has been utilised in the context of a reconnection diffusion region, for example Torbert et al., 2016a; Genestreti et al., 2018). This feature is important to turbulence

[1] `https://scholar.google.com/citations?user=OWZfs-4AAAAJ` (Accessed March 2025)

studies, as the small-scale behaviour of the turbulent electric field changes as it transitions from MHD-like dynamics at fluid scales to being dominated by the Hall term and kinetic effects at small scales (as demonstrated using MMS data by Stawarz et al., 2021).

In addition, data products containing high-quality 3D VDFs, and their corresponding fluid moments, have made possible in-depth studies of field-particle correlations (C. H. K. Chen et al., 2019), instabilities (e.g. Svenningsson et al., 2022; Cozzani et al., 2023), and velocity-space structures (Shuster et al., 2019; Graham et al., 2021; Shuster et al., 2023). These data are used in Chapters 5 and 6 to explore how turbulence gives rise to energy conversion, and how that energy is ultimately dissipated via thermalisation of the particle distribution. These studies would not be possible without the rich dataset MMS provides.

3.1.2 Mission Profile

The mission profile is designed so that MMS favourably encounters the dayside magnetopause and near-Earth magnetotail, to maximise opportunities to observe reconnection (Fuselier et al., 2016). The orbit precesses from the dayside, through the dawn flank, then nightside, and finally dusk flank over approximately 1 year. Apogee was initially 12 R_E but has since been raised to 25 R_E then 29 R_E. The mission was originally scheduled for 2 years of operation, but has been extended 3 times to-date (now on its 10th year). The precession and apogee-raising throughout the mission is demonstrated in Figure 3.1 (a). The MMS orbit is beneficial for the analysis undertaken in this thesis because the spacecraft is close to apogee in the vicinity of the magnetosheath (especially earlier in the mission lifetime), so extended periods of continuous observations of magnetosheath turbulence are possible. As the orbit precesses, it samples different parts of the magnetosheath, building up a useful dataset of observations for the studies in Chapters 4–6.

The spacecraft orbit in a tetrahedral formation, which elongates and flattens slightly throughout each orbit. The tetrahedron size is frequently changed, with the smallest separations around 7 km and the largest approximately 160 km. Comparing these separations to the characteristic scales in the magnetosheath (presented in Table 2.1) shows

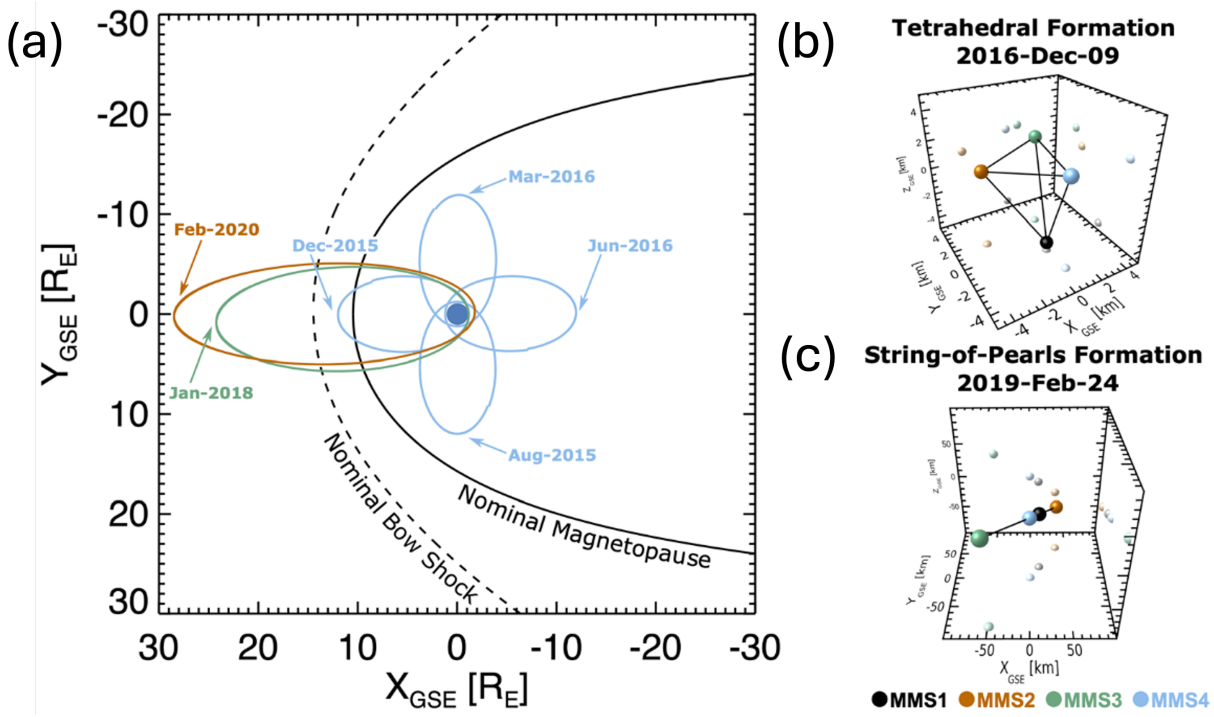


Figure 3.1: Overview of MMS orbits and formation types, reproduced from Stawarz and Genestreti (2023). (a) The different elliptical orbits during different phases of the mission. The blue orbits represent the precession of apogee over the course of a year, and the green and orange orbits show how apogee has been raised throughout the mission. The X–Y plane in Geocentric Solar Ecliptic (GSE) coordinates is shown, with nominal magnetopause (solid) and bow shock (dashed) by Shue et al. (1998) and Fairfield (1971), respectively. (b) The typical tetrahedral formation comprised by the four spacecraft, plotted relative to the barycenter of the formation. (c) Example string-of-pearls configuration.

that MMS routinely samples sub-ion scales (below d_i and ρ_i), almost reaching electron scales in some cases. Indeed, in some intervals d_e and ρ_e are sufficiently large that the interspacecraft separation facilitates sampling of sub-electron scale dynamics.

The orbits are designed so that the tetrahedron is configured optimally for good-quality gradient estimations (Harvey, 1998) when transiting the region of scientific interest (Fuselier et al., 2016). These parameters encode the geometric properties of the MMS polyhedron, based on the eigenvalues of the volumetric tensor $\boldsymbol{R}$, elements of which are defined as

$$R_{jk} = \frac{1}{N}\sum_{\alpha=1}^{N} r_{\alpha j} r_{\alpha k} \tag{3.1}$$

where N is the number of spacecraft ($N = 4$ for MMS), $r_{\alpha j}$ is the j-th component of the α-th spacecraft position $\mathbf{r}$, and the mean position is taken to be zero by choosing

the coordinate system origin to be the mesocenter (this description, and the following, are after Robert et al., 1998b). Since this tensor is symmetric, it can be represented as an ellipsoid in space with three principal axes (each lying in the direction of one of the eigenvectors). If these are given by the eigenvectors $\boldsymbol{R}^{(n)}$ of $\boldsymbol{R}$, the eigenvalues are ordered as

$$R^{(1)} \geq R^{(2)} \geq R^{(3)}, \tag{3.2}$$

representing the major, middle, and minor semi-axes of the pseudo-ellipsoid:

$$a = \sqrt{R^{(1)}}, \tag{3.3}$$

$$b = \sqrt{R^{(2)}}, \tag{3.4}$$

$$c = \sqrt{R^{(3)}}. \tag{3.5}$$

These are used to define the elongation $E = 1 - (b/a)$, planarity $P = 1 - (c/b)$, and characteristic size,[2] $L = 2a$. The elongation is a measure of prolateness (i.e. the formation is stretched along one direction), and planarity is a measure of oblateness (i.e. the polyhedron is squashed along one direction). The MMS orbit is optimised to have low E and P in scientific regions of interest, for reliable 3D gradient estimations (Fuselier et al., 2016). An example tetrahedron is shown in Figure 3.1 (b).

During orbit change manoeuvres, the opportunity is sometimes taken to fly the spacecraft in a colinear 'string of pearls' formation, as demonstrated in Figure 3.1 (c). During these periods it is not possible to measure 3D spatial gradients because the spacecraft is no longer in tetrahedral formation. In these periods, each spacecraft passes through roughly the same location in sequence, giving an approximate time slice of the region, allowing MMS to sample multiple length scales simultaneously.

[2] referred to as such by Robert et al. (1998b), but distinct from the characteristic spacecraft separation R_{sc} introduced later in the thesis.

3.1.3 Instrumentation

Fluxgate Magnetometer (FGM)

MMS's FIELDS instrument suite (Torbert et al., 2016b) contains two triaxial Fluxgate Magnetometer (FGM) sensors to provide vector DC magnetic field measurements. One sensor is a Digital Fluxgate (DFG), whereas the other is an Analogue Fluxgate (AFG), and they are both mounted on 5 m long booms. The basic principle of a FGM (see e.g. Verscharen et al., 2019) is a ring core composed of a ferromagnetic alloy, wrapped by a drive winding and a sense winding. A current is applied to the drive winding to saturate the ring core, and any changes to the magnetic flux in the core are detected by an induced voltage in the sense winding. In the absence of an external magnetic field, the driven fields in the ring core cancel out. However, when there is an external magnetic field the halves of the core producing the aligned and anti-aligned induced fields will not saturate at the same time, leading to a net change of flux in the sense winding which induces a voltage.

Both MMS FGM sensors have a low range and high range sensing mode. DFG is capable of measuring ± 650 nT and $\pm 10,500$ nT in low range and high range respectively, with noise densities at 1 Hz of < 8 pT/$\sqrt{\text{Hz}}$ and < 100 pT/$\sqrt{\text{Hz}}$. The values for AFG are similar, with measurement capability of ± 510 nT (low range) and ± 8200 nT (high range), with 1 Hz noise densities of 5 pT/$\sqrt{\text{Hz}}$ and 10 pT/$\sqrt{\text{Hz}}$, respectively. Full details of the design and calibration of the AFG and DFG are described in Russell et al. (2016). MMS DC **B** measurements are provided at 128 Hz, although the highest frequencies are often contaminated by noise and must be used in conjunction with AC search coil measurements (see below).

Search Coil Magnetometer (SCM)

Fluxgate Magnetometers are typically better suited to measuring DC background magnetic fields (Verscharen et al., 2019). To complement FGM, MMS's Search Coil Magnetometer (SCM) can be used for high-frequency AC measurements. SCM is a triaxial induction search coil wound around a ferromagnetic core which serves to amplify the

applied magnetic field (Torbert et al., 2016b; Le Contel et al., 2016). SCM is located 4 m along the AFG boom, providing 8192 Hz vector AC **B** measurements, designed to be used in the 1 Hz–6 kHz range. The instrument sensitivity is ≤ 2 pT/$\sqrt{\text{Hz}}$ at 10 Hz, ≤ 0.3 pT/$\sqrt{\text{Hz}}$ at 100 Hz, and ≤ 0.05 pT/$\sqrt{\text{Hz}}$ at 1 kHz (Le Contel et al., 2016). SCM data cannot be used to measure background or low-frequency **B** fluctuations, although it can be combined with FGM data to produce a full frequency spectrum of **B** (Argall et al., 2018).

Electric Field Double Probe (EDP)

Electric fields are measured by MMS using double probes, which sense the potential difference between spherical electrodes at the end of booms to avoid contamination by the spacecraft electric field. To produce 3D **E** field observations, a Spin-plane Double Probe (SDP) and Axial Double Probe (ADP) are used. The electric field data product is accurate to 0.5 mV/m between DC and 100 kHz frequencies (Torbert et al., 2016b). The SDP (Lindqvist et al., 2016) measures spin-plane electric field using the potential difference between four spherical electrodes at the end of 60 m long booms. The ADP (Ergun et al., 2016) senses the component of **E** along the spin-axis across an effective antenna length of ~ 29.2 m. The **E** data product released by MMS goes up to 8192 Hz, which matches the SCM for sub-electron scale investigations. EDP and SCM also have a non-continuous higher-frequency mode which captures 65,536 Hz electric and magnetic fields (Torbert et al., 2016b).

Fast Plasma Investigation (FPI)

One of the most exciting capabilities of MMS is its high-frequency particle distribution measurements. The Dual Electron Spectrometer (DES) and Dual Ion Spectrometer (DIS) are able to measure 3D sky-map distributions of electron and ion phase space density at 30 ms and 150 ms cadence, respectively (Pollock et al., 2016). Eight sensors for each spacecraft are distributed in pairs around the spacecraft perimeter. 3D phase space density is calculated by combining the measurements from each instrument to cover the

full azimuthal range of the sky-map.

FPI utilises Top Hat Electrostatic Analysers (ESAs), which are devices consisting of two concentric hemispherical shells nested closely together (Pollock et al., 2016; Verscharen et al., 2019). Particles enter via an aperture in the outer shell and are deflected by a potential difference across the narrow gap between the hemispheres. This potential difference is swept across a range of values to change the range of particle energy-per-charge that are able to reach the detectors. This sweeping process allows the instrument to build up a particle distribution, with geometric resolution defined by the spacing between collimator plates, and time resolution set by the dead time each detector is delayed by before it is able to measure another particle. Where detector field-of-view overlaps, particle counts can be combined to contribute to the distribution. It should be noted that the direction of a measurement pixel is opposite to the velocity of the particles it measures.

The structure of MMS particle distributions is $32 \times 16 \times 32$ measurements of phase space density, constituting 16,384 velocity space co-ordinates. These are 32 energy channels per time step, distributed across 16 polar phase angles from $0^\circ \leq \theta \leq 180^\circ$ (where 0° is the +Z axis), and 32 azimuth angles from $0^\circ \leq \phi \leq 360^\circ$ (starting from spacecraft +X axis and rotating counter clockwise around +Z). All angular bins are 11.25° in width, with $\theta = 5.625 + 11.25 \times p$ (for pixel number p from 0–15). Energy steps are logarithmically spaced, because higher resolution is needed at the center of the distribution, where the most phase space density resides.

In Phase 1A (starting 01/09/2015), MMS used alternating parity sweeps to double the energy resolution by changing the energy channels every other time step. By interleaving these measurements, phase space density observations for 64 energy channels (i.e. twice the energy resolution) are possible. During this phase DES and DIS measured 10 eV–30 keV across 32 energy steps interleaved across 2 parities. However, this is at the expense of halving the time resolution (arguably the most groundbreaking aspect of the measurements), so since Phase 1B (starting 26/09/2016) the energy stepping has been effectively disabled by using identical energy steps across the 2 parities. DES measures

6 eV–30 keV and DIS 2 eV–30 keV. The data used in this thesis come from both periods, but the individual energy steps are only important when analysing full VDFs rather than plasma moments, such as in Chapter 6. Plasma moments are calculated from the particle distributions numerically, rather than by fitting the measured distribution to different populations, and counting statistic uncertainties are propagated from the distributions to the moments to provide error estimates for these quantities.

3.2 Processing MMS Data

3.2.1 Resampling Time Series Data

The particle and field measurements produce data at different time cadences, so to combine data from different instruments it is necessary to employ interpolation and averaging schemes. Linear interpolation is used to upsample data, inserting points between the lower-resolution timestamps and then shifting all points forward or backward a partial increment in time to match the higher-resolution time steps (if necessary). Data gaps, which occur sporadically for a few consecutive points in some intervals, are also filled iby linear interpolation. However, interpolation is not suitable for down-sampling data, as the down-sampled data has no guarantee of compensating for spikes and troughs either side of the measurement step. Instead, the downsampling scheme used is box-averaging, where higher-resolution points within a rolling 'box' around the lower-resolution time steps are mean-averaged. This is especially the more suitable scheme for particle moments, as these consist of aggregations over the time step rather than instantaneous measurements.

The combined data products used by Chapters 4–6, but two illustrative examples of these are the particle-derived current density $\mathbf{j} = ne(\mathbf{v}_i - \mathbf{v}_e)$ and the mass-averaged single-fluid velocity $\mathbf{u} = (m_i\mathbf{v}_i + m_e\mathbf{v}_e)/(m_i + m_e)$. In the case of $\mathbf{j}$, the lower-cadence ion velocity $\mathbf{v}_i$ is interpolated onto the higher-cadence electron velocity $\mathbf{v}_e$. This operation is performed because the small-scale behaviour of $\mathbf{j}$ is dominated by $\mathbf{v}_e$, as demonstrated in Figure 3.3. In contrast, for $\mathbf{u}$ (which is a large-scale variable used to describe fluid motion) $\mathbf{v}_e$ is

averaged down onto the ion timescale because at large scales $\mathbf{u} \approx \mathbf{v}_i$ (because $m_i \gg m_e$).

3.2.2 Spintone

Each MMS probe is spin-stabilised, undergoing one full clockwise rotation approximately every 20 seconds (Burch et al., 2016). As a result of the de-spinning procedure, several data products are recalibrated by the MMS team to remove spintone effects. An additional product is provided which represents the spintone effect on the bulk velocities measured by DES and DIS. Subtracting this data product from the provided bulk velocities removes an artificial spike in the frequency spectrum (see Section 3.3) at ≈ 0.05 Hz (e.g. Bandyopadhyay et al., 2018). Spintone effects, particularly those related to internally-generated photoelectrons (see Section 3.2.4), may still be present in the 3D skymap distributions, which requires care when analysing features in the full VDFs.

3.2.3 FPI Noise Level

A significant portion of the analysis in Chapter 4 involves the power spectrum of particle moments. As such, the statistical uncertainty needs to be propagated into frequency-space to determine whether the noise level of FPI variables is being reached. The noise level is estimated using the method described by Gershman et al. (2015). This involves generating a zero-mean time series of white noise, where at each time step the noise level is a randomly generated value from a normal distribution which has a standard deviation equal to the FPI error provided by MMS (corresponding to the counting statistics propagated through the particle moment calculations). Thus, at every time step the value has a probability distribution given by

$$p(x) = \frac{1}{\sqrt{2\pi\sigma(v_i)^2}} \exp\left(-\frac{x^2}{2\sigma(v_i)^2}\right), \tag{3.6}$$

where $\sigma(v_i)$ is the instantaneous FPI error in the ion velocity moment. Then, the power spectrum of the random variable for each spacecraft is taken and averaged into a single statistical uncertainty which is an approximate noise floor. Based on this uncertainty level, the ranges of scale where spectral curves appear to be contaminated by noise can be

removed. This is done by isolating the range of frequency affected by noise and deleting it from the power spectrum (and any averages taken thereof, as in Chapter 4). The process described in this section is used to generate a noise level for the velocity as shown in 4.8, wherein it can be seen that the velocity moment measurements do reach the noise floor in this example.

3.2.4 Spacecraft Potential and Photoelectrons

As discussed in Section 3.1.3, FPI builds up a particle distribution by counting particles as it scans through different energy channels across a range of azimuthal and elevation directions (relative to the spacecraft spin axis). Due to attraction/repulsion experienced by electrons/ions within non-zero spacecraft potential V_{SC}, it is necessary to remove energy channels with $E < eV_{SC}$ (in the electron case) and correct the remaining channels (and all ion channels) by $+q_s V_{SC}$ (Graham et al., 2021). Electron VDFs can also be contaminated by photoelectrons, which are generated inside the ESAs leading to an artificial enhancement in phase space density at low energies (Gershman et al., 2017). This effect occurs more strongly in the sunward-pointing detectors, leading to a directional enhancement in measured electron phase space density. Electron distributions can also be distorted at low energies by positively-charged spin-plane and axial booms (Toledo-Redondo et al., 2019), and the motion of low-energy electrons can be disturbed by ion plumes when the Active Spacecraft Potential Control (ASPOC) system (Torkar et al., 2016) is turned on (Barrie et al., 2019). It is helpful to be mindful of these effects when analysing unusual VDF signatures, and when computing sensitive data products. For example, in Chapter 6, the velocity (energy) axis of all VDFs is shifted to account for the effect of the spacecraft potential, and the lowest 4 electron bins are removed from any calculations taking place on the full particle distribution. This process is detailed further in Section 6.2.

3.3 Power Spectra

3.3.1 Power Spectral Density

Power spectra are a useful tool to investigate fluctuation power as a function of scale. Since the turbulent cascade typically manifests as a power-law in frequency-space, the power spectrum is commonly employed as a means to analyse how the turbulent cascade distributes energy across different ranges of scale.

Throughout this study, Welch's periodogram method is used to compute the power spectrum (Welch, 1967). Let the n-th frame (i.e. element; time step) of the m-th block (subset of the time series; periodogram) be given by

$$x_m(n) \equiv w(n)x(n + mR) \qquad n = 0, 1, \ldots, M-1, M \qquad m = 0, 1, \ldots, K-1 \tag{3.7}$$

where w is the windowing function (used to taper the ends of each periodogram, making the data quasi-periodic), K is the number of available blocks, M is the number of nonzero samples (after windowing) and R is the offset (or overlap) between windows. The periodogram of the m-th block is then

$$P_{x_m,M}(\omega_k) = \frac{1}{M}\left(\mathrm{FFT}_{N,k}[x_m]\right)^2 \equiv \frac{1}{M}\left(\sum_{n=0}^{N-1} x_m(n)e^{-2\pi ink/N}\right)^2 \tag{3.8}$$

where FFT is the Fast Fourier Transform, $\omega_k = 2\pi/N$ is the frequency, Δt is the measurement resolution and N is the total length of the time series. After this, Welch's method for the power spectral density (PSD) is given by

$$\hat{S}_x^W \equiv \frac{M\Delta t}{K}\sum_{m=0}^{K-1} P_{x,M}(\omega_k) \tag{3.9}$$

which is merely the average of the periodograms corresponding to each block. In this work, a Hanning windowing function (Von Hann and DeCourcy Ward, 1903) was used with each time series split into 3 blocks of length $N/2$, overlapping by $N/4$. Since the intervals are expected to be statistically homogeneous, the power spectrum of each block

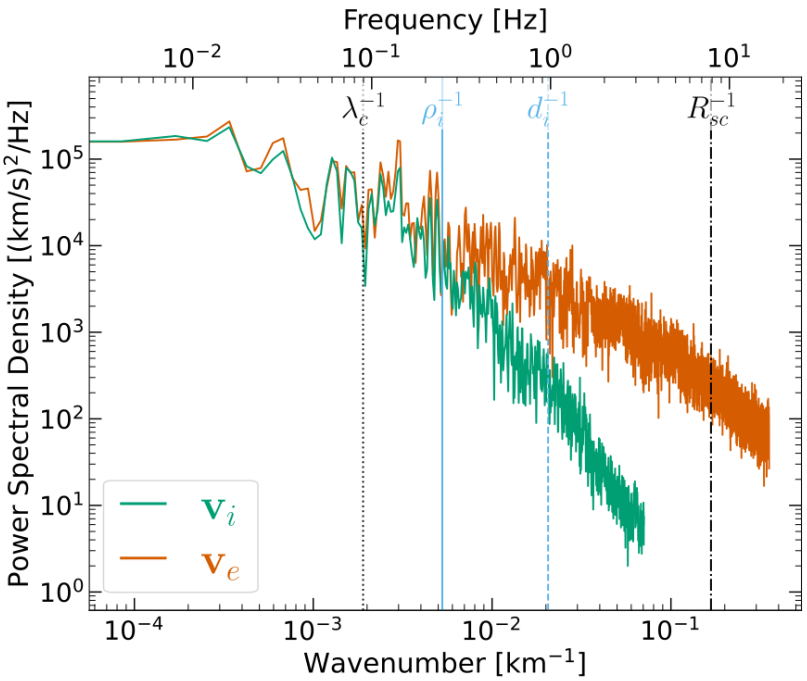


Figure 3.2: Trace Power Spectral Density (PSD) of electron and ion velocity moments as measured by the MMS FPI instruments for an interval of magnetosheath turbulence (2016-12-08/10:16:52–10:21:02). Vertical dashed lines denote wavenumbers associated with characteristic scales.

should be approximately the same. Averaging over the blocks reduces the noise in the spectrum.

To illustrate the concept of the power spectrum, as well as provide useful context for later chapters, Figure 3.2 shows the trace PSD of electron and ion velocity vectors as measured by FPI in an example turbulence interval. In this figure, a periodogram of length $0.5M$ is used, giving to 3 blocks overlapping by $M/2$. The PSD of $\mathbf{v}_i$ does not extend to as large k because the sampling rate is lower. By inspecting how the PSD behaves as a function of scale (where $l \sim 1/k$), it is clear that large-scale velocity fluctuation power is approximately equal between the two species, but at small scales there is significantly more power in $\mathbf{v}_e$ than $\mathbf{v}_i$. The point at which $\mathbf{v}_i$ begins to fall off faster than $\mathbf{v}_e$ is around the ion gyroradius, indicating that ion velocity fluctuations are suppressed in the sub-ion range, the range within which the ions are decoupled from the magnetic field.

3.3.2 Phase Scrambling

To probe whether random phase-alignments are present in a dataset consisting of two vectors dotted into each other (rather than a real relationship), it can be useful to scramble phases and perform the dot product on these new variables. This technique is employed in Chapter 5.

To illustrate the process, take the x-component of generalised variable $\mathbf{q}$ and compute the discrete Fast Fourier Transform (FFT) to obtain the Fourier series,

$$q_x[k] = \mathrm{FFT}(q_x[n]) = \sum_{n=0}^{N-1} q_x[n]\, e^{-2\pi i n k/N}, \tag{3.10}$$

where N is the length of the time series, n represents a given element of the time series, and k is a given frequency. The amplitude is thus

$$c_k = \sqrt{a_k^2 + b_k^2}, \tag{3.11}$$

where a_k and b_k are the real and imaginary coefficients from the Fourier series. The phase is then

$$\theta_k = \arctan\left(\frac{b_k}{a_k}\right), \tag{3.12}$$

which are shuffled randomly into a new order, applying the new ordering to c_k too. Then performing the inverse FFT as

$$q_x[n] = \frac{1}{N}\sum_{k=0}^{N-1} q_x[k] e^{2\pi i n k/N} \tag{3.13}$$

produces a phase-scrambled time series of q_x. Performing this operation on the other components of $\mathbf{q}$ and generalised variable $\mathbf{w}$, then re-combining into vectors and taking the dot product, yields the phase-scrambled $\mathbf{q} \cdot \mathbf{w}$.

3.4 Multi-spacecraft Techniques

3.4.1 Barycentric Estimator

The barycentric estimator is a method for computing a spatial gradient by assuming linear gradients between each spacecraft node and Taylor expanding (Paschmann and Daly, 1998; Shuster et al., 2019). For an arbitrary tensor quantity $\mathcal{Q}$ (a scalar, vector, or higher-order tensor), the barycentric estimator relies on Taylor expanding all other nodes around node 1 to first order

$$\mathcal{Q}_n \approx \mathcal{Q}_1 + \frac{\partial \mathcal{Q}}{\partial x}(x_n - x_1) + \frac{\partial \mathcal{Q}}{\partial y}(y_n - y_1) + \frac{\partial \mathcal{Q}}{\partial z}(z_n - z_1), \tag{3.14}$$

to produce a linear estimate of the gradient which can be solved for the barycenter value. The gradients $\partial\mathcal{Q}/\partial x$, $\partial\mathcal{Q}/\partial y$, and $\partial\mathcal{Q}/\partial z$ are treated as constants, so

$$\begin{bmatrix} (x_2 - x_1) & (y_2 - y_1) & (z_2 - z_1) \\ (x_3 - x_1) & (y_3 - y_1) & (z_3 - z_1) \\ (x_4 - x_1) & (y_4 - y_1) & (z_4 - z_1) \end{bmatrix} \cdot \begin{pmatrix} \partial_x \mathcal{Q} \\ \partial_y \mathcal{Q} \\ \partial_z \mathcal{Q} \end{pmatrix} = \begin{pmatrix} \mathcal{Q}_2 - \mathcal{Q}_1 \\ \mathcal{Q}_3 - \mathcal{Q}_1 \\ \mathcal{Q}_4 - \mathcal{Q}_1 \end{pmatrix}. \tag{3.15}$$

Solving this system gives

$$\begin{pmatrix} \partial_x \mathcal{Q} \\ \partial_y \mathcal{Q} \\ \partial_z \mathcal{Q} \end{pmatrix} = \begin{bmatrix} (x_2 - x_1) & (y_2 - y_1) & (z_2 - z_1) \\ (x_3 - x_1) & (y_3 - y_1) & (z_3 - z_1) \\ (x_4 - x_1) & (y_4 - y_1) & (z_4 - z_1) \end{bmatrix}^{-1} \begin{pmatrix} \mathcal{Q}_2 - \mathcal{Q}_1 \\ \mathcal{Q}_3 - \mathcal{Q}_1 \\ \mathcal{Q}_4 - \mathcal{Q}_1 \end{pmatrix}, \tag{3.16}$$

which, for an arbitrary-dimensional $\boldsymbol{Q}$ gives the gradient tensor $\nabla\boldsymbol{Q}$, which is a tensor of one rank higher than the variable $\boldsymbol{Q}$. For an example vector,

$$(\nabla \boldsymbol{Q})_{ij} = \begin{bmatrix} \partial_x \mathcal{Q}_x & \partial_x \mathcal{Q}_y & \partial_x \mathcal{Q}_z \\ \partial_y \mathcal{Q}_x & \partial_y \mathcal{Q}_y & \partial_z \mathcal{Q}_z \\ \partial_z \mathcal{Q}_x & \partial_z \mathcal{Q}_y & \partial_z \mathcal{Q}_z \end{bmatrix}, \tag{3.17}$$

which can be used to calculate the curl,

$$\nabla \times \boldsymbol{Q} = \begin{pmatrix} (\nabla \boldsymbol{Q})_{yz} - (\nabla \boldsymbol{Q})_{zy} \\ (\nabla \boldsymbol{Q})_{xz} + (\nabla \boldsymbol{Q})_{zx} \\ (\nabla \boldsymbol{Q})_{xy} - (\nabla \boldsymbol{Q})_{yx} \end{pmatrix}. \tag{3.18}$$

Similarly, the divergence is readily evaluated as

$$\nabla \cdot \boldsymbol{Q} = (\nabla \boldsymbol{Q})_{xx} + (\nabla \boldsymbol{Q})_{yy} + (\nabla \boldsymbol{Q})_{zz}. \tag{3.19}$$

The same process can be applied to a rank 2 tensor. In that case, the gradient tensor can be expressed as

$$(\nabla \boldsymbol{Q})_{ijk} = \begin{pmatrix} \begin{pmatrix} \partial_x Q_{xx} \\ \partial_y Q_{xx} \\ \partial_z Q_{xx} \end{pmatrix} & \begin{pmatrix} \partial_x Q_{xy} \\ \partial_y Q_{xy} \\ \partial_z Q_{xy} \end{pmatrix} & \begin{pmatrix} \partial_x Q_{xz} \\ \partial_y Q_{xz} \\ \partial_z Q_{xz} \end{pmatrix} \\ \begin{pmatrix} \partial_x Q_{yx} \\ \partial_y Q_{yx} \\ \partial_z Q_{yx} \end{pmatrix} & \begin{pmatrix} \partial_x Q_{yy} \\ \partial_y Q_{yy} \\ \partial_z Q_{yy} \end{pmatrix} & \begin{pmatrix} \partial_x Q_{yz} \\ \partial_y Q_{yz} \\ \partial_z Q_{yz} \end{pmatrix} \\ \begin{pmatrix} \partial_x Q_{zx} \\ \partial_y Q_{zx} \\ \partial_z Q_{zx} \end{pmatrix} & \begin{pmatrix} \partial_x Q_{zy} \\ \partial_y Q_{zy} \\ \partial_z Q_{zy} \end{pmatrix} & \begin{pmatrix} \partial_x Q_{zz} \\ \partial_y Q_{zz} \\ \partial_z Q_{zz} \end{pmatrix} \end{pmatrix}. \tag{3.20}$$

The divergence of a matrix is hence given by

$$\nabla \cdot \boldsymbol{Q} = \begin{pmatrix} (\nabla \boldsymbol{Q})_{xxx} + (\nabla \boldsymbol{Q})_{yxy} + (\nabla \boldsymbol{Q})_{zxz} \\ (\nabla \boldsymbol{Q})_{xyx} + (\nabla \boldsymbol{Q})_{yyy} + (\nabla \boldsymbol{Q})_{zyz} \\ (\nabla \boldsymbol{Q})_{xzx} + (\nabla \boldsymbol{Q})_{yzy} + (\nabla \boldsymbol{Q})_{zzz} \end{pmatrix}, \tag{3.21}$$

which is how the electron pressure term ($\mathbf{E}_{P_e} = \nabla \cdot \mathbf{P}_e / ne$) and the curlometer current ($\mathbf{j} = \nabla \times \mathbf{B}/\mu_0$) are calculated from MMS data.

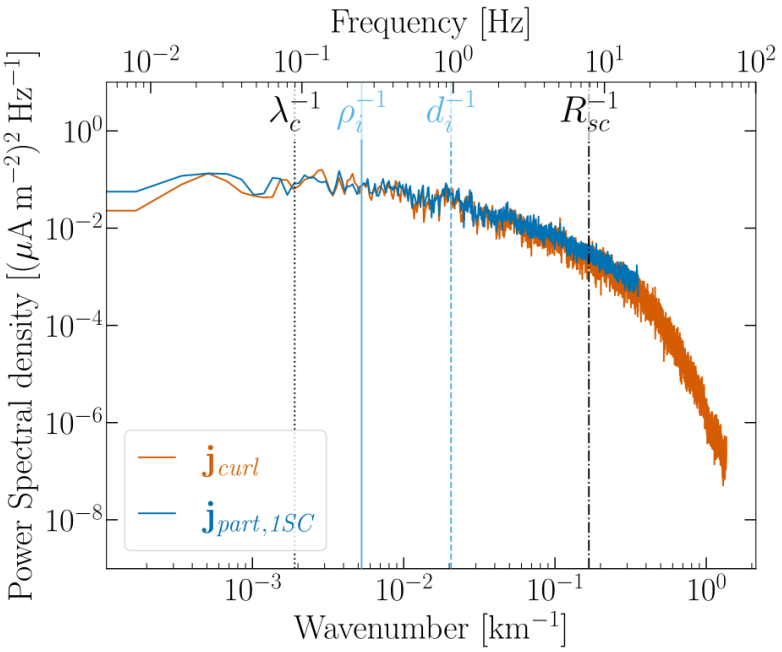


Figure 3.3: Power Spectral Density (PSD) of Single Spacecraft (1SC) $\mathbf{j}_{part} = ne(\mathbf{v}_i - \mathbf{v}_e)$ (i.e. the PSD is taken of $\mathbf{j}_{part}$ for all 4 spacecraft, then averaged) and $\mathbf{j}_{curl} = \nabla \times \mathbf{B}/\mu_0$. The measurement interval used is from 2016-12-08/10:16:52–10:21:02. The wavenumber is estimated using Taylor's hypothesis, as described in Section 3.5.

The Taylor expansion employed by Equation 3.14 assumes that gradients between the spacecraft probes are linear, so any calculation of a spatial gradient by MMS may become unreliable at scales smaller than the characteristic spacecraft separation,

$$R_{sc} = \frac{1}{4}\sum_{i=1}^{4}\sum_{j=1}^{4}|\mathbf{r}_i - \mathbf{r}_j|, \tag{3.22}$$

where $\mathbf{r}$ is the spacecraft position vector. This possibility is discussed further in the following section.

3.4.2 Checking Barycentric Estimator

To illustrate the reliability of the barycentric estimator method, the power spectrum of $\mathbf{j}$ as calculated from the particle velocities ($\mathbf{j}_{part}$, Equation 2.38) and Ampère's law ($\mathbf{j}_{curl}$, Equation 2.13), is plotted in Figure 3.3. It can be seen that the power spectrum of $\mathbf{j}_{curl}$ agrees well with that of $\mathbf{j}_{part}$, indicating that both methods sample the same fluctuation amplitudes as a function of scale. Since the barycentric estimator method is based on a 1st-order Taylor expansion, it assumes gradients between the spacecraft probes are linear,

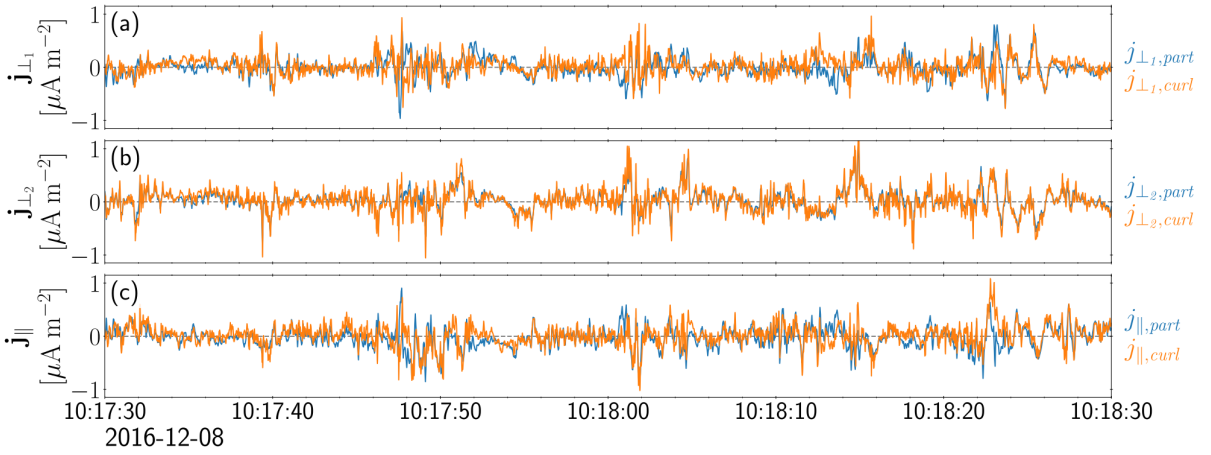


Figure 3.4: Time series of $\mathbf{j}_{part}$ and $\mathbf{j}_{curl}$ (see Figure 3.3 caption) for 2016-12-08/10:17:30–10:18:30. The vector components are in global Field-aligned Coordinates (FAC), where $[\perp_1, \perp_2, \parallel]$ are parallel to $[\mathbf{u}_0 \times \mathbf{B}_0, \mathbf{B}_0 \times (\mathbf{u}_0 \times \mathbf{B}_0), \mathbf{B}_0]$ directions.

meaning that a reduction in power is expected at $k \geq R_{sc}^{-1}$.

In this example, the spacecraft separation R_{sc} is close to the electron instrument cadence, so $\mathbf{j}_{curl}$ only falls off slightly below $k = R_{sc}^{-1}$. In other intervals with larger R_{sc} (smaller R_{sc}^{-1}), a discrepancy appears at small scales due to the barycentric estimator method failing to capture gradients beyond first-order at these scales. Similarly, at large scales (e.g. at $k < \lambda_c^{-1}$), there is a discrepancy between the two current density measurements which possibly arises due to the field increments between spacecraft becoming comparable to the noise level.

An excerpt from the data used to produce Figure 3.3 is plotted in Figure 3.4. In this period, it is apparent that the time series of the two methods for computing current density are in good agreement, component-by-component. Small discrepancies mostly occur in large or sharp current structures, which correspond to when the magnetic gradients may be comparable to the spacecraft separation scale. Overall, the examples shown in Figures 3.3 & 3.4, as well as the same plots for several other intervals (not shown), suggest that the barycentric estimator method gives a reliable approximation of spatial gradients, giving confidence to the measurement of $\mathbf{E}_{P_e}$ and $\mathbf{E}_{in}$ (which rely on this technique) in Chapter 4.

3.5 Taylor's Hypothesis

Taylor's hypothesis (Taylor, 1938) is important in satellite data analysis because it associates time series measured by spacecraft instruments with spatial slices through physical structures. Turbulence predictions are usually expressed in terms of wavenumber k, however spacecraft measure time series and as such are only able to measure frequency spectra (where the frequency is in the spacecraft frame). Any such frequency ω_{sc} will have a temporal component ω_{plas} in the plasma rest frame, and a spatial component which arises from the doppler shift, $\mathbf{k} \cdot \mathbf{u}_0$. It is possible to relate these quantities via

$$\omega_{sc} = \omega_{plas} + \mathbf{k} \cdot \mathbf{u}_0, \tag{3.23}$$

where $\mathbf{k}$ is the wavevector and $\mathbf{u}_0$ is the mean bulk velocity. If the bulk flow is fast enough, temporal changes will occur much slower than the time taken to advect over a point in space, such that

$$\omega_{plas} \ll \mathbf{k} \cdot \mathbf{u}_0. \tag{3.24}$$

Thus, a spacecraft transecting a plasma structure subject to these conditions will measure an effective spatial cut through the plasma instead of a time series (Sahraoui et al., 2020). A measured frequency f_{sc} can be converted to a wavenumber using the relation

$$k = \frac{2\pi f_{sc}}{|\mathbf{u}_0|}. \tag{3.25}$$

There are several ways in which the Taylor hypothesis is usually tested. If one assumes that the fluctuations are related to linear wave modes, comparing the bulk velocity to the phase speed of the different waves can be used to determine whether the hypothesis is valid (Matthaeus and Goldstein, 1982; Klein et al., 2014; Perri et al., 2017). Alternatively, it can be checked by comparing statistical quantities (usually the structure functions) computed using Taylor's hypothesis to multi-spacecraft quantities which don't assume Taylor's hypothesis is valid (C. H. K. Chen and Boldyrev, 2017; Chhiber et al., 2018; Stawarz et al., 2022). Finally, if the magnetic spectral breaks are taken to occur at ρ_i and

ρ_e, Taylor's hypothesis can be tested by comparing the actual frequencies of the breaks with the Taylor-shifted gyroscales (Sahraoui et al., 2012; Huang et al., 2014). However, as will be discussed in Chapter 4, the spectral break does not universally occur at these scales, so this method may not be reliable in some cases.

Using these methods (particularly, recently, the structure function comparison), Taylor's hypothesis has been shown to be valid at the MMS spacecraft separation scale (Chasapis et al., 2017; C. H. K. Chen and Boldyrev, 2017; Chhiber et al., 2018; Stawarz et al., 2019; Stawarz et al., 2021; Stawarz et al., 2022) and as such can be assumed to be valid at similar or larger scales (Stawarz et al., 2022). However, in some cases the assumption is violated (Stawarz et al., 2019), emphasising the importance of checking its validity when equating temporal measurements to spatial measurements. A further limitation of Taylor's hypothesis is that it measures the reduced wavenumber spectrum averaged onto the direction of background flow ($\omega_{\rm sc} \sim ku\cos\theta_{\rm ku}$). To fully describe the **k**-spectrum, it is necessary to use multi-spacecraft methods (e.g. Zhao et al., 2023).

3.6 Probability Density Functions

The Probability Density Function (PDF) of a dataset is a function which gives the relative likelihood of a randomly sampled data point to have a given value, normalised so that the integral of the PDF is 1. This is a powerful tool for understanding the distribution of values within a dataset, such as in intermittent turbulence (Section 2.3.3). Taking moments over the PDF reveals different characteristics of the distribution, which are discussed below.

The first-order moment is simply the mean, μ. The second-order moment is the variance, σ^2, which represents the spread of the distribution,

$$\sigma^2 = \frac{\sum_{i=1}^{N}(x_i - \mu)^2}{N}, \tag{3.26}$$

where x_i are the elements of the distribution, and N is the total number of points in the

distribution. The third-order moment is skewness, γ_1, which is a measure of asymmetry in the distribution, given by

$$\gamma_1 = \frac{\frac{1}{N}\sum_i (x_i - \mu)^3}{\sigma^3} = \frac{\frac{1}{N}\sum_i (x_i - \mu)^3}{(\frac{1}{N}\sum_i (x_i - \mu)^2)^{3/2}}. \tag{3.27}$$

The fourth-order moment is the kurtosis κ, which represents the tailedness of the distribution, is given by

$$\kappa = \frac{\frac{1}{N}\sum_i (x_i - \mu)^4}{\sigma^4} = \frac{\frac{1}{N}\sum_i (x_i - \mu)^4}{(\frac{1}{N}\sum_i (x_i - \mu)^2)^2}. \tag{3.28}$$

Kurtosis of a normal distribution is 3, smaller values have diminished tails, and larger values have enhanced tails. As such, high κ is a convenient diagnostic of intermittency (Greco et al., 2009).

Chapter 4

Turbulent Electric Fields Under Different Magnetosheath Conditions

Material in this chapter has been published as:

H. C. Lewis, J. E. Stawarz, L. Franci, L. Matteini, K. Klein, C. S. Salem, J. L. Burch, R. E. Ergun, B. L. Giles, C. T. Russell, and P.-A. Lindqvist (2023). "Magnetospheric Multiscale measurements of turbulent electric fields in earth's magnetosheath: How do plasma conditions influence the balance of terms in generalized Ohm's law?" In: *Physics of Plasmas* **30**:8, p. 082901. DOI: 10.1063/5.0158067

4.1 Introduction

Electric fields (**E**) are a crucial element in the unsolved problem of turbulent dissipation. Since magnetic fields cannot do work on the charged particles, it is the electric field which mediates energy exchange between the magnetic field **B** and particle velocity via the Lorentz force. The evolution of **B** is also intimately linked to **E**, via the induction law (Equation 2.48), so the behaviour of the electric field indicates the physical processes underlying the dynamics (see Section 2.3.4). As such, characterising the nature of **E** at different spatial scales, and under a variety of plasma conditions, is valuable to our un-

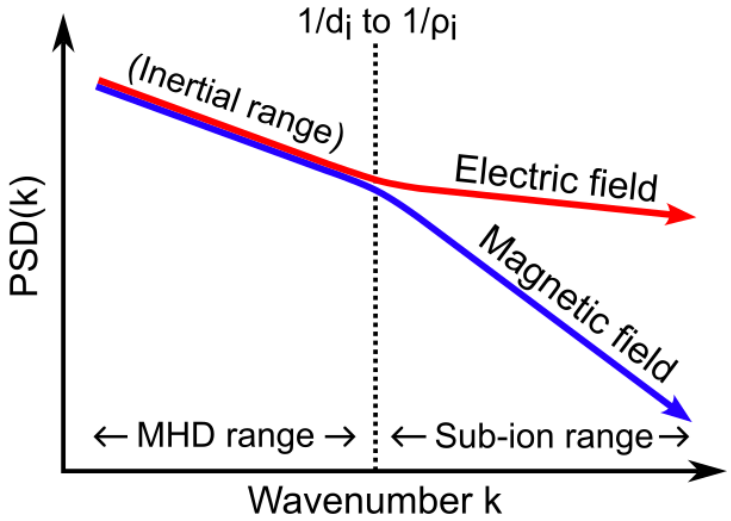


Figure 4.1: Schematic Power Spectral Density (PSD) of **B** and **E**, demonstrating the change in spectral behaviour when transitioning from the MHD inertial range into the sub-ion scales.

derstanding of how turbulence changes from the fluid regime dominated by MHD physics to sub-ion scales where kinetic effects come into play (see Section 2.3.1).

In the context of a turbulent plasma, **E** exhibits a spectral slope similar to **B** and **u** at MHD scales, which then becomes shallower below the ion scales[1] (Bale et al., 2005; Chaston et al., 2008; Stawarz et al., 2016; Matteini et al., 2016; C. H. K. Chen and Boldyrev, 2017). This is illustrated schematically in Figure 4.1. The enhancement in **E** fluctuations at small scales arises due to the growing importance of $\mathbf{E}_{Hall}$ and $\mathbf{E}_{P_e}$ (see Section 2.1.4) compared to $\mathbf{E}_{MHD}$ (Matteini et al., 2016), which has been observed in simulations (e.g. Howes et al., 2011; Franci et al., 2015b; Franci et al., 2018; Papini et al., 2019; Franci et al., 2020) and spacecraft measurements (Stawarz et al., 2021).

The shallower **E** spectrum suggests that there is a relative increase in energy density carried by electric field fluctuations compared to the magnetic field, although for there to be more energy in the electric field the PSD would need to be a factor of c^2 greater. This spectral behaviour has been associated with Kinetic Alfvén Waves (KAW) by comparing E^2/B^2 to the dispersion relation for KAWs (e.g. Howes et al., 2008; Schekochihin et al., 2009; C. H. K. Chen and Boldyrev, 2017; Dwivedi et al., 2019), although it has been

[1]Throughout, 'below the ion scales' refers to spatial scales smaller than around ρ_i and d_i.

demonstrated that KAW modes are not crucial to reproduce the electric field enhancement (e.g. Matthaeus et al., 2008; Papini et al., 2019). Changes in the spectral behaviour might also arise due to the potential onset of dissipative processes which interrupt and eventually terminate the turbulent cascade.

The balance of terms in generalised Ohm's law (Equation 2.44) reveals information about the nonlinear dynamics, helping to constrain turbulence theories and lay the groundwork for further studies examining energy conversion and dissipation in turbulent environments (such as in Chapter 5). Stawarz et al. (2021) examined the relative contributions from different terms in generalised Ohm's law for three turbulent magnetosheath intervals, characterising the behaviour of the spectra for each term. Within these intervals, fluctuations in $\mathbf{E}_{MHD}$ dominated the spectrum at large scales, transitioning to $\mathbf{E}_{Hall}$ around the ion scales. The relative contribution of $\mathbf{E}_{P_e}$ compared to $\mathbf{E}_{Hall}$ was approximately constant across scales, and the spatial part of $\mathbf{E}_{inertia}$ was small across the range of scales currently accessible by spacecraft measurements. Stawarz et al. (2021) also investigated the ratio of nonlinear to linear components of $\mathbf{E}_{MHD}$ and $\mathbf{E}_{Hall}$, showing that the former becomes more nonlinear at small scales due to increasing misalignment between $\mathbf{B}$ and $\mathbf{u}$ fluctuations as a result of the Hall effect modifying the MHD magnetic field, and that the latter remains constant across all scales.

The Stawarz et al. (2021) case study leaves several unanswered questions which are addressed in this study. It is still unknown how properties of the turbulence and ambient plasma conditions impact the balance of electric field contributions, and the ratio of nonlinear to linear contributions to each term. The work in this chapter constitutes a statistical survey of spectral characteristics, linking changes in these to variability in the properties of the surrounding plasma. The investigation covers how spectral features can be estimated based on characterisations of the way turbulence self-consistently organises the fluctuations and underlying ambient plasma parameters. The implication of the relationship between spectra, properties of turbulence, and ambient parameters in the context of validity of turbulence theories and approximations is discussed, elucidating

potential constraints for future theoretical and simulation studies. The results provide insight into electric field behaviour in plasma systems where high-quality multi-spacecraft observations are not available to directly measure individual electric field contributions.

4.2 Data Set and Methods

4.2.1 Interval Selection

This study examines the database of magnetosheath turbulence intervals compiled by Stawarz et al. (2022). The database contains 60 intervals of continuous 'burst' mode observations by MMS in the magnetosheath, the dates of which are given in Appendix B.1. The intervals are all several minutes in length, corresponding to multiple magnetic correlation lengths λ_c (the largest scale of turbulence fluctuations of the magnetic field in a system – see Section 2.3.2), are homogeneous on large scales, and have necessarily fast bulk flow speed u_0 compared to dynamic evolution of the plasma for Taylor's hypothesis (Taylor, 1938, see Section 3.5) to be satisfied (Stawarz et al., 2022). The intervals are well-suited to turbulence analyses thanks to these properties, allowing power spectra to be used to probe the turbulent cascade and for frequency spectra to be converted into wavenumber spectra and thus compared with known spatial scales.

The dataset is suitable for an investigation into the relative importance of generalised Ohm's law terms as a function of plasma conditions because the intervals cover a wide range of different background plasma parameters. The range of background parameters is shown in Figure 4.2; covering around 2.5 orders of magnitude in β_i, 2.7 in β_e, 1.3 in $\delta B_{rms}/B_0$, and 1.5 in v_A. The intervals feature strong variability in plasma variables such as $\mathbf{B}$, $\mathbf{u}$, and $\mathbf{E}$, which is typical of the turbulent magnetosheath. Finally, the intervals are multiple magnetic correlation lengths λ_c in duration (a turbulence parameter rather than a plasma parameter; see Section 2.3.2) and the average spacecraft separation $R_{sc} = \langle|\mathbf{R}_i - \mathbf{R}_j|\rangle$, for position $\mathbf{R}$ and spacecraft index $i \neq j \in \{1, 2, 3, 4\}$, is small enough to probe sub-ion scale gradients via the barycentric estimator method (Section 3.4.1).

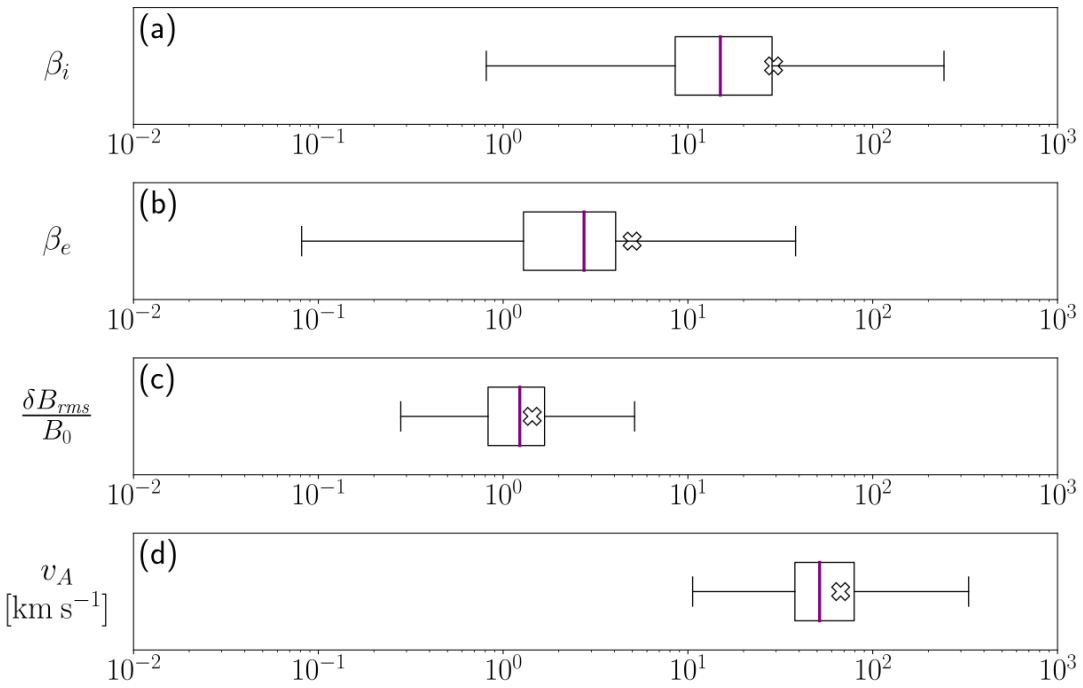


Figure 4.2: Range of background parameters: (a) β_i, (b) β_e, (c) $\delta B_{rms}/B_0$, and (d) v_A. The whiskers denote the most extreme values, the box represents the first quartile to the third quartile, the purple vertical line is the median, and the cross shows the mean.

Figure 4.3 demonstrates a typical turbulence period. Panels 4.3 (a) & (b) show **B** and **E** to be turbulent and homogeneous on large scales, exhibiting multi-scale fluctuations without large reduction or enhancement of amplitude across the full length of the interval. Panel 4.3 (c) shows the bulk velocity, including the local v_A, where it can be seen that bulk flow is typically faster than the Alfvén speed and that there is a relatively fast background flow compared to the fluctuations. Panel 4.3 (d) demonstrates significant fluctuations in the density are present, by up to a factor of 2, and that quasineutrality is maintained between n_e and n_i. Panels 4.3 (e) & (f) show the current density, which exhibits bursty signatures where the sharp peaks correspond to current sheets in regions of sharp magnetic gradients/rotations. Comparing the two panels reveals that the current can be calculated consistently either by the particle method or the barycentric estimator method. Panels 4.3 (g)–(k) show the calculated terms of generalised Ohm's law (Section 2.1.4) with different y-axis limits. Panels 4.3 (i) & (j) in particular highlight the similar location and relative magnitude of spikes in $|E_{Hall}|$ and $|E_{P_e}|$, with $|E_{P_e}|$ typically having smaller amplitude. Panel 4.3 (k) shows the the very small signal strength in $\mathbf{E}_{inertia}$. Finally, panel 4.3 (l)

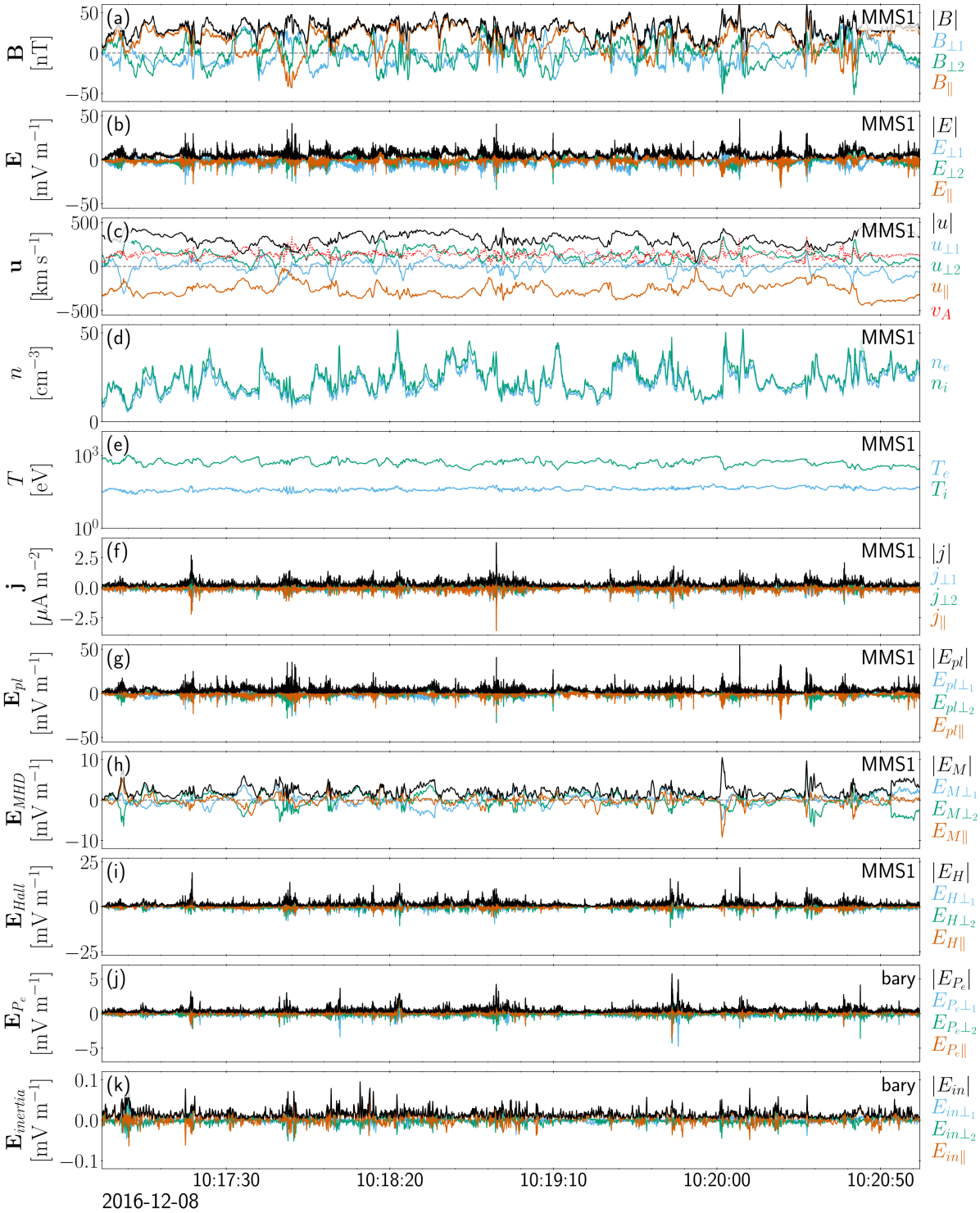


Figure 4.3: Time series of variables for the example interval from 2016-12-08/10:16:52–10:21:02. Text on the right-hand side of each panel indicates whether the variable is a Single Spacecraft (1SC) quantity (see Section 4.2.2) from a specific spacecraft, or the barycenter average over all four spacecraft. Vector quantities are in Field-aligned Coordinates (FAC), with $[\perp_1, \perp_2, \parallel]$ defined parallel to the local $[\mathbf{u} \times \mathbf{B}, \mathbf{B} \times \mathbf{u} \times \mathbf{B}, \mathbf{B}]$, respectively.

shows the fluctuating scalar isotropic temperatures, where the electrons are hotter than the ions.

4.2.2 Computing Generalised Ohm's Law

The four key terms in generalised Ohm's law, $\mathbf{E}_{MHD}$, $\mathbf{E}_{Hall}$, $\mathbf{E}_{P_e}$, and $\mathbf{E}_{inertia}$, are computed using the method used by Stawarz et al. (2021), outlined in the following. The component of $\mathbf{E}$ arising from the advection of magnetic structure in the background flow is removed by subtracting $-\mathbf{u}_0 \times \mathbf{B}$ (where $\mathbf{u}_0$ is the mean vector single-fluid velocity $\approx \langle \mathbf{v}_i \rangle$) from the observed electric field, $\mathbf{E}_{obs}$. This is defined as the plasma-frame electric field,

$$\mathbf{E}_{pl} = \mathbf{E}_{obs} + \mathbf{u}_0 \times \mathbf{B}. \tag{4.1}$$

The same process is applied to $\mathbf{E}_{MHD}$, redefining it as

$$\mathbf{E}_{MHD} = -\mathbf{u} \times \mathbf{B} + \mathbf{u}_0 \times \mathbf{B} = -\delta\mathbf{u} \times \mathbf{B}, \tag{4.2}$$

where $\delta\mathbf{u} = \mathbf{u} - \mathbf{u}_0$ is the time-varying difference from the background flow. The single-fluid velocity is calculated as $\mathbf{u} = (m_e\mathbf{v}_e + m_i\mathbf{v}_i)/(m_e + m_i)$, using $\mathbf{v}_e$ downsampled to $\mathbf{v}_i$ because $\mathbf{u}$ is dominated by $\mathbf{v}_i$ at observable scales (see Figure 3.2). $\mathbf{E}_{Hall}$ is calculated using the particle current density $\mathbf{j} = ne(\mathbf{v}_i - \mathbf{v}_e)$, with $\mathbf{v}_i$ interpolated onto the electron timescale because $\mathbf{j}$ is dominated by $\mathbf{v}_e$ at small scales (as shown in Figure 3.2), where the Hall term is important. The current is verified by comparing with the current from Ampère's Law, $\mathbf{j} = \nabla \times \mathbf{B}/\mu_0$, computed by the barycentric estimator method (Robert et al., 1998a, see Section 3.4.1). Finally, $\mathbf{E}_{inertia}$ cannot be fully computed because it contains both a spatial and temporal component, which cannot be independently resolved due to Taylor's hypothesis. As such, the inertia term is computed as

$$\mathbf{E}_{inertia} = \frac{m_e}{ne^2}\left[\nabla \cdot \left(\mathbf{uj} + \mathbf{ju} - \frac{\mathbf{jj}}{ne}\right)\right]. \tag{4.3}$$

4.2.3 Computing Power Spectra

Fluctuation power in turbulent variables exhibits different scalings across different wavenumber bands, making the power spectrum a convenient tool to compare the relative importance of variables as a function of scale. In this chapter, power spectral density is computed using the Welch's method (Welch, 1967) as described in Section 3.3. Where variables are vectors or tensors, the trace power spectrum (e.g. $\mathrm{PSD}[\mathbf{q}] = \mathrm{PSD}[q_x] + \mathrm{PSD}[q_y] + \mathrm{PSD}[q_z]$) is taken, unless otherwise stated. The electromagnetic fields and plasma moments are measured by the four MMS spacecraft simultaneously, so one can calculate Single Spacecraft (1SC) power spectra to reveal information about scales smaller than the spacecraft separation. Alternatively, any variables containing spatial gradients are computed using the barycentric estimator method (denoted by subscript *bary*; defined in Section 3.4.1), which is evaluated at the barycenter of the MMS tetrahedron and as such filters out power at scales comparable to or smaller than the spacecraft separation. To compare 1SC and barycenter spectra – which reveals the impact of barycenter averaging – the 1SC variables are averaged onto the barycenter after computing the power spectrum, i.e. $\mathrm{PSD}[\mathbf{E}_{MHD}] = \langle \mathrm{PSD}[\mathbf{E}_{MHD,1SC}] \rangle_{bary}$.

Figure 4.4 shows power spectra of plasma variables and generalised Ohm's law terms for the same example interval as in Figure 4.3. Panel 4.4 (a) shows typical power spectra of normalised $\mathbf{E}_{pl}$, $\mathbf{B}$, $\mathbf{u}$, $\mathbf{j}$ and n. All variables have similar trends at large scales and diverge in the ρ_i to d_i range, with $\mathbf{E}_{pl}/v_A B_0$ and $\mu_0 \rho_i \mathbf{j}/B_0$ following a shallower power law than $\mathbf{B}/B_0$, $\mathbf{u}/v_A$, and n/n_0. Panel 4.4 (b) shows power spectra of the generalised Ohm's law terms. Each term exhibits a different power law and amplitude, related to how the dynamics vary between terms. $\mathbf{E}_{inertia}$ has small fluctuation power compared to the other three terms at all accessible scales, which is also observed in every other interval, so this term is not considered further. Spectral characteristics of the remaining terms, particularly the interplay between them and how this changes depending on the plasma conditions, will be introduced in the following section and explored throughout this chapter.

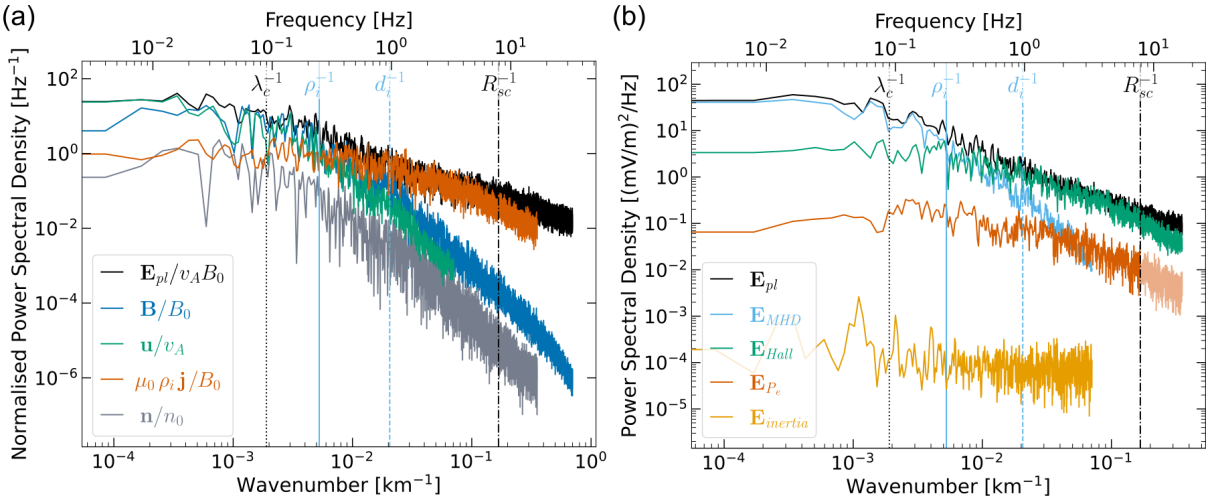


Figure 4.4: Power spectra of plasma variables and electric field terms for interval 2016-12-08/10:16:52–10:21:02. (a) Power spectra of selected normalised quantities: $\mathbf{E}_{pl}/v_A B_0$, $\mathbf{B}/B_0$, $\mathbf{u}/v_A$, $\mathbf{j}\mu_0\rho_i/B_0$, and $\mathbf{n}/n_0$. Vertical lines represent the wavenumbers associated with the scales λ_c, ρ_i, d_i, and R_{sc}. (b) The power spectra of $\mathbf{E}_{pl}$, $\mathbf{E}_{MHD}$, $\mathbf{E}_{Hall,1SC}$, $\mathbf{E}_{P_e}$, and $\mathbf{E}_{inertia}$, where $\mathbf{E}_{pl}$ is averaged onto the electron cadence. $\mathbf{E}_{P_e}$ measurements at scales smaller than R_{sc} have been faded to indicate where the breakdown of the first-order gradient approximation could be impacting reliability.

When comparing $\mathbf{E}_{Hall}$ to $\mathbf{E}_{MHD}$, the former term is averaged onto the measurement cadence of the latter (the ion timescale, 150 ms cadence), and then the average of the 1SC power spectra is taken such that $(E_{Hall}/E_{MHD})^2 = \langle \mathrm{PSD}[\mathbf{E}_{Hall,1SC}]/\mathrm{PSD}[\mathbf{E}_{MHD,1SC}] \rangle_{\mathrm{bary}}$. Conversely, when comparing $\mathbf{E}_{P_e}$ to $\mathbf{E}_{Hall}$, $\mathbf{E}_{Hall}$ stays on its original sampling cadence and the power spectrum of the barycenter average is used, such that $(E_{P_e}/E_{Hall})^2 = \mathrm{PSD}[\langle \mathbf{E}_{Hall,1SC} \rangle_{\mathrm{bary}}]/\mathrm{PSD}[\mathbf{E}_{P_e}]$. Consequently, E_{P_e}/E_{Hall} cannot be evaluated at length scales smaller than R_{sc}.

4.3 Dimensional Analysis

The interplay between the different terms in generalised Ohm's law determines the overall behaviour of the electric field by describing its evolution as a sum of contributions arising from different physical effects. To understand how the balance between these contributions changes in response to differing ambient plasma conditions, as well as the way the turbulence self-consistently organises the fluctuations, the relationship between power spectra of electric field terms is investigated in this chapter. Starting with the

Fourier transforms of the MHD, Hall, and electron pressure terms in generalised Ohm's law (Equation 2.44), which are given in Equations 2.93, 2.94, and 2.95, respectively, a dimensional analysis approach is taken in this section to reduce the complexity arising from the convolutions. By using simplifying assumptions the behaviour of the convolutions can be estimated. Later in this chapter, the convolutions will be constrained observationally and compared to these dimensional estimates in order to learn about the role of plasma conditions on the spectral behaviour of the turbulent electric field.

4.3.1 Conventions

It is helpful in turbulence studies to decompose variables $\mathcal{Q}(t)$ into a background $\mathcal{Q}_0 = \langle \mathcal{Q}(t) \rangle$ and fluctuating deviation from the mean $\delta\mathcal{Q}(t) = \mathcal{Q}(t) - \mathcal{Q}_0$. Additionally, when calculating the power spectral density of a fluctuating variable (see Section 3.3) one obtains the fluctuation amplitude as a function of wavenumber k, which is denote by $\delta\mathcal{Q}(k)$. Taking $k_l = 1/l$ as the wavenumber associated with a given spatial scale l, we can isolate a contribution to the fluctuation intensity from a given scale as $\delta\mathcal{Q}(k_l)$. With these tools, different ways to characterise a scale-dependent fluctuation can be defined. First, the root mean square (rms) fluctuation $\delta\mathcal{Q}_{rms} = \sqrt{\langle(\delta\mathcal{Q})^2\rangle}$ is equivalent to integrating the power spectrum over all wavenumbers (which is likely to be weighted towards large scales due to the power-law decay of fluctuation amplitudes typically exhibited by turbulence). Alternatively, integrating across a range of k, $\Delta k = [k - \delta k, k + \delta k]$, gives the power associated with that range of wavenumbers. A quotient of two fluctuating quantities, $\delta\mathcal{Q}_1(k)/\delta\mathcal{Q}_2(k)$, can be evaluated at some k_l or integrated (or averaged if the ratio is not decaying with k) over some Δk to understand the balance of fluctuation power at or between some scales. The following section will frequently characterise fluctuating variables as single numbers, where the method chosen encodes some physical information about the scale-dependence of the variables.

4.3.2 Ratios Between Generalised Ohm's Law Terms

The dynamics of $\mathbf{E}$ are dominated by $\mathbf{E}_{MHD}$, $\mathbf{E}_{Hall}$, and $\mathbf{E}_{P_e}$, as seen in the example spectrum in Figure 4.4 (b). The relationship between the different terms varies on an interval-by-interval basis, however there are some quantifiable features of the spectra which reflect characteristics of the dynamics. The first of these is the Hall scale (k_{Hall}), which refers to the length scale at which $\mathbf{E}_{MHD}$ and $\mathbf{E}_{Hall}$ exchange spectral dominance. By taking the ratio E_{Hall}/E_{MHD} and neglecting the angles between vectors (which is not a priori the obvious thing to do, but will be shown in the results of this chapter to be a valid assumption), the scale dependent relationship is found to be

$$\frac{E_{Hall}}{E_{MHD}} \sim \frac{\left|\frac{1}{ne}\,\mathbf{j}\times\mathbf{B}\right|}{|-\delta\mathbf{u}\times\mathbf{B}|} \sim \frac{\left|\frac{1}{ne}\frac{\nabla\times\mathbf{B}}{\mu_0}\times\mathbf{B}\right|}{|-\delta\mathbf{u}\times\mathbf{B}|} \sim \frac{\frac{1}{ne\mu_0}k\,\delta B\,B}{\delta u\,B}, \tag{4.4}$$

where k is a wavenumber coming from $\nabla\times\mathbf{B}$. To simplify further, using the relationship

$$d_i = \sqrt{\frac{m_i}{ne^2\mu_0}} = \frac{1}{ne\mu_0}\sqrt{\mu_0 n m_i}, \tag{4.5}$$

Equation 4.4 becomes

$$\frac{E_{Hall}}{E_{MHD}} \sim \frac{d_i}{\sqrt{\mu_0 m_i n}}\frac{k\delta B}{\delta u} \sim k d_i \frac{\delta b_A}{\delta u}, \tag{4.6}$$

where the magnetic fluctuation in Alfvén units $\delta b_A = \delta B/\sqrt{\mu_0 m_i n}$ (where $n = n_0 + \delta n$). To approximate k_{Hall} requires taking $E_{Hall}/E_{MHD} = 1$ and solving for k, such that

$$k_{Hall} = \frac{1}{d_i}\frac{\delta u}{\delta b_A}. \tag{4.7}$$

Second, the dynamics of $\mathbf{E}_{P_e}$ and $\mathbf{E}_{Hall}$ are typically observed to be spectrally similar, except with more power in $\mathbf{E}_{Hall}$. To arrive at a dimensional analysis expression for the ratio of these terms, $\mathbf{E}_{Hall}$ is expanded as in Equation 4.4, then the numerator and denominator are multiplied by $P_{e,0}/P_{e,0}$ and B_0^2/B_0^2, respectively, giving

$$\frac{\left|\frac{1}{ne}\,\nabla\cdot\mathbf{P}_e\right|}{\left|\frac{1}{ne}\,\mathbf{j}\times\mathbf{B}\right|} \sim \frac{|\nabla\cdot\mathbf{P}_e|}{|\nabla\times\delta\mathbf{B}/\mu_0\times\mathbf{B}|} \sim \frac{|n_0 T_{e,0}\nabla\cdot\mathbf{P}_e/P_{e,0}|}{|\nabla\times(\delta\mathbf{B}/B_0)\times(\mathbf{B}/B_0)\,B_0^2/\mu_0|}. \tag{4.8}$$

Utilising the expression for the electron plasma beta,

$$\beta_e = \frac{n_0 T_{e,0}}{B_0^2/2\mu_0}, \tag{4.9}$$

Equation 4.8 can be simplified and treated dimensionally as

$$\frac{\beta_e}{2}\frac{|\nabla \cdot \mathbf{P}_e/P_{e,0}|}{|\nabla \times (\delta\mathbf{B}/B_0) \times (\mathbf{B}/B_0)|} \sim \frac{\beta_e}{2}\frac{\delta P_e/P_{e,0}}{\delta B/B_0}\frac{B_0}{\langle|B|\rangle}, \tag{4.10}$$

where $\langle|B|\rangle = \langle\sqrt{|\mathbf{B}_0|^2 + 2\delta\mathbf{B}\cdot\mathbf{B}_0 + |\delta\mathbf{B}|^2}\rangle$ is the average magnitude of the magnetic field, which becomes B_0 in the case of small fluctuation amplitudes. When making $\mathbf{j}\times\mathbf{B}$ dimensionless, $\langle|B|\rangle$ has been included to incorporate the fluctuation amplitudes. Equation 4.10 does not contain an explicit k dependence, which is consistent with expectations provided that δP_e has the same spectral scaling as $\delta B\langle|B|\rangle$.

4.3.3 Ratios of Nonlinear to Linear Contributions

Each term can be further decomposed into background (non-fluctuating), linear (single fluctuating variable) and nonlinear (multiple fluctuating variables) components. Nonlinear variables are associated with scale-transfer terms related to turbulence, whereas linear variables in isolation produce wave-like behaviour, so measuring the ratio of nonlinear to linear contributions of a term is a way of understanding which processes are driving the dynamics of that term. Such factors are important in turbulence theories since they usually involve assumptions about the nature of the nonlinear fluctuations, often related to the rate of nonlinear interactions, τ_{nl}, as compared to linear wave periods, τ_l (see Section 2.3). As such, the ratio of nonlinear to linear terms can be taken as a proxy for a $1/\chi$ parameter.

To understand how the ratio of nonlinear to linear contributions varies under different conditions for the three dominant terms in generalised Ohm's law, dimensional analysis techniques are again employed to estimate the ratio of nonlinear to linear elements of each term, hereafter denoted as $R^{NL/L}$. For $\mathbf{E}_{MHD}$ and $\mathbf{E}_{Hall}$, the ratios are are given

respectively by

$$R_{MHD}^{NL/L} = \frac{|-\delta\mathbf{u}\times\delta\mathbf{B}|}{|-\delta\mathbf{u}\times\mathbf{B}_0|} \sim \frac{\delta B}{B_0}, \tag{4.11}$$

$$R_{Hall}^{NL/L} = \frac{|\delta\mathbf{j}\times\delta\mathbf{B}|/ne}{|\delta\mathbf{j}\times\mathbf{B}_0|/ne} \sim \frac{\delta B}{B_0}, \tag{4.12}$$

where the $-\mathbf{u}_0\times\delta\mathbf{B}$ linear part of the $\mathbf{E}_{MHD}$ term is missing since we are in the frame moving with the bulk plasma velocity, and the $\mathbf{j}_0\times\delta\mathbf{B}$ linear part of $\mathbf{E}_{Hall}$ is neglected as we expect there to be no large-scale currents.

In the case of $\mathbf{E}_{P_e}$, two linear terms are present: one associated with density fluctuations δn; and the other associated with temperature fluctuations $\delta\mathbf{T}_e$. The electric fields associated with δn, $\delta\mathbf{T}_e$, the 'combined' linear term, and the nonlinear contribution $\delta n\delta\mathbf{T}_e$ are given respectively by

$$\mathbf{E}_{\delta n} = -\frac{\delta n\nabla\cdot\mathbf{T}_{e,0}}{ne}, \tag{4.13}$$

$$\mathbf{E}_{\delta T_e} = -\frac{n_0\nabla\cdot\delta\mathbf{T}_e}{ne}, \tag{4.14}$$

$$\mathbf{E}_{\delta T_e+\delta n} = -\frac{\nabla\cdot(n_0\delta\mathbf{T}_e+\delta n\mathbf{T}_{e,0})}{ne}, \tag{4.15}$$

$$\mathbf{E}_{\delta n\delta T_e} = -\frac{\nabla\cdot(\delta n\delta\mathbf{T}_e)}{ne}. \tag{4.16}$$

Since there are two linear terms, $R_{P_e}^{NL/L}$ can be expressed as

$$R_{P_e}^{NL/\delta T_e} = \frac{|\mathbf{E}_{\delta n\delta T_e}|}{|\mathbf{E}_{\delta T_e}|} \sim \frac{\delta n}{n_0}, \tag{4.17}$$

$$R_{P_e}^{NL/\delta n} = \frac{|\mathbf{E}_{\delta n\delta T_e}|}{|\mathbf{E}_{\delta n}|} \sim \frac{\delta T_e}{T_{e,0}}, \tag{4.18}$$

$$R_{P_e}^{NL/combined} = \frac{|\mathbf{E}_{\delta n\delta T_e}|}{|\mathbf{E}_{\delta T_e+\delta n}|} \sim \frac{\delta n\delta T_e}{n_0\delta T_e+\delta n T_{e,0}}, \tag{4.19}$$

where we have assumed that the divergence of the nonlinear component is the same as that of the linear components.

4.4 Results

4.4.1 The Hall Scale

The wavenumber k_{Hall} corresponds to the smallest spatial scale at which the turbulent electric field is dominated by fluctuations in the MHD term. Figure 4.5 (a) shows the square root of the ratio of E_{Hall} to E_{MHD} as a function of scale for an example interval, with k_{Hall} defined as the wavenumber representing the intersection of this curve with $E_{Hall}/E_{MHD} = 1$. To reduce the impact of spectral noise and the unequal density of points across wavenumber space on the determination of k_{Hall}, the measured ratio of spectra is averaged over equal-width bins in log space and then a linear fit is taken of this curve. The intersection of this fit with $E_{Hall}/E_{MHD} = 1$ gives the measured k_{Hall}.

Equation 4.6 expresses k_{Hall} as a function of d_i and $\delta u/\delta b_A$. In the example interval, k_{Hall} falls between $kd_i = 1$ and $k\rho_i = 1$, suggesting that $\delta u/\delta b_A$ is playing a nontrivial role in setting the location of k_{Hall} in this interval. Figure 4.5 (b) shows the scale dependence of $\delta u/\delta b_A$ as quantified by the square root of the ratio of the power spectral densities. For the example interval, the ratio is roughly constant at large scales from approximately the magnetic correlation length to the ion scales, with a slight excess of magnetic fluctuation energy. Such an excess may be consistent with non-Alfvénic fluctuations at large scales in the magnetosheath; however, even in the context of incompressible MHD turbulence and in the solar wind, an excess of magnetic energy is an observed feature (Matthaeus et al., 1986; Wicks et al., 2013; Lee et al., 2010; Stawarz et al., 2012; Franci et al., 2015a; Franci et al., 2015b; Bowen et al., 2018). At smaller scales, starting around $k\rho_i = 1$ and k_{Hall}, the magnetic energy becomes increasingly dominant, consistent with the behaviour of kinetic scale dynamics and the reduced importance of $\mathbf{u}$ at sub-ion scales. The excess of magnetic energy across the spectrum is qualitatively consistent with the fact that $k_{Hall} < d_i^{-1}$ in this interval.

Figure 4.6 compares measured values of k_{Hall} to the dimensional expression (Equation 4.7) for all 60 of the intervals examined in this study. Given that there are multiple ways

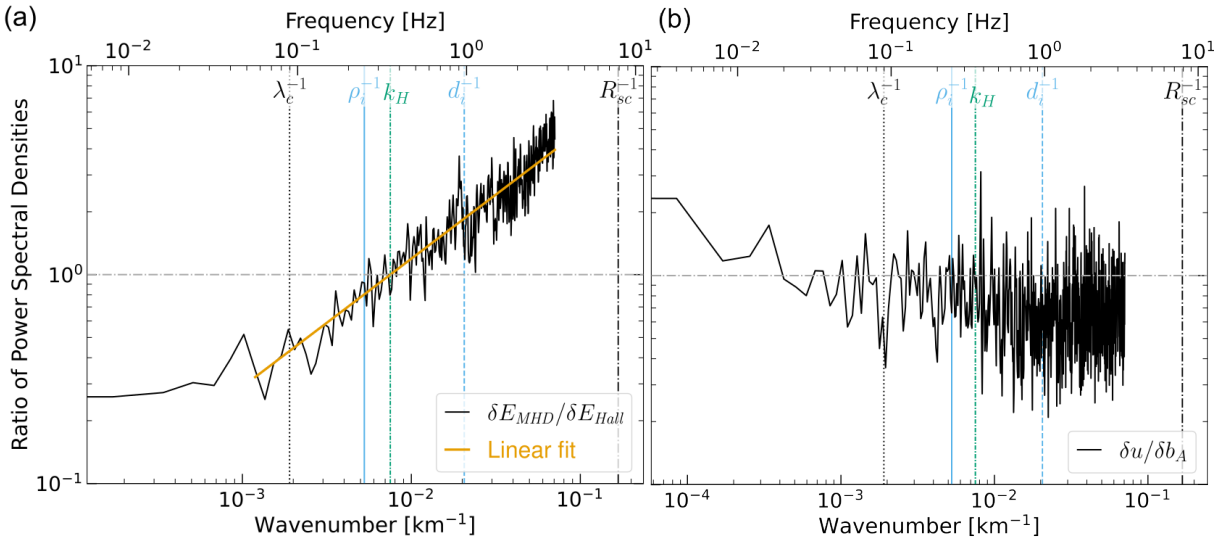


Figure 4.5: (a) The ratio of the spectra of $E_{Hall,1SC}$ to $E_{MHD,1SC}$ for interval (2016-12-08/10:16:52–10:21:02), including the best-fit line derived from a smoothed spectrum (not shown, see text). (b) The ratio of 1SC spectra of δu to δb_A for the same interval. Measured k_{Hall} is denoted in panels (a) and (b) by the green dash-dotted vertical line.

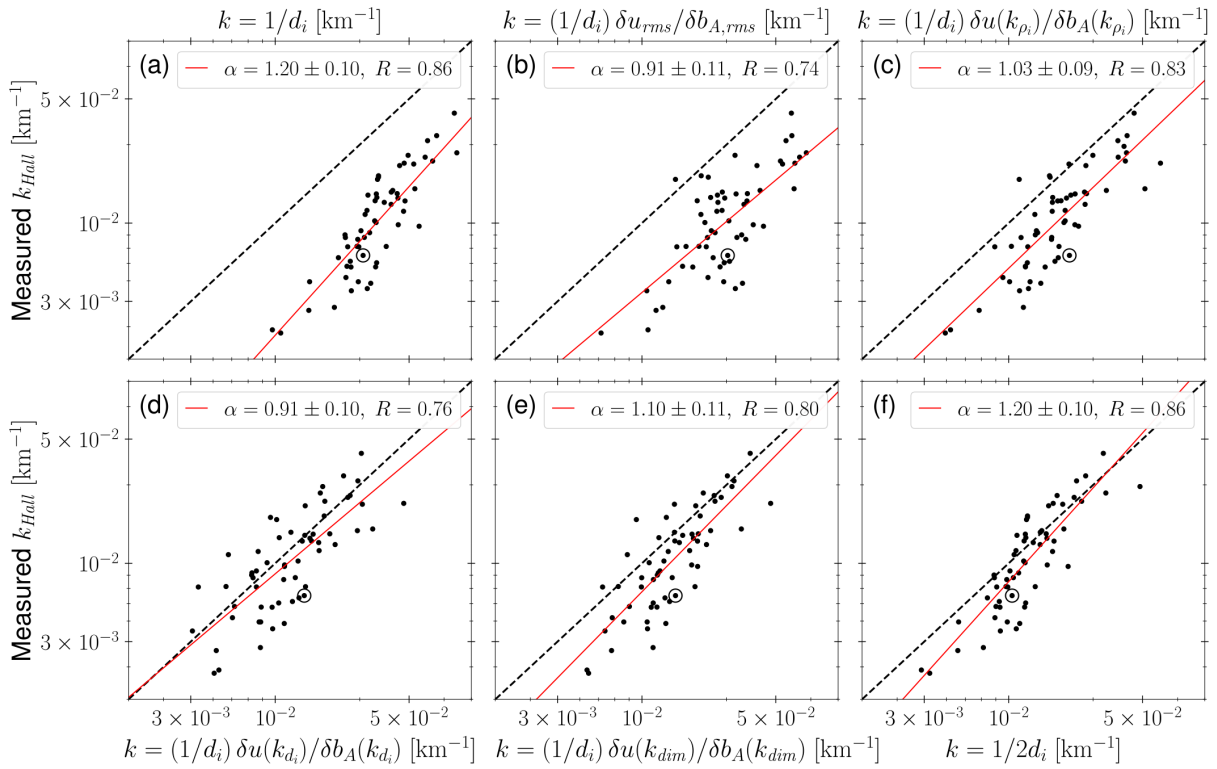


Figure 4.6: The trends between measured k_{Hall} and different ways of evaluating the dimensional analysis expression for k_{Hall} for all 60 intervals. In each panel, the diagonal dashed line corresponds to agreement, the red line corresponds to a best fit line calculated linear regression in log space, and the example interval (2016-12-08/10:16:52–10:21:02) shown in Figures 4.4 & 4.5 is surrounded by a hollow black circle to identify it.

to characterise the scale-dependent term $\delta u/\delta b_A$, a number of different options have been tested, which each has a different implication for the full behaviour of the terms. These are shown in Figure 4.6, which compares the measured k_{Hall} to a different dimensional approximation in each panel.

The Alfvénic assumption ($\delta u/\delta b_A = 1$) would imply that the dynamics are wholly controlled by Alfvénic behaviour. Panel 4.6 (a) shows that this approximation overestimates the value of k_{Hall}, suggesting that there is an excess in magnetic fluctuations compared to velocity fluctuations in the magnetosheath. Similarly, Panel 4.6 (b) shows that taking the rms fluctuations ($\delta u_{rms}/\delta b_{A,rms}$) overestimates k_{Hall} in most cases, indicating that the large-scale ratio of the fluctuations does not control the crossover scale between MHD and sub-ion dynamics.

Further examination of $\delta u/\delta b_A$ evaluated at a variety of relevant scales based on the square root of the ratio of power spectral densities reveals the most appropriate approximation to use. Panel 4.6 (c) shows $\delta u/\delta b_A$ evaluated at at $k\rho_i = 1$, which systematically overestimates the measured value; Panel 4.6 (d) shows $kd_i = 1$, which also overestimates the measured value, but is closer to a linear trend; and Panel 4.6 (e) shows the effect of evaluating $kd_i\delta u/\delta b_A = 1$ as a scale-dependent expression, defining $k_{dim} = 1/d_i \times (\delta u/\delta b_A)_{k_{dim}}$. Comparing these panels, it is evident that evaluating $\delta u/\delta b_A$ at $kd_i = 1$ gives the closest reproduction of k_{Hall}, with a gradient of 0.91 and a correlation coefficient of 0.76, and the smallest systematic offset. This is shown in greater detail in Figure 4.7. The agreement suggests that scales adjacent to d_i are most important in determining where the transition to Hall term dominance of the electric field occurs, which aligns with expectations as Hall dynamics arise from a decoupling of the ion fluid from the plasma dynamics. A similar trend is obtained for k_{dim}, albeit with a greater offset at smaller k_{Hall}.

Further refinements are possible, such as by breaking up the fluctuations $\delta u/\delta b_A$ into components perpendicular and parallel to the mean field $\mathbf{B}_0$. No combination of components is found to produce significantly better agreement, indicating that there are no preferred fluctuation directions which are solely controlling the MHD–Hall dynamics in

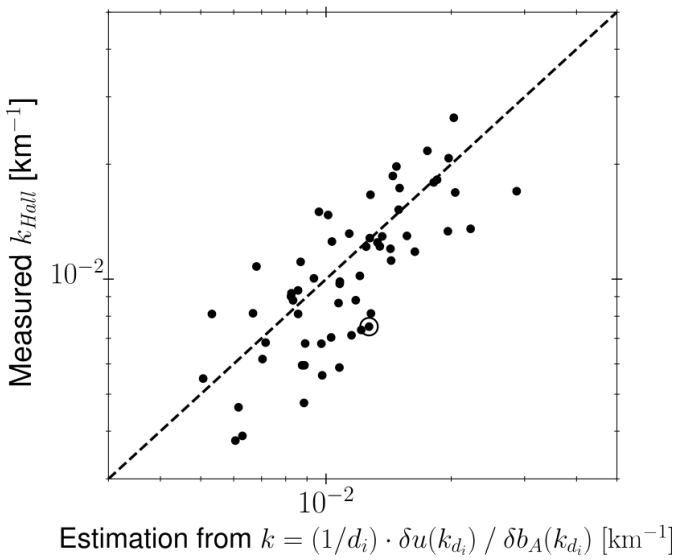


Figure 4.7: The trend between measured k_{Hall} and the dimensional expression from Equation 4.7 using $(\delta u/\delta b_A)_{kd_i=1}$, for all intervals. The diagonal dashed line corresponds to agreement, and the example interval (2016-12-08/10:16:52–10:21:02) shown in Figures 4.4 & 4.5 is surrounded by a hollow black circle to identify it.

these turbulent intervals. Indeed, many of the intervals have large fluctuation amplitudes relative to the background magnetic field and seemingly near-isotropic fluctuations (Stawarz et al., 2022). Based on the observed values of $\delta u/\delta b_A$ evaluated at $kd_i = 1$, as well as those feeding into k_{dim}, $\delta u/\delta b_A$ is empirically consistent with 0.5 for the intervals examined in this study, as shown in Panel 4.6 (f). This indicates that, for this selection of magnetosheath plasma data, $k_{Hall}\, d_i \sim 0.5$ and thus the spatial scale associated with the Hall scale is around $2d_i$, as the typical ratio of $\delta u/\delta b_A$ in the sub-ion scale range is approximately 0.5. Using this empirical result in the dimensional analysis is also fairly effective in terms of predicting the measured k_{Hall} across all intervals.

The scatter in Figure 4.7 could arise from several sources, such as the approximations used to obtain the dimensional analysis expression for k_{Hall}, inexact measurements of k_{Hall} due to variability in the curve of the power spectrum, or artificial enhancements in the velocity measurements as they approach the noise floor. One of the principal simplifications of the dimensional analysis expression is that scale-dependent alignment between different vector quantities is neglected. Investigating alignment properties between δu, δb_A, and δb, and subsequently including characteristic values of these into the dimensional analysis expressions, yielded no noticeable improvements, implying that they are not directly

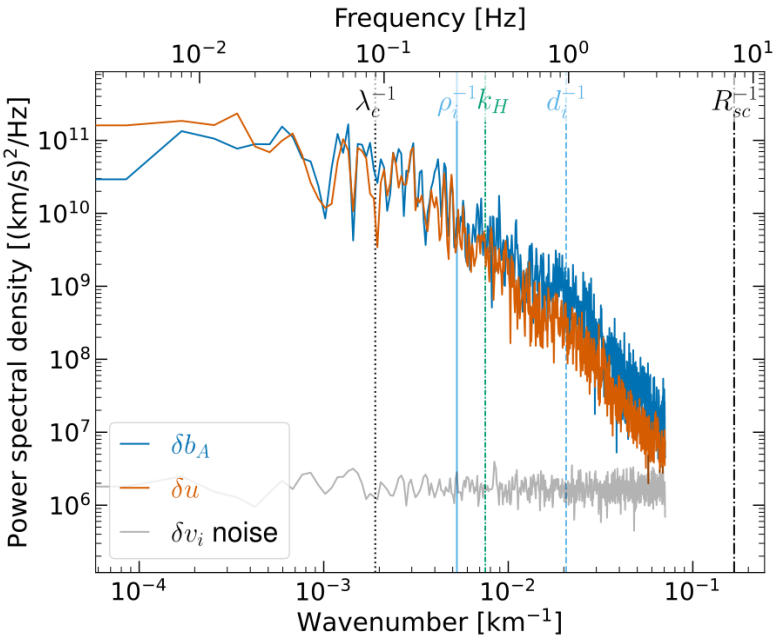


Figure 4.8: Power spectra of δb_A, δu, and statistical uncertainty in δv_i calculated from FPI counting statistics. In the interval shown (2015-11-15/05:27:36–05:32:10), the noise floor is reached, causing a flattening of δu.

feeding into the location of k_{Hall}.

The noise level of the bulk velocity fluctuation is checked using the method described in Section 3.2.3 (Gershman et al., 2015). For context, the power spectra of δb_A, δu, and the noise level in δv_i are shown in Figure 4.8. In this example, the bulk velocity is reaching the noise floor, which causes it to flatten off. In all cases where velocity measurements appear to reach the noise floor, the affected range is removed in computations of characteristic values of $\delta b_A/\delta u$. The procedure of checking and removing ranges of scales where velocity fluctuations have reached the noise floor gives confidence that scatter in Figure 4.7 is primarily arising due to uncertainty in determining the exact value of k_{Hall}, rather than error or statistical uncertainty in the measurements.

4.4.2 Relative Amplitude of $\mathbf{E}_{P_e}$ and $\mathbf{E}_{Hall}$

Below k_{Hall}, the spectrum of $\mathbf{E}$ is dominated by a combination of $\mathbf{E}_{Hall}$ and $\mathbf{E}_{P_e}$. The ratio E_{P_e}/E_{Hall} represents the proportion of the fluctuation energy arising from the non-ideal term $\mathbf{E}_{P_e}$ compared to $\mathbf{E}_{Hall,bary}$. This ratio is shown as a function of scale in Figure 4.9 (a) for an example interval, in which it can be seen that for $k\rho_i > 1$ the spectrum

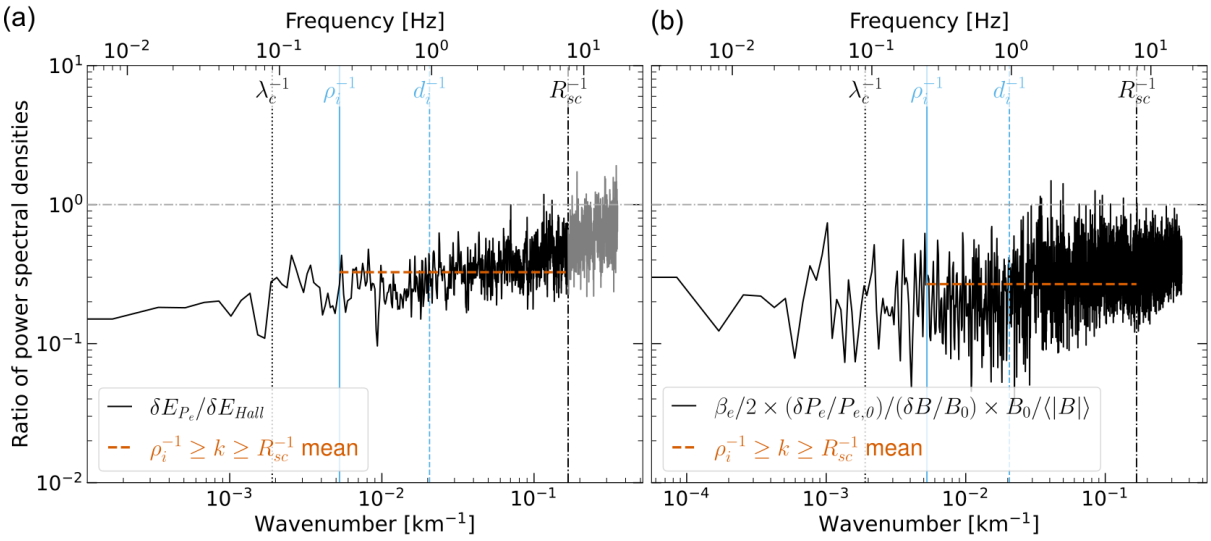


Figure 4.9: (a) The ratio of the spectra of $E_{Hall,bary}$ to E_{P_e} for example interval (2016-12-08/10:16:52–10:21:02). The orange horizontal dashed line represents the mean of this spectrum in the range $\rho_i^{-1} \geq k \geq R_{sc}^{-1}$, computed from bins spaced equally in log-space. (b) The ratio of 1SC spectra of $\delta P_e/P_{e,0}$ to $\delta B/B_0$, multiplied by the factors $\beta_e/2$ and $B_0/\langle|B|\rangle$, for the same interval. The orange horizontal dashed line which spans from $\rho_i^{-1} \geq k \geq R_{sc}^{-1}$ represents the mean of this spectrum in this range.

is shallow, with a gradual uptick at smaller scales. In other examples (not shown), the spectrum ranges between a slight downwards slope, to almost completely flat, to a slight upwards gradient.

Appealing to the dimensional expression in Equation 4.10, the scale-dependent part of E_{P_e}/E_{Hall} is related to $(\delta P_e/P_{e,0})/(\delta B/B_0)$, which is plotted as a function of scale in Figure 4.9 (b) and is found to follow a similar trend as a function of scale in the sub-ion range as the measured ratio of spectra. This ratio has been rescaled by the constant factors $\beta_e/2$ and $B_0/\langle|B|\rangle$. The shallow gradient of the spectrum is approximately in line with Equation 4.10, which indicates that there should be no overall scale-dependence of the ratio, i.e. that magnetic and density fluctuations have the same power-law as per theoretical expectations in the nearly incompressible limit (Montgomery et al., 1987; Schekochihin et al., 2009). Comparable behaviour has been found in the solar wind (C. H. K. Chen et al., 2012) and hybrid kinetic simulations (Franci et al., 2015a), where similar power laws have been reported for B and n at sub-ion scales, which is consistent with similar scaling between B and P_e if the fluctuations are isothermal. However, the

presence of temperature fluctuations may lead to a more subtle relationship between the pressure and magnetic field.

The factor $B_0/\langle|B|\rangle$, which is accounting for variations in the magnitude of $\mathbf{B}$, is a necessary factor to include, at least in the magnetosheath. This term encodes how much the fluctuations perturb the magnitude of the magnetic field, ranging from around 10^{-1} to 1 in this dataset. Beyond the inclusion of the magnetic field strength fluctuation, another factor to consider is that there are different ways to quantify the electron pressure fluctuation δP_e. For example, one could consider fluctuations in the isotropised pressure, $p_e = \mathrm{Tr}[\mathbf{P}_\mathrm{e}]/3$. However, this does not take into account individual or unbalanced fluctuations in the diagonal terms that may be giving rise to electron temperature anisotropy, as such it only accounts for variations in the overall amount of pressure, as opposed to variations in the amount of anisotropy. The scale-dependent pressure fluctuation is computed by taking the power spectrum of each of the diagonal terms then summing (i.e. the trace power spectrum of the $\mathbf{P}_e$ tensor, equivalent to 3 times the power spectrum of the isotropic pressure). In principle, the off-diagonal components could also contribute to the dynamics, but upon further investigation it was found that including the off-diagonal parts of $\mathbf{P}_e$ into δP_e does not improve agreement, implying that these do not significantly contribute to E_{P_e}/E_{Hall}. It is still unknown whether the spectrum of off-diagonal terms in the pressure tensor would need to be included in a situation where those dominate, as this is not a case that has been observed by MMS.

To quantify E_{P_e}/E_{Hall} and $\delta P_e/\delta B$, the average value of the smoothed measured ratio in log-space between $k\rho_i = 1$ and $kR_{sc} = 1$ is used, as denoted by the horizontal orange dashed lines (respectively) in Figures 4.9 (a) and (b). Investigating the spectrum for every interval revealed that the sub-ion ratio either had a shallow gradient or was flat. In the example interval, the gradient is upwards towards smaller scales. It was found that using the mean value, rather than taking into account the upwards/downwards trend present in some intervals, was the most effective way of characterising the ratio. This is demonstrated in Figure 4.10, which shows the agreement between the measured E_{P_e}/E_{Hall} and the

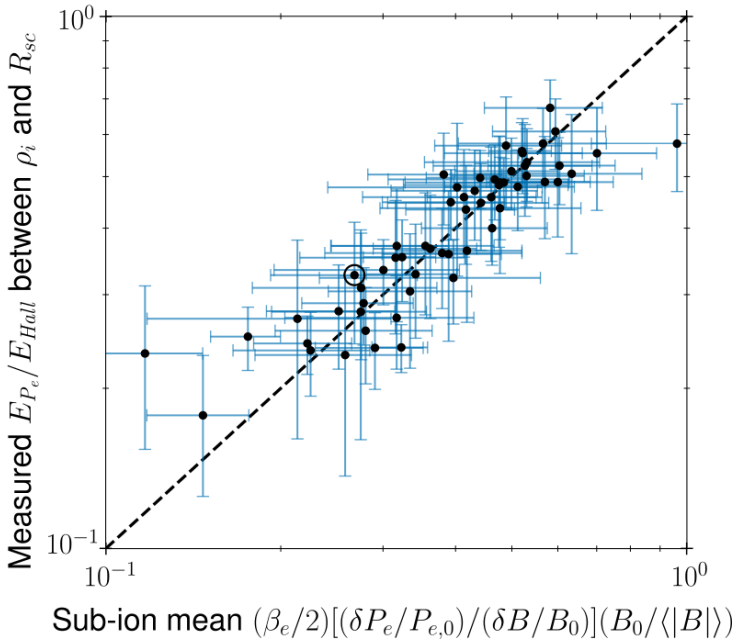


Figure 4.10: Trends between the measured value of E_{P_e}/E_{Hall} and the value estimated from Equation 4.10, both evaluated between $k\rho_i = 1$ and $kR_{sc} = 1$. Error representing the standard deviation of the data going into each interval average denoted by a scatter point. In both panels, the diagonal dashed line corresponds to agreement, and the example interval (2016-12-08/10:16:52–10:21:02) shown in Figures 4.4, 4.5, and 4.9 is denoted by a hollow black circle.

dimensional analysis expression in Equation 4.10 for all intervals. The general trend shows good agreement, indicating that the dimensional estimate works well. As such, it can be concluded that it is indeed necessary to include $B_0/\langle|B|\rangle$ into the expression for E_{P_e}/E_{Hall} in the magnetosheath, and that one needs to take into account the fluctuations in the diagonal components of the electron pressure tensor in order to include the anisotropy fluctuations. This shows that the level of fluctuations compared to the background, as well as fluctuations in the anisotropy, have an impact on the relative importance of Hall and electron pressure dynamics. By taking these steps the ratio of E_{P_e} to E_{Hall} in the sub-ion range can be characterised.

A simple error analysis was performed for the scatter points using the standard deviations around the mean for both axes of each scatter point, as shown in Figure 4.10, which demonstrates uncertainties of order ~ 0.1 for both axes. The implication of the majority of points being within error bars of the agreement line is that the gradual upwards/downwards trend in E_{P_e}/E_{Hall} is not significantly altering the dimensional char-

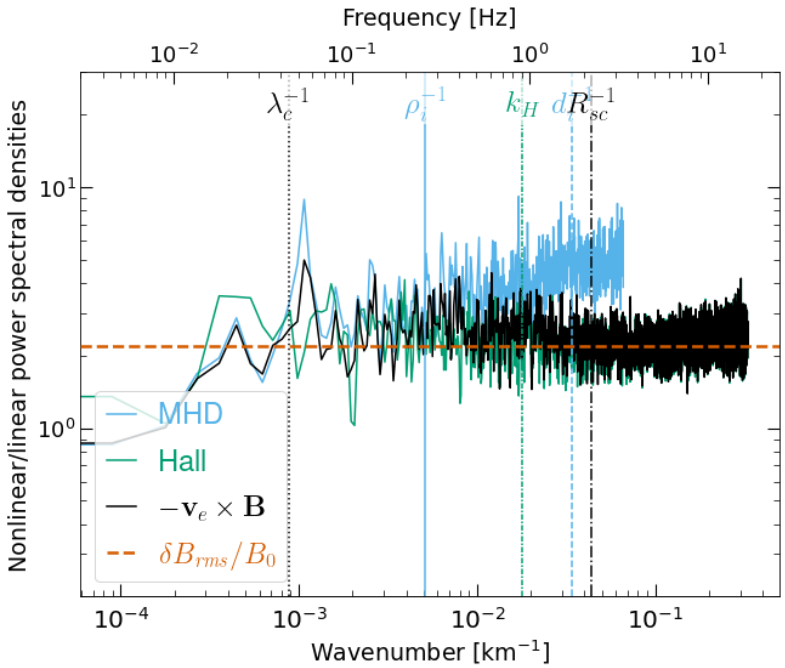


Figure 4.11: Ratios of the power spectra of the nonlinear and linear components of $\mathbf{E}_{MHD,1SC}$, $\mathbf{E}_{Hall,1SC}$ and $(-\mathbf{v}_e \times \mathbf{B})_{1SC}$ for interval (2018-04-27/17:56:24–18:03:50), which is not the same example as mostly used throughout this chapter so far. The horizontal dash-dotted line corresponds to $\delta B_{rms}/B_0$.

acterisation. Additionally, the three leftmost points in the scatter plot appear to be systematically enhanced compared to the dimensional analysis estimate, which indicates that the computation of $\mathbf{E}_{P_e}$ may be contaminated by noise. However, a noise floor is not clearly identifiable when analysing the power spectrum, so there may be another source of uncertainty affecting these intervals.

4.4.3 Nonlinear and Linear $\mathbf{E}_{MHD}$ and $\mathbf{E}_{Hall}$

Just as the $\mathbf{E}$ dynamics as described by generalised Ohm's law can be split into different terms corresponding to separate physical effects, so too can each term be decomposed into contributions from nonlinear and linear components. Figure 4.11 shows an example of the ratios of power spectra of nonlinear and linear terms contributing to $\mathbf{E}_{MHD}$, $\mathbf{E}_{Hall}$ and $\mathbf{E}_{MHD} + \mathbf{E}_{Hall} = -\mathbf{v}_e \times \mathbf{B}$, where the nonlinear and linear components of $-\mathbf{v}_e \times \mathbf{B}$ are computed separately. The nonlinear to linear terms, which are given in Section 4.3.3, are computed relative to the global mean of each variable before the ratio of power spectra is taken.

At scales larger than the ion scales (in this case between λ_c and ρ_i) $R_{MHD}^{NL/L}$ and $R_{Hall}^{NL/L}$ are constant as a function of scale and centered around $\delta B_{rms}/B_0$, indicating that there is a balance between the linear and nonlinear terms in the system. At smaller scales, $R_{MHD}^{NL/L}$ diverges from $\delta B_{rms}/B_0$ to become increasingly nonlinear. This occurs due to dealignment of $\delta\mathbf{B}$ and $\delta\mathbf{u}$ at smaller scales, whereas alignment between $\mathbf{B}_0$ and $\delta\mathbf{u}$ does not vary with scale, leading to a relative strengthening of the nonlinear term (Parashar et al., 2018; Stawarz et al., 2021).

The dealignment may be occurring due to $\mathbf{E}_{Hall}$ causing beyond-MHD modifications to the magnetic field at scales below k_{Hall}. The ratio of nonlinear to linear terms (NL/L) for the MHD term, $R_{MHD}^{NL/L}$, is evaluated at length scales between λ_c and ρ_i, in the range where the ratio of nonlinear to linear components is unaffected by the Hall effect. $R_{Hall}^{NL/L}$, on the other hand, remains constant as a function of scale, in such a way that the combination of $\mathbf{E}_{MHD}$ and $\mathbf{E}_{Hall}$, $-\mathbf{v}_e \times \mathbf{B}$, also remains approximately constant as a function of scale from the correlation length down to the smallest observable scales. As such, the dominant dynamics in generalised Ohm's law at any given scale appear to arrange themselves such that they maintain a balance between the linear and nonlinear contributions. The ratio between the two terms is set by the strength of $\delta B_{rms}/B_0$ across all scales, which is weighted towards the behaviour of the largest-scale fluctuations, implying that the largest-scale properties of the fluctuation amplitudes are determining the relative importance of nonlinear and linear terms.

From Section 4.3, the relative scaling of nonlinear to linear MHD and Hall terms both reduce to $\delta B/B_0$ within the dimensional analysis treatment. Figure 4.12 (a) shows $R_{MHD}^{NL/L}$ averaged over the scale range $k\lambda_c = 1$ to $k\rho_i = 1$ as compared to $\delta B_{rms}/B_0$ for all the intervals, and Figure 4.12 (b) shows $R_{Hall}^{NL/L}$ averaged over the scale range $k\lambda_c > 1$ compared to $\delta B_{rms}/B_0$ for all intervals. In all cases the ratios appear to be roughly consistent with the behaviour shown in the example interval and clearly scale with the ratio $\delta B_{rms}/B_0$. A scaling with $\delta B/B_0$ is in agreement with Equations 4.11 and 4.12, where in this case the ratio of large-scale magnetic field fluctuations to average background field, $\delta B_{rms}/B_0$,

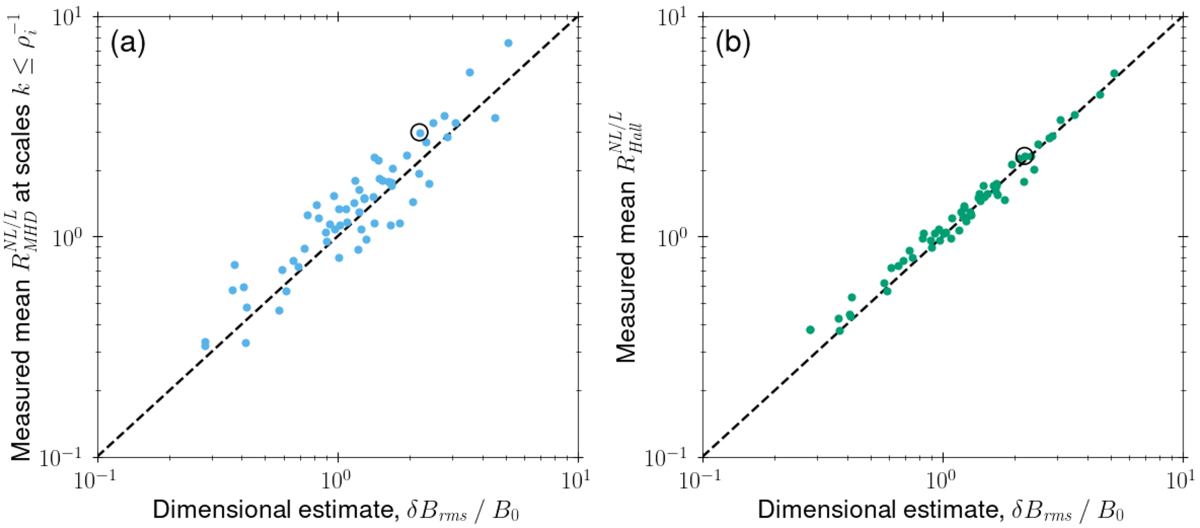


Figure 4.12: (a) The relationship between measured $R_{MHD}^{NL/L}$ averaged over scales between $k\lambda_c = 1$ and $k\rho_i = 1$, and $\delta B_{rms}/B_0$, for all intervals. (b) The relationship between measured $R_{Hall}^{NL/L}$ averaged over scales smaller than the correlation length,and $\delta B_{rms}/B_0$, for all intervals. In both panels the dashed diagonal line represents agreement, and the interval (2018-04-27/17:56:24–18:03:50) from Figure 4.11 is denoted by a hollow by a black circle.

is determining the relative scaling of nonlinear to linear contributions.

Since the constant ratio of linear to nonlinear terms is being set by $\delta B_{rms}/B_0$, there exist intervals that are strongly dominated by the nonlinear dynamics as well as intervals which are dominated by the linear dynamics even while maintaining a balance between them. The spread in the scatter trends may be associated with how well the estimate of the mean value of the ratio has converged given the variability in the ratio, which has a greater impact on the MHD term because a smaller range of scales means that fewer data points are used to calculate the average. For the magnetic field, it is expected that this is the more significant source of uncertained compared to the uncertainty on the actual measurement of **B**.

4.4.4 Nonlinear and Linear $\mathbf{E}_{P_e}$

$R_{P_e}^{NL/L}$ is a more complex quantity to evaluate because $\mathbf{E}_{P_e}$ consists of two linear terms as well as a nonlinear term. When the same dimensional approach as in Section 4.4.3 – using the rms as the characteristic fluctuation amplitude – is applied to all components of

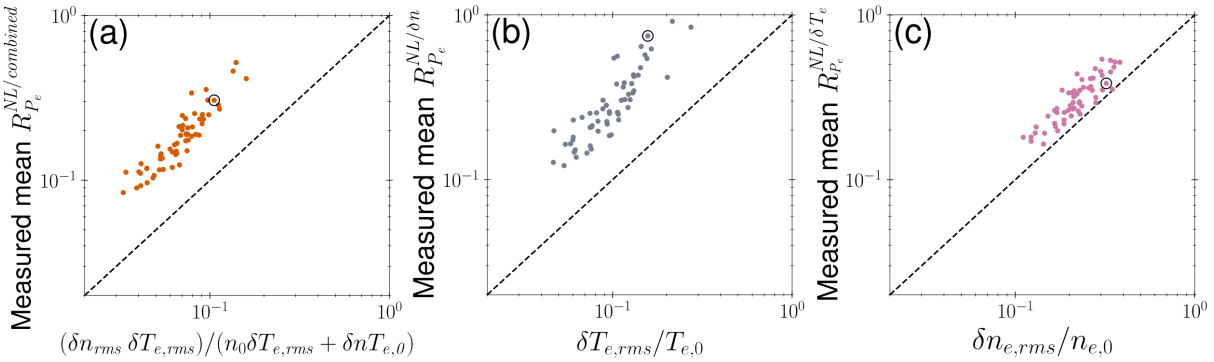


Figure 4.13: Measured values in the sub-ion range plotted against dimensional estimates characterised by the rms fluctuation amplitude. (a) $R_{P_e}^{NL/combined}$ compared to dimensional estimate from 4.19. (b) $R_{P_e}^{NL/\delta n}$ compared to 4.18. (c) $R_{P_e}^{NL/\delta T_e}$ compared to 4.17. In all panels, the diagonal dashed line corresponds to agreement and the example interval (2016-12-08/10:16:52–10:21:02) is identified by a hollow black circle which surrounds the scatter point.

$R_{P_e}^{NL/L}$, the dimensional estimation fails to account for measured values in all 60 intervals. The discrepancy is shown in Figure 4.13 (a), in which it can readily be observed that all scatter points are above the agreement line, indicating that the dimensional estimation is underestimating the measured value.

It is interesting to note that every interval has a measured $R_{P_e}^{NL/L} < 1$, showing that the electron pressure divergence term is dominated by its linear components for all intervals, in contrast to $R_{MHD}^{NL/L}$ and $R_{Hall}^{NL/L}$. Additionally, when the fluctuation amplitudes are evaluated at characteristic scales such as $k\rho_i = 1$ and $kd_i = 1$, or when they are averaged between $k\rho_i = 1$ and $kR_{sc} = 1$, agreement is still not found. Lack of agreement is also true for the ratio of nonlinear to individual linear terms given by Equations 4.17 & 4.18, as seen in Figures 4.13 (b) & (c), respectively, implying that the underestimation is not coming from correlation between the two linear terms in the denominator of $R_{P_e}^{NL/L}$. The relative scaling of nonlinear to linear parts of $\mathbf{E}_{P_e}$ can not be characterised as a function of plasma conditions using the simple dimensional form of the expressions – instead, the full convolution between variables needs to be accounted for.

Since $R_{P_e}^{NL/L}$ cannot be reproduced using simple dimensional estimates, it is instead necessary to break down the contributions to this term and qualitatively compare the be-

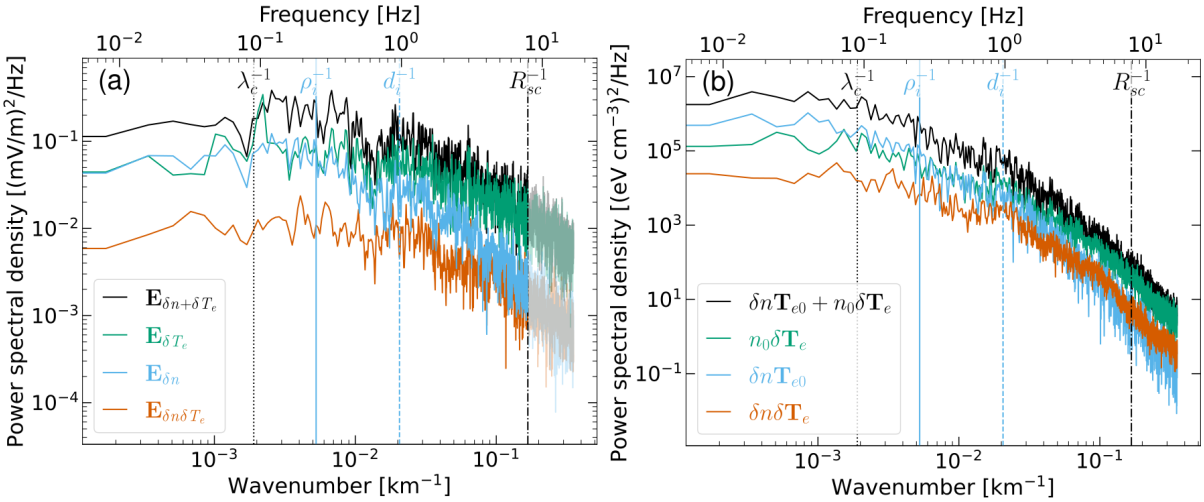


Figure 4.14: (a) Power spectra of $\mathbf{E}_{\delta n}$, $\mathbf{E}_{\delta T_e}$, $\mathbf{E}_{\delta n+\delta T_e}$, and $\mathbf{E}_{\delta n\delta T_e}$, for the example interval (2016-12-08/10:16:52–10:21:02). Each curve corresponds to the power spectrum of an individual component of the electron pressure term, which are calculated at the barycenter as per the gradient estimation technique used to compute the divergence. Power spectra of the contributions from the diagonal components of the temperature tensor are computed before being summed together. (b) The various linear and nonlinear combinations of background and fluctuating n and $\mathbf{T}_e$ that feed into $\delta\mathbf{P}_e$, for the same interval. The power spectrum of each variable is computed for each spacecraft before being averaged together, to reduce variability in the spectrum.

haviour of each. The electric field terms that contribute to $\mathbf{E}_{P_e}$ are given by Equations 4.13–4.16, the power spectra of which are shown in Figure 4.14 (a). From this figure, the ratio $E_{\delta n\delta T_e}/E_{\delta T_e}$ and the ratio $E_{\delta n\delta T_e}/E_{\delta T_e+\delta n}$ both appear to be independent of scale, whereas $E_{\delta n}$ becomes smaller below the ion scales, resulting in a larger $E_{\delta n\delta T_e}/E_{\delta n}$ at smaller scales. This behaviour indicates that the electric field associated with temperature fluctuations is increasingly dominating the linear component of the electron pressure term towards larger wavenumbers, implying that temperature fluctuations are playing a more important role in the $\mathbf{E}_{P_e}$ dynamics than density fluctuations.

The increasing importance of $E_{\delta T_e}$ relative to $E_{\delta n}$ at sub-ion scales is readily apparent in the example spectrum in Figure 4.14 (a) and may have important consequences as it suggests violation of purely isothermal dynamics in the sub-ion scales. It could be that the changing relative importance of linear terms precludes a simple dimensional estimation from being employed on this term. It has been demonstrated in Figure 4.14 (a) that the linear contributions to $\mathbf{E}_{P_e}$ are dominating the term, so any estimate for the relative scaling of nonlinear to linear parts may be sensitive to the relative dynamics of the $\mathbf{E}_{\delta n}$

and $\mathbf{E}_{\delta T_e}$ contributions. This could explain why $R_{P_e}^{NL/L}$ cannot be captured by a simple dimensional approximation.

Figure 4.14 (b) shows power spectra of the linear and nonlinear components of $\mathbf{P}_e$ for an example interval, which corresponds to the variables whose divergence are associated with components of the electron pressure term. The combination of the two linear variables is dominant at all accessible wavenumbers, which is the same for all intervals and in agreement with the observation that $\mathbf{E}_{P_e}$ is dominated by linear components. The trends are broadly the same as those of the different contributions to $\mathbf{E}_{P_e}$, as illustrated in Figure 4.14 (a). The linear term $n_0\delta\mathbf{T}_e$ becomes progressively larger relative to $\delta n\mathbf{T}_{e,0}$ at sub-ion scales. This suggests that temperature fluctuations are increasingly more important than density fluctuations at small scales, which indicates that the similar findings for $\mathbf{E}_{\delta T_e}$ and $\mathbf{E}_{\delta n}$ are not solely arising due to differences between the divergence of each fluctuating variable.

4.5 Discussion

4.5.1 The Hall Scale: Underlying Dependences

The relationships demonstrated in Section 4.4 convey only part of the complex interdependence between the electrodynamics and the turbulence properties and ambient plasma conditions within the magnetosheath. It has been shown that $k_{Hall} \sim 1/d_i \times (\delta u/\delta b_A)$, which means that the length scale where the Hall fluctuations become dominant, k_{Hall}, scales with $1/d_i$ and the ratio of velocity to magnetic fluctuations. The value of $\delta u/\delta b_A$ is a scale-dependent quantity that is influenced by an excess of magnetic energy at MHD scales, before beginning to drop off as velocity decouples when the Hall effect takes over. The fact that large-scale $\delta u/\delta b_A$ does not control k_{Hall} suggests that the diverging δu and δb_A spectra at sub-ion scales may be playing a role in the dynamics. It is interesting that k_{Hall} is not best described using $(\delta u/\delta b_A)_{k_{Hall}}$, as this implies that the relative fluctuation amplitude at scales other than those adjacent to k_{Hall} are feeding into the location of the

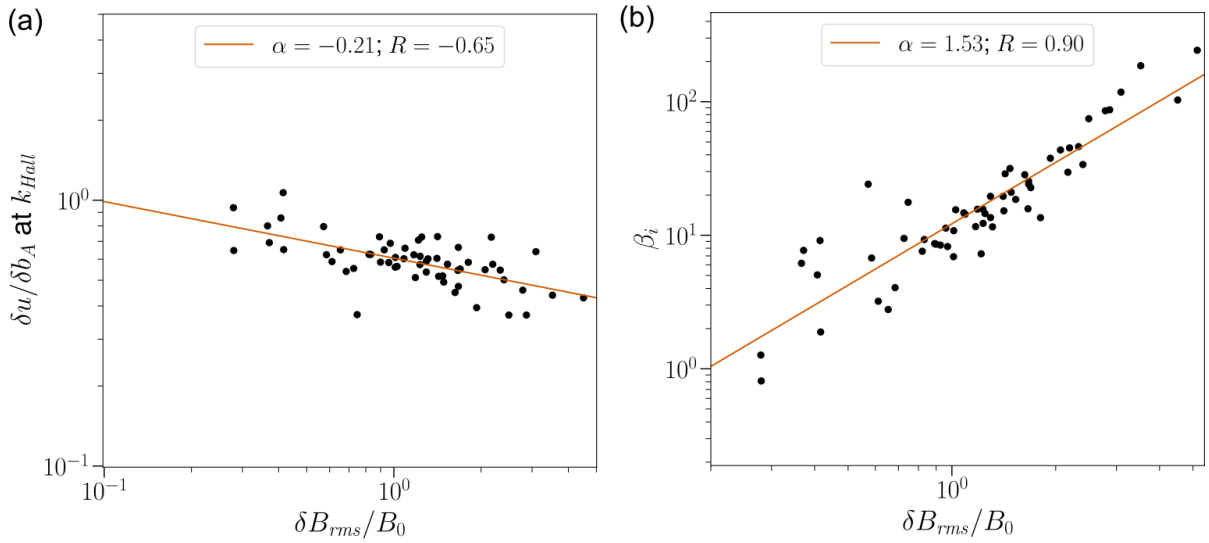


Figure 4.15: Power-law relationships between (a) $\delta u/\delta b_A$ and $\delta B_{rms}/B_0$, and (b) β_i and $\delta B_{rms}/B_0$. The orange line represents the power law obtained by taking the line of best fit in log-space. α signifies the power law and R is the correlation coefficient.

change in dynamics, implying moderately nonlocal behaviour (in potential violation of the local approximation used in most cascade theories).

Additionally, there may be an underlying dependence of $\delta u/\delta b_A$ itself on the ambient plasma conditions. This means k_{Hall} has a combination of explicit dependence on plasma parameters as well as underlying dependences coming from $\delta u/\delta b_A$. If the fluctuations were Alfvénic, or if there was no dependence of $\delta u/\delta b_A$ on plasma conditions, one would expect $k_{Hall} \sim d_i^{-1}$. However, the best fit line is calculated as $k_{Hall} \sim d_i^{-1.2}$ based on Figure 4.6 (a). Beyond this, investigating the underlying dependences of $\delta u/\delta b_A$ on other parameters reveals the relationship $\delta u/\delta b_A \sim (\delta B_{rms}/B_0)^{-0.21}$, as shown in Figure 4.15 (a). This shows that the fluctuations in velocity and magnetic field become closer to being Alfvénic for intervals with smaller magnetic field fluctuations compared to the background, which is consistent with small amplitude fluctuations being more wave-like. To summarise, in the case of intervals with smaller background fluctuations, k_{Hall} approaches $1/d_i$. A future investigation may wish to extend this trend to intervals with very small $\delta B_{rms}/B_0$ to see if k_{Hall} becomes smaller than $1/d_i$, as well as check whether δB contributions from other length scales exhibit stronger control over the behaviour.

When checking $\delta B_{rms}/B_0$ against other parameters, a scaling of $\beta_i \sim (\delta B_{rms}/B_0)^{1.53}$ was

uncovered for the set of magnetosheath intervals used, as seen in Figure 4.15 (b), which folds into the expression for k_{Hall} as

$$k_{Hall} \sim \frac{\beta_i^{-0.14}}{d_i}. \tag{4.20}$$

Since $\beta_i = \rho_i^2/d_i^2$, it follows that $k_{Hall} \sim \rho_i^{-0.28} d_i^{-0.72}$, which introduces a dependence on ρ_i that was not originally apparent from the dimensional analysis. Based on Equation 4.20, the (normalised) spatial Hall scale, $l_{Hall}/d_i \sim \beta_i^{0.14}$, can be compared to empirical estimates for the **B** spectral break scale inferred from solar wind observations and numerical simulations (C. H. K. Chen et al., 2014; Franci et al., 2016),

$$\frac{l_{break}}{d_i} \sim \frac{1}{3}\left(1 + \beta_i^{1/2} - \frac{\beta_i^{1/4}}{2}\right). \tag{4.21}$$

In this dataset, β_i ranges from 0.81–243.03. Across this range, the curve of l_{break}/d_i as a function of β_i is not similar to that of l_{Hall}/d_i. Qualitatively, l_{break}/d_i is less than l_{Hall}/d_i at small β_i, then rises faster than l_{Hall}/d_i, overtaking around $\beta_i \approx 20$. However, the extent of the relationship between l_{Hall} and l_{break} has not been fully investigated here, and could form the basis of a future study. It would be interesting to further test the relationship on intervals with a wider range of $\beta_i \leq 1$, if such conditions can exist in the magnetosheath.

4.5.2 Pressure vs Hall: Underlying Dependences

It has been shown that the value of $(E_{P_e}/E_{Hall})_{sub\text{-}ion}$ has a functional dependence on $\beta_e/2$, $((\delta P_e/P_{e,0})/(\delta B/B_0))_{sub\text{-}ion}$, and $B_0/\langle|B|\rangle$. The latter two quantities have direct dependences on $\beta = \beta_e + \beta_i$, with $((\delta P_e/P_{e,0})/(\delta B/B_0))_{sub\text{-}ion} \sim \beta^{-0.68}$, and $B_0/\langle|B|\rangle$ featuring two populations with different relationships to β, shown in Figures 4.16 (a) & (b), respectively. There is a population with relatively small $\delta B_{rms}/B_0$ in which $B_0/\langle|B|\rangle \sim 1$ and is independent of β. Another population, corresponding to large $\delta B_{rms}/B_0$ has $B_0/\langle|B|\rangle \sim \beta^{-0.33}$. These populations may be explained by considering the definition of

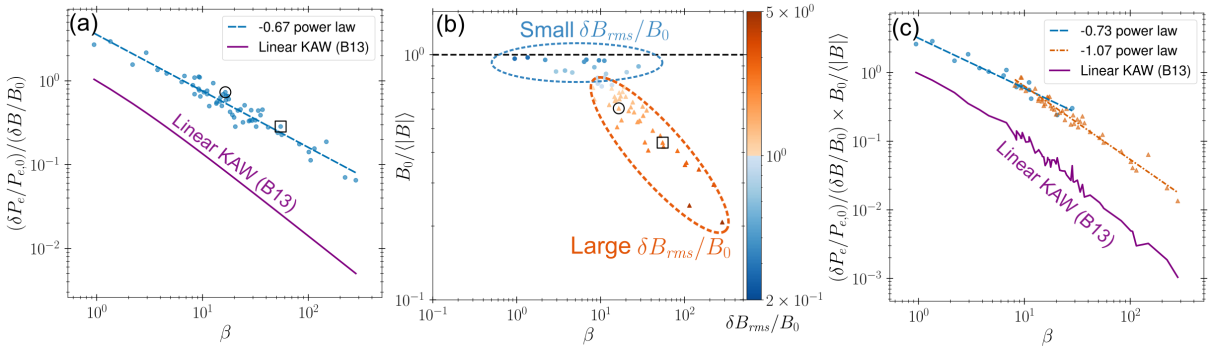


Figure 4.16: (a) The relationship between $(\delta P_e/P_{e,0})/(\delta B/B_0)$ and β, compared to the Boldyrev et al. (2013) (labeled B13) Kinetic Alfvén Waves (KAW) prediction. (b) The relationship between $B_0/\langle|B|\rangle$ and β, with $\delta B_{rms}/B_0$ on the color axis. (c) The relationship between $(\delta P_e/P_{e,0})/(\delta B/B_0) \times B_0/\langle|B|\rangle$ and β for both populations of $\langle|B|\rangle$, also compared with the B13 prediction (multiplied by the $B_0/\langle|B|\rangle$ prefactor for each interval). The example interval (2016-12-08/10:16:52–10:21:02) and the interval from Figure 4.11 (2018-04-27/17:56:24–18:03:50) are denoted by a hollow black circle and hollow black square, respectively.

$\langle|B|\rangle/B_0$,

$$\frac{\langle|B|\rangle}{B_0} = \left\langle \sqrt{1 + \frac{2\delta B_\parallel}{B_0} + \left(\frac{\delta B_\parallel}{B_0}\right)^2 + \left(\frac{\delta B_\perp}{B_0}\right)^2} \right\rangle \geq 1, \tag{4.22}$$

which puts an upper limit on the ratio $B_0/\langle|B|\rangle$, which will happen when the fluctuations are very small compared to the background.

When combining the dependences revealed in Figures 4.16 (a) and 4.16 (b), two power-law scalings governing the dependence of E_{P_e}/E_{Hall} with β emerge, as shown in Figure 4.16 (c): $((\delta P_e/P_{e,0})/(\delta B/B_0))_{sub\text{-}ion} \times B_0/\langle|B|\rangle \sim \beta^{-0.75}$ for small-fluctuation intervals and $((\delta P_e/P_{e,0})/(\delta B/B_0))_{sub\text{-}ion} \times B_0/\langle|B|\rangle \sim \beta^{-1.07}$ for large-fluctuation intervals. Folding these relationships into the original expression for $(E_{P_e}/E_{Hall})_{sub\text{-}ion}$ gives

$$\left(\frac{E_{P_e}}{E_{Hall}}\right)_{sub-ion} \sim \begin{cases} \beta_e \beta^{-0.75}, & \text{small } \delta B_{rms}/B_0 \\ \beta_e \beta^{-1.07}, & \text{large } \delta B_{rms}/B_0. \end{cases} \tag{4.23}$$

which serves as an approximation for the observed value of $(E_{P_e}/E_{Hall})_{sub\text{-}ion}$.

It would be desirable to extend this research to a much wider dynamic range of E_{P_e}/E_{Hall} (if this exists – see end of this paragraph) and β, in order to further explore the trends of both populations. In particular, regions with low fluctuation amplitudes and high beta

to confirm whether the $\beta^{-0.75}$ extends to large β alongside the $\beta^{-1.07}$ trend. Additionally, identifying regions with strong fluctuation amplitudes and low beta would be useful as it would show whether the $\beta^{-1.07}$ trend plateaus for small β, in accordance with the trend of the other population. Such intervals may be unlikely to occur in the magnetosheath, as when $\delta B_{rms}/B_0$ is large this implies small B_0^2, which must then be countered by an appropriately small $T_{i,0}$ to generate small β. However, in this dataset variation in β is typically driven by changes in B_0^2, which covers ~ 2.3 orders of magnitude, whereas $T_{i,0}$ only varies over ~ 1 order of magnitude. In addition to extending the trends, these findings indicate that it may be difficult to identify magnetosheath intervals where $E_{P_e} \geq E_{Hall}$. This means that, given $\beta = \beta_e + \beta_i \geq \beta_e$ and, in this dataset, $\beta_i/\beta_e > 1$, neither population is expected to produce $E_{P_e}/E_{Hall} > 1$ in the turbulent magnetosheath. Even in the unlikely case that $\beta \approx \beta_e$ in the magnetosheath, for $E_{P_e}/E_{Hall} > 1$ one would need to identify an interval with $\beta_e \sim 10^4$ (for small $\delta B_{rms}/B_0$) or $\beta_e \approx 0$ (for large $\delta B_{rms}/B_0$).

4.5.3 Kinetic Alfvén Wave Predictions

The functional dependence of $(\delta P_e/P_{e,0})/(\delta B/B_0)$ on β noted here can be compared to the expectation from linear Kinetic Alfvén Waves (KAW) theory (Boldyrev et al., 2013, hereafter 'B13'), which is often invoked in theoretical descriptions of kinetic scale plasma turbulence (Bale et al., 2005; Schekochihin et al., 2009; Roberts et al., 2022). Imposing the assumption of isothermal $\mathbf{T}_e$ justifiable in various space plasmas (e.g. Schekochihin et al., 2009), but shown earlier in this chapter to be violated within the magnetosheath, the relative amplitude of scalar isotropic electron pressure to magnetic fluctuations is given by (Boldyrev et al., 2013)

$$\frac{\delta p_e/n_0 T_{e,0}}{\delta B/B_0} \sim \frac{\delta n/n_0}{\delta B/B_0} \sim \left(\frac{\beta^2}{2} + \frac{\beta}{2}\right)^{-1/2}. \tag{4.24}$$

This expression is found to underestimate the measured value for the whole dataset, as shown in Figures 4.16 (a) & (c), in agreement with the findings of Stawarz et al. (2021). Equation 4.24 is a factor of ~ 3 smaller than the observed value of $(\delta P_e/P_{e,0})/(\delta B/B_0)$

for small β, dropping off faster than $(\delta P_e/P_{e,0})/(\delta B/B_0)$ with larger β, as shown in Figure 4.16 (a).

There may be several factors that lead to the disagreement between Equation 4.24 and the observations. One possibility could be that the dynamics are KAW-like, but the assumptions that go into Equation 4.24, such as isothermal and isotropic electrons, are violated. The results of Section 4.4.4 suggest that the temperature fluctuations are playing a role in the dynamics in the magnetosheath, thus rendering the isothermal approximation invalid – an assumption which is commonly made in theoretical descriptions of plasma turbulence (Schekochihin et al., 2009). Furthermore, electron distributions are observed to have anisotropy in the temperature within the magnetosheath (average $T_{e,\perp}/T_{e,\parallel}$ varies between 0.69–1.03 for this range of intervals, but instantaneous values have a far wider range), and taking into account the fluctuations associated with this anisotropy was necessary when comparing E_{P_e} to E_{Hall}. The role of anisotropy-driven kinetic microinstabilities in magnetosheath thermodynamics (and associated energy conversion related to the electric field) is explored in Chapter 5. Beyond this, distributions can deviate from bi-Maxwellians, which is an effect explored in Chapter 6.

Another possible factor which leads to disagreement between KAW physics and measurements is that a different wave mode may be relevant, for example whistler waves. Boldyrev et al. (2013) derive an expression for $(\delta n/n_0)^2/(\delta B/B_0)^2$ in the case of whistler waves,

$$\frac{(\delta n/n_0)^2}{(\delta B/B_0)^2} = \frac{1}{2}\frac{\omega_{pi}^4}{k_\parallel^4 c^4}, \tag{4.25}$$

however this is expected to be small since the denominator on the right hand side contains $k_\parallel^4$, which is typically large. As such, whistler waves are not expected to explain the behaviour; instead, it is likely that no single wave mode is dominating the dynamics in the magnetosheath. It may be that the strong nonlinearity observed in many of the intervals is fundamentally altering the dynamics and that fully nonlinear solutions are needed to account for the observed relationship.

4.6 Summary

In this chapter, the spectral properties of generalised Ohm's law terms have been evaluated in a statistical sense, using a large dataset of MMS measurements of Earth's magnetosheath. Terms in generalised Ohm's law amount to successive corrections to the ideal MHD conditions, incorporating additional physical effects which become relevant at different spatial scales. As such, understanding how the electric field operates in a given situation reveals information about how the plasma dynamics arise. Thus, the turbulent electric field is a powerful tool to probe the nonlinear dynamics of turbulent space plasmas.

The power spectrum of each electric field term contains a convolution of multiple fluctuating variables, indicating that contributions to the dynamics are dependent on a variety of spatial scales. Furthermore, the relative importance of nonlinear and linear components within each term determines how the turbulence operates, constituting an important characteristic upon which descriptions of turbulence can be built. The aim of this study has been to unravel the complex interdependence between the contributions to the total electric field, as well as between the nonlinear and linear components, by approximating the full convolutions in terms of underlying plasma conditions and properties of the turbulent fluctuations. This study has advanced our understanding of the impact of variability in magnetosheath properties on the relevance of different physical effects in controlling the dynamics.

Characteristics of the relative importance of $\mathbf{E}_{MHD}$, $\mathbf{E}_{Hall}$, and $\mathbf{E}_{P_e}$ have been identified which are present in all intervals, but vary from one interval to the next. These are the crossover between MHD and Hall dynamics, k_{Hall}, the ratio of electron pressure to Hall contributions, E_{P_e}/E_{Hall}, and the ratio of nonlinear to linear contributions from each term. The work presented here confirms expectations that k_{Hall} typically occurs around the ion scales, and that $(E_{P_e}/E_{Hall})_{sub\text{-}ion}$ is approximately constant as a function of scale. $R^{NL/L}_{MHD}$ is constant at scales larger than the ion scales, $R^{NL/L}_{Hall}$ is constant across all accessible scales, and these ratios demonstrate a scale-by-scale balance between the linear

and nonlinear terms is achieved that can be dominated by either the nonlinear or linear terms. $\mathbf{E}_{P_e}$ is dominated by linear components, typically a mixture of contributions from δn and $\delta \mathbf{T}_e$ at large scales, then by contributions from $\delta \mathbf{T}_e$ at small scales, which calls into question the fact that many studies neglect temperature fluctuations altogether.

Equations have been developed to approximate how k_{Hall}, E_{P_e}/E_{Hall}, $R_{MHD}^{NL/L}$, and $R_{Hall}^{NL/L}$ depend on the properties of the turbulence and ambient plasma conditions. This is in agreement with work by Franci et al. (2020), which showed that properties of the turbulent cascade are mainly dependent on ambient plasma conditions rather than the type of large-scale driver. The Hall scale most clearly depends on $1/d_i$ and $\delta u/\delta b_A$ evaluated at the ion inertial length. At sub-ion scales, E_{P_e}/E_{Hall} depends on β_e, $(\delta P_e/P_{e,0})/(\delta B/B_0)$ averaged over the sub-ion scales, with all three of the anisotropic diagonal components of $\mathbf{P}_e$ included into δP_e, and $B_0/\langle|B|\rangle$. At scales larger than the ion scales, $R_{MHD}^{NL/L}$ and, across all scales, $R_{Hall}^{NL/L}$ is constant and goes as $\delta B_{rms}/B_0$, indicating that the balance between the background field and large-scale magnetic fluctuations controls the relative nonlinearity to linearity of these terms.

Several of the key properties of the turbulent fluctuations, namely $\delta u/\delta b_A$, $(\delta P_e/P_{e,0})/(\delta B/B_0)$ and $B_0/\langle|B|\rangle$, have underlying dependences on plasma conditions such that k_{Hall} and E_{P_e}/E_{Hall} are expressible solely as empirical functions of ambient plasma parameters. An evaluation of the Hall scale gives $k_{Hall} \sim \beta_i^{-0.14} \times (1/d_i)$. For the relative amplitude of electron pressure to Hall fluctuations, the relationship $(\delta P_e/P_{e,0})/(\delta B/B_0) \sim \beta^{-0.68}$ is uncovered. Such a scaling is not consistent with the isothermal linear KAW approximation. Indeed, temperature fluctuations are playing a significant role in generating the non-ideal electric field. Additionally, two populations of $B_0/\langle|B|\rangle$ behaviour are identified, corresponding to small and large $\delta B_{rms}/B_0$, respectively. When combined, the two populations feed into $(E_{P_e}/E_{Hall})_{sub\text{-}ion}$, corresponding to $\beta_e/\beta^{0.75}$ (small $\delta B_{rms}/B_0$) and $\beta_e/\beta^{1.07}$ (large $\delta B_{rms}/B_0$), respectively.

This work opens the door to a variety of further research directions. Investigating how the findings of this study compare to different plasma systems, covering an extrapolation

beyond the extrema of the intervals used here – as well as completely different parameter regimes – would give useful insight into the applicability and limitations of these results. A formal analysis of the relationship between the Hall scale and the magnetic field spectrum break scale may reveal the role of the sub-ion electric field in changing the magnetic field dynamics, particularly in regions with a well-developed inertial range such as the solar wind. Another further study may aim to incorporate temperature fluctuations into the KAW treatment of $(\delta P_e/P_{e,0})/(\delta B/B_0)$, to determine whether KAW physics is important in the dynamics of the magnetosheath. Beyond this, it is clear that simple dimensional analysis expressions cannot reliably approximate the relative scaling of linear and nonlinear contributions to $\mathbf{E}_{P_e}$, so it would be interesting to uncover why dimensional analysis methods break down for this term, and not others. Such a study may give insights into the nature of the interplay between the two linear terms which jointly dominate the $\mathbf{E}_{P_e}$ dynamics.

It would be interesting to explore whether the results in this chapter are linked to systematic variations with distance from the bow shock, or more generally with position within the magnetosheath, as a result of recently driven turbulence evolving as it develops. This would contribute to the body of work assessing the different spectral ranges of turbulence present throughout the magnetosheath. A cursory assessment reveals no obvious links between the Ohm's law characteristics and location in the magnetosheath, but a different dataset may be required to extensively explore this aspect (potentially based on the 2023 MMS unbiased magnetosheath campaign). Similarly, it would be interesting to examine whether the results in this chapter are linked to systematic variations with upstream solar wind conditions.

This chapter explores contributions to the turbulent electric field and how they change relative to one another based on changes to the turbulent plasma environment. This has direct implications for energy conversion and the dissipation of turbulent fluctuation energy as the electric field facilitates these processes in collisionless space plasmas. The chosen direction for further work in this thesis is to explore the role of the electric field in

mediating energy transfer between the electromagnetic field and the particles. In Chapter 5, electric field-driven energy transfer will be studied in the context of processes which regulate the plasma thermodynamics, such as kinetic microinstabilities, to build up a picture of how the turbulent electric field modulates magnetosheath energetics.

Chapter 5

Linking Turbulent Energy Conversion to Kinetic Microinstabilities

Material in this chapter has been published as:

H. C. Lewis, J. E. Stawarz, L. Matteini, L. Franci, K. G. Klein, R. T. Wicks, C. S. Salem, T. S. Horbury, and J. H. Wang (2024). "Turbulent Energy Conversion Associated With Kinetic Microinstabilities in Earth's Magnetosheath". In: *Geophysical Research Letters* **51**:24, e2024GL112038. DOI: 10.1029/2024GL112038

5.1 Introduction

In collisionless plasmas, internal energy needs to be redistributed via wave–particle interactions, which requires that free energy is used to grow the wave. There are various ways by which free energy can be converted to work, but the common factor is that, since magnetic fields cannot do work on particles, energy transfer occurs via interactions with the electric field. Chapter 4 discussed the variable precedence of different electric field contributions depending on the surrounding magnetosheath conditions; this chapter

investigates energy conversion which occurs as the result of coupling between the current density and different electric field contributions (see Section 2.3.4). In this chapter, by studying signatures of energy conversion associated with turbulent fluctuations, the relationship between turbulence and the redistribution of free energy via processes which regulate the thermodynamics of the magnetosheath is explored.

The dynamics of the magnetosheath are influenced by solar wind turbulence as it is processed by the bow shock, as well as fluctuations driven by the shock itself (Huang et al., 2017; Sahraoui et al., 2020; Rakhmanova et al., 2021). In addition to strong fluctuations, the magnetosheath is host to complex VDFs which deviate significantly from Maxwellian distributions (Shuster et al., 2019). The non-Maxwellian features can act as a source of free energy, as the Maxwellian distribution is the equilibrium state. The shape of the VDF – like the turbulent fluctuations – is influenced by the bow shock as well as dynamics in the magnetosheath. Non-Maxwellian VDFs are susceptible to instabilities (see Section 2.4), which reduce the free energy in the VDF by scattering particles in velocity space and driving the plasma to relax into a state closer to thermodynamic equilibrium, exciting plasma wave modes (Gary, 1993; Treumann and Baumjohann, 1997). In the absence of collisions, it is processes like these which are expected to account for changes to the VDFs, acting to equilibrate the distribution functions in opposition to competing processes which perturb them.

Both turbulence and VDF instabilities are involved in energy transfer between electromagnetic energy and particle energy. Since magnetic fields cannot do work on the particles, energy exchange between the fields and bulk flow energy is mediated by $\mathbf{j}\cdot\mathbf{E}$ (Baumjohann and Treumann, 1996, see Section 2.1.4). Taking the contribution from the electric field in the frame moving with the electron bulk velocity,

$$\mathbf{E}' = \mathbf{E} + \mathbf{v}_e \times \mathbf{B}, \tag{5.1}$$

and coupling it into the total current density gives the Joule dissipation, $\mathbf{j}\cdot\mathbf{E}'$ (Zenitani et al., 2011a; Vörös et al., 2019). This term is the collisionless analogue of Ohmic heating,

ηj^2, and it is an important step in the dissipation process (Birn and Hesse, 2005; Birn and Hesse, 2009; Zenitani et al., 2011b) because it encapsulates energy conversion related to non-ideal (i.e. beyond ideal MHD) electric fields, which are capable of decoupling particle motion from $\mathbf{B}$. How the eventual dissipation of turbulent fluctuation energy at kinetic scales occurs is still an open topic of debate (see discussions in e.g. Matthaeus et al., 2020; Pezzi et al., 2021a; Bandyopadhyay et al., 2023), emphasising the importance of studying how non-ideal energy conversion interacts with the processes which underlie small-scale thermodynamics in collisionless plasmas.

In contrast to ηj^2, which is positive by definition, $\mathbf{j} \cdot \mathbf{E}'$ is reversible and therefore sign-indefinite, although space plasma observations typically find it to be positive on average (Matthaeus et al., 2020). Positive values correspond to transfer from fields to flow (loading), whereas negative values correspond to conversion from the flow to the fields (generating) (Birn and Hesse, 2005). Signatures of intense positive and negative $\mathbf{j} \cdot \mathbf{E}'$ are present throughout the magnetosheath. A key question in the study of collisionless plasma turbulence and its associated dissipation is understanding the origin of both the positive and negative energy conversion signatures, how they may relate to specific fundamental plasma processes, and how those signatures ultimately link to irreversible dissipation.

Within the magnetosheath, $\mathbf{E}'$ is dominated by the electron pressure divergence electric field (from Equation 2.44), because the inertia term is negligible (as demonstrated in Chapter 4)

$$\mathbf{E}' \approx \mathbf{E}_{P_e} = -\frac{1}{ne} \nabla \cdot \mathbf{P}_e, \tag{5.2}$$

down to the smallest spatial scales which can be sampled by spacecraft instruments (Vasyliunas, 1975; Lyons and Pridmore-Brown, 1990; Hesse and Winske, 1993; Vörös et al., 2019; Stawarz et al., 2021). As seen in Chapter 4, instrumental resolution within the magnetosheath is regularly sufficient to sample $\mathbf{E}_{P_e}$ well into the sub-ion range, but rarely below the electron characteristic scales. However, $\mathbf{E}_{P_e}$ can only be computed via the barycentric estimator method, which assumes linear gradients below R_{sc} and requires tetrahedral multipoint measurements (Section 3.4.1). As such, this chapter primarily uses

$\mathbf{E}'$ based on the electric field measurements from MMS as it is the more straightforward and reliable electric field component to measure, in addition to making possible the inclusion of data taken after the electron spectrometer on MMS4 shut down in June 2018. Additionally, despite being a Single Spacecraft (1SC) variable, $\mathbf{E}'$ also contains the full inertia term, meaning that the $\partial\mathbf{j}/\partial t$ component of $\mathbf{E}_{inertia}$ (which cannot be explicitly computed from time series data when Taylor's hypothesis (Taylor, 1938, Section 3.5) is employed) is accounted for.

As established in Section 2.4, prior studies have demonstrated that temperature anisotropy ($T_{s,\perp}/T_{s,\parallel} \neq 1$) is constrained by the parallel plasma beta $\beta_{s,\parallel} = 2n_s T_{s,\parallel}\mu_0/B^2$. Investigations of the solar wind and magnetosheath have observed this effect for the protons (Gary et al., 1995; Gary et al., 1997; Hellinger et al., 2006; Maruca et al., 2012; Matteini et al., 2013; Maruca et al., 2018; Bandyopadhyay et al., 2022a) and electrons (Gary et al., 2005; Xu and T. Chen, 2012; X. Zhang et al., 2018; Graham et al., 2021). The constraint put on $T_{s,\perp}/T_{s,\parallel}$ by $\beta_{s,\parallel}$ is thought to be linked to a number of different instabilities (Gary, 1993), for which empirical functional forms have been developed to parametrise the growth rate contours as a function of dimensionless parameters S_e, α_e (electrons) and a, β_0 (ions). These curves are expressed as

$$\frac{T_{e,\perp}}{T_{e,\parallel}} = 1 + S_e\,\beta_{e,\parallel}^{-\alpha_e} \tag{5.3}$$

for the electrons (Gary and J. Wang, 1996) and

$$\frac{T_{i,\perp}}{T_{i,\parallel}} = 1 + \frac{a}{(\beta_{i,\parallel} - \beta_0)^b} \tag{5.4}$$

for the ions (Hellinger et al., 2006).

When plotted on the temperature anisotropy–parallel beta plane (hereafter shortened to the anisotropy–beta plane), these curves serve as boundaries of the accessible region of parameter space, indicating that rapidly-growing kinetic microinstabilities have a controlling influence on the shape of VDFs. Electron parameter space is bounded by the electron whistler and oblique electron firehose instabilities, whereas the ions are influenced by the

ion cyclotron, ion mirror, parallel ion firehose, and oblique ion firehose instabilities. This chapter examines how local anisotropy of the VDF or local $\beta_{\parallel}$ associated with the turbulent dynamics in the magnetosheath interplay with these kinetic microinstabilities to regulate the energy conversion and dissipation in collisionless plasma turbulence. As discussed in Section 2.4, the instability growth rate thresholds are derived using linear Vlasov theory under the assumption of perturbations to single bi-Maxwellian components for each species growing in a uniform background, in apparent contradiction with the nonlinear, nonuniform conditions characteristic of turbulence. One explanation for how linear theory is applicable in turbulent conditions is that the local nonlinear timescales have been found to be much slower than linear growth rates in extreme regions of anisotropy–beta parameter space (Bandyopadhyay et al., 2022b; Qudsi et al., 2020). However, this is not always true, especially in the solar wind (Klein et al., 2019a; Klein et al., 2021).

The links between turbulence and small-scale instabilities have recently started to be explored for the protons, for example in hybrid simulations of Alfvénic turbulence (Markovskii et al., 2019; Bott et al., 2021) and in the solar wind (Opie et al., 2023). However, this is still an open problem. The resonant interactions responsible for particle energisation have been the subject of detailed studies in recent years (e.g. Howes et al., 2017; Klein et al., 2017; C. H. K. Chen et al., 2019; Verniero et al., 2021; Afshari et al., 2021; Jiang et al., 2024), however they are difficult to investigate statistically because of their purely kinetic nature and how complex it is to look at individual features through many 3D VDFs across a turbulent interval. Instead, a fluid approach is adopted using $\mathbf{j} \cdot \mathbf{E}'$ to assess the net transfer of energy to and from the particles, neglecting how the dissipation takes place in detail on a particle-by-particle basis. An exploration is made of how this fluid heating step is organised with respect to the plasma microinstabilities, to highlight how turbulent fluctuations are interacting with the VDFs to create conditions which are locally susceptible to the kinetic microinstabilities which regulate the plasma thermodynamics.

5.2 Methods

5.2.1 Preparing the Dataset

Rapid VDF measurements by the Fast Plasma Investigation (FPI) instrument suite on Magnetospheric Multiscale (MMS) – namely electron and ion velocity distributions sampled at cadences of 0.03 s and 0.15 s, respectively – facilitate in-depth exploration of sub-ion scale turbulence that was not possible with prior missions. The dataset used in this chapter consists of 24.4 hours of 1SC burst-mode data from 163 intervals of continuous magnetosheath measurements by MMS1. This is a significant expansion on the database of intervals compiled by Stawarz et al. (2022) used in Chapter 4, with additions extending to the end of the 2019–2020 MMS dayside season. The intervals range from 3–43 minutes in length, with a mean of 9 minutes. There are no large-scale inhomogeneities and all are long enough to cover multiple correlation lengths (the largest scale of turbulent fluctuations). More information about the intervals is compiled in Appendix B.1.

Intervals are aggregated to create a single time series of variables on the electron and ion measurement cadence, as appropriate. Velocity moments of the VDFs are used to compute $\mathbf{j} = en(\mathbf{v}_i - \mathbf{v}_e)$, invoking quasineutrality and interpolating $\mathbf{v}_i$ onto the electron timescale, since small-scale fluctuations in $\mathbf{j}$ are dominated by $\mathbf{v}_e$ (Stawarz et al., 2021), as demonstrated in Figure 3.2. $\mathbf{E}'$ is calculated on the electron instrument cadence, which requires averaging $\mathbf{E}$ and $\mathbf{B}$ onto the electron cadence to match $\mathbf{j}$. Instantaneous local values of the parallel plasma beta $\beta_{s,\parallel}$ and temperature anisotropy $T_{s,\perp}/T_{s,\parallel}$ for species s are used, where the ion values are interpolated onto the electron cadence under the assumption that small-scale fluctuations in these parameters can be neglected. The impact of performing the following analysis on data downsampled onto the ion cadence (0.15 s) has been examined, finding that the results are qualitatively similar.

Figures 5.1 (a) & (b) show how microinstabilities constrain accessible regions of anisotropy–beta parameter space in this dataset. Electron whistler & firehose and ion instability thresholds are plotted using the parametric curves defined in Gary and J. Wang (1996)

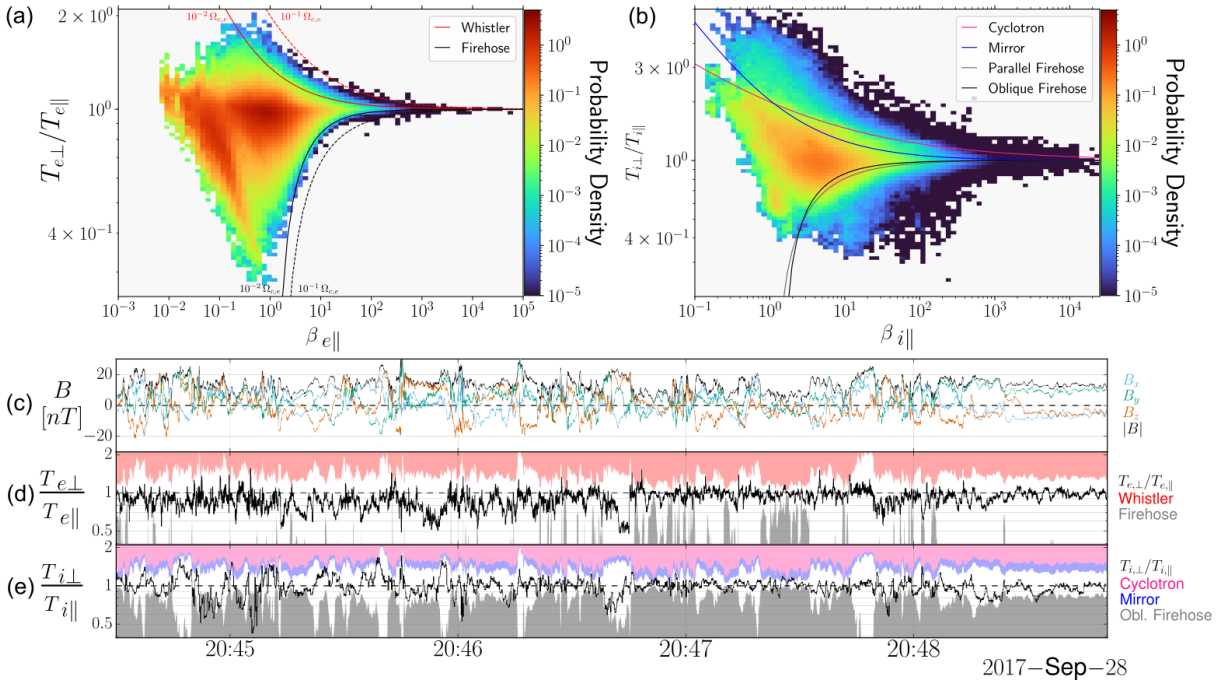


Figure 5.1: Probability density plotted on the anisotropy–beta plane, with an example time series. Panel (a) represents parameter space for the electrons, where solid and dashed lines correspond to $\gamma = 10^{-2}\,\Omega_{c,e}$ and $\gamma = 10^{-1}\,\Omega_{c,e}$ growth rate thresholds, respectively. Panel (b) shows ion parameter space, with $\gamma = 10^{-2}\,\Omega_{c,i}$ instability thresholds. Panels (c)–(e) illustrate motion through parameter space through changing anisotropy, as well as the variability in thresholds, during 2017-09-28/20:44:30—20:48:51. Panel (c) shows the turbulent magnetic field. Panels (d) and (e) show the temperature anisotropy of the electrons and ions, respectively. Shaded areas represent instantaneous $\gamma = 10^{-2}\,\Omega_c$ instability thresholds for each species (the $\gamma = 10^{-1}\,\Omega_{c,e}$ thresholds are not shown as $\gamma = 10^{-2}\,\Omega_c$ will be met first.

Threshold	Species	Growth Rate γ	S_e	α_e	a	β_0	b
Whistler	Electron	$10^{-2}\,\Omega_{c,e}$	0.36	0.55	/	/	/
Whistler	Electron	$10^{-1}\,\Omega_{c,e}$	1.00	0.49	/	/	/
Firehose	Electron	$10^{-2}\,\Omega_{c,e}$	−1.23	0.88	/	/	/
Firehose	Electron	$10^{-1}\,\Omega_{c,e}$	−1.32	0.61	/	/	/
Cyclotron	Ion	$10^{-2}\,\Omega_{c,i}$	/	/	1.001	0.0	−0.330
Mirror	Ion	$10^{-2}\,\Omega_{c,i}$	/	/	1.041	−0.0039	−0.608
Parallel Firehose	Ion	$10^{-2}\,\Omega_{c,i}$	/	/	−1.144	−0.0625	−0.774
Oblique Firehose	Ion	$10^{-2}\,\Omega_{c,i}$	/	/	−1.193	0.2301	−0.926

Table 5.1: The dimensionless parameters for the instability growth rate thresholds displayed on the anisotropy–beta plane in this chapter. S_e & α_e fit the electron curve as in Equation 5.3 and a, β_0, & b fit the ion curve as in Equation 5.4. The ion species is assumed to be composed entirely of protons. Growth rate curves courtesy of Gary and J. Wang (1996), Gary and Nishimura (2003), and Maruca et al. (2018).

& Gary and Nishimura (2003), and Maruca et al. (2018), respectively. In fitting these thresholds, it is assumed that VDFs are anisotropic Maxwellians and that there is no anisotropy for one species when computing the growth curves of the other. The values of the dimensionless parameters for the thresholds in use are given in Table 5.1. Despite nonzero background non-Maxwellianity (which will be discussed further in Chapter 6) and overlap between times when $T_{e,\perp}/T_{e,\parallel} \neq 1$ and $T_{i,\perp}/T_{i,\parallel} \neq 1$ within this dataset, the plots in Figure 5.1 demonstrate that the vast majority of probability density lies within instability growth rate thresholds of $\gamma = 10^{-2}\,\Omega_c$, as seen in previous studies (Maruca et al., 2018; Graham et al., 2021). Probability density, also known as normalised occurrence rate, is equal to the number of samples within the bin divided by the total number of samples, divided by the area of the bin to account for the unequal bin sizes. The probability density is thus normalised so that the integral over the whole distribution is equal to 1.

Comparing Figures 5.1 (a) and (b), the ions are typically able to deviate further from the plotted instability growth rate curves, and crucially the ion probability density appears more diffuse across parameter space, irrespective of instability thresholds. In both panels, the greatest occupancy of parameter space is concentrated around $T_\perp/T_\parallel \sim 1$ and $\beta_\parallel \sim 10^{-1}$—$10^{1}$, indicating the typical conditions in the magnetosheath. Figures 5.1 (c) to (e) show that turbulent fluctuations generate local changes to both anisotropy and instability thresholds such that the plasma is locally driven closer or farther from the unstable regions, indicating that a typical interval moves significantly around parameter space as opposed to filling an isolated region close to its average.

To illustrate the distribution of $T_\perp/T_\parallel$ and $\beta_\parallel$ throughout this dataset, histograms and marginal distributions are plotted in Figure 5.2. Figure 5.2 (a) shows that $T_{e\perp}/T_{e\parallel}$ is not directly correlated with $T_{i\perp}/T_{i\parallel}$. Since the instability growth rate thresholds are parametrised based on the assumption that each species exhibits anisotropy only when the other is isotropic, the absence of a correlation between the two species implies that the underlying assumptions are not systematically violated. However, the distributions are

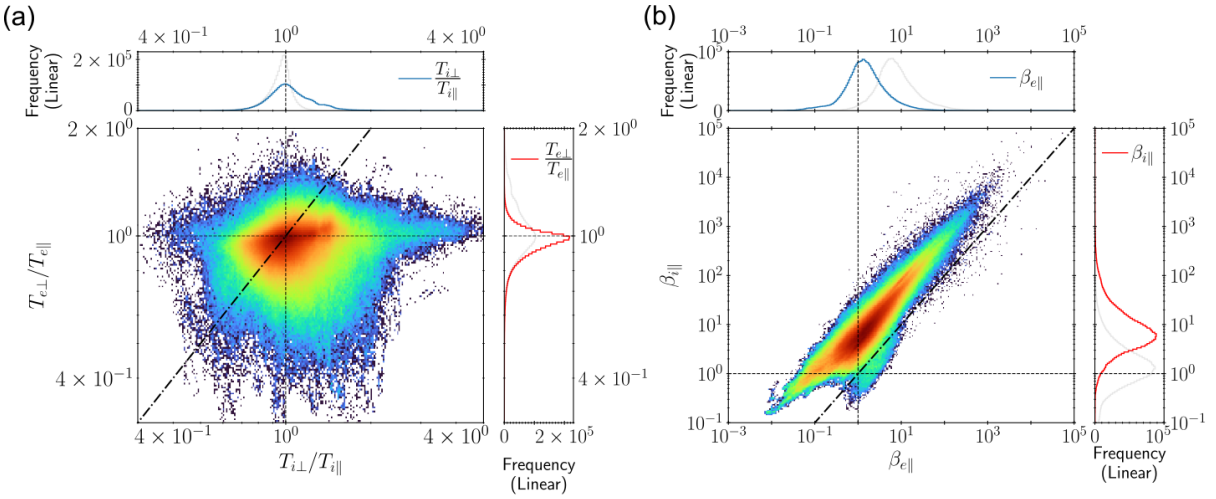


Figure 5.2: Histograms of temperature anisotropy and parallel plasma beta for both species, including individual histograms of each quantity on the margins. Panel (a) compares electron and ion temperature anisotropy. Panel (b) compares electron and ion parallel beta. In both panels, the dash-dotted black line corresponds to agreement. In the marginal distributions, the frequency (number of points) scale is linear and the greyed-out line corresponds to the other species' distribution. In the 2D histograms, the colour scale is logarithmic.

not uniform. $T_{e\perp}/T_{e\parallel}$ is more sharply-peaked, indicating fewer extreme values compared to $T_{i\perp}/T_{i\parallel}$. This is consistent with electrons undergoing faster interactions than the ions leading to more isotropic VDFs, or with greater errors in the ion VDFs.

Figure 5.2 (b) compares $\beta_{e,\parallel}$ and $\beta_{i,\parallel}$, which, assuming quasineutrality, depend on the relationship between $T_{e,\parallel}$ and $T_{i\parallel}$. There is an approximately linear trend parallel to the agreement line, offset such that $\beta_{i\parallel}$ is usually greater than $\beta_{e,\parallel}$, which is expected because the ions are typically hotter than the electrons. There is a region with $\beta_{e,\parallel} > \beta_{i\parallel}$, but this accounts for a small fraction of the data. The marginal panels show that the distributions of values are very similar, with $\beta_{e,\parallel}$ smaller such that there are more instances where $\beta_{e,\parallel} \leq 1$, showing that the dynamics of the electron fluid are more readily influenced by magnetic field behaviour.

5.2.2 Interpretation of Anisotropy–Beta Plots

Before proceeding to the results, there are some aspects which must be borne in mind when interpreting anisotropy–beta plots, especially when plotting the distribution of a variable other than the probability density on the z-axis. A third variable may not be

organised solely by the instantaneous values of $\beta_{\parallel}$ and $T_{\perp}/T_{\parallel}$ and the kinetic microinstabilities which grow at extreme combinations of these values. Instead, there can be a more complex relationship between the x-, y-, and z-axes, arising due to an underlying functional dependence or the overlaying of multiple populations. For example, in the solar wind fast and slow streams have different distributions in anisotropy–beta space because of how the proton anisotropy evolves as the solar wind propagates away from the Sun (Hellinger et al., 2006), meaning they must be treated separately to identify differences in how they respond to anisotropy-driven instabilities. Fortunately, this study uses turbulent magnetosheath data, which does not have well-defined disparities between different internal conditions like the fast and slow solar wind. However, the data set contains wide variation in background conditions (such as β, $\delta B/B_0$, and others – see Chapter 4), which have to be considered when interpreting the plots.

Due to the aggregation of many intervals with different ambient conditions, the instability growth rate thresholds used (Gary and J. Wang, 1996; Gary and Nishimura, 2003; Maruca et al., 2012) may not be the most appropriate for this dataset. These thresholds were chosen because they are calculated for magnetosheath data with no alpha population, however they are based on $\beta \sim 1$ plasma with independent anisotropy between the two species. These conditions are not always satisfied in Earth's magnetosheath, but these nominal instability contours are provided for reference. However, it is important to remember that the displayed thresholds are just contours of an exponential increase in maximum growth rate which occurs as the data moves into more unstable regions of parameter space. The most appropriate contour which well-contains this dataset may be between – or beyond – those displayed in the subsequent figures.

5.3 Results

5.3.1 $\mathbf{j} \cdot \mathbf{E}'$ on the Anisotropy–Beta Plane

To investigate how energy conversion to/from the electromagnetic fields is organised with respect to kinetic microinstabilities, $\langle|\mathbf{j} \cdot \mathbf{E}'|\rangle$ and $\langle\mathbf{j} \cdot \mathbf{E}'\rangle$ are plotted on the anisotropy–beta plane in Figure 5.3. To account for any large-scale variability in the amplitude of fluctuations between intervals, the time series of $\mathbf{j} \cdot \mathbf{E}'$ is normalised by its mean-removed Root Mean Square (rms) value,

$$\sqrt{\langle(\mathbf{j}(t) \cdot \mathbf{E}'(t) - \langle\mathbf{j}(t) \cdot \mathbf{E}'(t)\rangle)^2\rangle}, \tag{5.5}$$

on an interval-by-interval basis. The data in these units represents an energy conversion fluctuation where a value of 1 corresponds to the characteristic fluctuation amplitude for the interval from which a given data point originates.

Figure 5.3 (a) shows that mean signed energy conversion is positive across most of parameter space, and that it is particularly strong near the firehose and whistler instability thresholds. The center of the distribution is weakly net-positive, accounting for the majority of overall energy conversion and suggesting that there is an average dissipation of electromagnetic energy into particle energisation. At low $\beta_{e,\parallel}$, there are regions of negative average energy conversion which partially overlap with enhancements in $\langle|\mathbf{j} \cdot \mathbf{E}'|\rangle$. Concordantly, Figure 5.3 (b) shows that there is enhanced $\langle|\mathbf{j} \cdot \mathbf{E}'|\rangle$ – corresponding to a greater mean amplitude of energy conversion signals – in regions susceptible to oblique electron firehose and electron whistler instabilities. Qualitatively, high $\langle|\mathbf{j} \cdot \mathbf{E}'|\rangle$ is most strongly concentrated around the firehose threshold, extending to $\gamma \leq 10^{-2}\,\Omega_{c,e}$. In comparison, the enhancement associated with the whistler instability begins at $\gamma \geq 10^{-2}\,\Omega_{c,e}$. Interestingly, there is an enhancement along the low–$\beta_{e,\parallel}$ edge of the distribution for $T_{e,\parallel} > T_{e,\perp}$. Despite being partially obscured in the full set of intervals, closer investigation reveals that this feature is robust for different subsets of intervals. Given that this signature is not in the vicinity of the standard instability thresholds, the significance of enhanced

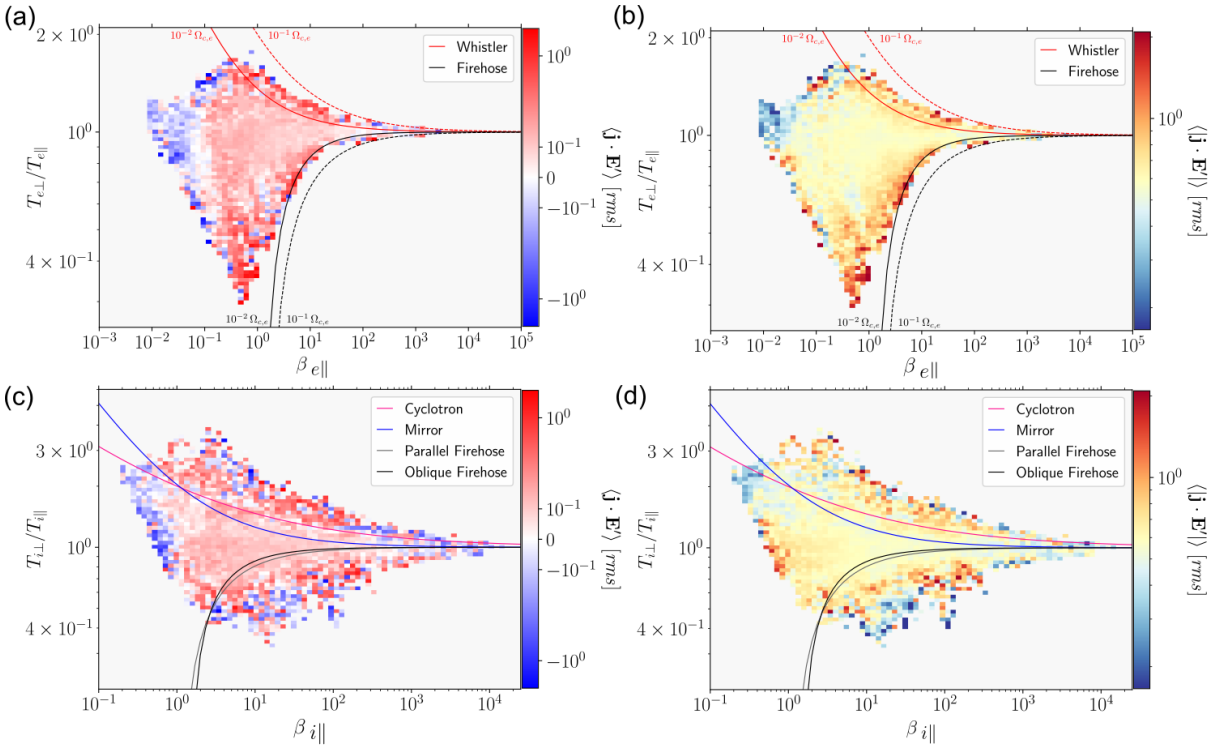


Figure 5.3: Average amplitude of energy conversion signals distributed on the anisotropy–beta plane. (a) $\langle \mathbf{j} \cdot \mathbf{E}' \rangle$ in $T_{e,\perp}/T_{e,\parallel}$–$\beta_{e,\parallel}$ parameter space with instability thresholds of $\gamma = 10^{-2}\,\Omega_{c,e}$ (solid line) and $\gamma = 10^{-1}\,\Omega_{c,e}$ (dashed line). (b) $\langle |\mathbf{j} \cdot \mathbf{E}'| \rangle$ on the same plane. (c) $\langle \mathbf{j} \cdot \mathbf{E}' \rangle$ in $T_{i,\perp}/T_{i,\parallel}$–$\beta_{i,\parallel}$ parameter space with instability thresholds of $\gamma = 10^{-2}\,\Omega_{c,i}$. (d) $\langle |\mathbf{j} \cdot \mathbf{E}'| \rangle$ on the same plane. In all panels, bins with fewer than 5 points in total or originating from only 1 interval are excluded.

$\langle |\mathbf{j} \cdot \mathbf{E}'| \rangle$ in this region of parameter space is less clear.

There are interesting comparisons to draw with how energy conversion is organised across ion parameter space. Figure 5.3 (c) shows that, as for electrons, $\langle |\mathbf{j} \cdot \mathbf{E}'| \rangle$ is enhanced along ion instability boundaries. However, the enhancement is most pronounced beyond the instability thresholds, suggesting that a faster growth rate is required to overcome the effects which are driving the ion VDFs into unstable regions. An enhancement on the low–$\beta_{i,\parallel}$ edge is also visible, albeit partially obscured as in the electron plot. This similarity may be expected because the time steps that are at $\beta < 1$ are mainly driven by large magnetic fields, appearing as low–$\beta_{\parallel}$ points on both species' planes. Figure 5.3 (d) shows that $\langle \mathbf{j} \cdot \mathbf{E}' \rangle$ in ion parameter space is more sign-indefinite than the electrons beyond the instability thresholds, with average net conversion from fields to flow only being maintained in the stable center of the distribution.

5.3.2 Parallel and Perpendicular Components of $\mathbf{j} \cdot \mathbf{E}'$

In the previous section, it was established that that non-ideal energy conversion between electromagnetic and particle energy (via $\mathbf{j} \cdot \mathbf{E}'$) is enhanced in regions that are more susceptible to anisotropy–beta instabilities and at low parallel beta. One aspect that is unique to the non-ideal electric field is that it is capable of accelerating particles parallel to the magnetic field, as well as perpendicular energisation and energy transport across field lines. The total energy conversion will not be solely in the direction parallel to $\mathbf{B}$, so the term is decomposed into parts arising from parallel and perpendicular $\mathbf{j} \cdot \mathbf{E}'$. To do this, $\mathbf{j}$ and $\mathbf{E}'$ are projected into a local field-aligned coordinate system where $\hat{z}$ is aligned with the instantaneous $\mathbf{B}$. Then, the parallel components are multiplied and the dot product of the two perpendicular components is taken, as

$$(\mathbf{j} \cdot \mathbf{E}')_{\parallel} = j_{\parallel} E'_{\parallel}, \tag{5.6}$$

$$(\mathbf{j} \cdot \mathbf{E}')_{\perp} = \mathbf{j}_{\perp} \cdot \mathbf{E}'_{\perp} = j_{\perp 1} E'_{\perp 1} + j_{\perp 2} E'_{\perp 2}. \tag{5.7}$$

It should be noted that $j_{\parallel} E'_{\parallel}$ and $\mathbf{j}_{\perp} \cdot \mathbf{E}'_{\perp}$ cannot be exclusively associated with parallel and perpendicular energisation, respectively, as there must be a cross-term related to the mirror force linking the parallel and perpendicular directions. Here, $j_{\parallel} E'_{\parallel}$ and $\mathbf{j}_{\perp} \cdot \mathbf{E}'_{\perp}$ can be thought of as terms from the energy equation (Equation 2.36) projected into the local field-aligned coordinate system. These two terms are given the same treatment as in Section 5.3.1, by normalising each variable by its interval-rms and aggregating into a single dataset.

Figures 5.4 (a)–(d) show how average signed values and magnitudes of $j_{\parallel} E'_{\parallel}$ and $\mathbf{j}_{\perp} \cdot \mathbf{E}'_{\perp}$ are distributed on the $T_{e,\perp}/T_{e,\parallel}$–$\beta_{e,\parallel}$ plane. Figure 5.4 (a) shows that the average parallel energy conversion is largely positive across parameter space, with an enhancement along the electron firehose edge and a small region of negative average at low–$\beta_{e,\parallel}$ around $T_{e,\perp}/T_{e,\parallel}$. These trends are contextualised by Figure 5.4 (b), which shows that the average magnitude of $j_{\parallel} E'_{\parallel}$ is significantly enhanced along the electron firehose edge. The center

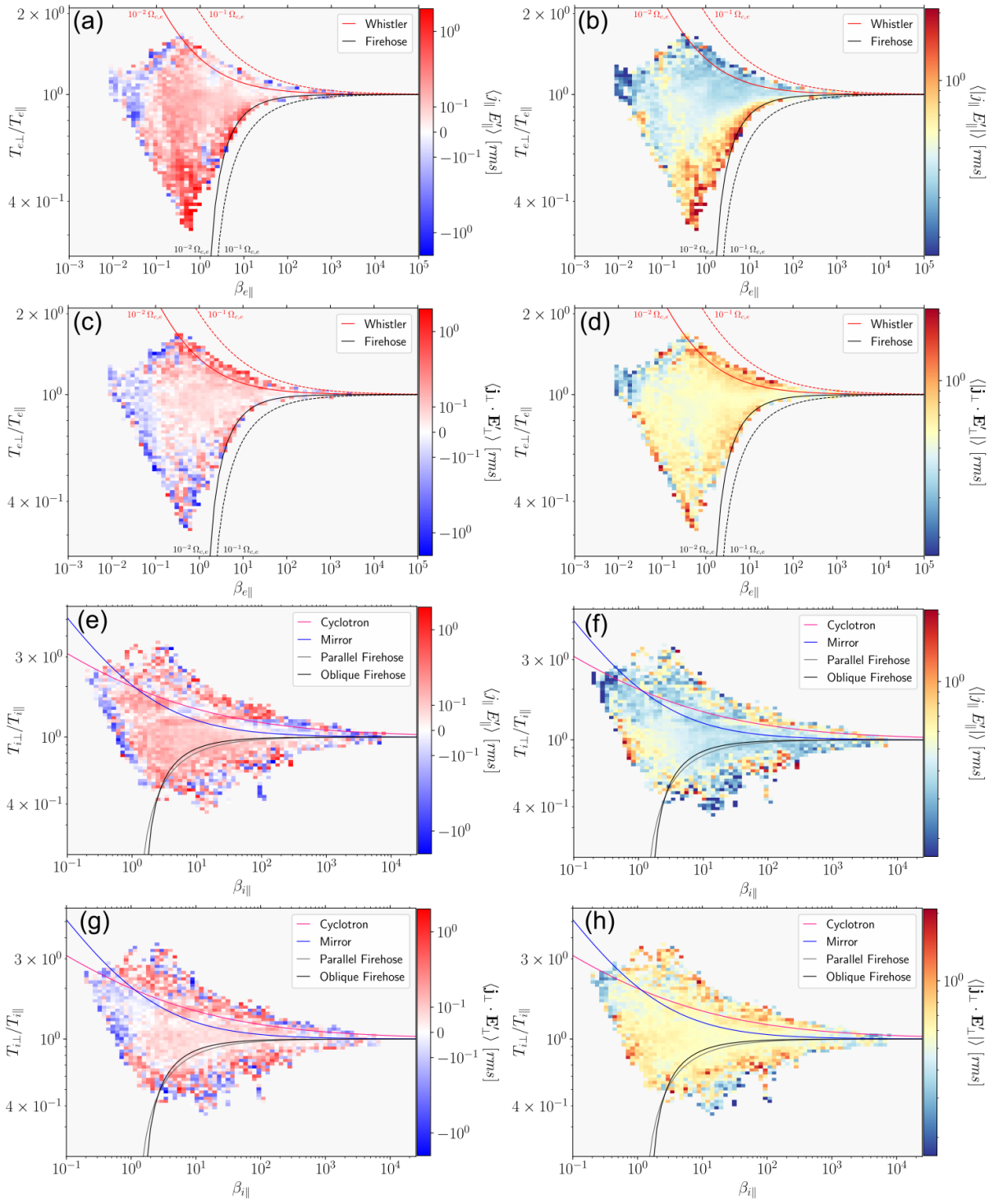


Figure 5.4: Average parallel and perpendicular energy conversion signals distributed on the anisotropy–beta plane. Instability thresholds for the electrons (a)–(d) and ions (e)–(h) are the same as in Figure 5.3. The electron/ion panels, respectively, have plotted on the colour axis: (a/e) $\langle j_\parallel E'_\parallel \rangle$; (b/f) $\langle |j_\parallel E'_\parallel| \rangle$; (c/g) $\langle \mathbf{j}_\perp \cdot \mathbf{E}'_\perp \rangle$; (d/h) $\langle |\mathbf{j}_\perp \cdot \mathbf{E}'_\perp| \rangle$. In all panels, bins with fewer than 5 points in total or originating from fewer than 2 intervals are excluded.

of the distribution has low average magnitude, and there is not an enhancement along the low-β_e edge, which is in contrast to the full electron $\langle|\mathbf{j}\cdot\mathbf{E}'|\rangle$ plot in Figure 5.3 (b). Figures 5.4 (a) & (b) together suggest that parallel energy conversion is largely concentrated in areas which may be more susceptible to the electron firehose instability, but reduced in other regions of parameter space.

In contrast to the parallel energy conversion in Figures 5.4 (a) & (b), Figures 5.4 (c) & (d) present the distribution of average value and magnitude of $\mathbf{j}_\perp \cdot \mathbf{E}'_\perp$ on the electron anisotropy–beta plane. Figure 5.4 (c) shows that $\langle \mathbf{j}_\perp \cdot \mathbf{E}'_\perp \rangle$ is more sign-indefinite in the center of the distribution and along the electron firehose instability edge. Along the electron whistler edge there is an enhancement in average perpendicular energy conversion, and the low–$\beta_{e,\parallel}$ region is generally negative. The center of the distribution has smaller values, possibly as a result of a more balanced number of positive and negative values cancelling out in the average of these bins. Figure 5.4 (d) shows $\langle|\mathbf{j}_\perp \cdot \mathbf{E}'_\perp|\rangle$ in central bins has a generally higher value than $\langle|j_\parallel E'_\parallel|\rangle$, more similar to what is observed for $\langle|\mathbf{j}\cdot\mathbf{E}'|\rangle$ in Figure 5.3 (b). This indicates that the majority of energy conversion contributions come from the perpendicular component, which is in agreement with MMS observations of turbulence in Earth's magnetotail (Ergun et al., 2020). Figure 5.4 (d) also shows that there are enhancements along the whistler, firehose, and low–$\beta_{e,\parallel}$ edges, albeit a much-diminished trend along the electron firehose boundary compared to $\langle|j_\parallel E'_\parallel|\rangle$ and $\langle|\mathbf{j}\cdot\mathbf{E}'|\rangle$.

Turning now to the $T_{i,\perp}/T_{i,\parallel}$–$\beta_{i,\parallel}$ plane, Figures 5.4 (e) & (f) represent $\langle j_\parallel E'_\parallel\rangle$ and $\langle|j_\parallel E'_\parallel|\rangle$, respectively. Much like the total $\mathbf{j}\cdot\mathbf{E}'$, the energy conversion as distributed with respect to the ion variables has more spread and is less sign-definite than the electron equivalent. This is expected, as the parallel and perpendicular energy conversion terms are simply components of the total term. As shown in Figure 5.4 (e), $\langle j_\parallel E'_\parallel\rangle$ has a similar distribution to $\mathbf{j}\cdot\mathbf{E}'$ as in Figure 5.3 (c); the center (where most points reside) is broadly positive, there is an enhancement in strength and reduction in sign-definiteness in the regions susceptible to anisotropy–beta instabilities, and there is a negative region at low values of $\beta_{e,\parallel}$. Figure 5.4 (d) corroborates these trends, but adds important context by displaying a reduction

in $\langle |j_\parallel E'_\parallel| \rangle$. This is reminiscent of the electron analogue in Figure 5.4 (b), suggesting that $j_\parallel E'_\parallel$ is generally smaller, but especially smaller for $j_\parallel E'_\parallel < 0$, which indicates that parallel energy conversion tends to be into the particles rather than the electromagnetic field. The only areas of enhanced $\langle |j_\parallel E'_\parallel| \rangle$ in Figure 5.4 (d) are sparsely in the instability regions, as well as a small region in low–$\beta_{i,\parallel}$.

Figures 5.4 (g) & (h) show the average value and magnitude of $\mathbf{j}_\perp \cdot \mathbf{E}'_\perp$, respectively. These plots are reminiscent of the electron versions in Figures 5.4 (c) & (d). In Figure 5.4 (g), $\langle \mathbf{j}_\perp \cdot \mathbf{E}'_\perp \rangle$ is enhanced along the instability and low–$\beta_{i,\parallel}$ edges, with a diminished (but still positive) energy conversion in the distribution center. A negative trend is present at low–$\beta_{i,\parallel}$, although this is not as extensive at $T_{i,\perp}/T_{i,\parallel} < 1$ as in Figures 5.4 (e) or (c). Despite being nearly sign-definite at $\beta_{i,\parallel} \gtrsim 1$ in the center of the distribution, the regions associated with instabilities are more variable. Finally, Figure 5.4 (h) shows that $\langle |\mathbf{j}_\perp \cdot \mathbf{E}'_\perp| \rangle$ is greater than $\langle |j_\parallel E'_\parallel| \rangle$ in the center of the distribution, and that there are enhancements along all edges, like the electron plane. The contrast between Figures 5.4 (f) and (h) reinforces the conclusion that most of the energy conversion is in the perpendicular component, but that the perpendicular part has closer to equal distributions of positive and negative energy conversion, leading to apparent reduction of average energy conversion in Figures 5.4 (e) and (g).

5.3.3 Statistics of $\mathbf{j} \cdot \mathbf{E}'$ within Enhancement Regions

To investigate the statistical trends identified in anisotropy–beta parameter space, bins are manually selected and grouped into regions of apparent enhanced $\langle |\mathbf{j} \cdot \mathbf{E}'| \rangle$ to investigate their properties. Certain regions have unclear boundaries (particularly those in ion parameter space), which introduces some variability, however the main highlighted features are not impacted by this. Note that the enhancements associated with the ion cyclotron and ion mirror instabilities have been treated as a single region. Figure 5.5 shows the Probability Density Function (PDF) in each manually-defined region for bins in the range $[-3.5, 3.5]$ rms units, within which the vast majority (98.10%) of points lie. For context, 54.77% of the dataset has $\mathbf{j} \cdot \mathbf{E}' > 0$ rms units, but only 10.10% has $\mathbf{j} \cdot \mathbf{E}' \geq 1$

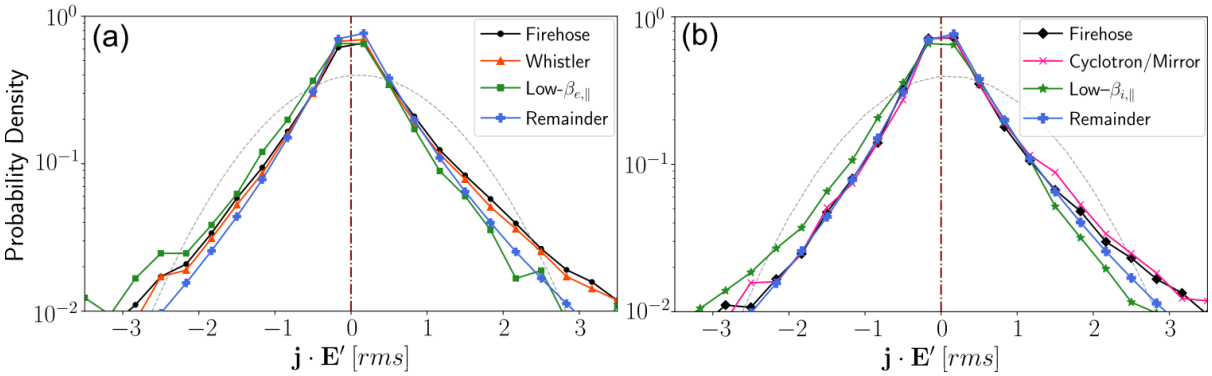


Figure 5.5: Probability Density Function (PDF) of $\mathbf{j} \cdot \mathbf{E}'$ for (a) electron and (b) ion enhancement regions. Markers represent the center of histogram bins. The dashed grey curve indicates a normal distribution with the same mean and standard deviation as the entire dataset.

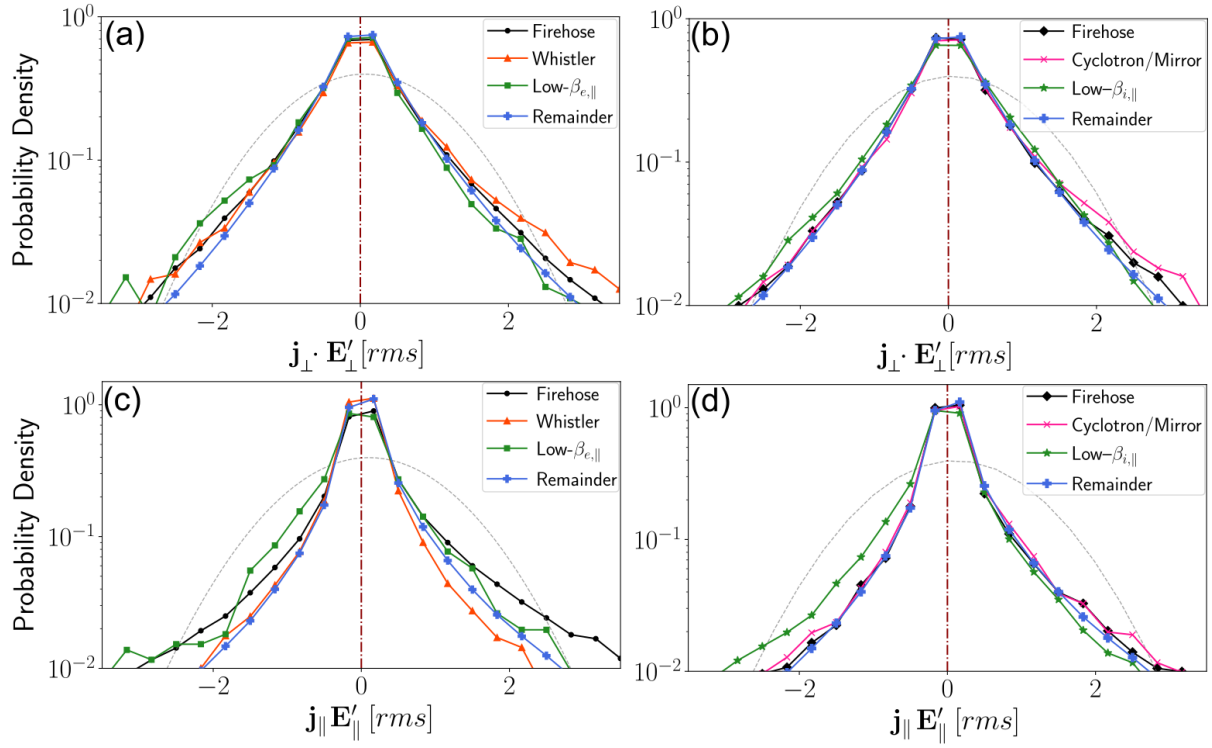


Figure 5.6: Probability Density Function (PDF) of $\mathbf{j} \cdot \mathbf{E}'$ components in enhanced regions of anisotropy–beta parameter space. (a) & (b) show the PDF of $\mathbf{j}_\perp \cdot \mathbf{E}'_\perp$ in enhancement regions associated with the electron and ion instabilities, respectively. (c) & (d) show PDFs of $j_\parallel E'_\parallel$. Markers correspond to the center of each histogram bin. The dashed grey curve indicates a normal distribution with the same mean and standard deviation as the entire dataset.

rms units and 6.58% has $\mathbf{j} \cdot \mathbf{E}' \leq -1$ rms units.

All regions, including the remainders, have nonzero skewness and high kurtosis. Figure 5.5 (a) shows there is a slight enhancement in the negative tails of the electron PDF relative to the remainder, but a more significant enhancement on the positive side, leading to net positive $\mathbf{j} \cdot \mathbf{E}'$. The low–$\beta_{e,\parallel}$ region has diminished positive tail, but the heaviest negative tail of all the regions. Bins with $|\mathbf{j} \cdot \mathbf{E}'| \gtrsim 2$ rms units do not have enough counts to discern a reliable trend. Figure 5.5 (b) demonstrates that ion instability regions are nearly identical to the remainder in the negative tail, but are enhanced on the positive side. The low–$\beta_{i,\parallel}$ region is reminiscent of its electron counterpart because they largely share similar points; the negative tails are heavier than positive, and the peak value is smaller. These trends will be discussed qualitatively in Section 5.4.

To understand how components of total $\mathbf{j} \cdot \mathbf{E}'$ give rise to the observed enhancement regions, the PDFs of $\mathbf{j}_\perp \cdot \mathbf{E}'_\perp$ and $j_\parallel E'_\parallel$ in those regions are plotted in Figure 5.6. Figures 5.6 (a) & (b) are almost symmetric around $\mathbf{j}_\perp \cdot \mathbf{E}'_\perp \approx 0$, with enhanced core, diminished flanks, and enhanced tails which are reminiscent of the $\mathbf{j} \cdot \mathbf{E}'$ case. Figures 5.6 (c) & (d) illustrate that small $j_\parallel E'_\parallel$ is unbalanced, with more positive values than negative, except in the case of low-β. Comparing the two rows suggests that the parallel component tends to be more positive than the perpendicular component, but $|j_\parallel E'_\parallel|$ is less likely to be large than $|\mathbf{j}_\perp \cdot \mathbf{E}'_\perp|$. The qualitative similarity between the PDFs of $\mathbf{j}_\perp \cdot \mathbf{E}'_\perp$ and $\mathbf{j} \cdot \mathbf{E}'$ reflects the fact that the perpendicular component accounts for most of energy conversion (in agreement with other studies, e.g. Ergun et al., 2020).

Comparing Figure 5.6 (a) with Figure 5.6 (c) reveals differences between perpendicular and parallel energy conversion in the different electron enhancement regions. Figure 5.6 (a) shows an increase in positive $\mathbf{j}_\perp \cdot \mathbf{E}'_\perp$ in the region which is susceptible to the electron whistler instability, signifying a link between the $(T_{e,\perp} > T_{e,\parallel})$–driven instability and perpendicular energy conversion. Similarly, 5.6 (c) demonstrates an increase in $j_\parallel E'_\parallel$ in the electron firehose instability region, especially for $j_\parallel E'_\parallel > 0$, which shows that the $T_{e,\parallel} > T_{e,\perp}$ process is associated with parallel energy conversion. This is interesting

because $\mathbf{j}\cdot\mathbf{E}'$ mediates energy exchange between the electromagnetic fields and the particle energy, but parallel and perpendicular components of the energy conversion need not necessarily lead to enhancements in parallel and perpendicular temperature, respectively.

The comparison between Figure 5.6 (b) with Figure 5.6 (d) shows that differences between the instability enhancement regions are not as prominent for the ions as the electrons. The cyclotron/mirror region (which is associated with $T_{i,\perp} > T_{i,\parallel}$), has a slight enhancement for positive $\mathbf{j}_\perp \cdot \mathbf{E}'_\perp$ compared to the other regions, but it is not as pronounced as for the analogous electron whistler instability region. However, in all panels of Figure 5.6, but especially for the parallel component, negative energy conversion (from the fluid to the fields) is increased in the low–$\beta_\parallel$ region. This implies that the process which gives rise to increased negative energy conversion at low-$\beta_\parallel$ is dominated by parallel energy conversion, which may be related to how the parallel component is noted to be correlated with $T_\parallel$ enhancements.

5.4 Discussion

By investigating the statistical relationship between energy conversion (associated with turbulent fluctuations) and anisotropy–beta instabilities (processes which are partly responsible for mediating the plasma thermodynamics), the aim is to explore how turbulence may be linked to thermodynamic processes in the magnetosheath. This section discusses possible interpretations of these findings and the consequences for magnetosheath plasma thermodynamics.

5.4.1 Understanding Energy Conversion Statistics

To contextualise the observed energy conversion signals it is helpful to identify which processes may be relating them to kinetic microinstabilities. First, turbulent fluctuations locally driving the plasma towards an instability threshold by distorting the distribution would be expected to give a positive energy conversion signature. This corresponds to free energy being injected which puts the VDF into an unstable configuration. Second,

the growth of wave modes as a result of instability criteria being met is expected to give a negative energy conversion signature, as it relies on the instability process extracting free-energy from the distribution in order to drive electromagnetic fluctuations. Third, the reconfiguration of the VDF from a more- to less-unstable state, due to the scattering of free energy in velocity space, may not show up in $\mathbf{j} \cdot \mathbf{E}$.

In this dataset, the presence of strong fluctuations in $\mathbf{j} \cdot \mathbf{E}'$ along the unstable boundaries of the distribution is indicative of a link between turbulence and the underlying instability processes. Largely positive $\langle \mathbf{j} \cdot \mathbf{E}' \rangle$ across parameter space indicates that the predominant observation is of the extraction of energy from turbulent fluctuations into the fluid flow. However, around the instability thresholds there is a mixture of net-positive and net-negative bins, particularly for the ions, which suggests the results are also sampling part of wave growth due to instabilities.

Table 5.2 gives the average values of $\mathbf{j} \cdot \mathbf{E}'$ and $|\mathbf{j} \cdot \mathbf{E}'|$ in each manually-defined region as introduced in Section 5.3.3. Comparing to the remainder (all bins which are not in at least one of the enhancement regions) gives an indication of how the statistics are different when susceptible to the influence of kinetic microinstabilities and at low $\beta_{\parallel}$. The three electron regions represent 3.18% of the total dataset, including 3.04% associated with the electron firehose and whistler instabilities. $\langle \mathbf{j} \cdot \mathbf{E}' \rangle$ in the electron instability regions shows that the average energy conversion direction is from the fields to the fluid flow, and that the average value is increased compared to the remainder. This is consistent with electron VDFs being driven into unstable configurations by fluid heating associated with turbulent fluctuations. The low–$\beta_{e,\parallel}$ region has net energy conversion from the fluid flow into the fields, which suggests observations are of the scattering of particles leading to the reduction of free energy in the VDF in favour of growing wave modes.

The fraction of the total dataset which is in ion regions is lower, at 1.65%, with only 0.98% of measurements associated with enhancements in $\mathbf{j} \cdot \mathbf{E}'$ at the ion cyclotron and firehose instabilities. Trends in $\langle \mathbf{j} \cdot \mathbf{E}' \rangle$ in the ion regions are similar to those in the electron regions, with net positive energy conversion along instability thresholds and net negative

Region	**Data** (%)	$\langle \mathbf{j} \cdot \mathbf{E}' \rangle$	$\langle \lvert \mathbf{j} \cdot \mathbf{E}' \rvert \rangle$	**Var.**	**Skew.**	**Kur.**
Electron firehose	2.48	0.159	0.779	2.00	3.01	79.20
Electron whistler	0.56	0.150	0.721	1.76	5.25	164.99
Electron low–$\beta_{e,\parallel}$	0.14	−0.059	0.755	3.15	−15.96	648.70
Electron remainder	96.82	0.104	0.583	0.97	1.89	94.50
Ion firehose	0.54	0.127	0.683	1.67	2.92	61.60
Ion cyclotron/mirror	0.44	0.155	0.713	2.23	5.55	224.16
Ion low–$\beta_{i,\parallel}$	0.67	−0.040	0.667	1.79	−1.33	824.73
Ion remainder	98.35	0.106	0.587	0.99	2.09	85.51

Table 5.2: Mean net and amplitude of $\mathbf{j} \cdot \mathbf{E}'$, variance, skewness, and kurtosis by region.

Region	**Data** (%)	$\langle \mathbf{j}_\perp \cdot \mathbf{E}'_\perp \rangle$	$\langle \lvert \mathbf{j}_\perp \cdot \mathbf{E}'_\perp \rvert \rangle$	**Var.**	**Skew.**	**Kur.**
Electron firehose	2.48	0.061	0.686	1.41	1.74	63.54
Electron whistler	0.56	0.171	0.805	2.39	6.09	196.67
Electron low–$\beta_{e,\parallel}$	0.14	−0.111	0.748	2.09	−1.56	47.19
Electron remainder	96.82	0.059	0.588	0.98	1.77	80.54
Ion firehose	0.54	0.088	0.671	1.55	2.70	46.15
Ion cyclotron/mirror	0.44	0.126	0.737	2.20	7.25	293.59
Ion low–$\beta_{i,\parallel}$	0.67	0.013	0.658	1.15	0.78	47.00
Ion remainder	98.35	0.059	0.590	0.99	1.77	80.04

Table 5.3: Mean net and amplitude of $\mathbf{j}_\perp \cdot \mathbf{E}'_\perp$, variance, skewness, and kurtosis by region.

Region	**Data (%)**	$\langle \mathbf{j}_\parallel \cdot \mathbf{E}'_\parallel \rangle$	$\langle \lvert \mathbf{j}_\parallel \cdot \mathbf{E}'_\parallel \rvert \rangle$	**Var.**	**Skew.**	**Kur.**
Electron firehose	2.48	0.186	0.751	3.13	4.78	111.98
Electron whistler	0.56	0.014	0.356	0.66	−1.94	71.39
Electron low–$\beta_{e,\parallel}$	0.14	0.029	0.657	4.20	22.22	951.35
Electron remainder	96.82	0.101	0.419	0.95	3.38	275.64
Ion firehose	0.54	0.105	0.510	1.87	2.96	168.96
Ion cyclotron/mirror	0.44	0.107	0.520	1.90	3.49	251.38
Ion low–$\beta_{i,\parallel}$	0.67	−0.070	0.542	2.35	1.66	1296.34
Ion remainder	98.35	0.103	0.425	0.99	3.98	246.07

Table 5.4: Mean net and amplitude of $j_\parallel E'_\parallel$, variance, skewness, and kurtosis by region.

conversion at small $\beta_{i,\parallel}$. The trends in energy conversion, which will be explored in the following paragraphs, are broadly similar between the electron and ion species.

The average amplitude of signals represents how much energy conversion is occurring regardless of direction, without positive and negative values cancelling each other out

(which can be understood by observing the small differences in probability density between positive and negative histogram bins of the same magnitude in Figure 5.5). The electron firehose region has the strongest $\langle|\mathbf{j}\cdot\mathbf{E}'|\rangle$ enhancement, with a 33.6% increase compared to the remainder of the data. The electron whistler region has the smallest increase at 23.6%, but this is still larger than the enhancement in any of the ion regions. The low–$\beta_{e,\parallel}$ region has a 29.5% increase, showing that more energy conversion is occurring on average in this region than in the remainder, albeit on average directed from bulk flow to electromagnetic energy.

Compared to the remainder, the ion instability regions have enhanced $\langle|\mathbf{j}\cdot\mathbf{E}'|\rangle$, by 16.4% (ion firehose) and 21% (ion cyclotron), indicating that smaller energy conversion signatures are present around ion instability thresholds than at equivalent electron boundaries. This implies that energy conversion fluctuations to and from the ion VDFs are on average weaker where kinetic microinstabilities are growing or acting compared to the electron case, possibly as a result of the ions being more nonthermal due to their lower thermal velocity. Similarly to its electron analogue, the low–$\beta_{i,\parallel}$ region has negative $\langle\mathbf{j}\cdot\mathbf{E}'\rangle$ and increased $\langle|\mathbf{j}\cdot\mathbf{E}'|\rangle$.

For electrons, MMS may not sample particle distributions fast enough to resolve all dynamics. This, in conjunction with clear net positive $\langle\mathbf{j}\cdot\mathbf{E}'\rangle$, suggests preferential observation of the driving of electron VDFs into unstable regions, rather than energy conversion related to the growth of waves themselves. In contrast, ion dynamics take place on longer timescales, potentially indicating why fluctuations can be observed more clearly, explaining why $\langle|\mathbf{j}\cdot\mathbf{E}'|\rangle$ is enhanced but $\langle\mathbf{j}\cdot\mathbf{E}'\rangle$ is more sign-indefinite in unstable regions.

Wave propagation may bias these statistics against observing negative $\mathbf{j}\cdot\mathbf{E}'$ in the electrons, as Svenningsson et al. (2022) found most electron whistler waves are observed away from their source region. Other instabilities may also generate waves which rapidly propagate away from their source region, although the non-propagating electron firehose mode is expected to dominate compared to the propagating mode (Cozzani et al., 2023). On the other hand, waves resulting directly from ion instabilities have been observed in the solar

wind (Gary et al., 2016; McManus et al., 2024). Additionally, due to Taylor's hypothesis (Taylor, 1938, see Section 3.5), which is verified to be true for the 60 of these intervals used in Chapter 4 (Stawarz et al., 2022), MMS generally observes spatial slices due to plasma advection rather than temporal slices due to evolution. To account for these effects, a simulation study into $\mathbf{j} \cdot \mathbf{E}'$ and kinetic microinstabilities would be valuable to track how the instability cycle is linked to turbulence as plasma evolves through the magnetosheath.

In addition, Table 5.2 contains the higher-order moments of the distribution (see Section 3.6. Studying the values in Table 5.2 reveals that the remainder of the ion and electron distributions both have variance just under 1, as these regions contain most of the data (which is normalised to the variance of each interval). All enhancement regions have larger variance, corresponding to a wider spread in values, because they preferentially contain some of the more intense signatures. The skewness in the remainder is smaller than all the enhancement regions, but still positive, meaning that the distribution is asymmetric around its mean, weighted towards positive (fields to flow) energy conversion signals. This suggests that there are other types of energy conversion/dissipation processes acting in the magnetosheath which are not directly linked to the anisotropy–driven instabilities.

The regions associated with instabilities have enhanced skewness, corresponding to an even greater weighting towards large positive $\mathbf{j} \cdot \mathbf{E}'$ values. In contrast, the low-$\beta_{\parallel}$ regions have negative skewness, indicating a weighting towards values smaller than the mean. In both cases, the means are negative, so this shows that there are more large negative energy conversion signals in these regions – more so in the low-$\beta_{e,\parallel}$ region than the low-$\beta_{i,\parallel}$ one. Kurtosis is very high in all cases, corresponding to heavy tails compared to a normal distribution. The high kurtosis of the electron whistler, ion cyclotron/mirror, and especially both low-$\beta_{\parallel}$ regions indicates that large current signals are enhanced in these regions, giving rise to enhanced $\langle|\mathbf{j} \cdot \mathbf{E}'|\rangle$ compared to the remainder. Interestingly, the electron firehose and ion firehose regions have reduced kurtosis compared to the remainder (although larger), suggesting instead that their respective increases in $\langle|\mathbf{j} \cdot \mathbf{E}'|\rangle$ arise due to an overall shifting of the distribution towards more net-positive $\langle\mathbf{j} \cdot \mathbf{E}'\rangle$.

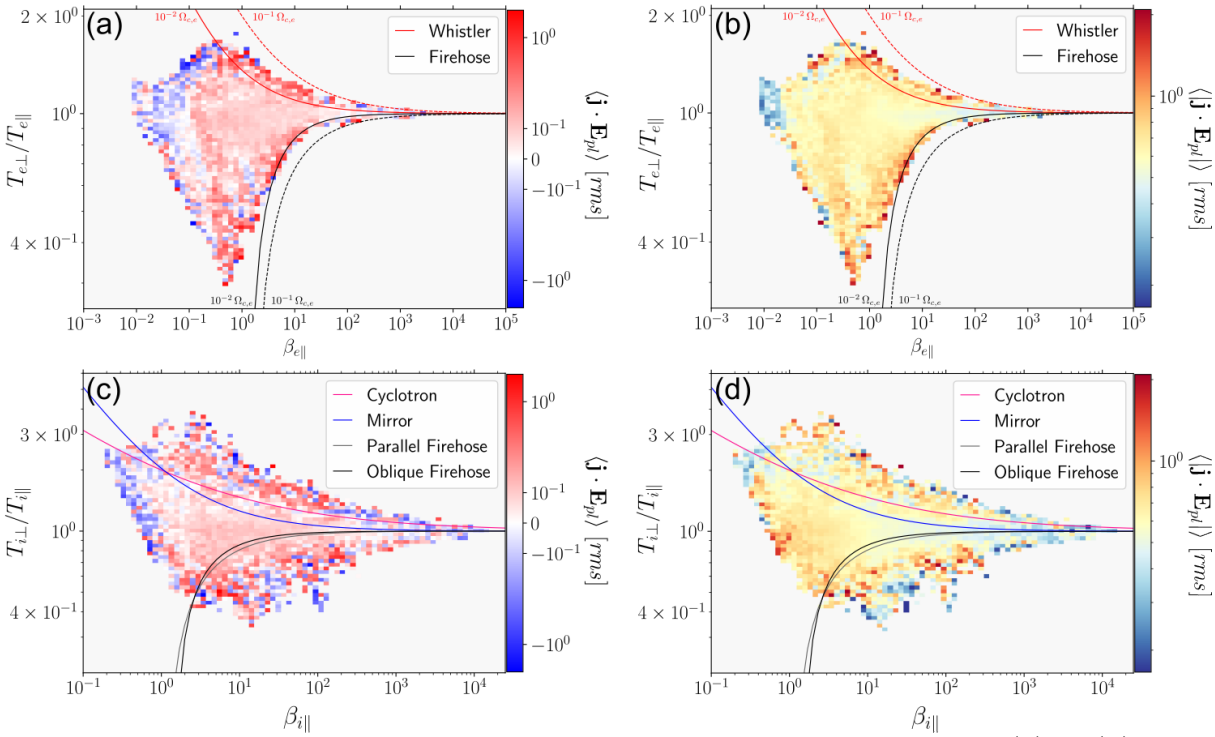


Figure 5.7: Distribution of $\mathbf{j}\cdot\mathbf{E}_{pl}$ on the anisotropy–beta plane. Panels (a) & (b) show the distribution of average net and average absolute value with respect to the electron instability thresholds. Likewise, (c) & (d) show the distribution of those variables with respect to the ion instability thresholds. Only bins containing at least 5 points, or from at least 2 intervals, are shown. The instability thresholds are the same as those in prior figures, defined in Table 2.2.

5.4.2 Alternate Energy Conversion Signatures

This chapter focuses on $\mathbf{j}\cdot\mathbf{E}'$ (as well as $\mathbf{j}_\perp\cdot\mathbf{E}'_\perp$ and $j_\parallel E'_\parallel$) as the representation of energy conversion between the electromagnetic fields and particle energy, because it is closely associated with dissipation. This term is the non-ideal (i.e., arising from beyond-MHD effects only) component of the total $\mathbf{j}\cdot\mathbf{E}$, so $\mathbf{j}\cdot\mathbf{E}'$ is the energy conversion due to the electric field in the frame moving with the electron bulk flow. Analogously, one can investigate energy conversion in the frame moving with the background plasma flow, $\mathbf{j}\cdot\mathbf{E}_{pl} = \mathbf{j}\cdot(\mathbf{E}+\mathbf{u}_0\times\mathbf{B})$. This component corresponds to the total energy conversion except that from the motion of the background flow.

Figure 5.7 shows how $\mathbf{j}\cdot\mathbf{E}_{pl}$ (normalised into rms units by dividing by the mean-removed interval rms) is distributed on the anisotropy–beta plane, for direct comparison with $\mathbf{j}\cdot\mathbf{E}'$ in Figure 5.3. Figures 5.7 (a)–(d) show how trends in $\mathbf{j}\cdot\mathbf{E}_{pl}$ are strongly reminiscent of those

in $\mathbf{j} \cdot \mathbf{E}'$. There is an enhancement in the average magnitude of energy conversion along the instability thresholds, although less marked than for the non-ideal energy conversion. The majority of bins, especially in the high-probability density center of the distribution, exhibit positive energy conversion signals. Along the low–$\beta_{\parallel,e}$ and low–$\beta_{\parallel,i}$ edges, there is a slight enhancement in the average magnitude in some bins, but a tendency for negative average signed values, indicating that the conversion of energy is into the fields in this region of parameter space. In all, this figure demonstrates that energy conversion measures other than $\mathbf{j} \cdot \mathbf{E}'$ produce qualitatively similar results to those discussed in Section 5.3.1, giving confidence to the results described within that chapter, and solidifying the choice to focus on the non-ideal energy conversion due to its close links to dissipation. An implication of $\mathbf{j} \cdot \mathbf{E}'$ and $\mathbf{j} \cdot \mathbf{E}_{pl}$ having similar distribution across parameter space is that the non-ideal part is providing the main part of the energy conversion, dominating the structure with respect to instability growth rate thresholds.

One process which may be playing a key role in the local distortion of VDFs and excitation of kinetic microinstabilities is turbulence-driven magnetic reconnection, which has recently been attracting significant attention in the magnetosheath. Prior studies have demonstrated that turbulence-driven reconnection events are actively occurring throughout the magnetosheath (e.g. Retinò et al., 2007; Sundkvist et al., 2007; Phan et al., 2018; S. Wang et al., 2019; I. Gingell et al., 2019), including within some of the intervals used in this study (Stawarz et al., 2022). Collisionless magnetic reconnection is well known to generate VDF anisotropy in the outflows and along the separatrices (Egedal et al., 2013), which potentially contributes to driving the distribution in the magnetosheath towards the instability boundaries. In fact, observations of magnetic reconnection in other contexts have clearly demonstrated the generation of firehose fluctuations through this mechanism (Cozzani et al., 2023).

An example of $\mathbf{j} \cdot \mathbf{E}'$ associated with magnetic reconnection in the electron firehose instability enhancement region is shown in Figure 5.8. Structures were automatically identified from all regions which had $|\mathbf{j} \cdot \mathbf{E}'| > 5$ rms within an enhancement region. This thresh-

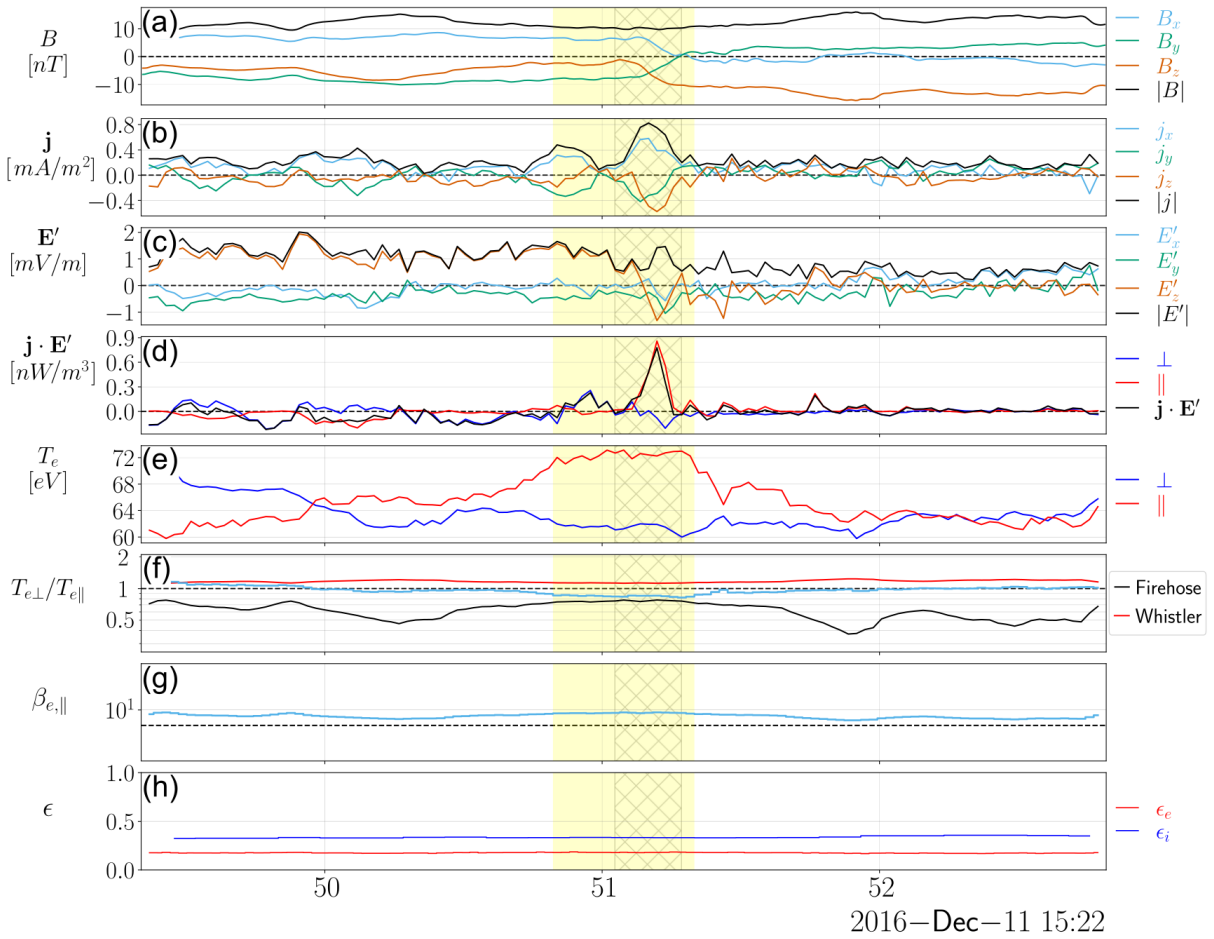


Figure 5.8: Time series of a large-$\mathbf{j}\cdot\mathbf{E}'$ structure during electron firehose instability conditions associated with electron-only magnetic reconnection. The event occurs at around 2016-12-11/15:22:51 in the magnetosheath. Panels show: (a) magnetic field; (b) current density; (c) non-ideal electric field; (d) $\mathbf{j}\cdot\mathbf{E}'$ and components, where $\perp$ represents $\mathbf{j}_\perp\cdot\mathbf{E}'_\perp$ and $\parallel$ represents $j_\parallel E'_\parallel$; (e) perpendicular and parallel electron temperature; (f) electron temperature anisotropy, where the firehose and whistler lines correspond to the instability margins at the instantaneous $\beta_{e,\parallel}$; (g) electron parallel beta; (h) electron and ion non-bi-Maxwellianity (see Section 2.3.4 and Chapter 6). The yellow shaded region denotes where the plasma is within the electron firehose enhancement region. The hatched horizontal span is an electron-only magnetic reconnection event as identified by Stawarz et al. (2022).

old is significantly larger than the majority of energy conversion, but has been chosen to isolate clearly identifiable peaks. In Figure 5.8, an electron-only magnetic reconnection event occurs at a $\mathbf{B}$ rotation, leading to increases in $\mathbf{j}$ and $\mathbf{E}'$ which generate a large positive $j_\parallel E'_\parallel$. This event occurs while the temperature anisotropy is depressed such that the plasma is unstable to the electron firehose instability, as a result of a significant increase in the parallel component of the electron temperature. The nature of this event may

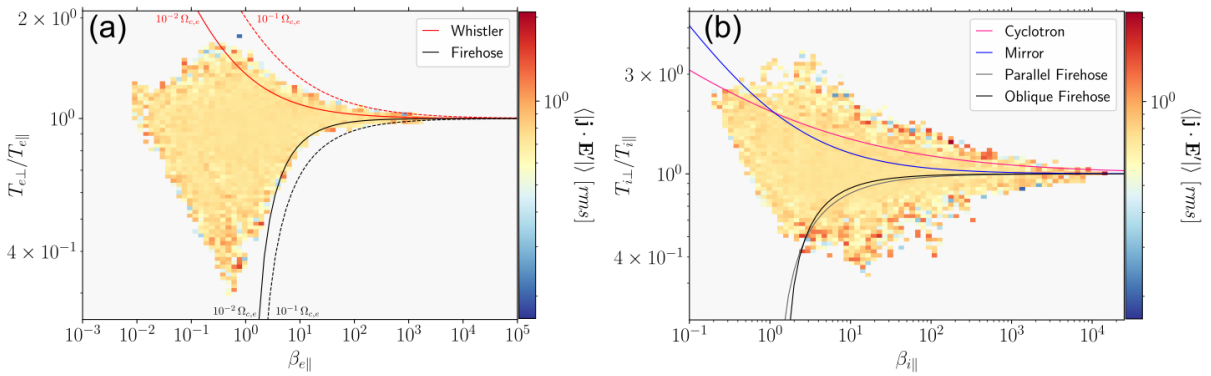


Figure 5.9: Average magnitude of phase-scrambled $\mathbf{j} \cdot \mathbf{E}'$ on the anisotropy–beta plane. Instability thresholds and colour axis limits are the same as Figure 5.3 panels (b) and (d). Bins without 5 points, or containing points from only 1 interval, are removed from the distributions.

suggest that the magnetic reconnection has generated a large anisotropy due to a parallel conversion of energy from the fields to the particles, which drives the distribution toward the firehose unstable region.

Other examples of processes which can modify the internal energy are the divergence of the vector heat flux density (Du et al., 2020), and dissipation associated with an increase in entropy due to collisions (Liang et al., 2019; Liang et al., 2020; Argall et al., 2022; Barbhuiya et al., 2024). Even in weakly collisional plasmas, non-Maxwellian features in the VDF are subject to intraspecies collisions as a result of the dissipation of strong velocity-space gradients (e.g. Schekochihin et al., 2009; Pezzi et al., 2021a). Such entropy studies may provide a novel way of assessing the scattering of particles in the distribution function associated with the instabilities. Further studies may utilise future spacecraft missions or simulations to expand on the results presented here and investigate the links between energy conversion measures in the context of local turbulence-driven distortions to the VDFs which may be giving rise to kinetic microinstabilities. Chapter 6 will further explore underlying structures – both physical and velocity-space – which contribute to energy conversion in the magnetosheath.

5.4.3 Validating trends on the Anisotropy–Beta Plane

To confirm that the trends in $\mathbf{j} \cdot \mathbf{E}'$ are real, rather than arising due to random phase-alignments between $\mathbf{j}$ and $\mathbf{E}'$, a phase-scrambling technique was employed as described in Section 3.3.2. It is not possible to randomise the phase of vector $\mathbf{j}$ and $\mathbf{E}'$ while constraining the result to have the same magnitude at each time step. Instead, each vector component has its phase randomised in Fourier space before converting back into a vector time series and taking the dot product.

Figure 5.9 shows the average magnitude of phase-scrambled $\mathbf{j} \cdot \mathbf{E}'$ on the (a) electron and (b) ion anisotropy–beta planes. In both panels, the distribution is approximately uniform across the central regions of parameter space. In areas with fewer points per bin, some variability arises, although this is not severe enough to call into question the trends observed in Figure 5.3. Indeed, it is to be expected that some outlying values will appear in low-occupancy bins because the mean will be less well-defined. This is important to bear in mind when interpreting the distribution of a variable on the anisotropy–beta plane.

Confidence in interpretations of anisotropy–beta distributions can be improved by altering the bin sizes. In this case, 80×80 bins are used for the figures presented in this chapter. However, the trends are still qualitatively similar when using as low as 40×40 bins, and reminiscent when using higher numbers (although with more variability due to increased numbers of low-count bins). In Section 5.3.3, all bins in each area where $\langle|\mathbf{j} \cdot \mathbf{E}'|\rangle$ is qualitatively enhanced are combined. This serves to reduce visual bias from low-count bins, producing the PDFs in Figure 5.5. Overall, distributions on the anisotropy–beta plane should be interpreted with care, making sure to validate qualitative trends and minimise the impact of any visual bias. When done so, this gives confidence to results involving distributions on this plane.

At high betas, even a minuscule anisotropy will be strong enough to destabilise the relatively weak magnetic fields. This situation arises in astrophysical plasmas, but even in the

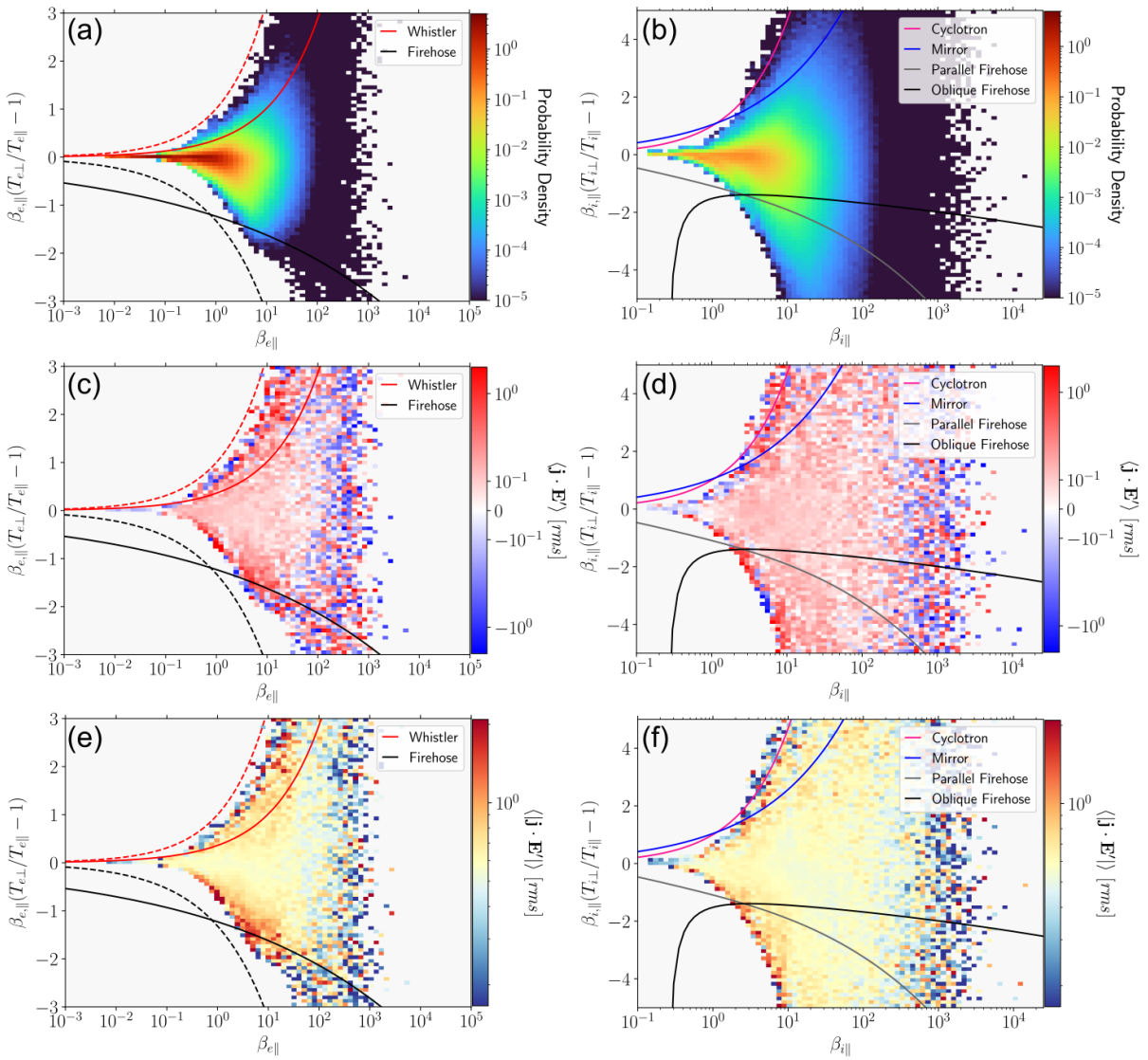


Figure 5.10: $\mathbf{j} \cdot \mathbf{E}'$ distributed on the $\beta_\parallel(T_\perp/T_\parallel - 1)$–$\beta_\parallel$ plane, to better resolve the high-$\beta_\parallel$ funnel. The left and right columns show the electron and ion columns respectively. Panels (a) & (b) show probability density. Panels (c) & (d) show the average signed non-ideal energy conversion via $\mathbf{j} \cdot \mathbf{E}'$. Panels (e) & (f) show average magnitude of $\mathbf{j} \cdot \mathbf{E}'$. The instability thresholds are those introduced previously, translated into the new y-axis. The histograms represent an 80x80 grid of bins.

magnetosheath the anisotropy–beta plots are sensitive to uncertainty in the temperature anisotropy at large beta (Cozzani et al., 2023). At high $\beta_\parallel$, the instability thresholds show that an instability will grow rapidly for small deviations from isotropy. As such, small uncertainties can lead to the conditions being incorrectly classified as unstable to $T_\perp > T_\parallel$ or $T_\parallel > T_\perp$ instabilities. In the first instance, it sufficient to simply bear this fact in mind when drawing conclusions about the high–$\beta_\parallel$ funnel in parameter space. Beyond that, the y-axis can be remapped to $\beta_\parallel(T_\perp/T_\parallel - 1)$ (as explored in e.g. Kunz et al., 2018;

Gorman and Klein, 2024), inverting the problem area and allowing us to probe higher $\beta_\parallel$ with less sensitivity to temperature anisotropy uncertainty.

Figure 5.10 shows probability density, $\langle \mathbf{j} \cdot \mathbf{E}' \rangle$, and $\langle |\mathbf{j} \cdot \mathbf{E}'| \rangle$, on the $\beta_\parallel(T_\perp/T_\parallel - 1)$–$\beta_\parallel$ plane. Given that the parametric thresholds for instability growth rates are defined for $\beta_\parallel \sim 1$ (Gary and J. Wang, 1996; Gary and Nishimura, 2003; Maruca et al., 2012), it is unsurprising that these thresholds diverge in regions of extreme $\beta_\parallel$ when remapped onto the new y-axis. Ignoring the thresholds themselves, the trends are robust – qualitatively reminiscent of the other plane – with enhancements in average energy conversion along the fringes of the distribution associated with kinetic microinstabilities. Beyond $\beta_\parallel \gtrsim 10^2$, bin occupancy is too low to draw reliable trends. For small $\beta_\parallel$, the bins contain many points over a very small range of $\beta_\parallel(T_\perp/T_\parallel - 1)$, so it is difficult to discern the low–$\beta_\parallel$ edge which was observed on the other plane. There appears to be a reduction in $\langle |\mathbf{j} \cdot \mathbf{E}'| \rangle$ and shift to slightly negative $\langle \mathbf{j} \cdot \mathbf{E}' \rangle$, which is consistent with the presence of a low–$\beta_\parallel$ reduction in average energy conversion.

5.5 Summary

This chapter presented a statistical investigation into non-ideal energy conversion associated with kinetic microinstabilities, revealing enhanced levels of $\mathbf{j} \cdot \mathbf{E}'$ close to temperature anisotropy–beta instability thresholds. In these regions, compared to the remainder of the distribution, energy conversion has increased amplitude and larger positive net value, indicating that the driving of VDFs into unstable configurations is observed more often than redistribution of free energy in the VDF via scattering of particles and the subsequent growth of wave modes. It is found that the greatest enhancement in $\langle \mathbf{j} \cdot \mathbf{E}' \rangle$ and $\langle |\mathbf{j} \cdot \mathbf{E}'| \rangle$ occurs in the region susceptible to the electron firehose instability. In contrast, the largest increase of average $\mathbf{j} \cdot \mathbf{E}'$ in ion parameter space occurs on the edge closest to the ion cyclotron instability threshold.

Breaking down $\mathbf{j} \cdot \mathbf{E}'$ into $\mathbf{j}_\perp \cdot \mathbf{E}'_\perp$ and $j_\parallel E'_\parallel$ reveals that the majority of non-ideal energy conversion comes from the perpendicular component, but that there is a significant

enhancement in parallel energy conversion observed near the electron firehose instability thresholds. $j_\parallel E'_\parallel$ is also found to be more positive on average than $\mathbf{j}_\perp \cdot \mathbf{E}'_\perp$, suggesting that there is less energy imparted into the fields coming from processes acting through parallel currents and electric fields. In contrast to the electrons, the ion firehose edge does not exhibit a significant enhancement in the average parallel energy conversion. In addition to different components of $\mathbf{j} \cdot \mathbf{E}'$, trends in $\langle \mathbf{j} \cdot \mathbf{E}' \rangle$ and $\langle |\mathbf{j} \cdot \mathbf{E}'| \rangle$ are qualitatively consistent with average values of $\mathbf{j} \cdot \mathbf{E}_{pl}$ across anisotropy–beta parameter space. Enhancements in the absolute value of energy conversion are most pronounced when using $\mathbf{j} \cdot \mathbf{E}'$, indicating a stronger link between fluctuations in the non-ideal component of energy conversion and kinetic microinstabilities compared to the background plasma-frame energy conversion.

In addition to the known effect of parallel beta constraining temperature anisotropy, which has been shown to be related to an enhancement in average energy conversion, an additional region of interest has been discovered which is present in both parameter spaces. There is increased negative energy conversion (with a smaller absolute value than the net of the reminder) along the low–$\beta_\parallel$ edge, at $T_{e,\perp}/T_{e,\parallel} < 1$ for the electrons and $T_{i,\perp}/T_{i,\parallel} \sim 1$ for the ions, highlighting these regions as areas where significant energy is being imparted into electromagnetic activity. The origin of this effect is not yet understood, but may be arising from a new instability process which becomes important at low parallel beta. As a starting point to understand this region of parameter space, the non-Maxwellianity is explored in Chapter 6.

Despite accounting for a small percentage of the overall observations, it has been shown that non-ideal energy conversion is enhanced when VDFs are configured such that they may lead to the growth of anisotropy-driven kinetic microinstabilities. Turbulent fluctuations are playing a key role in the link between the instabilities and thermodynamics, by driving fluctuations in temperature anisotropy and local parallel beta. It is suggested that, while the kinetic microinstabilities are not solely responsible for the large-scale energy budget of the magnetosheath, the instability growth—excitation—scattering cycle is playing an important active role in how turbulent fluctuations influence the plasma

thermodynamics.

Following the work presented in this chapter, it would be interesting to explore what role non-Maxwellian VDFs are playing in the observed energy conversion statistics. Magnetosheath VDFs are typically found to exhibit a flat-top distribution, (e.g. Formisano et al., 1973), which, by their non-bi-Maxwellian nature, contribute to extra sources of free energy in the VDF which are not accounted for by the anisotropy–beta instability thresholds (Klein et al., 2018; Klein et al., 2019b). Magnetosheath VDFs frequently exist as flat-top distributions with energetic tails (e.g. Formisano et al., 1973), which are related to processing of the solar wind by Earth's bow shock. However, turbulent fluctuations may be playing a role in accelerating non-thermal particles via the turbulent dissipation mechanism (e.g. Wan et al., 2012; Karimabadi et al., 2014; Chasapis et al., 2015; Matthaeus et al., 2015; Chasapis et al., 2017; Yordanova et al., 2021; Bandyopadhyay et al., 2021), contributing to local enhancements in non-Maxwellianity such as energetic tails. Some work has been done to uncover how non-Maxwellianity is organised with respect to the anisotropy-driven kinetic microinstabilities (such as Graham et al., 2021; Walters et al., 2023), but it is not known how energy conversion related to the turbulent fluctuations interplays with dynamic VDF structure in the magnetosheath.

Chapter 6 links trends in the non-Maxwellianity to energy conversion, contextualising the results of this chapter in terms of underlying physical and velocity-space structures which give rise to these statistics, as well as the relationship between the turbulent energy conversion fluctuations and signatures of non-Maxwellian VDFs.

Chapter 6

Characterising Non-Maxwellianity of VDFs in Earth's Magnetosheath

6.1 Introduction

Having undergone processing by the bow shock, the magnetosheath consists of decelerated, heated, and compressed solar wind plasma, subject to dynamically-new turbulence in addition to shocked solar wind fluctuations (Huang et al., 2017; Sahraoui et al., 2020; Rakhmanova et al., 2021, see also Section 2.2.3). Plasma in the magnetosheath is collisionless, as its collisional mean free path of $\sim 10^5\,\mathrm{R_E}$ is several orders of magnitude greater than the system size of $\sim 10\,\mathrm{R_E}$ (Stawarz and Genestreti, 2023). As such, VDFs can exist in a state far from thermal equilibrium, deviating significantly from Maxwellian distributions (Shuster et al., 2019; Perri et al., 2020; Graham et al., 2021).

Pristine solar wind electron distributions typically consist of an anisotropic Maxwellian core at low energies (which can be represented by a bi-Maxwellian distribution), with a power-law distribution at higher energies. Together, these can be approximated by kappa distributions (e.g. Livadiotis et al., 2018; Verscharen et al., 2019). Processing by the bow shock reforms electron VDFs into flat-top distributions (Montgomery et al., 1970;

Feldman et al., 1983). Recent work suggests that the formation of flat-top electron distributions is the result of stochastic processes which happen due to electron demagnetisation and adiabatic behaviour within electric field structures created by the shock (Stasiewicz, 2023). Proton distributions in the magnetosheath are also significantly disturbed from their upstream core and beam structure, exhibiting non-Maxwellian high-energy tails (e.g. Formisano et al., 1973; Schwartz et al., 2022). Non-Maxwellianity in proton VDFs downstream of the bow shock represents a significant source of free energy in velocity space imparted onto the protons, as temperature anisotropy (e.g. Greco et al., 2012; Maruca et al., 2018) and additional non-Maxwellian features (Perri et al., 2020).

Non-Maxwellian VDFs are subject to various wave–particle and wave–wave interactions which act to redistribute free energy via kinetic instabilities (e.g. Gary, 1993; Treumann and Baumjohann, 1997; Verscharen et al., 2019; Verscharen et al., 2022, see also Section 2.4). As established in Chapter 5, temperature anisotropy-driven kinetic microinstabilities constrain $T_{s,\perp}/T_{s,\parallel}$ based on $\beta_{s,\parallel}$ in the magnetosheath (see also e.g. Gary et al., 2005; Maruca et al., 2018; Graham et al., 2021). However, since magnetosheath VDFs are rarely perfect bi-Maxwellians, it is not clear how additional sources of free energy in the VDF impact the action of anisotropy–driven instabilities. As introduced in Section 2.3.4, ϵ and $\sqrt{Q}$ are two dimensionless parameters which can be used to assess whether VDFs have additional sources of free energy beyond those captured by temperature anisotropy-driven instability threshold curves used in Chapter 5.

In this chapter, signatures of non-Maxwellianity in magnetosheath VDFs are explored, with the aim of characterising typical behaviour and explaining observed variability and its possible links to energy conversion observed in Chapter 5. It has been shown that turbulence has an important role in imparting energy into the particles so that anisotropy-driven kinetic microinstabilities may grow wave modes and isotropise the distributions, however the impact of additional sources of free energy (beyond anisotropy) in velocity space is unknown. The results of this chapter feed into the important question of how turbulence links into the thermodynamic regulation of the magnetosheath, with appli-

cations to collisionless dissipation and the role of reversible kinetic processes in energy redeposition.

6.2 Methods

The Fast Plasma Investigation (FPI) instrument suite (Pollock et al., 2016, see Section 3.1.3) on board MMS is capable of measuring electron and ion VDFs fast enough to capture sub-ion scale structures, with instrument cadences of 0.03 s (electrons) and 0.15 s (ions), respectively. By providing full particle distributions in addition to velocity moments calculated thereof, MMS facilitates in-depth studies of velocity space characteristics and non-Maxwellian features present in magnetosheath VDFs. These VDFs and their moments, as well as high-resolution **B** and **E** measurements, can be used to explore the physical structures giving rise to energy conversion in unstable regions of anisotropy–beta parameter space. This study uses the same data set as in Chapter 5, which is described in detail in Section 5.2.1 and provided in Appendix B.1.

Computing ϵ involves taking the velocity space integral of the absolute difference between a measured distribution, f_s, and a model distribution, g_s, based on the same moments as the measured distribution. MMS VDFs are used for f_s, then the numerical particle moments from integrating f_s (provided by the MMS team) are used to produce a model distribution. For each energy channel, energy values are corrected for the spacecraft potential and then converted to velocities via

$$v = \sqrt{\frac{2e(\mathcal{E} + q_s V_{SC})}{m_s}}, \tag{6.1}$$

where $\mathcal{E}$ is the energy in eV and V_{SC} is the spacecraft potential in volts. Photoelectron effects often contaminate the first 4 electron energy channels, so bins with $\mathcal{E} < 28\ eV$ are removed when calculating ϵ_e (see Section 3.2.4; Graham et al., 2021). To avoid unphysical contributions to ϵ from low/zero count bins at large energies or small densities, energy channels in g_s are masked out based on where $f_s(\mathbf{v}) = 0$. Once the parameter has been

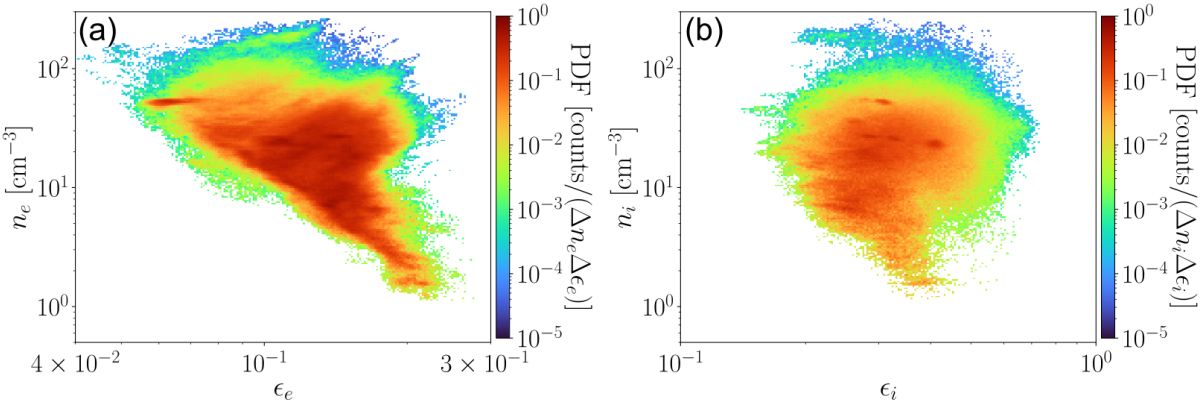


Figure 6.1: Probability density histogram of n against ϵ in log space for (a) the electrons and (b) the ions. Isolated concentrations of probability density come from quasi-perpendicular intervals where the number density undergoes only small fluctuations.

calculated for each time step, short data gaps are filled using linear interpolation.

Graham et al. (2021) find that ϵ_e is inversely proportional to n_e, attributing this feature firstly to distinct hot and cold populations found in the magnetospheric measurements (their study uses all burst data from the first MMS dayside campaign, rather than only magnetosheath data from multiple campaigns as in this study), and secondly to decreased particle counts causing larger statistical uncertainty. The first effect is physical, but unlikely to affect this study because the magnetosheath has only a single temperature component. The second effect is instrumental, and is likely to be present in this investigation. As illustrated in Figure 6.1 (a), there is an inverse relationship between n_e and ϵ_e, at least for some of this data, as reported for magnetopause observations by Graham et al. (2021). Despite a large spread in the distribution, it is clear that many of the largest values of ϵ occur at very low density. This must be borne in mind during interpretation of the non-Maxwellianity results in the following sections. In Figure 6.1 (b), it is less clear whether n_i is inversely proportional to ϵ_i, as many large values of ϵ_i occur at $n_i \gg 0$.

Finally, in addition to the overall value of non-Maxwellianity, in the following sections it is helpful to investigate fluctuations of a quantity $\mathcal{Q}$ with respect to its interval mean, defined as $\delta\mathcal{Q} = \mathcal{Q} - \langle\mathcal{Q}\rangle_{interval}$, to isolate fluctuations from variable backgrounds. This definition is used for fluctuations in the density, agyrotropy, and energy conversion, but in the case of non-Maxwellianity the fluctuation is additionally normalised to the interval

mean itself,

$$\delta\epsilon_s = \frac{\epsilon_s - \langle\epsilon_s\rangle_{interval}}{\langle\epsilon_s\rangle_{interval}}. \tag{6.2}$$

This is necessary to account for the scale of fluctuations relative to the background, which varies from interval to interval as well as the level of the background.

6.3 Characterising Background Non-Maxwellianity

The non-Maxwellianity parameter is always nonzero within this data set, with ϵ_e ranging from 0.041–0.28 and ϵ_i from 0.14–0.72. In this dataset, ϵ_e is generally lower than ϵ_i, the latter having a greater range and larger fluctuations around the background compared to the former. The rms fluctuation in ϵ_e ranges from 0.0028–0.026, whereas the rms fluctuation in ϵ_i ranges from 0.0080–0.10, illustrating that there is significantly more variability in the ions than the electrons. The ϵ parameter is sensitive to several aspects of the VDF, such as beams, energetic tails, agyrotropy, and granularity in low-count bins in velocity space. In this section, the properties of mean-averaged VDFs for a selection of magnetosheath intervals are studied in order to characterise which features give rise to background non-Maxwellianity. This background non-Maxwellianity feeds into the thermodynamics of the system, representing a potential source of free energy beyond that which can give rise to anisotropy-driven instabilities.

To visualise the structure of non-Maxwellian VDFs, 2D slices are taken using a 20° elevation limit with respect to reference directions in velocity space. The chosen directions form a right-handed coordinate system, pointing along $\mathbf{v} \times \mathbf{B}$, $\mathbf{B} \times \mathbf{v} \times \mathbf{B}$ (i.e. along the component of the velocity perpendicular to the local magnetic field), and $\mathbf{B}$. Here, $\mathbf{v}$ is the species bulk velocity. In the calculation of ϵ, a drifting bi-Maxwellian is used, so to emulate this the projected VDF is converted to a cartesian grid and then shifted into a frame moving with the species bulk velocity. Finally, the shifted cartesian grid is interpolated onto the original spherical grid representing the velocity space cells sampled by MMS instrumentation, leading to some smearing of bins where the shifted VDF bins overlap multiple MMS bins. This is particularly apparent at the center of the distribution,

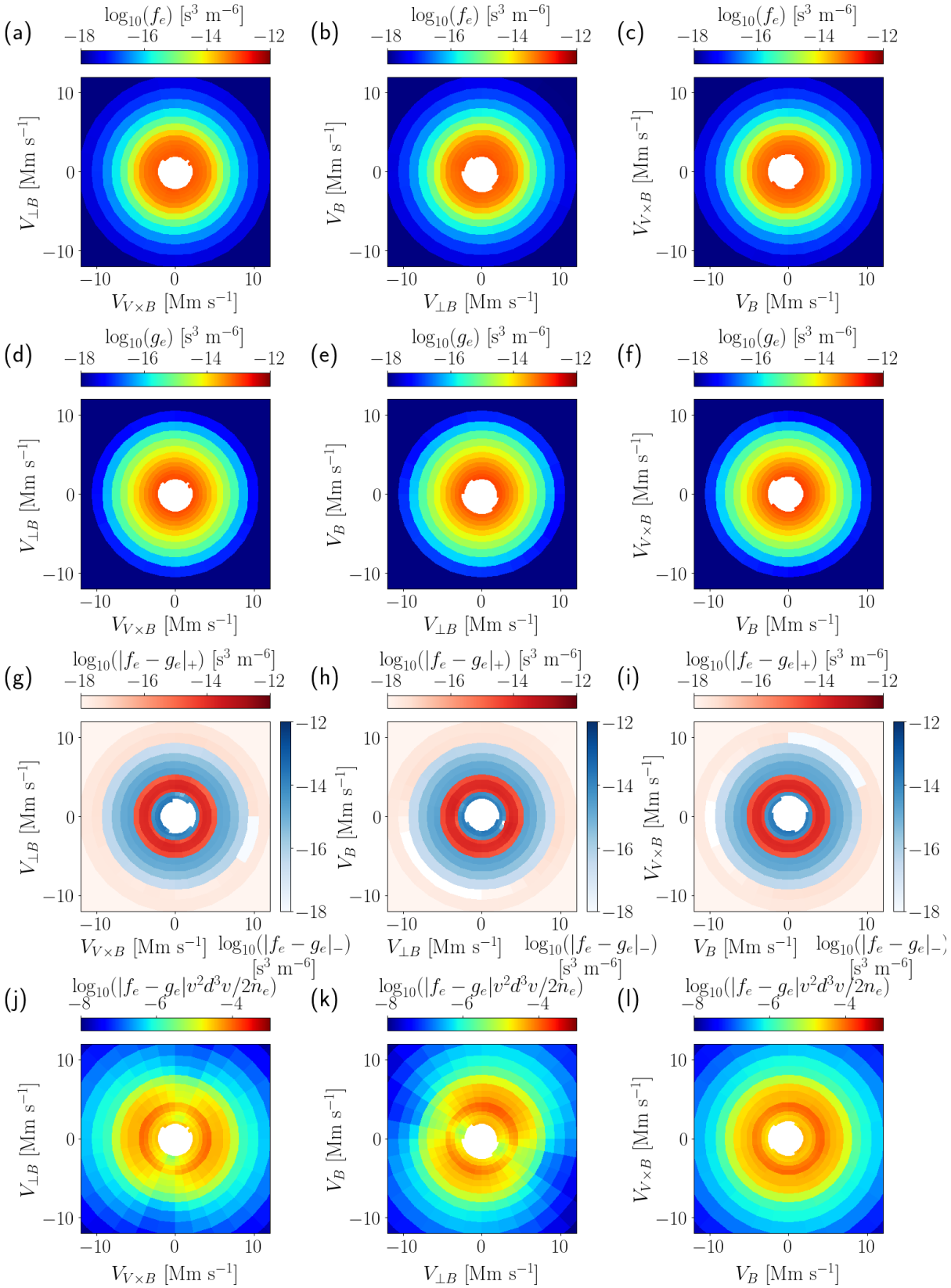


Figure 6.2: Slices through the background electron VDF for 2017-11-13/19:30:44–19:38:42. Colour axes show: (a)–(c) measured phase space density; (d)–(f) model bi-Maxwellian phase space density g_e based on the moments of f_e; (g)–(i) signed difference between $f_e - g_e$, where red denotes super-Maxwellian ($f_e > g_e$) and blue denotes sub-Maxwellian $f_e < g_e$; (j)–(l) the non-Maxwellianity integrand, representing the velocity space volume integrated absolute difference between f_e and g_e.

where the spherical gap in phase space relating to masked-off bins removed due to spacecraft potential contamination is stretched along the bulk velocity direction. To compute the background VDF for a given interval, slices are taken of each VDF time step. The mean of those slices is what is plotted in the following Figures. In intervals where energy stepping (see Section 3.1.3) is still taking place, the same process is used but alternate time steps are interleaved to produce 64 energy channels.

Figure 6.2 illustrates a typical background electron VDF taken from a quasi-parallel magnetosheath interval with qualitatively uniform fluctuations in ϵ_e around the background. The companion plot of background ion VDF in the same interval is displayed in Figure 6.3 (discussed later). Several intervals with steadily fluctuating non-Maxwellianity signatures were investigated in this process, with qualitatively similar results which will also be discussed later. In these figures, each row represents the three reference direction-aligned 2D slices through VDFs of different data products. The first row is the measured phase space density f_s; the second row is the the phase space density of the model bi-Maxwellian with the same moments as f_s and g_s; the third row is the absolute difference (plotted logarithmically) between f_s and g_s, using the red and blue colour scales to represent super- and sub-Maxwellian regions of measured phase space density, respectively; and the fourth row displays the integrand of the non-Maxwellianity parameter, which is the information conveyed in both colour axes of the third row weighted by the velocity space volume element of each bin.

Figure 6.2 panels (g)–(i) show that f_e is sub-Maxwellian in the core, super-Maxwellian on the shoulder of the core, then sub-Maxwellian again in the flanks, before finally having weakly super-Maxwellian tails (although this is weak with respect to the center of the distribution, not accounting for the drop in phase space density of both f_e and g_e at larger velocities). This shape is consistent with a flat-top distribution as a result of processing by the bow shock (Montgomery et al., 1970; Feldman et al., 1983). Panels (j)–(l) elucidate the structure giving rise to ϵ_e, showing in panels (j) and (k) two hemispheres aligned obliquely to the mean field direction. In other intervals, this two-lobe shape is

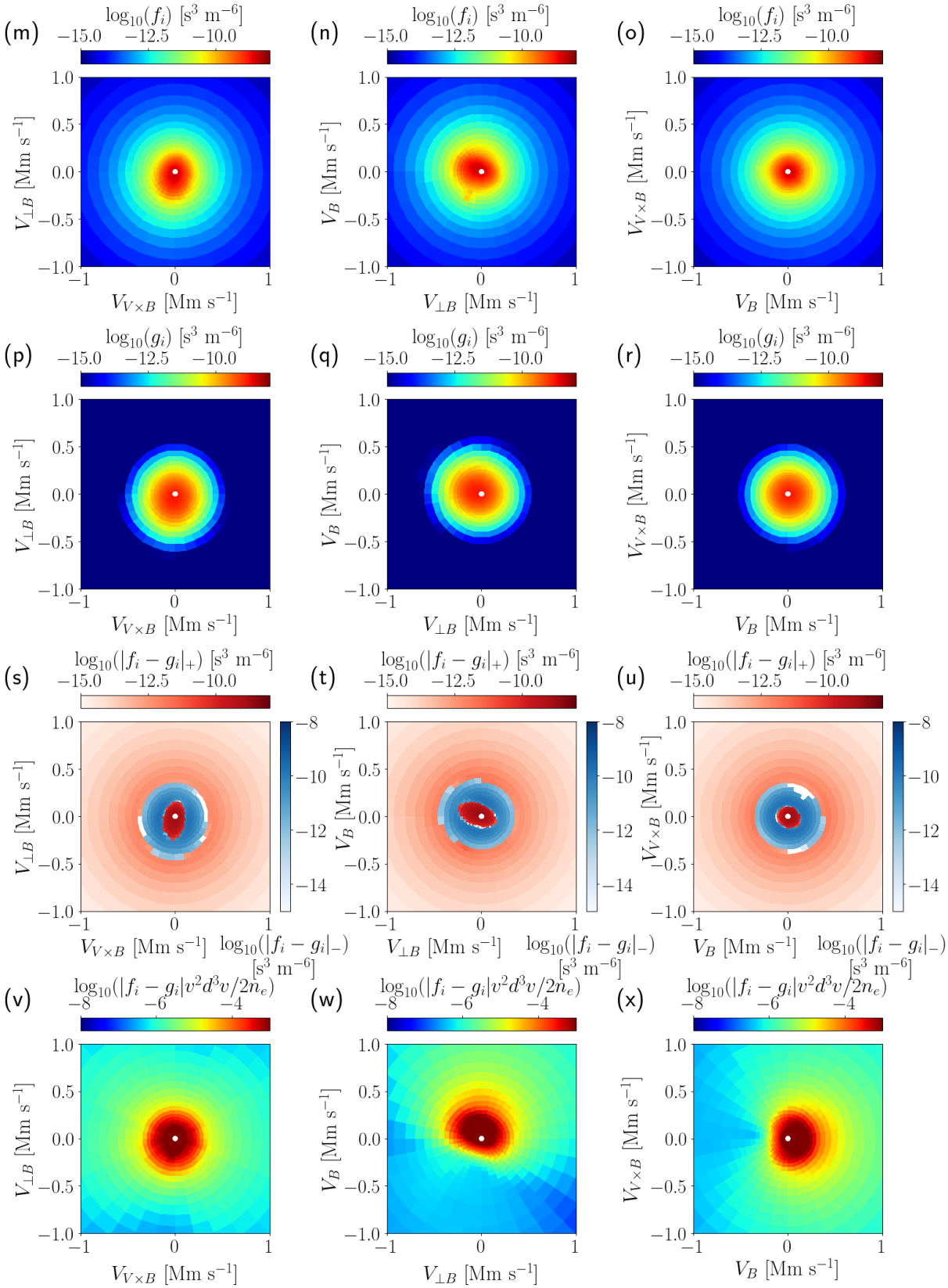


Figure 6.3: Following on from Figure 6.2, slices through the background ion VDF for 2017-11-13/19:30:44–19:38:42. Colour axes show: (m)–(o) measured phase space density; (p)–(r) model bi-Maxwellian phase space density g_i based on the moments of f_i; (s)–(u) signed difference between $f_i - g_i$, where red denotes super-Maxwellian ($f_i > g_i$) and blue denotes sub-Maxwellian $f_i < g_i$; (v)–(x) the non-Maxwellianity integrand, representing the velocity space volume integrated absolute difference between f_i and g_i.

also present, though not aligned along the same direction. The origin of this feature is unknown, but it is confirmed to not be due to the process of shifting the distribution into the zero bulk flow frame, which is corroborated by the fact that the electron bulk speed is very small compared to the velocity range measured by FPI.

Following on from the previous figure, Figure 6.3 shows the background ion VDF for the same interval. Firstly, it must be noted that the bulk speed $u_i = 300$ km s^{-1} is a considerable fraction (around 30%) of the axis limits, so the fine structure and general shape of the variables in the 2D slices is more likely to be modified by the process of shifting into the bulk flow frame. This is responsible for the small 'beam'-style structure visible in panel (n). Panels (s) to (u) show a super-Maxwellian core, with sub-Maxwellian flanks, and super-Maxwellian tails in line with expectations (e.g. Formisano et al., 1973; Schwartz et al., 2022). There is an elongation of the super-Maxwellian core in a direction almost perpendicular to the magnetic field, however this is not observed in all intervals that were checked, and for those in which it is present the direction is not consistent. Panels (v) to (x) represent the typical qualitative shape of the non-Maxwellianity integrand, where it appears to be one lobe with a phase space deficiency where a second lobe would be, offset from the distribution center. The direction of this feature varies throughout the intervals, so it is not clear what gives rise to it. Importantly, it is not the same direction as the center of the two-lobe electron non-Maxwellianity structure acknowledged in the previous paragraph.

Despite differences between the example interval and others that were investigated (not shown), qualitative features are consistent. To further exemplify the background properties of the VDF which are giving rise to non-Maxwellianity, the Pitch Angle Distribution (PAD) can be used. The PAD represents the VDF integrated around the background $\mathbf{B}$ field. In Figure 6.4 the PADs of the electrons and ions are given in directions $\theta = 0°$ (parallel), $\theta = 90°$ (perpendicular), and $\theta = 180°$ (antiparallel) to $\mathbf{B}$. Panels (a) to (c) show that the electron PAD resembles a flat-top distribution with sub-Maxwellian phase space density at the center, with an enhancement at lowest energies due to photoelectron

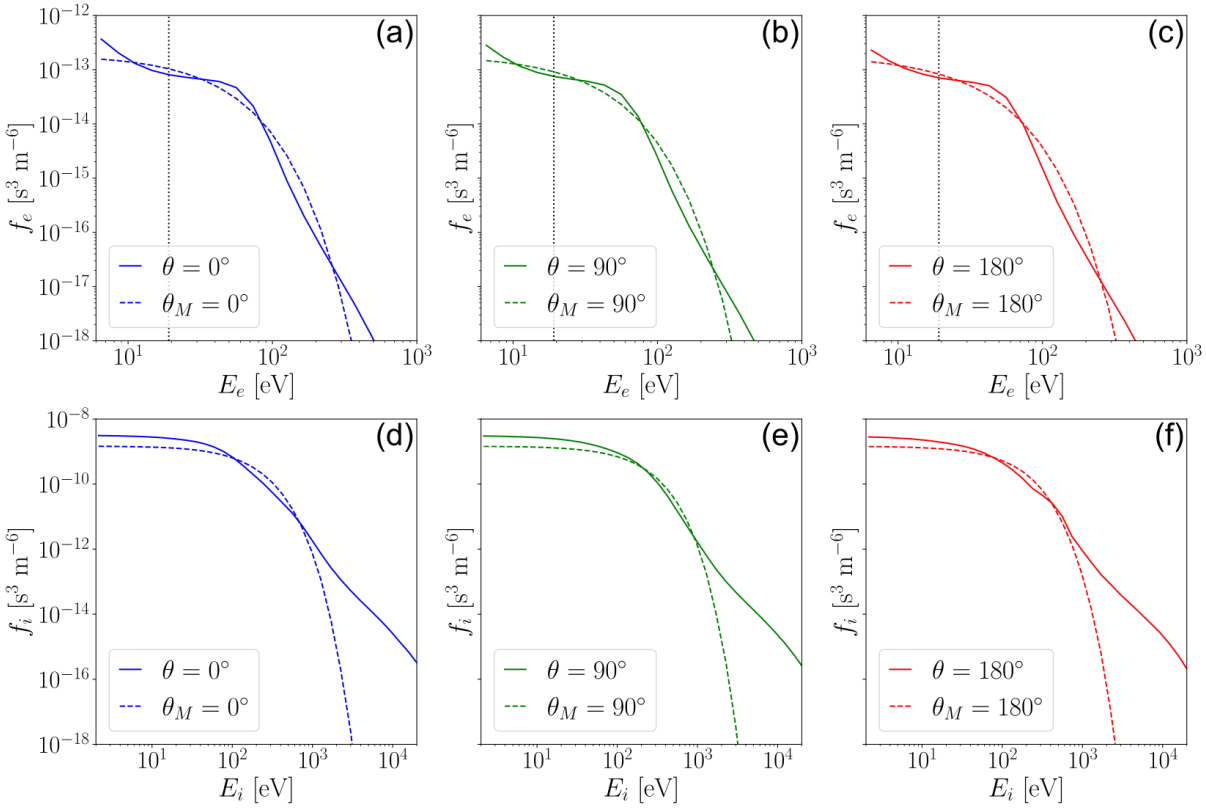


Figure 6.4: Observed and model Pitch Angle Distribution (PAD) for 2017-11-13/19:30:44–19:38:42, the same interval as shown in Figures 6.2 & 6.3. Panels (a)–(c) show the electron PAD at θ (observed) and θ_M (model) of 0°, 90°, and 180° with respect to the mean **B**. The dotted line shows the top of the fourth energy channel, below which bins don't contribute to ϵ_e. Panels (d)–(f) show the ion PAD at the same angles. Solid lines denote PAD of the observed distribution and dashed lines represent the PAD of the model bi-Maxwellian VDF with the same moments.

effects. This enhancement occurs below the bins which are cut off in the calculation of ϵ_e, so it is not being treated as a real non-Maxwellian feature. Panels (d) to (f) show that the ion distributions exhibit a super-Maxwellian center, sub-Maxwellian flanks, and enhanced energetic tails. This is interpreted as a flat-top distribution or a nearly bi-Maxwellian core (where the difference from bi-Maxwellian is an enhancement of phase space density). A small notch in panel (f) represents an additional anti-parallel beam-like feature present in the example interval.

The PADs in Figure 6.4 typify the properties of the background particle distributions, which, despite varying between intervals, have qualitatively similar shapes. A schematic view of this shape is presented in Figure 6.5 for idealised VDFs symmetric in all directions relative to the magnetic field. In panel (a), the proposed true shape of the electron PAD

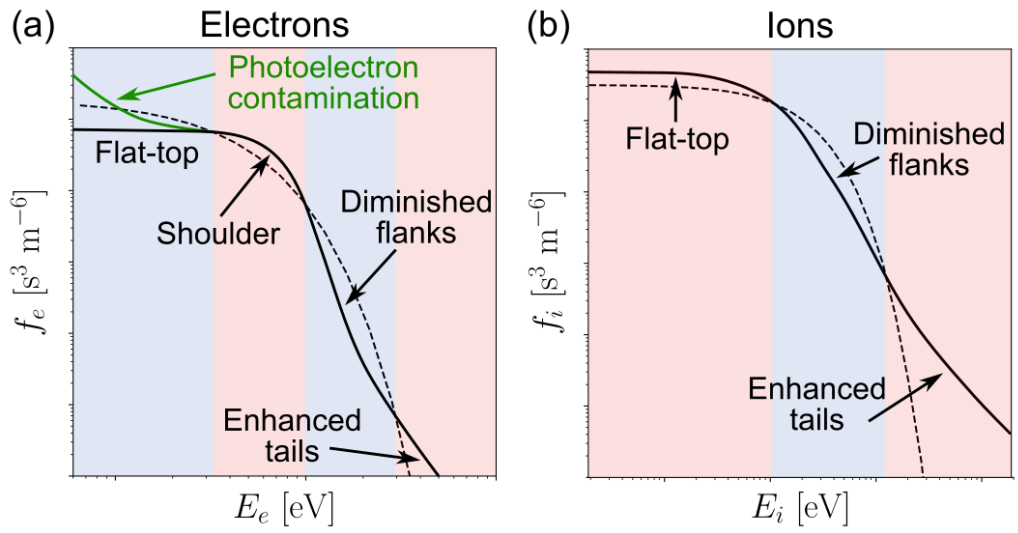


Figure 6.5: Schematic pitch angle distributions indicating the typical background behaviour of the background magnetosheath distributions. Red and blue shading represent super-Maxwellian and sub-Maxwellian phase space density, respectively. Photoelectron contamination is denoted in panel (a) in green.

is indicated as a flat-top, with photoelectrons artficially enhancing phase space density in the lowest energy channels. f_e is typically lower than f_i because the electrons fill a larger velocity range in phase space (as the energy to velocity conversion is dependent on particle mass), albeit at much lower phase space density.

The principal difference between different shapes of electron distributions is how pronounced the shoulder of the flat-top core is, with some intervals barely becoming super-Maxwellian in this region. When the shoulder is weaker, the flanks are also closer to the bi-Maxwellian, but the tails are still enhanced in all cases. The intervals with larger $\langle \epsilon_e \rangle$ tend to correspond to a shift to the right, so that differences between f_e and g_e occur at higher velocities. This trend is mirrored in the ions. Differences in the shape of the ion PAD generally manifest as changes to the level of enhancement in the core compared to the bi-Maxwellian, with some intervals becoming only slightly super-Maxwellian in this range.

6.4 Non-Maxwellianity in Anisotropy–Beta Space

6.4.1 Non-Maxwellianity

The impact of non-Maxwellian VDFs on the plasma thermodynamics via the action of kinetic instabilities is still poorly understood. Enhanced non-Maxwellianity represents additional sources of free energy with which instability mechanisms can be excited. In the previous section, it is established that neither the protons or electrons are perfect bi-Maxwellians in the magnetosheath, with variation in background levels between intervals as well as smaller-scale fluctuations around this background. Yet, observations in Chapter 5 (see Figure 5.1) confirm that growth rate thresholds for anisotropy-driven instabilities constrain accessible regions of anisotropy–beta parameter space – an effect which doesn't account for non-Maxwellianity. The thresholds are based on the assumption of bi-Maxwellian distributions with $T_{i,\perp}/T_{i,\parallel} = 0$ when $T_{e,\perp}/T_{e,\parallel} \neq 0$ (and vice versa), neither of which conditions are satisfied in this data set, so it is interesting to understand what role non-Maxwellianity may be playing in the dynamics.

Figure 6.6 shows the distribution of different non-Maxwellianity measures on the anisotropy–beta plane. In panel (a), a significant increase in $\delta\epsilon_e$ can be seen at low $\beta_{e,\parallel}$ for $T_{e,\perp}/T_{e,\parallel} < 1$, coinciding with an increase in ϵ_e in panel (b). The whistler region has $\delta\epsilon_e < 0$ on average, indicating fluctuations towards bi-Maxwellianity are occurring when the plasma is unstable to the whistler instability. In contrast, points around the firehose edge have a weakly positive $\delta\epsilon_e$. Panel (b) shows increasing average ϵ_e towards smaller-$\beta_{e,\parallel}$ bins, which may be related to n, as explored later. This relationship appears also to depend on $T_{e,\perp}/T_{e,\parallel}$, with larger $\langle\epsilon_e\rangle$ at a given $\beta_{e,\parallel}$ when anisotropy is further from 1. This feature may be related to how well the anisotropy moments are capturing the shape of the VDF, as at very high anisotropy one may expect there to be a higher likelihood of non-Maxwellian features being present. Due to a lack of points with $T_{e,\perp}/T_{e,\parallel} \gg 1$, it is not possible to confirm whether this trend is symmetric.

Panels (c) and (d) show the fluctuation and value of ϵ_i in anisotropy–beta parameter

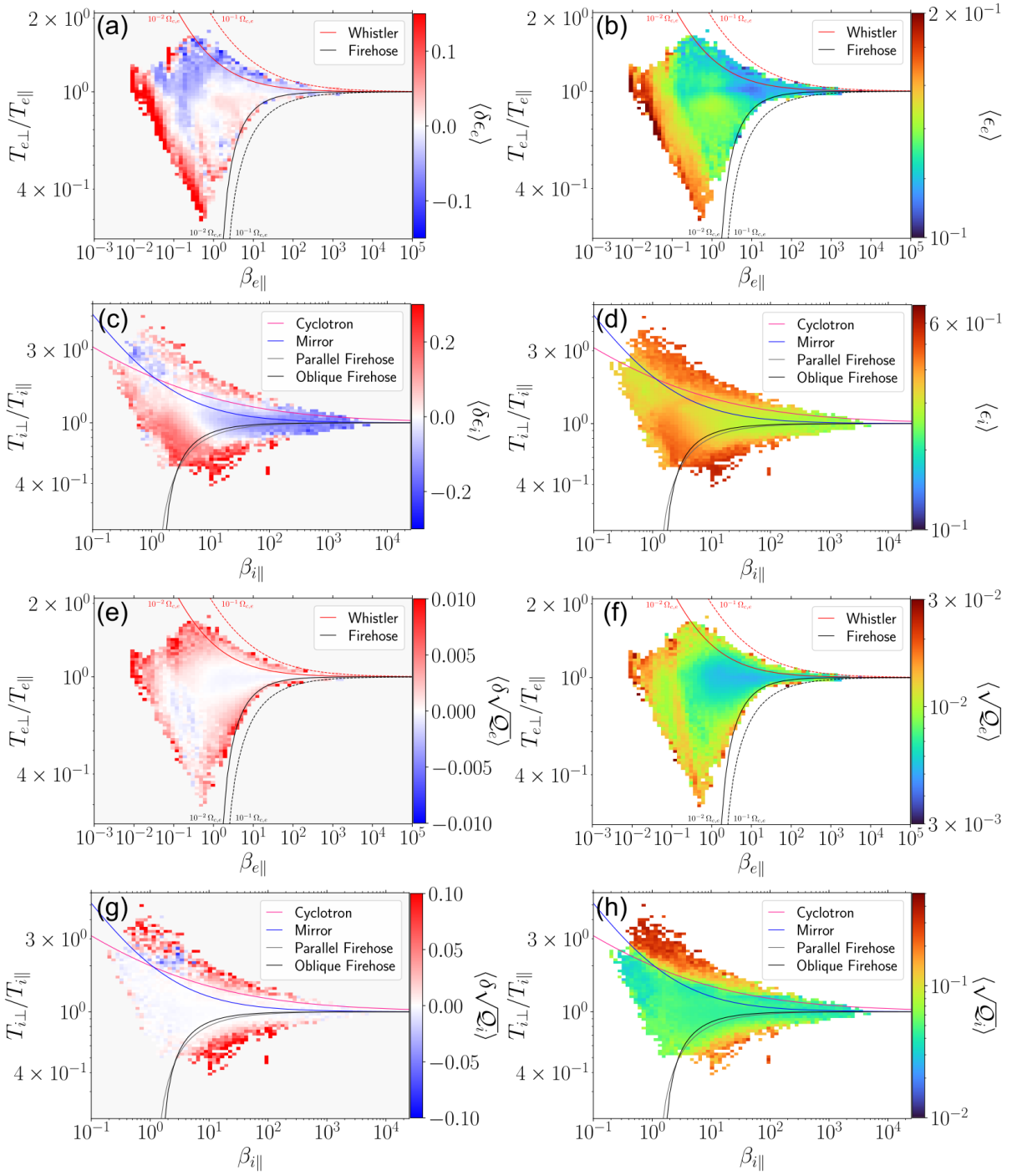


Figure 6.6: Non-Maxwellianity and agyrotropy parameters distributed on the anisotropy–beta plane. Panels in the left-hand column show bin-average difference from interval mean, and panels in the right-hand column show the bin-average value of the parameter. The distributions are of (a)–(b) ϵ_e, (c)–(d) ϵ_i, (e)–(f) $\sqrt{Q_e}$, (g)–(h) $\sqrt{Q_i}$, respectively. Bins containing fewer than 5 points or points from only 1 interval are excluded. Angled brackets refer to the average within the histogram cell. Colour scales on the right-hand column are logarithmic.

space, exhibiting different trends to the electron plane. The strong concentration of $\delta\epsilon_i < 0$ around $T_{i,\perp}/T_{i,\parallel} = 1$ suggests approximately isotropic VDFs are largely free from non-Maxwellian features, albeit only at $\beta_{i,\parallel} \gtrsim 10^1$. Enhanced $\delta\epsilon_i$ along both instability thresholds contrasts with panel (a), indicating that ion non-Maxwellianity is fluctuating above the background when in unstable configurations. This could be arising due to additional sources of free energy which may partly contribute to why ion parameter space is poorly constrained by the growth rate thresholds compared to the electrons. Unlike panel (b), panel (d) shows that ϵ_i is less strongly related to the parallel beta. The largest non-Maxwellianity signatures occur at extreme values of $T_{i,\perp}/T_{i,\parallel}$, although not at $\beta_{i,\parallel} \gtrsim 10^2$, suggesting that the relationship between non-Maxwellianity and the density is weaker for ions than electrons, as corroborated by Figure 6.1.

Given that non-Maxwellianity represents a source of free energy beyond the established link between non-ideal energy conversion and anisotropy-driven instabilities, it is informative to compare Figure 6.6 to distributions of $\mathbf{j} \cdot \mathbf{E}'$ in Figure 5.3. It should be noted that ϵ_i is computed on the ion timescale, whereas the ion panels in Figure 5.3 use upsampled ion axes data to match the electron-cadence $\mathbf{j} \cdot \mathbf{E}'$, leading to an apparent increase in parameter space occupancy in the latter plot for the same minimum bin count threshold. For the electrons, ϵ_e is not enhanced in the unstable regions where $\mathbf{j} \cdot \mathbf{E}'$ is large, suggesting that the energy conversion is strongly linked to the anisotropy-driven instabilities rather than additional instability mechanisms. Negative $\mathbf{j} \cdot \mathbf{E}'$ on the low-$\beta_{e,\parallel}$ edge coincides with a significant increase in $\delta\epsilon_e$ (and ϵ_e), suggesting that the highly non-Maxwellian VDFs may be leading to energy transfer from the particles into the fields.

6.4.2 Agyrotropy

The agyrotropy parameter represents a type of non-Maxwellianity caused by velocity space asymmetry about the **B**-aligned direction, manifesting as differences to the two perpendicular diagonal terms and off-diagonal terms in the temperature tensor. To isolate how this component is distributed with respect to anisotropy-driven instabilities, $\delta\sqrt{Q}$ and $\sqrt{Q}$ are plotted on the anisotropy–beta plane in Figure 6.6. Panel (e) shows that $\delta\sqrt{Q_e}$

is large along the instability boundaries, despite $\delta\epsilon_e$ being reduced and approximately 0 along the whistler and firehose edges, respectively. There is also a significant positive $\delta\sqrt{Q_e}$ along the other boundaries of the distribution, even at $T_{e,\perp}/T_{e,\parallel} \sim 1$, which aligns with the increase in $\delta\epsilon_e$ at low $\beta_{e,\parallel}$. These trends suggest that not only are the kinetic microinstabilities linked to agyrotropy which isn't noticeably captured by $\delta\epsilon_e$, but at other extreme regions such at low $\beta_{e,\parallel}$ distributions have enhanced agyrotropic features. Panel (f) shows that the largest $\sqrt{Q_e}$ occurs at low $\beta_{e,\parallel}$, and that it is not significantly enhanced along the instability boundaries. The latter observation shows that positive $\delta\sqrt{Q_e}$ observed in the instability regions is still not a large $\sqrt{Q_e}$ (i.e. the fluctuation is not large relative to the background), explaining why it does not show up in the non-Maxwellianity parameter in panel (a). From panels (e) and (f), it is clear that there is enhanced agyrotropy along the edges of the distributions but it is not contributing significantly to the non-Maxwellianity parameter as seen in panels (a) and (b).

The distribution of fluctuations of ion agyrotropy is shown in panel (g), wherein it can be seen that the largest enhancements in $\delta\sqrt{Q_i}$ occur beyond the instability thresholds. Unlike $\delta\epsilon_i$, there is only a very weak increase in $\delta\sqrt{Q_i}$ at small values of $\beta_{i,\parallel}$. This observation is corroborated by panel (h), which shows that large values of $\sqrt{Q_i}$ also occur in unstable regions, coinciding with where $\delta\sqrt{Q_i}$ is large. Values of $\sqrt{Q_i}$ are around an order of magnitude greater than those of $\sqrt{Q_e}$, suggesting that they are contributing more significantly to the non-Maxwellianity trends than in the electron case. The agyrotropic component of the ion VDFs in these regions could be partly responsible for the poor constraint of parameter space by the ion anisotropy-driven instabilities compared to the electrons.

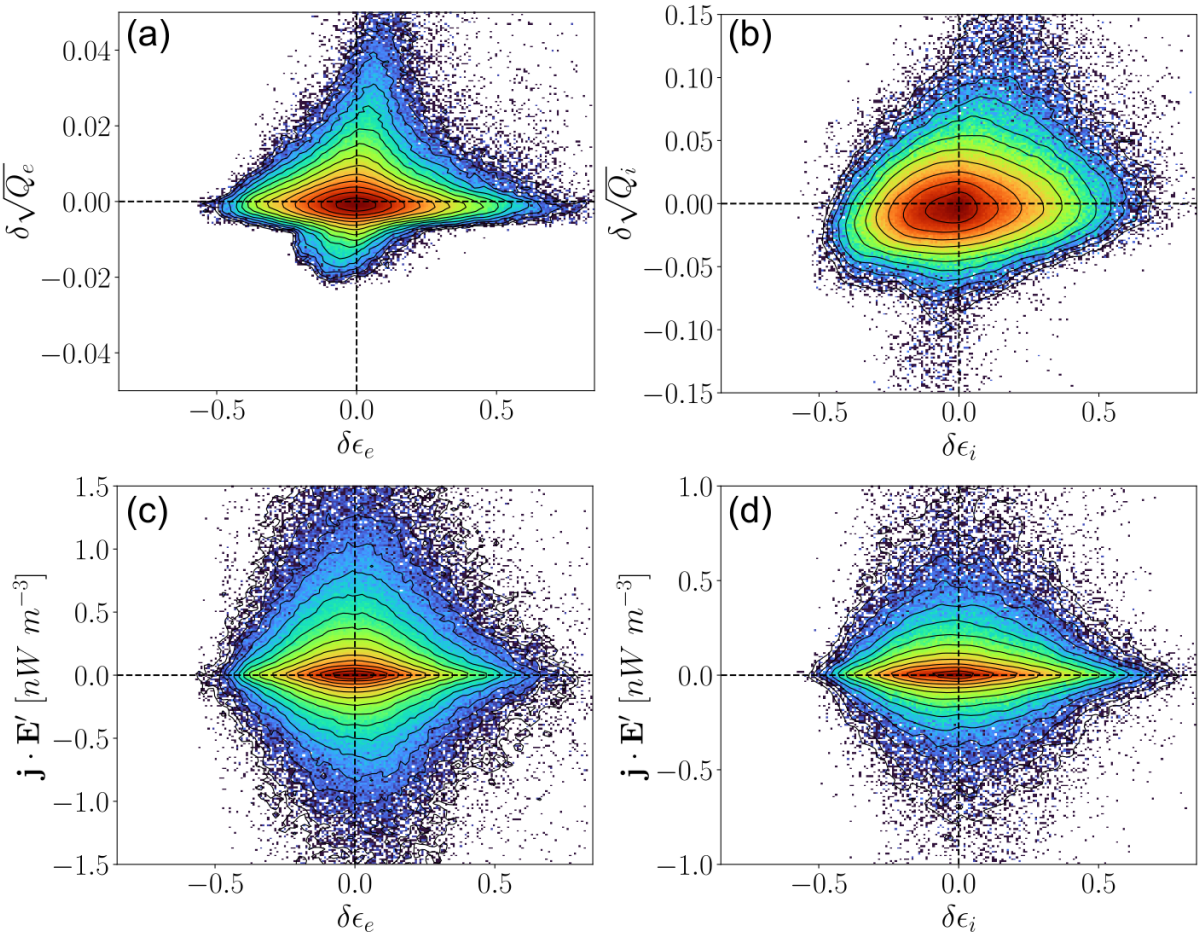


Figure 6.7: Probability density of non-Maxwellianity fluctuations compared to (a)–(b) agyrotropy and (c)–(d) non-ideal energy conversion. The left- and right-hand columns show electron and ion variables, respectively. In panel (d), the downsampled $\mathbf{j}\cdot\mathbf{E}'$ is used. The colour axis is logarithmic, with three contours per order of magnitude from a kernel density estimation of the probability density.

6.5 Fluctuations in the Non-Maxwellianity

6.5.1 Fluctuating Parameters

Fluctuations $\delta\epsilon$ around the background value range from small variations due to granularity in the measured distributions up to several rms in size coming from changes to the distribution structure itself. To understand the relevance of fluctuations in non-Maxwellianity, $\delta\epsilon$ is plotted against key variables in Figure 6.7. Panel (a) shows the histogram of $\delta\epsilon_e$ against $\delta\sqrt{Q_e}$, to investigate the link between fluctuations in agyrotropy and fluctuations in the overall non-Maxwellianity. The core of the distribution is approximately symmetric around $\delta\epsilon_e$, but large positive $\delta\sqrt{Q_e}$ occurs preferentially at $\delta\epsilon_e > 0$, and large negative $\delta\sqrt{Q_e}$ is most frequent at $\delta\epsilon_e < 0$. This suggests that extreme fluc-

tuations in agyrotropy are associated with an increase in non-Maxwellianity (as would be expected), but the largest non-Maxwellianities are generally arising due to sources other than agyrotropy. One explanation for this is that large off-diagonal pressure tensor components (on which $\sqrt{Q}$ is based) do not always correspond to changes in phase space density (Graham et al., 2021). The lack of probability density $\delta\sqrt{Q_e} < 0$ for all $\delta\epsilon_e$ is a result of $\langle\sqrt{Q_e}\rangle$ typically being close to 0.

In panel (b), it is seen that the ion version of the distribution is less structured. Again, extreme values indicate a correlation between $\delta\epsilon_i$ and $\delta\sqrt{Q_i}$, but the main concentration of points suggests only a very weak relationship between these two variables. This is interesting, as it implies the ion non-Maxwellianity is less-closely tied to the ion agyrotropy, possibly because the ion VDFs generally have a background agyrotropic component which contributes to the background non-Maxwellianity, and fluctuations are due to other changes to the VDF. Perri et al. (2020) found that $\sqrt{Q_i}$ was moderately correlated with ε_i (the Greco et al. (2012) non-Maxwellianity), but in MMS data it was much weaker. However, ε_i is more susceptible to changes in density than ϵ_i, so it is possible that in the MMS case the agyrotropy is contaminated at low densities by noise in the off-diagonal pressure terms.

To further investigate the relationship between fluctuations in non-Maxwellianity and non-ideal energy conversion (as discussed in Section 6.4.1, $\delta\epsilon$ is plotted against $\mathbf{j}\cdot\mathbf{E}'$ for the electrons and ions in Figures 6.7 (c) & (d), respectively. Panel (a) demonstrates that large values of $|\mathbf{j}\cdot\mathbf{E}'|$ occur preferentially but not exclusively at positive values of $\delta\epsilon_e$ (seen as a slight skewness), suggesting more energy conversion is happening when the non-Maxwellianity is locally larger than the background. The same trend is noticeable for the ions in panel (b), albeit with smaller values of $|\mathbf{j}\cdot\mathbf{E}'|$ due to the downsampling onto ion cadence smoothing over sharp energy conversion features. From these panels, it is apparent that there is a weak relationship between enhanced energy conversion and positive fluctuations in non-Maxwellianity, implying that observations of $\mathbf{j}\cdot\mathbf{E}'$ are accounting for processes both taking and giving energy to non-Maxwellian VDFs. One interpretation of

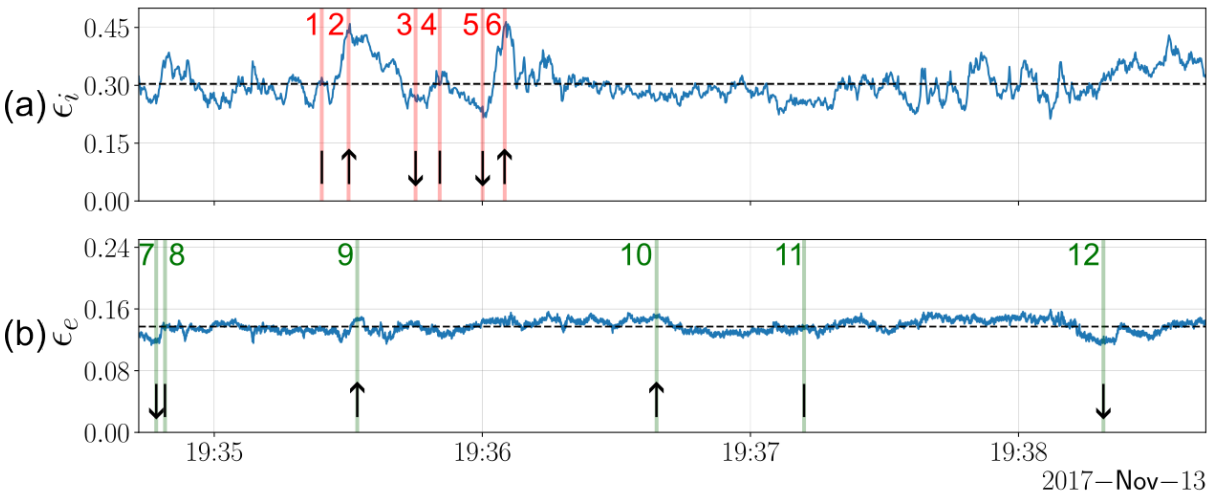


Figure 6.8: Time series of (a) ϵ_i and (b) ϵ_e within the example interval (2017-11-13/19:30:44–19:38:42). The dashed horizontal lines represent the mean of each variable. Points chosen for further investigation are denoted by vertical lines (note the thickness of these does not reflect the averaging time period). Arrows represent the fluctuation direction with respect to the mean, with no arrow meaning the data point is approximately at the mean value.

this is that the results are evidence for the role of additional VDF free-energy in exciting mechanisms which modify the energetics in the magnetosheath. However, as discussed previously and in Chapter 5, anisotropy-driven kinetic instabilities are the more influential driver of energy conversion.

6.5.2 Non-Maxwellianity in an Example Interval

In this section, the fluctuating non-Maxwellianity is explored in a brief case study for the example interval used throughout this Chapter (2017-11-13/19:30:44–19:38:42). The aim is to showcase an example of how ϵ varies throughout a typical interval, and explore what gives rise to these variations. However, it is impractical to be exhaustive even in this short interval, as there are still nearly 8000 electron VDF measurements in this time period. Instead, large positive and negative fluctuations, as well as two instances of average ϵ, are investigated. Figure 6.8 shows the non-Maxwellianity throughout the interval, with selected time periods numbered 1–6 and 7–12 for the ions and electrons, respectively. Comparing the panels, it is clear that ϵ_i is more variable than ϵ_e, as expected, and that fluctuations in one parameter are not necessarily correlated with the other.

The following are short qualitative descriptions of the features observed at each numbered time step in Figure 6.8 (a), where *average/enhancement/reduction* represents the instantaneous value of ϵ_i with respect to the interval mean:

1. *Average*: Qualitatively similar to interval mean, faint beam.
2. *Enhancement*: Strong beam structure, highly asymmetric VDF.
3. *Reduction*: Closer to bi-Maxwellian VDF, but antiparallel beam.
4. *Average*: Beam not present, close to interval mean structure.
5. *Reduction*: Weak beam present, otherwise close to bi-Maxwellian.
6. *Enhancement*: Strong beam structure, highly asymmetric VDF.

These observations indicate that strong beams are a possible driver of enhanced non-Maxwellianity. However, when there is a faint beam (or no beam), ϵ_i is being influenced by changes to how symmetric the core and flanks of the VDF are, with the remaining component coming from the strength of the energetic tails. In the electron case, in time steps 7–12 variations are largely coming from granularity in the VDF, with no noticeable beams or other coherent velocity space structures. This is likely due to the higher speed of the electrons, undergoing more interactions which erode sharp gradients in velocity space. The following aspects are noted, but it should be remembered that the changes are subtle:

7. *Reduction*: Diminished energetic tails.
8. *Average*: Close to interval background; granularity.
9. *Enhancement*: More granularity, reduction in phase space density, flatter core.
10. *Enhancement*: Granular, especially in tails, flat top.
11. *Average*: Flat top but with weak tails.
12. *Reduction*: Lower phase space density, less pronounced shoulder.

Studying the normalised non-Maxwellianity fluctuations ($\delta\epsilon$) and agyrotropy fluctuations ($\delta\sqrt{Q}$) for the example interval sheds light on the results of Figure 6.7. The time series of

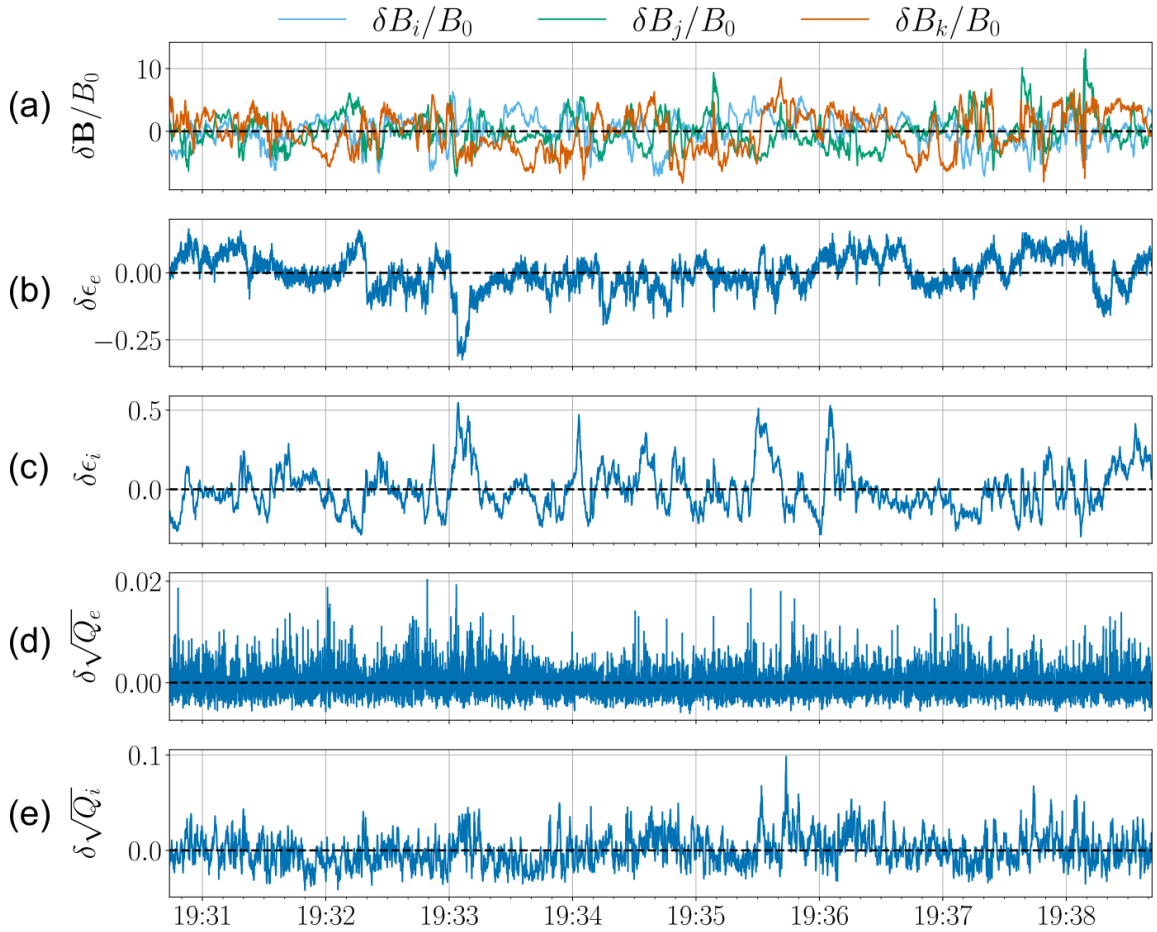


Figure 6.9: Time series of fluctuating magnetic field, non-Maxwellianity, and agyrotropy for 2017-11-13/19:30:44–19:38:42. The mean (= 0) is given by a dashed black line.

these parameters and the fluctuating normalised magnetic field vector are shown in Figure 6.9 (for a longer time period than Figure 6.8). Firstly, it is confirmed that fluctuations in ϵ_i are greater than ϵ_e even relative to the mean. Next, $\delta\epsilon_e$ and $\delta\epsilon_i$ are fluctuating on similar scale sizes to the magnetic field, suggesting that the fluctuations may be driven by the large-scale turbulent structure, rather than the localised structures. In contrast, $\delta\sqrt{Q_i}$ undergoes generally faster fluctuations, and $\delta\sqrt{Q_e}$ varies on very small timescales which may be partly associated with noise.

To further explore the turbulent nature of the non-Maxwellianity parameter, the power spectrum is plotted in Figure 6.10. It is seen that both $\delta\epsilon_e$ and $\delta\epsilon_i$ follow a similar power-law trend to $\delta\mathbf{B}/B_0$, albeit at lower power. At $f \sim 10^0$ Hz the non-Maxwellianity parameters begin to level off, likely due to noise, with $\delta\epsilon_e$ reaching its noise floor for at least half of a decade in frequency. This could explain the observation from Figure 6.7

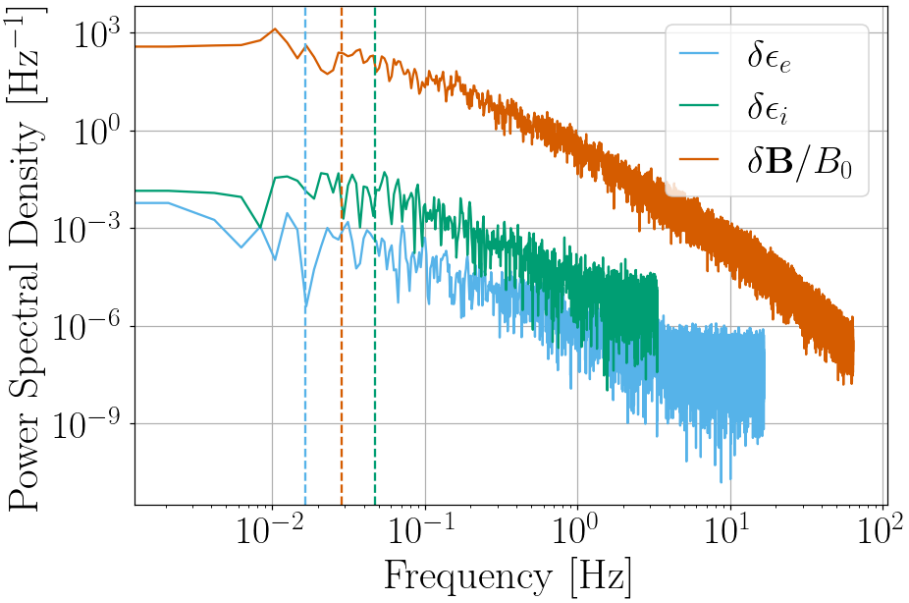


Figure 6.10: Power spectral density of non-Maxwellianity fluctuations and normalised magnetic field fluctuations. Dashed vertical lines represent the correlation length of the curve with the same colour. The mean is removed and the spectrum consists of a single Hanning-windowed periodogram.

that $\delta\epsilon$ and $\mathbf{j} \cdot \mathbf{E}'$ are only weakly correlated, as the high-frequency fluctuations in non-Maxwellianity contain very little fluctuation power on the scales where energy conversion signals are measured.

To characterise the largest scale of the turbulent fluctuations, the correlation length (see Section 2.3) is estimated as the integral of the correlation function up to the first zero crossing. These values are denoted by vertical dashed lines in Figure 6.10, wherein it can be noted that they are similar to λ_c of the magnetic field, which has been corroborated with values from Stawarz et al. (2022). This process was repeated for the 60 intervals from that study (the interval list used in Chapter 4, Appendix B.1), so that λ_c of $\delta\epsilon_e$ & $\delta\epsilon_i$ and $\delta\mathbf{B}$ may be compared. The reason the additional intervals are not used is because the correlation length calculation relies on the validity of Taylor's hypothesis (Taylor, 1938, see Section 3.5), which has not been rigorously verified as performed in the analysis by Stawarz et al. (2022). This comparison is shown in Figure 6.11, where there is an approximately linear scaling in log space, discounting intervals where the aforementioned process of estimating λ_c is qualitatively poor. From this result, it is suggested non-Maxwellianity in the VDF is being influenced by the turbulent dynamics on approximately the same scales

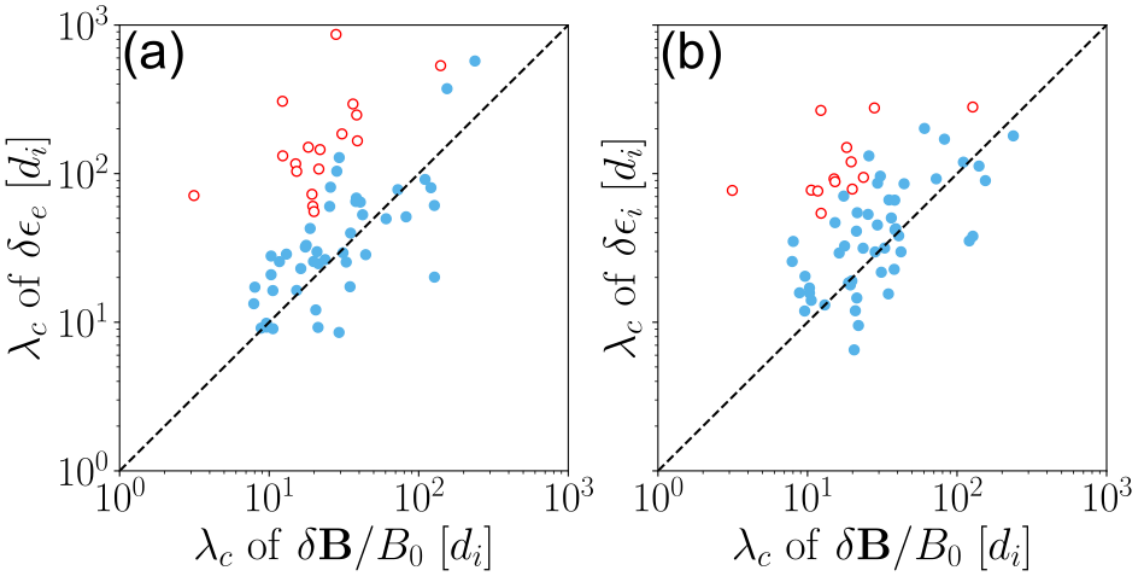


Figure 6.11: Comparison of estimated correlation length, λ_c, of the normalised vector magnetic field and the fluctuating non-Maxwellianity for each species. Where the estimation of the correlation scale is qualitatively poor, based on manual inspection of the correlation functions, points are demarcated by hollow red circles. One point of $\delta\epsilon_e \sim 10^{-1}\ d_i$ has been cut off by the plot limits.

as the magnetic field. This explains why strong correlations are not found between the energy conversion term and the non-Maxwellianity parameter, despite non-Maxwellianity representing a source of free energy for wave-particle interactions. However, it is still possible for the two quantities to be weakly regionally correlated, even if not point-to-point correlated.

6.6 Summary

Magnetosheath VDFs typically exist in a non-Maxwellian state, representing a potential source of free energy which can be redistributed by wave-particle interactions. Deviations typically go beyond anisotropy, including energetic tails, beams, and flat top distributions, leading to a breakdown of the assumptions behind temperature anisotropy-driven kinetic microinstabilities. Yet, these instabilities are observed to effectively constrain values of the anisotropy based on the local parallel beta, an effect linked to turbulent energy conversion in Chapter 5. VDFs departing from bi-Maxwellianity are characterised by a non-zero non-Maxwellianity parameter ϵ (Graham et al., 2021), which is observed to vary between 0.041–0.28 for the electrons and 0.14–0.72 for the ions. Levels of background

non-Maxwellianity vary between distinct intervals, as do the levels of fluctuations.

The background non-Maxwellianity arises from different velocity space structure between the two species. Electrons exhibit a sub-Maxwellian 'flat-top' distribution, with enhanced shoulders, diminished flanks, and energetic tails. This shape is formed when the electrons undergo processing by the shock (Montgomery et al., 1970; Feldman et al., 1983). In contrast, the ions have a super-Maxwellian core, with sub-Maxwellian flanks and more energetic tails than the electrons. Background ion non-Maxwellianity exhibits greater variation compared to the electrons, often due to beams and agyrotropic background distributions, which are less common in the electron VDFs.

Fluctuations of the non-Maxwellianity of ion VDFs arise due to significant velocity space structures, such as beams, enhanced tails (compared to the already super-Maxwellian background), and highly agyrotropic distributions. A small component comes from granularity in velocity space, where particle counts cause small differences between the observed and model distributions. In the electron case, non-Maxwellianity is lower and varies less relative to its smaller mean, with most variability arising due to granularity in velocity space and the potential for instrumental effects to disrupt measurements at low energies. In both species, non-Maxwellianity fluctuations occur on larger scales than individual energy conversion structures associated with kinetic microinstabilities, which explains why correlations between $\delta\epsilon$ and $\mathbf{j} \cdot \mathbf{E}'$ are weak. It is also noted that despite the additional sources of free energy coming from deviations away from bi-Maxwellian distributions, anisotropy-driven instabilities still appear to play a dominant role in thermodynamic regulation of the magnetosheath.

Not only is turbulence driving energy conversion into the particles which can give rise to wave-particle interactions that regulate the magnetosheath thermodynamics, but it also causes variability to the non-Maxwellianity of magnetosheath VDFs. Particularly in the ions, this represents a source of additional free energy in the VDF which may partially explain why the ions appear less strongly bound by anisotropy–driven instabilities. The host of kinetic processes made possible by these non-equilibrium velocity distributions

are expected to ultimately lead to dissipation of turbulent fluctuation energy at microscopic scales. An interesting problem for future studies is to investigate the additional mechanisms made possible by non-Maxwellian VDFs in the magnetosheath, to further characterise the dissipation process in collisionless plasmas.

Chapter 7

Conclusions

Turbulence is one of the great unsolved problems of classical physics. It is found in all corners of the Universe, heating astrophysical plasmas, churning Earth's oceans, and perfectly mixing a milky cup of tea. Despite knowing the equations which govern turbulent flow for more than two centuries, many features of its behaviour remain shrouded in mystery, particularly when it is coupled to electromagnetic forces and in the absence of collisions between particles. Fortunately, nature presents us with a unique laboratory for the study of plasma turbulence on our planet's doorstep. Studying turbulence in the magnetosheath not only reveals important information about the fundamental physics operating in turbulent systems, but also informs our understanding of the solar wind–magnetosphere coupling that leads to potentially harmful space weather. The latest generation of space missions, along with new developments in computer simulations and theory, allow us to probe deeper into turbulence than ever before. As such, the field is progressing rapidly, with new missions on the horizon – such as HelioSwarm (Klein et al., 2023) and Plasma Observatory (Retinò et al., 2022) – which promise to further demystify this ubiquitous phenomenon.

The key open questions in plasma turbulence surround how the nonlinear dynamics operate across different scale ranges and under different plasma conditions, and the extent to which these dynamics self-consistently excite different dissipative processes in collision-

less systems. The comparative role of nonlinear and linear forces forms the foundation of many turbulence theories, constraining the way in which energy is transferred from injection at large scales, through the lossless inertial range, to dissipation at small scales (Schekochihin, 2022; Marino and Sorriso-Valvo, 2023). In the absence of collisions, the cascade proceeds to such small scales that the MHD fluid description of turbulence gives way to kinetic physics (Verscharen et al., 2019). Because collisionless plasmas can exist in a state far from thermodynamic equilibrium, numerous channels are activated by which kinetic processes can reversibly transport energy between different forms (Treumann and Baumjohann, 1997). The essence of the dissipation problem is thus: How is energy in the fluctuations on average converted into particle energy, and how is the plasma eventually thermalised (Matthaeus et al., 2020; Pezzi et al., 2021a)?

All turbulence theories make assumptions about how the nonlinear forces are organised, and how they balance with the linear forces. To address this fundamental question, Chapter 4 investigates how competing forces encoded within the different terms in generalised Ohm's law behave behave relative to each other, and how that varies with respect to surrounding magnetosheath conditions. Furthermore, the electric fields generated by these forces are intrinsically linked to dissipation. MMS is uniquely capable of directly measuring nearly all of the terms in generalised Ohm's law at high resolution (Stawarz et al., 2021), providing observational constraints on the assumptions going into theory. We might expect the relative importance of these effects to depend on ambient plasma conditions (Franci et al., 2020), as well as the nature of the fluctuations, which may be further influenced by how the fluctuations are excited in the plasma, such as shock-driven turbulence (Bessho et al., 2022), the reflection of Alfvénic fluctuations in the solar atmosphere (Verdini and Velli, 2007), secondary instabilities in the Kelvin-Helmholtz instability (Di Mare et al., 2019), etc.

Chapter 4 demonstrates key results on the scale at which MHD dynamics give way to the Hall effect, the relative importance of Hall and ambipolar and diamagnetic electric fields (e.g., the electron pressure term) in the turbulent plasma, and the balance between

linear and nonlinear effects. The Hall scale (at which the MHD term gives way to the Hall term) is found to vary with the ion inertial length, modulated by the ion-scale ratio of magnetic to velocity field fluctuations. Therefore, in a purely-Alfvénic situation the MHD approximation breaks down at d_i, but in non-Alfvénic regimes the scale is different (closer to $2d_i$ in the magnetosheath). This indicates that an excess of magnetic energy in the magnetosheath causes Hall physics to become important at larger scales than otherwise. These results would need to be taken into account in MHD studies of non-Alfvénic turbulent systems. Assessment of the relative importance of the nonlinear to linear parts of the MHD and Hall terms (which is analogous to the χ parameter for the ratio of nonlinear to linear timescales from turbulence theory) shows that these depend on $\delta B_{rms}/B_0$. This is unexpected in the case of the Hall term, which only dominates at small scales, whereas the rms fluctuation is weighted towards the large scales, suggesting that the nonlinear dynamics must transmit this information to the small scales. Nonlinear contributions dominate when $\delta B_{rms}/B_0 > 1$, and vice versa, showing that the way in which the turbulence self-consistently arranges itself is dependent on the large-scale driver.

The scale-dependent ratio of electron pressure to Hall electric fields (encoding the importance of thermal effects, which can potentially break the frozen-in condition and accelerate particles along the magnetic field) is also investigated in Chapter 4. It is shown that the spectral ratio of these terms varies with three parameters: β_e; the ratio $B_0/\langle|B|\rangle$; and the sub-ion ratio $(\delta P_e/P_{e,0})/(\delta B/B_0)$ (including fluctuations of the pressure anisotropy). Once again, the properties of turbulence are important as well as ambient conditions. Furthermore, it is found that the component of the electric field generated by temperature gradients can be stronger than that arising from density gradients, showing the magnetosheath cannot be treated as an isothermal plasma. This is incompatible with KAW theories (e.g. that of Boldyrev et al., 2013), indicating the need for further developments of turbulence theory to fully characterise magnetosheath turbulence at sub-ion scales. This also means that simulation studies which aim to reproduce small-scale dynamics will need to incorporate electron temperature fluctuations.

An empirical analysis of the turbulence properties which factor into the scaling laws found in Chapter 4 reveals underlying dependences on the ambient plasma parameters, suggesting that the nonlinear forces in the magnetosheath largely depend on ambient conditions, rather than the nature of the fluctuations being purely controlled by the driving mechanism. The ratio of ion-scale magnetic to velocity field fluctuations is found to depend on β_i, which introduces a relationship between the Hall scale and the ion gyroradius ($k_{Hall} \sim \rho_i^{-0.28} d_i^{-0.72}$).

Notably, this scaling is distinct from the scaling for the break point in the magnetic spectrum inferred from solar wind observations and simulations (C. H. K. Chen et al., 2014; Franci et al., 2016). It will be interesting to further explore how the Hall scale is related to the magnetic spectral break and disentangle whether this discrepancy is mainly related to additional physics setting the magnetic break scale or differences between the nature of solar wind and magnetosheath turbulence. A similar analysis for the electron pressure to Hall electric field ratio reveals a two power-law scaling: $\sim \beta_e \beta^{-0.75}$ when $\delta B_{rms}/B_0$ is small and $\sim \beta_e \beta^{-1.07}$ when $\delta B_{rms}/B_0$ is large. This shows that the relative importance of the pressure term depends more strongly on β when the magnetic field fluctuations are strong relative to their background. While in this dataset these two scalings occupy distinct ranges of beta, it is intriguing to further explore whether both scalings can exist for the same values of beta representing distinct regimes of turbulence.

The results of Chapter 4 provide key observational constraints for how the nonlinear forces in turbulence are organised relative to one another, and how they vary over the accessible parameter regime in the magnetosheath. The work is valuable to the study of remote astrophysical plasmas (where in situ measurements are not possible) as well as computational studies (where choices regarding which physical effects to simulate have consequences for the tractability and choice of simulation techniques available). It would be valuable to investigate how the scalings uncovered in Chapter 4 extrapolate to regimes beyond the magnetosheath, such as the solar wind, where Alfvénicity and the large-scale turbulence driver are different. The upcoming HelioSwarm mission (Klein et al., 2023) will

be capable of measuring the Hall scale in the solar wind by calculating the current across several spatial scales simultaneously (using nested tetrahedra within its nine-spacecraft formation). This will advance our understanding of the applicability of MHD physics throughout the heliosphere, allowing for a direct comparison between the solar wind and shock-driven magnetosheath turbulence.

Chapter 4 therefore addresses how the nonlinear electric field dynamics operate within different turbulent regimes. Following this, Chapters 5 and 6 present an investigation into energy conversion and thermalisation, to unravel how the multitude of kinetic processes possible in a collisionless plasma lead to net dissipation and heating. Specifically, local non-ideal energy conversion via $\mathbf{j} \cdot \mathbf{E}'$ and associated deformations to the VDF are explored in the context of anisotropy-driven kinetic microinstabilities. This class of kinetic process is shown to constrain temperature anisotropy in the solar wind (e.g. Verscharen et al., 2019) and magnetosheath (Gary et al., 2005; Maruca et al., 2018) by redistributing free energy in velocity space, playing a role in the thermodynamics of the plasma. Recently, it has been found that the instabilities (which are based on linear theory in a homogeneous background) are able to grow sufficiently fast to overcome the inherent nonlinear timescales of turbulence (Bandyopadhyay et al., 2022b). However, it remains to be seen how turbulent energy conversion and eventual thermalisation couples into these mechanisms. This problem is addressed in Chapters 5 and 6.

Chapter 5 quantifies the role of kinetic microinstabilities in the energy conversion stage of dissipation, showing that average $\mathbf{j} \cdot \mathbf{E}'$ is enhanced in unstable regions. However, since energy conversion is sign-indefinite (Matthaeus et al., 2020) – where $\mathbf{j} \cdot \mathbf{E}' > 0$ represents energy imparted into the particles by the electromagnetic field, and $\mathbf{j} \cdot \mathbf{E}' < 0$ represents the opposite case – it is not a priori clear how the instability cycle is leading to net dissipation. Net-positive energy conversion is observed, suggesting turbulent fluctuations impart their energy into the VDF, driving it into an unstable configuration. The implication is then that microinstabilities excite waves which quickly propagate to other plasma regions, fast enough that they evade measurement by MMS due to instrumental limitations. This

interpretation is consistent with the fact that the ion instability regions are less net-positive than the electrons, because ion processes generally occur on slower timescales than electron ones (Gary, 1993), so part of the wave-excitation phase is being measured.

An interesting tendency for negative average $\mathbf{j} \cdot \mathbf{E}'$ in the lowest-$\beta_\parallel$ regions is uncovered, even though there is no microinstability mechanism affecting this parameter regime (Gary, 1993; Treumann and Baumjohann, 1997). The origin of this effect is thus unknown, implying that dominant magnetic pressure (compared to thermal pressure, as encoded by the β) is somehow resulting in energy being taken from the particles into the fields. A useful extension to this work would be to utilise a dispersion solver which can accept arbitrary VDF configurations – such as the Arbitrary Linear Plasma Solver (ALPS) code (Verscharen et al., 2018) – to identify what instabilities may be acting in this region. Since the intervals which give rise to this effect are mostly found to remain in a similar $\beta_\parallel$ regime (as opposed to in other parts of anisotropy–beta parameter space, where individual intervals move around significantly), there could be a configuration-space instability acting, or the effect could be as a result of the large-scale driver of turbulence.

Comparing the results of $\mathbf{j} \cdot \mathbf{E}'$ with $\mathbf{j} \cdot \mathbf{E}_{pl}$ reveals qualitatively similar trends, suggesting that the non-ideal term (which is part of the plasma-frame energy term) is driving the enhanced energy conversion in unstable regions, rather than the convective contribution. This strengthens the link between kinetic microinstabilities and dissipation, as it is only the non-ideal energy conversion which can lead to particle acceleration parallel to the magnetic field. Furthermore, it is found that $j_\parallel E'_\parallel$ is weak in all cases except when unstable to the electron firehose instability (the electron instability activates when there is an excess in $T_{e,\parallel}$). This is interpreted as evidence for the electron firehose instability leading to particle acceleration parallel to magnetic field lines, an important feature of dissipation. In contrast, $\mathbf{j}_\perp \cdot \mathbf{E}'_\perp$ is excited most along the electron whistler instability threshold, but is also increased in all extreme anisotropy–beta conditions and generally makes up the majority of energy conversion observed in the magnetosheath. Despite being less clear, the trends with respect to ion instabilities are consistent with their electron

counterparts.

Enhanced energy conversion signals concentrated in unstable regions correspond to local events, associated with a wide variety of physical processes such as magnetic reconnection, magnetic holes, and other current structures which generate non-ideal electric fields. A valuable further study would be to formally categorise the multitude of processes occurring in unstable regions, to understand the role each mechanism plays in net energy conversion and the potential relationship to the microinstabilities. The cumulative effect of the turbulence in unstable regions is net energy conversion from the fields to the particles, where the amount of energy converted is greater on average than in stable regions. Despite accounting for a small percentage of magnetosheath observations, unstable plasma regions seem to be significantly contributing to net energy conversion into the particles. Thus, anisotropy-driven kinetic microinstabilities are an important link between turbulent fluctuations and dissipation.

Having shown that local regions close to instability boundaries are where enhanced energy conversion is observed, a question remains as to how the microinstabilities link to thermalisation. Anisotropy-driven instabilities redistribute free energy from excess parallel or perpendicular temperature to excite wave modes, thereby thermalising that aspect of the distribution. However, due to the lack of collisions in the magnetosheath, VDFs typically exist in non-equilibrium configurations significantly more complex than anisotropic Maxwellians (Perri et al., 2020; Graham et al., 2021). As such, there is more free energy in velocity space which may induce further instabilities. This feature is explored in Chapter 6, wherein the effect of VDF non-Maxwellianity (ϵ) and agyrotropy ($\sqrt{Q}$) is investigated with respect to anisotropy-driven microinstabilities. This gives context to the results of Chapter 5 and probes the elusive thermalisation step of dissipation.

The non-Maxwellianity parameter is found to fluctuate around a steady background value, where the background and level of fluctuations vary from interval to interval. In the electrons, the background distributions are flat-tops, with variations primarily arising due to large-scale deformations based on changes to the ambient parameters, and granularity

in the VDF at smallest scales. In contrast, ion non-Maxwellianity has a higher background and stronger fluctuations, coming from changes to the background VDF shape, beams, and agyrotropy. This is reflective of the fact that ions undergo fewer interactions due to their slower speed, and are, as such, generally thermalised to a lesser degree. In unstable regions, ϵ_i, $\sqrt{Q_i}$, and $\sqrt{Q_e}$ are enhanced, suggesting that the turbulence giving rise to increased $\mathbf{j} \cdot \mathbf{E}'$ is also injecting energy into these aspects of the VDF structure. However, the same trends are not observed in ϵ_e, potentially due to the small size of the values compared to the noise. This may be improved upon by undertaking a similar analysis utilising a fully-kinetic simulation.

One interpretation of these findings is that the cumulative effect of small energy conversion structures is enhanced $\sqrt{Q}$ and ϵ. However, the alternative view is that variations to the distribution are driven by large-scale turbulence, which is more likely to be the case based on the correlation lengths of ϵ and B, which are similar. This is consistent with the lack of a strong correlation between point-to-point non-Maxwellianity and $\mathbf{j} \cdot \mathbf{E}'$, although there is a slight enhancement to $\delta\epsilon$ during periods of significant energy conversion. A future direction for this work would be to categorise the alterations to the velocity distribution as a result of the observed regions of enhanced energy conversion near anisotropy-driven instability thresholds. This could be achieved using field-particle correlation techniques (Klein et al., 2017). Furthermore, computing terms of the Vlasov equation, along the lines of Shuster et al. (2019), may elucidate how energy imparted into the particles by positive $\mathbf{j} \cdot \mathbf{E}'$ is transported through velocity space once it has been imparted to the particles.

The results of Chapter 6 indicate that, while microinstabilities are responsible for reducing temperature anisotropy in unstable regions, the same turbulent fluctuations which give rise to increased anisotropy may also be giving rise to non-Maxwellian features in the distribution. Even though non-Maxwellianity represents extra free energy in velocity space, Chapter 5 showed that anisotropy-driven instabilities strongly constrain the parameter space accessible to magnetosheath plasma, acting to thermalise the distributions. Consequently, kinetic microinstabilities are likely a predominant process in mediating

collisionless dissipation in the magnetosheath.

Overall, the work in this thesis addresses how turbulence operates in a collisionless regime. By characterising how the turbulent electric field contributions self-consistently organise under a variety of magnetosheath conditions, it has been shown that the balance of competing nonlinear forces depends on ambient plasma parameters as well as the characteristics of the fluctuations that, in principle, may be influenced by the turbulent driver. Beyond this, an investigation into the links between turbulence and kinetic microinstabilities has revealed enhanced energy conversion in unstable periods, showing that this class of kinetic mechanism is playing an important role in facilitating collisionless dissipation.

The results have applications to remote plasma systems where in situ measurements are not available, the observational constraint of assumptions going into turbulence theories and simulations, and the solar wind–magnetosphere space weather impact chain. The foundations have been laid for several future studies into the nonlinear dynamics of turbulence in space plasmas and the processes by which net dissipation is ultimately achieved. The exciting future HelioSwarm and Plasma Observatory missions will unleash a new generation of turbulence studies, making possible for the first time simultaneous multi-spacecraft measurements at fluid and ion scales. These new missions, in addition to the maturing data sets provided by existing missions, promise to push the boundaries of turbulence research further than ever before, helping scientists demystify the universal phenomenon of turbulence.

Bibliography

Adhikari, S., Matthaeus, W. H., Parashar, T. N., Shay, M. A., and Cassak, P. A. (2023a). "Statistics of Pressure Fluctuations in Turbulent Kinetic Plasmas". In: *Monthly Notices of the Royal Astronomical Society*, stad2871. DOI: 10.1093/mnras/stad2871.

Adhikari, S., Shay, M. A., Parashar, T. N., Matthaeus, W. H., Pyakurel, P. S., Stawarz, J. E., and Eastwood, J. P. (2023b). "Effect of a guide field on the turbulence like properties of magnetic reconnection". In: *Physics of Plasmas* **30**:8, p. 082904. DOI: 10.1063/5.0150929.

Afshari, A. S., Howes, G. G., Kletzing, C. A., Hartley, D. P., and Boardsen, S. A. (2021). "The Importance of Electron Landau Damping for the Dissipation of Turbulent Energy in Terrestrial Magnetosheath Plasma". In: *Journal of Geophysical Research: Space Physics* **126**:12, e2021JA029578. DOI: 10.1029/2021JA029578.

Alexandrova, O., Chen, C. H. K., Sorriso-Valvo, L., Horbury, T. S., and Bale, S. D. (2013). "Solar Wind Turbulence and the Role of Ion Instabilities". In: *Space Science Reviews* **178**:2-4, pp. 101–139. DOI: 10.1007/s11214-013-0004-8.

Alexandrova, O., Lacombe, C., and Mangeney, A. (2008). "Spectra and anisotropy of magnetic fluctuations in the Earth's magnetosheath: Cluster observations". In: *Annales Geophysicae* **26**:11, pp. 3585–3596. DOI: 10.5194/angeo-26-3585-2008.

Alexandrova, O., Lacombe, C., Mangeney, A., Grappin, R., and Maksimovic, M. (2012). "Solar Wind Turbulent Spectrum at Plasma Kinetic Scales". In: *The Astrophysical Journal* **760**:2, p. 121. DOI: 10.1088/0004-637X/760/2/121.

Alexandrova, O., Saur, J., Lacombe, C., Mangeney, A., Mitchell, J., Schwartz, S. J., and Robert, P. (2009). "Universality of Solar-Wind Turbulent Spectrum from MHD to Electron Scales". In: *Physical Review Letters* **103**:16, p. 165003. DOI: 10.1103/PhysRevLett.103.165003.

Alexandrova, O., Jagarlamudi, V. K., Hellinger, P., Maksimovic, M., Shprits, Y., and Mangeney, A. (2021). "Spectrum of kinetic plasma turbulence at 0.3–0.9 astronomical units from the Sun". In: *Physical Review E* **103**:6, p. 063202. DOI: 10.1103/PhysRevE.103.063202.

Alfvén, H. (1942). "Existence of electromagnetic-hydrodynamic waves". In: *Nature* **150**:3805, pp. 405–406. DOI: 10.1038/150405d0.

André, M., Vaivads, A., Buchert, S. C., Fazakerley, A. N., and Lahiff, A. (2004). "Thin electron-scale layers at the magnetopause". In: *Geophysical Research Letters* **31**:3, p. L03803. DOI: 10.1029/2003GL018137.

Andrés, N., Galtier, S., and Sahraoui, F. (2018). "Exact law for homogeneous compressible Hall magnetohydrodynamics turbulence". In: *Physical Review E* **97**:1, p. 013204. DOI: 10.1103/PhysRevE.97.013204.

Argall, M. R., Barbhuiya, M. H., Cassak, P. A., Wang, S., Shuster, J., Liang, H., Gershman, D. J., Torbert, R. B., and Burch, J. L. (2022). "Theory, observations, and simulations of kinetic entropy in a magnetotail electron diffusion region". In: *Physics of Plasmas* **29**:2, p. 022902. DOI: 10.1063/5.0073248.

Argall, M. R., Fischer, D., Contel, O. L., Mirioni, L., Torbert, R. B., Dors, I., Chutter, M., Needell, J., Strangeway, R., Magnes, W., and Russell, C. T. (2018). *The Fluxgate-*

Searchcoil Merged (FSM) Magnetic Field Data Product for MMS. DOI: 10.48550/ARXIV.1809.07388.

Bale, S. D., Kellogg, P. J., Mozer, F. S., Horbury, T. S., and Reme, H. (2005). "Measurement of the electric fluctuation spectrum of magnetohydrodynamic turbulence". In: *Physical Review Letters* **94**:21, p. 215002. DOI: 10.1103/PhysRevLett.94.215002.

Bandyopadhyay, R., Begley, L. J., Maruca, B. A., McComas, D. J., Szalay, J. R., Allegrini, F., Ebert, R. W., Gershman, D. J., Connerney, J. E. P., and Bolton, S. J. (2022a). "Beta-Dependent Constraints on Ion Temperature Anisotropy in Jupiter's Magnetosheath". In: *Geophysical Research Letters* **49**:15, e2022GL098053. DOI: 10.1029/2022GL098053.

Bandyopadhyay, R., Chasapis, A., Matthaeus, W. H., Parashar, T. N., Haggerty, C. C., Shay, M. A., Gershman, D. J., Giles, B. L., and Burch, J. L. (2021). "Energy dissipation in turbulent reconnection". In: *Physics of Plasmas* **28**:11, p. 112305. DOI: 10.1063/5.0071015.

Bandyopadhyay, R., Chasapis, A., Chhiber, R., Parashar, T. N., Maruca, B. A., Matthaeus, W. H., Schwartz, S. J., Eriksson, S., Le Contel, O., Breuillard, H., Burch, J. L., Moore, T. E., Pollock, C. J., Giles, B. L., Paterson, W. R., Dorelli, J., Gershman, D. J., Torbert, R. B., Russell, C. T., and Strangeway, R. J. (2018). "Solar Wind Turbulence Studies Using MMS Fast Plasma Investigation Data". In: *The Astrophysical Journal* **866**:2, p. 81. DOI: 10.3847/1538-4357/aade93.

Bandyopadhyay, R., Qudsi, R. A., Gary, S. P., Matthaeus, W. H., Parashar, T. N., Maruca, B. A., Roytershteyn, V., Chasapis, A., Giles, B. L., Gershman, D. J., Pollock, C. J., Russell, C. T., Strangeway, R. J., Torbert, R. B., Moore, T. E., and Burch, J. L. (2022b). "Interplay of turbulence and proton-microinstability growth in space plasmas". In: *Physics of Plasmas* **29**:10, p. 102107. DOI: 10.1063/5.0098625.

Bandyopadhyay, R., Yang, Y., Matthaeus, W. H., Parashar, T. N., Roytershteyn, V., Chasapis, A., Gershman, D. J., Giles, B. L., and Burch, J. L. (2023). "Collisional-

like dissipation in collisionless plasmas". In: *Physics of Plasmas* **30**:8, p. 080702. DOI: 10.1063/5.0146986.

Banerjee, S. and Galtier, S. (2013). "Exact relation with two-point correlation functions and phenomenological approach for compressible magnetohydrodynamic turbulence". In: *Physical Review E* **87**:1, p. 013019. DOI: 10.1103/PhysRevE.87.013019.

Barbhuiya, M. H., Cassak, P. A., Adhikari, S., Parashar, T. N., Liang, H., and Argall, M. R. (2024). "Higher-order nonequilibrium term: Effective power density quantifying evolution towards or away from local thermodynamic equilibrium". In: *Physical Review E* **109**:1, p. 015205. DOI: 10.1103/PhysRevE.109.015205.

Barenghi, C. F., Skrbek, L., and Sreenivasan, K. R. (2014). "Introduction to quantum turbulence". In: *Proceedings of the National Academy of Sciences* **111**:supplement_1, pp. 4647–4652. DOI: 10.1073/pnas.1400033111.

Barrie, A. C., Cipriani, F., Escoubet, C. P., Toledo-Redondo, S., Nakamura, R., Torkar, K., Sternovsky, Z., Elkington, S., Gershman, D., Giles, B., and Schiff, C. (2019). "Characterizing spacecraft potential effects on measured particle trajectories". In: *Physics of Plasmas* **26**:10, p. 103504. DOI: 10.1063/1.5119344.

Baumjohann, W. and Treumann, R. A. (1996). *Basic space plasma physics*. Imperial College Press. DOI: 10.1142/p015.

Beresnyak, A. and Lazarian, A. (2008). "Strong imbalanced turbulence". In: *The Astrophysical Journal* **682**:2, pp. 1070–1075. DOI: 10.1086/589428.

Bessho, N., Chen, L.-J., Stawarz, J. E., Wang, S., Hesse, M., Wilson, L. B., and Ng, J. (2022). "Strong reconnection electric fields in shock-driven turbulence". In: *Physics of Plasmas* **29**:4, p. 042304. DOI: 10.1063/5.0077529.

Birkeland, K. (1914). "A Possible Connection Between Magnetic and Meteorologic Phenomena". In: *Monthly Weather Review* **42**:4, pp. 211–211. DOI: 10.1175/1520-0493(1914)42<211a:APCBMA>2.0.CO;2.

Birn, J. and Hesse, M. (2005). "Energy release and conversion by reconnection in the magnetotail". In: *Annales Geophysicae* **23**:10, pp. 3365–3373. DOI: 10.5194/angeo-23-3365-2005.

Birn, J. and Hesse, M. (2009). "Reconnection in substorms and solar flares: analogies and differences". In: *Annales Geophysicae* **27**:3, pp. 1067–1078. DOI: 10.5194/angeo-27-1067-2009.

Biskamp, D., Schwarz, E., Zeiler, A., Celani, A., and Drake, J. F. (1999). "Electron magnetohydrodynamic turbulence". In: *Physics of Plasmas* **6**:3, pp. 751–758. DOI: 10.1063/1.873312.

Biskamp, D. (2003). *Magnetohydrodynamic Turbulence*. 1st ed. Cambridge University Press. DOI: 10.1017/CBO9780511535222.

Boldyrev, S. (2006). "Spectrum of Magnetohydrodynamic Turbulence". In: *Physical Review Letters* **96**:11, p. 115002. DOI: 10.1103/PhysRevLett.96.115002.

Boldyrev, S., Horaites, K., Xia, Q., and Perez, J. C. (2013). "Toward a theory of astrophysical plasma turbulence at subproton scales". In: *The Astrophysical Journal* **777**:1, p. 41. DOI: 10.1088/0004-637X/777/1/41.

Boldyrev, S. and Perez, J. C. (2012). "Spectrum of Kinetic-Alfvén Turbulence". In: *The Astrophysical Journal* **758**:2, p. L44. DOI: 10.1088/2041-8205/758/2/144.

Boltzmann, L. (1896). *Lectures on Gas Theory, 1896-1898*. University of California Press, reprinted by Dover Publications: New York, 1995.

Bott, A. F. A., Arzamasskiy, L., Kunz, M. W., Quataert, E., and Squire, J. (2021). "Adaptive Critical Balance and Firehose Instability in an Expanding, Turbulent, Collisionless

Plasma". In: *The Astrophysical Journal Letters* **922**:2, p. L35. DOI: 10.3847/2041-8213/ac37c2.

Bowen, T. A., Mallet, A., Bonnell, J. W., and Bale, S. D. (2018). "Impact of Residual Energy on Solar Wind Turbulent Spectra". In: *The Astrophysical Journal* **865**:1, p. 45. DOI: 10.3847/1538-4357/aad95b.

Boyd, T. J. M. and Sanderson, J. J. (2003). *The physics of plasmas*. Cambridge: Cambridge University Press. DOI: 10.1017/CBO9780511755750.

Breuillard, H., Yordanova, E., Vaivads, A., and Alexandrova, O. (2016). "The effects of kinetic instabilities on small-scale turbulence in earth's magnetosheath". In: *The Astrophysical Journal* **829**:1, p. 54. DOI: 10.3847/0004-637X/829/1/54.

Breuillard, H. et al. (2018). "New insights into the nature of turbulence in the earth's magnetosheath using magnetospheric MultiScale mission data". In: *The Astrophysical Journal* **859**:2, p. 127. DOI: 10.3847/1538-4357/aabae8.

Bruno, R. and Carbone, V. (2013). "The solar wind as a turbulence laboratory". In: *Living Reviews in Solar Physics* **10**:1, p. 2. DOI: 10.12942/lrsp-2013-2.

Buchanan, M. (2016). "Everything is plasma". In: *Nature Physics* **12**:5, pp. 394–394. DOI: 10.1038/nphys3756.

Burch, J. L., Moore, T. E., Torbert, R. B., and Giles, B. L. (2016). "Magnetospheric Multiscale Overview and Science Objectives". In: *Space Science Reviews* **199**:1-4, pp. 5–21. DOI: 10.1007/s11214-015-0164-9.

Buzulukova, N. and Tsurutani, B. (2022). "Space Weather: From solar origins to risks and hazards evolving in time". In: *Frontiers in Astronomy and Space Sciences* **9**: p. 1017103. DOI: 10.3389/fspas.2022.1017103.

Carbone, F. et al. (2021). "Statistical study of electron density turbulence and ion-cyclotron waves in the inner heliosphere: Solar Orbiter observations". In: *Astronomy & Astrophysics* **656**: A16. DOI: 10.1051/0004-6361/202140931.

Carbone, V. (2012). "Scalings, Cascade and Intermittency in Solar Wind Turbulence". In: *Space Science Reviews* **172**:1-4, pp. 343–360. DOI: 10.1007/s11214-012-9907-z.

Chandran, B. D. G., Schekochihin, A. A., and Mallet, A. (2015). "Intermittency and Alignment in Strong RMHD Turbulence". In: *The Astrophysical Journal* **807**:1, p. 39. DOI: 10.1088/0004-637x/807/1/39.

Chapman, S. (1917). "On the Times of Sudden Commencement of Magnetic Storms". In: *Proceedings of the Physical Society of London* **30**:1, pp. 205–214. DOI: 10.1088/1478-7814/30/1/317.

Chasapis, A., Retinò, A., Sahraoui, F., Vaivads, A., Khotyaintsev, Y. V., Sundkvist, D., Greco, A., Sorriso-Valvo, L., and Canu, P. (2015). "Thin Current Sheets and Associated Electron Heating in Turbulent Space Plasma". In: *The Astrophysical Journal* **804**:1, p. L1. DOI: 10.1088/2041-8205/804/1/L1.

Chasapis, A., Matthaeus, W. H., Parashar, T. N., Fuselier, S. A., Maruca, B. A., Phan, T. D., Burch, J. L., Moore, T. E., Pollock, C. J., Gershman, D. J., Torbert, R. B., Russell, C. T., and Strangeway, R. J. (2017). "High-resolution Statistics of Solar Wind Turbulence at Kinetic Scales Using the Magnetospheric Multiscale Mission". In: *The Astrophysical Journal Letters* **844**:1, p. L9. DOI: 10.3847/2041-8213/aa7ddd.

Chasapis, A., Matthaeus, W. H., Parashar, T. N., Wan, M., Haggerty, C. C., Pollock, C. J., Giles, B. L., Paterson, W. R., Dorelli, J., Gershman, D. J., Torbert, R. B., Russell, C. T., Lindqvist, P.-A., Khotyaintsev, Y., Moore, T. E., Ergun, R. E., and Burch, J. L. (2018a). "In Situ Observation of Intermittent Dissipation at Kinetic Scales in the Earth's Magnetosheath". In: *The Astrophysical Journal* **856**:1, p. L19. DOI: 10.3847/2041-8213/aaadf8.

Chasapis, A., Yang, Y., Matthaeus, W. H., Parashar, T. N., Haggerty, C. C., Burch, J. L., Moore, T. E., Pollock, C. J., Dorelli, J., Gershman, D. J., Torbert, R. B., and Russell, C. T. (2018b). "Energy conversion and collisionless plasma dissipation channels in the turbulent magnetosheath observed by the magnetospheric multiscale mission". In: *The Astrophysical Journal* **862**:1, p. 32. DOI: 10.3847/1538-4357/aac775.

Chaston, C., Bonnell, J., McFadden, J. P., Carlson, C. W., Cully, C., Le Contel, O., Roux, A., Auster, H. U., Glassmeier, K. H., Angelopoulos, V., and Russell, C. T. (2008). "Turbulent heating and cross-field transport near the magnetopause from THEMIS". In: *Geophysical Research Letters* **35**:17, L17S08. DOI: 10.1029/2008GL033601.

Chen, C. H. K. (2016). "Recent progress in astrophysical plasma turbulence from solar wind observations". In: *Journal of Plasma Physics* **82**:6. DOI: 10.1017/s0022377816001124.

Chen, C. H. K. and Boldyrev, S. (2017). "Nature of kinetic scale turbulence in the earth's magnetosheath". In: *The Astrophysical Journal* **842**:2, p. 122. DOI: 10.3847/1538-4357/aa74e0.

Chen, C. H. K., Horbury, T. S., Schekochihin, A. A., Wicks, R. T., Alexandrova, O., and Mitchell, J. (2010). "Anisotropy of Solar Wind Turbulence between Ion and Electron Scales". In: *Physical Review Letters* **104**:25, p. 255002. DOI: 10.1103/PhysRevLett.104.255002.

Chen, C. H. K., Klein, K. G., and Howes, G. G. (2019). "Evidence for electron Landau damping in space plasma turbulence". In: *Nature Communications* **10**: p. 740. DOI: 10.1038/s41467-019-08435-3.

Chen, C. H. K., Leung, L., Boldyrev, S., Maruca, B. A., and Bale, S. D. (2014). "Ion-scale spectral break of solar wind turbulence at high and low beta". In: *Geophysical Research Letters* **41**:22, pp. 8081–8088. DOI: 10.1002/2014GL062009.

Chen, C. H. K., Salem, C. S., Bonnell, J. W., Mozer, F. S., and Bale, S. D. (2012). "Density Fluctuation Spectrum of Solar Wind Turbulence between Ion and Electron Scales". In: *Physical Review Letters* **109**:3, p. 035001. DOI: 10.1103/PhysRevLett.109.035001.

Chhiber, R., Chasapis, A., Bandyopadhyay, R., Parashar, T. N., Matthaeus, W. H., Maruca, B. A., Moore, T. E., Burch, J. L., Torbert, R. B., Russell, C. T., Le Contel, O., Argall, M. R., Fischer, D., Mirioni, L., Strangeway, R. J., Pollock, C. J., Giles, B. L., and Gershman, D. J. (2018). "Higher-Order Turbulence Statistics in the Earth's Magnetosheath and the Solar Wind Using Magnetospheric Multiscale Observations". In: *Journal of Geophysical Research: Space Physics* **123**:12, pp. 9941–9954. DOI: 10.1029/2018JA025768.

Chiappetta, F., Yordanova, E., Vörös, Z., Lepreti, F., and Carbone, V. (2023). "Energy Conversion through a Fluctuation–Dissipation Relation at Kinetic Scales in the Earth's Magnetosheath". In: *The Astrophysical Journal* **957**:2, p. 98. DOI: 10.3847/1538-4357/acfca2.

Colagrossi, A., Marrone, S., Colagrossi, P., and Le Touzé, D. (2021). "Da Vinci's observation of turbulence: A French-Italian study aiming at numerically reproducing the physics behind one of his drawings, 500 years later". In: *Physics of Fluids* **33**:11, p. 115122. DOI: 10.1063/5.0070984.

Coleman Jr., P. J. (1968). "Turbulence, Viscosity, and Dissipation in the Solar-Wind Plasma". In: *The Astrophysical Journal* **153**: p. 371. DOI: 10.1086/149674.

Cozzani, G., Khotyaintsev, Y. V., Graham, D. B., and André, M. (2023). "Direct Observations of Electron Firehose Fluctuations in the Magnetic Reconnection Outflow". In: *Journal of Geophysical Research: Space Physics* **128**:5, e2022JA031128. DOI: 10.1029/2022JA031128.

Crookes, W. (1879). *On radiant matter a lecture delivered to the British Association for the Advancement of Science, at Sheffield, Friday, August 22, 1879 / by William Crookes.* London : [s.n.], DOI: 10.5962/bhl.title.32913.

De Morgan, A., De Morgan, S., and Smith, D. (1915). *A budget of paradoxes.* A budget of paradoxes. Open Court Publishing Company.

Del Sarto, D., Pegoraro, F., and Califano, F. (2016). "Pressure anisotropy and small spatial scales induced by velocity shear". In: *Physical Review E* **93**:5, p. 053203. DOI: 10.1103/PhysRevE.93.053203.

Di Mare, F., Sorriso-Valvo, L., Retinò, A., Malara, F., and Hasegawa, H. (2019). "Evolution of Turbulence in the Kelvin–Helmholtz Instability in the Terrestrial Magnetopause". In: *Atmosphere* **10**:9, p. 561. DOI: 10.3390/atmos10090561.

Du, S., Zank, G. P., Li, X., and Guo, F. (2020). "Energy dissipation and entropy in collisionless plasma". In: *Physical Review E* **101**:3, p. 033208. DOI: 10.1103/PhysRevE.101.033208.

Dungey, J. W. (1961). "Interplanetary magnetic field and the auroral zones". In: *Physical Review Letters* **6**:2, pp. 47–48. DOI: 10.1103/PhysRevLett.6.47.

Dwivedi, N. K., Kumar, S., Kovacs, P., Yordanova, E., Echim, M., Sharma, R. P., Khodachenko, M. L., and Sasunov, Y. (2019). "Implication of kinetic Alfvén waves to magnetic field turbulence spectra: Earth's magnetosheath". In: *Astrophysics and Space Science* **364**:6, p. 101. DOI: 10.1007/s10509-019-3592-2.

Eastwood, J. P., Biffis, E., Hapgood, M. A., Green, L., Bisi, M. M., Bentley, R. D., Wicks, R., McKinnell, L.-A., Gibbs, M., and Burnett, C. (2017). "The Economic Impact of Space Weather: Where Do We Stand?" In: *Risk Analysis* **37**:2, pp. 206–218. DOI: 10.1111/risa.12765.

Eddington, A. S. (1910). "The Envelopes of Comet Morehouse (1908 c)". In: *Monthly Notices of the Royal Astronomical Society* **70**:5, pp. 442–458. DOI: 10.1093/mnras/70.5.442.

Egedal, J., Le, A., and Daughton, W. (2013). "A review of pressure anisotropy caused by electron trapping in collisionless plasma, and its implications for magnetic reconnection". In: *Physics of Plasmas* **20**:6, p. 061201. DOI: 10.1063/1.4811092.

Ergun, R. E., Tucker, S., Westfall, J., Goodrich, K. A., Malaspina, D. M., Summers, D., Wallace, J., Karlsson, M., Mack, J., Brennan, N., Pyke, B., Withnell, P., Torbert, R., Macri, J., Rau, D., Dors, I., Needell, J., Lindqvist, P.-A., Olsson, G., and Cully, C. M. (2016). "The Axial Double Probe and Fields Signal Processing for the MMS Mission". In: *Space Science Reviews* **199**:1-4, pp. 167–188. DOI: 10.1007/s11214-014-0115-x.

Ergun, R. E. et al. (2020). "Observations of Particle Acceleration in Magnetic Reconnection–driven Turbulence". In: *The Astrophysical Journal* **898**:2, p. 154. DOI: 10.3847/1538-4357/ab9ab6.

Escoubet, C. P., Fehringer, M., and Goldstein, M. (2001). "Introduction;The Cluster mission". In: *Annales Geophysicae* **19**:10/12, pp. 1197–1200. DOI: 10.5194/angeo-19-1197-2001.

Fairfield, D. H. (1971). "Average and unusual locations of the Earth's magnetopause and bow shock". In: *Journal of Geophysical Research* **76**:28, pp. 6700–6716. DOI: 10.1029/JA076i028p06700.

Falceta-Gonçalves, D., Kowal, G., Falgarone, E., and Chian, A. C. .-. (2014). "Turbulence in the interstellar medium". In: *Nonlinear Processes in Geophysics* **21**:3, pp. 587–604. DOI: 10.5194/npg-21-587-2014.

Federrath, C. (2013). "On the universality of supersonic turbulence". In: *Monthly Notices of the Royal Astronomical Society* **436**:2, pp. 1245–1257. DOI: 10.1093/mnras/stt1644.

Feldman, W. C., Anderson, R. C., Bame, S. J., Gary, S. P., Gosling, J. T., McComas, D. J., Thomsen, M. F., Paschmann, G., and Hoppe, M. M. (1983). "Electron velocity distributions near the Earth's bow shock". In: *Journal of Geophysical Research: Space Physics* **88**:A1, pp. 96–110. DOI: 10.1029/JA088iA01p00096.

Ferrand, R., Galtier, S., Sahraoui, F., Meyrand, R., Andrés, N., and Banerjee, S. (2019). "On Exact Laws in Incompressible Hall Magnetohydrodynamic Turbulence". In: *The Astrophysical Journal* **881**:1, p. 50. DOI: 10.3847/1538-4357/ab2be9.

Ferrand, R., Galtier, S., and Sahraoui, F. (2021). "A compact exact law for compressible isothermal Hall magnetohydrodynamic turbulence". In: *Journal of Plasma Physics* **87**:2, p. 905870220. DOI: 10.1017/S0022377821000374.

Feynman, R. P., Leighton, R. B., Sands, M., and Hafner, E. M. (1965). "The Feynman Lectures on Physics; Vol. I". In: *American Journal of Physics* **33**:9, pp. 750–752. DOI: 10.1119/1.1972241.

Formisano, V., Moreno, G., Palmiotto, F., and Hedgecock, P. C. (1973). "Solar wind interaction with the Earth's magnetic field: 1. Magnetosheath". In: *Journal of Geophysical Research* **78**:19, pp. 3714–3730. DOI: 10.1029/JA078i019p03714.

Franci, L., Landi, S., Matteini, L., Verdini, A., and Hellinger, P. (2015a). "High-Resolution Hybrid Simulations of Kinetic Plasma Turbulence at Proton Scales". In: *The Astrophysical Journal* **812**:1, p. 21. DOI: 10.1088/0004-637X/812/1/21.

Franci, L., Landi, S., Matteini, L., Verdini, A., and Hellinger, P. (2016). "Plasma Beta Dependence of the Ion-Scale Spectral Break of Solar Wind Turbulence: High-Resolution 2d Hybrid Simulations". In: *The Astrophysical Journal* **833**:1, p. 91. DOI: 10.3847/1538-4357/833/1/91.

Franci, L., Landi, S., Verdini, A., Matteini, L., and Hellinger, P. (2018). "Solar wind turbulent cascade from MHD to sub-ion scales: Large-size 3D hybrid particle-in-cell

simulations". In: *The Astrophysical Journal* **853**:1, p. 26. DOI: 10.3847/1538-4357/aaa3e8.

Franci, L., Stawarz, J. E., Papini, E., Hellinger, P., Nakamura, T., Burgess, D., Landi, S., Verdini, A., Matteini, L., Ergun, R., Le Contel, O., and Lindqvist, P.-A. (2020). "Modeling MMS observations at the earth's magnetopause with hybrid simulations of alfvénic turbulence". In: *The Astrophysical Journal* **898**:2, p. 175. DOI: 10.3847/1538-4357/ab9a47.

Franci, L., Verdini, A., Matteini, L., Landi, S., and Hellinger, P. (2015b). "Solar wind turbulence from MHD to sub-ion scales: High-resolution hybrid simulations". In: *The Astrophysical Journal Letters* **804**:2, p. L39. DOI: 10.1088/2041-8205/804/2/L39.

Frisch, U. (1995). *Turbulence: The legacy of A. N. Kolmogorov*. Cambridge: Cambridge University Press. DOI: 10.1017/CBO9781139170666.

Fuselier, S. A., Lewis, W. S., Schiff, C., Ergun, R., Burch, J. L., Petrinec, S. M., and Trattner, K. J. (2016). "Magnetospheric Multiscale Science Mission Profile and Operations". In: *Space Science Reviews* **199**:1-4, pp. 77–103. DOI: 10.1007/s11214-014-0087-x.

Galtier, S., Nazarenko, S. V., Newell, A. C., and Pouquet, A. (2000). "A weak turbulence theory for incompressible magnetohydrodynamics". In: *Journal of Plasma Physics* **63**:5, pp. 447–488. DOI: 10.1017/S0022377899008284.

Galtier, S. (2008). "von Kármán–Howarth equations for Hall magnetohydrodynamic flows". In: *Physical Review E* **77**:1, p. 015302. DOI: 10.1103/PhysRevE.77.015302.

Gary, S. P. (1993). *Theory of Space Plasma Microinstabilities*. 1st ed. Cambridge University Press. DOI: 10.1017/CBO9780511551512.

Gary, S. P., Jian, L. K., Broiles, T. W., Stevens, M. L., Podesta, J. J., and Kasper, J. C. (2016). "Ion-driven instabilities in the solar wind: Wind observations of 19 March 2005".

In: *Journal of Geophysical Research: Space Physics* **121**:1, pp. 30–41. DOI: 10.1002/2015JA021935.

Gary, S. P., Lavraud, B., Thomsen, M. F., Lefebvre, B., and Schwartz, S. J. (2005). "Electron anisotropy constraint in the magnetosheath: Cluster observations". In: *Geophysical Research Letters* **32**:13, 2005GL023234. DOI: 10.1029/2005GL023234.

Gary, S. P. and Nishimura, K. (2003). "Resonant electron firehose instability: Particle-in-cell simulations". In: *Physics of Plasmas* **10**:9, pp. 3571–3576. DOI: 10.1063/1.1590982.

Gary, S. P., Thomsen, M. F., Yin, L., and Winske, D. (1995). "Electromagnetic proton cyclotron instability: Interactions with magnetospheric protons". In: *Journal of Geophysical Research: Space Physics* **100**:A11, pp. 21961–21972. DOI: 10.1029/95JA01403.

Gary, S. P. and Wang, J. (1996). "Whistler instability: Electron anisotropy upper bound". In: *Journal of Geophysical Research: Space Physics* **101**:A5, pp. 10749–10754. DOI: 10.1029/96JA00323.

Gary, S. P., Wang, J., Winske, D., and Fuselier, S. A. (1997). "Proton temperature anisotropy upper bound". In: *Journal of Geophysical Research: Space Physics* **102**:A12, pp. 27159–27169. DOI: 10.1029/97JA01726.

Genestreti, K. J. et al. (2018). "MMS observation of asymmetric reconnection supported by 3-D electron pressure divergence". In: *Journal of Geophysical Research (Space Physics)* **123**:3, pp. 1806–1821. DOI: 10.1002/2017JA025019.

Gershman, D. J., Avanov, L. A., Boardsen, S. A., Dorelli, J. C., Gliese, U., Barrie, A. C., Schiff, C., Paterson, W. R., Torbert, R. B., Giles, B. L., and Pollock, C. J. (2017). "Spacecraft and Instrument Photoelectrons Measured by the Dual Electron Spectrometers on MMS". In: *Journal of Geophysical Research: Space Physics* **122**:11. DOI: 10.1002/2017JA024518.

Gershman, D. J., Dorelli, J. C., F.-Viñas, A., and Pollock, C. J. (2015). "The calculation of moment uncertainties from velocity distribution functions with random errors". In: *Journal of Geophysical Research: Space Physics* **120**:8, pp. 6633–6645. DOI: 10.1002/2014JA020775.

Gingell, I., Schwartz, S. J., Eastwood, J. P., Burch, J. L., Ergun, R. E., Fuselier, S., Gershman, D. J., Giles, B. L., Khotyaintsev, Y. V., Lavraud, B., Lindqvist, P.-A., Paterson, W. R., Phan, T. D., Russell, C. T., Stawarz, J. E., Strangeway, R. J., Torbert, R. B., and Wilder, F. (2019). "Observations of Magnetic Reconnection in the Transition Region of Quasi-Parallel Shocks". In: *Geophysical Research Letters* **46**:3, pp. 1177–1184. DOI: 10.1029/2018GL081804.

Goldreich, P. and Sridhar, S. (1995). "Toward a theory of interstellar turbulence. II. Strong alfvenic turbulence". In: *The Astrophysical Journal* **438**: p. 763. DOI: 10.1086/175121.

Goldreich, P. and Sridhar, S. (1997). "Magnetohydrodynamic Turbulence Revisited". In: *The Astrophysical Journal* **485**:2, pp. 680–688. DOI: 10.1086/304442.

Gorman, W. and Klein, K. G. (2024). "Mind the gap: non-local cascades and preferential heating in high-β Alfvénic turbulence". In: *Monthly Notices of the Royal Astronomical Society: Letters* **531**:1, pp. L1–L7. DOI: 10.1093/mnrasl/slae018.

Graham, D. B., Khotyaintsev, Y. V., André, M., Vaivads, A., Chasapis, A., Matthaeus, W. H., Retinò, A., Valentini, F., and Gershman, D. J. (2021). "Non-Maxwellianity of Electron Distributions Near Earth's Magnetopause". In: *Journal of Geophysical Research: Space Physics* **126**:10. DOI: 10.1029/2021JA029260.

Grappin, R., Mangeney, A., and Marsch, E. (1990). "On the origin of solar wind MHD turbulence: Helios data revisited". In: *Journal of Geophysical Research: Space Physics* **95**:A6, pp. 8197–8209. DOI: 10.1029/JA095iA06p08197.

Greco, A., Chuychai, P., Matthaeus, W. H., Servidio, S., and Dmitruk, P. (2008). "Intermittent MHD structures and classical discontinuities". In: *Geophysical Research Letters* **35**:19, 2008GL035454. DOI: 10.1029/2008GL035454.

Greco, A., Matthaeus, W. H., Perri, S., Osman, K. T., Servidio, S., Wan, M., and Dmitruk, P. (2018). "Partial Variance of Increments Method in Solar Wind Observations and Plasma Simulations". In: *Space Science Reviews* **214**:1, p. 1. DOI: 10.1007/s11214-017-0435-8.

Greco, A., Matthaeus, W. H., Servidio, S., Chuychai, P., and Dmitruk, P. (2009). "Statistical Analysis of Discontinuities in Solar Wind ¡i¿ace¡/I¿ Data and Comparison with Intermittent Mhd Turbulence". In: *The Astrophysical Journal* **691**:2, pp. L111–L114. DOI: 10.1088/0004-637X/691/2/L111.

Greco, A., Valentini, F., Servidio, S., and Matthaeus, W. H. (2012). "Inhomogeneous kinetic effects related to intermittent magnetic discontinuities". In: *Physical Review E* **86**:6, p. 066405. DOI: 10.1103/PhysRevE.86.066405.

Greenstadt, E. W. (1972). "Binary index for assessing local bow shock obliquity". In: *Journal of Geophysical Research* **77**:28, pp. 5467–5479. DOI: 10.1029/JA077i028p05467.

Gringauz, K. I., Bezrokikh, V. V., Ozerov, V. D., and Rybchinskii, R. E. (1960). "A Study of the Interplanetary Ionized Gas, High-Energy Electrons and Corpuscular Radiation from the Sun by Means of the Three-Electrode Trap for Charged Particles on the Second Soviet Cosmic Rocket". In: *Soviet Physics Doklady* **5**: p. 361.

Gurnett, D. A. and Bhattacharjee, A. (2005). *Introduction to Plasma Physics: With Space and Laboratory Applications*. 1st ed. Cambridge University Press. DOI: 10.1017/CBO9780511809125.

Hadid, L. Z., Sahraoui, F., Kiyani, K. H., Retinò, A., Modolo, R., Canu, P., Masters, A., and Dougherty, M. K. (2015). "Nature of the MHD and kinetic scale turbulence in the

magnetosheath of saturn: Cassini observations". In: *The Astrophysical Journal* **813**:2, p. L29. DOI: 10.1088/2041-8205/813/2/L29.

Harvey, C. C. (1998). "Spatial gradients and the volumetric tensor". In: *ISSI Scientific Reports Series* **1**: pp. 307–322.

Hellinger, P., Papini, E., Verdini, A., Landi, S., Franci, L., Matteini, L., and Montagud-Camps, V. (2021). "Spectral Transfer and Kármán–Howarth–Monin Equations for Compressible Hall Magnetohydrodynamics". In: *The Astrophysical Journal* **917**:2, p. 101. DOI: 10.3847/1538-4357/ac088f.

Hellinger, P., Trávníček, P., Kasper, J. C., and Lazarus, A. J. (2006). "Solar wind proton temperature anisotropy: Linear theory and WIND/SWE observations". In: *Geophysical Research Letters* **33**:9, p. L09101. DOI: 10.1029/2006GL025925.

Hellinger, P., Verdini, A., Landi, S., Franci, L., and Matteini, L. (2018). "von Kármán–Howarth Equation for Hall Magnetohydrodynamics: Hybrid Simulations". In: *The Astrophysical Journal Letters* **857**:2, p. L19. DOI: 10.3847/2041-8213/aabc06.

Hesse, M. and Cassak, P. A. (2020). "Magnetic reconnection in the space sciences: Past, present, and future". In: *Journal of Geophysical Research: Space Physics* **125**:2, e2018JA025935. DOI: https://doi.org/10.1029/2018JA025935.

Hesse, M. and Winske, D. (1993). "Hybrid simulations of collisionless ion tearing". In: *Geophysical Research Letters* **20**:12, pp. 1207–1210. DOI: 10.1029/93GL01250.

Hodgson, R. (1859). "Mr. Carrington regrets having omitted previously to communicate the following passage in a letter from M. Schwabe, dated March, which is plainly intended for others as well as himself". In: *Monthly Notices of the Royal Astronomical Society* **20**:1, pp. 15–16. DOI: 10.1093/mnras/20.1.15.

Horbury, T. S., Wicks, R. T., and Chen, C. H. K. (2012). "Anisotropy in Space Plasma Turbulence: Solar Wind Observations". In: *Space Science Reviews* **172**:1-4, pp. 325–342. DOI: 10.1007/s11214-011-9821-9.

Horbury, T. S., Forman, M., and Oughton, S. (2008). "Anisotropic scaling of magnetohydrodynamic turbulence". In: *Physical Review Letters* **101**:17. DOI: 10.1103/physrevlett.101.175005.

Howes, G. G., Dorland, W., Cowley, S. C., Hammett, G. W., Quataert, E., Schekochihin, A. A., and Tatsuno, T. (2008). "Kinetic Simulations of Magnetized Turbulence in Astrophysical Plasmas". In: *Physical Review Letters* **100**:6, p. 065004. DOI: 10.1103/PhysRevLett.100.065004.

Howes, G. G., Tenbarge, J. M., Dorland, W., Quataert, E., Schekochihin, A. A., Numata, R., and Tatsuno, T. (2011). "Gyrokinetic simulations of solar wind turbulence from ion to electron scales". In: *The Astrophysical Journal* **107**:3, p. 035004. DOI: 10.1103/PhysRevLett.107.035004.

Howes, G. G. (2024). "The fundamental parameters of astrophysical plasma turbulence and its dissipation: non-relativistic limit". In: *Journal of Plasma Physics* **90**:5, p. 905900504. DOI: 10.1017/S0022377824001090.

Howes, G. G., Klein, K. G., and Li, T. C. (2017). "Diagnosing collisionless energy transfer using field–particle correlations: Vlasov–Poisson plasmas". In: *Journal of Plasma Physics* **83**:1, p. 705830102. DOI: 10.1017/S0022377816001197.

Huang, S. Y., Hadid, L. Z., Sahraoui, F., Yuan, Z. G., and Deng, X. H. (2017). "On the Existence of the Kolmogorov Inertial Range in the Terrestrial Magnetosheath Turbulence". In: *The Astrophysical Journal* **836**:1, p. L10. DOI: 10.3847/2041-8213/836/1/L10.

Huang, S. Y., Sahraoui, F., Deng, X. H., He, J. S., Yuan, Z. G., Zhou, M., Pang, Y., and Fu, H. S. (2014). "Kinetic turbulence in the terrestrial magnetosheath: Cluster

observations". In: *The Astrophysical Journal Letters* **789**:2, p. L28. DOI: 10.1088/2041-8205/789/2/L28.

Iroshnikov, P. S. (1964). "Turbulence of a conducting fluid in a strong magnetic field". In: *Soviet Astronomy* **7**: p. 566.

Irving Langmuir (1928). "Oscillations in ionized gases". In: *Proceedings of the National Academy of Sciences* **14**:8, pp. 627–637. DOI: 10.1073/pnas.14.8.627.

Jiang, W., Verscharen, D., Jeong, S.-Y., Li, H., Klein, K. G., Owen, C. J., and Wang, C. (2024). "Velocity-space Signatures of Resonant Energy Transfer between Whistler Waves and Electrons in the Earth's Magnetosheath". In: *The Astrophysical Journal* **960**:1, p. 30. DOI: 10.3847/1538-4357/ad0df8.

Johlander, A., Vaivads, A., Khotyaintsev, Y. V., Gingell, I., Schwartz, S. J., Giles, B. L., Torbert, R. B., and Russell, C. T. (2018). "Shock ripples observed by the MMS spacecraft: ion reflection and dispersive properties". In: *Plasma Physics and Controlled Fusion* **60**:12, p. 125006. DOI: 10.1088/1361-6587/aae920.

Johnson, J. R., Wing, S., and Delamere, P. A. (2014). "Kelvin Helmholtz Instability in Planetary Magnetospheres". In: *Space Science Reviews* **184**:1-4, pp. 1–31. DOI: 10.1007/s11214-014-0085-z.

Karimabadi, H., Roytershteyn, V., Vu, H. X., Omelchenko, Y. A., Scudder, J., Daughton, W., Dimmock, A., Nykyri, K., Wan, M., Sibeck, D., Tatineni, M., Majumdar, A., Loring, B., and Geveci, B. (2014). "The link between shocks, turbulence, and magnetic reconnection in collisionless plasmas". In: *Physics of Plasmas* **21**:6, p. 062308. DOI: 10.1063/1.4882875.

Karimabadi, H., Roytershteyn, V., Wan, M., Matthaeus, W. H., Daughton, W., Wu, P., Shay, M., Loring, B., Borovsky, J., Leonardis, E., Chapman, S. C., and Nakamura, T. K. M. (2013). "Coherent structures, intermittent turbulence, and dissipation in high-

temperature plasmas". In: *Physics of Plasmas* **20**:1, p. 012303. DOI: 10.1063/1.4773205.

Kaufmann, R. L. and Paterson, W. R. (2009). "Boltzmann H function and entropy in the plasma sheet". In: *Journal of Geophysical Research: Space Physics* **114**:A9, n/a–n/a. DOI: 10.1029/2008JA014030.

Kavosi, S. and Raeder, J. (2015). "Ubiquity of Kelvin–Helmholtz waves at Earth's magnetopause". In: *Nature Communications* **6**:1, p. 7019. DOI: 10.1038/ncomms8019.

Khotyaintsev, Y. V., Vaivads, A., Retinò, A., André, M., Owen, C. J., and Nilsson, H. (2006). "Formation of inner structure of a reconnection separatrix region". In: *Physical Review Letters* **97**:20, p. 205003. DOI: 10.1103/PhysRevLett.97.205003.

Kiyani, K. H., Osman, K. T., and Chapman, S. C. (2015). "Dissipation and heating in solar wind turbulence: from the macro to the micro and back again". In: *Philosophical Transactions of the Royal Society A: Mathematical, Physical and Engineering Sciences* **373**:2041, p. 20140155. DOI: 10.1098/rsta.2014.0155.

Klein, K. G. and Howes, G. G. (2016). "Measuring Collisionless Damping in Heliospheric Plasmas Using Field–Particle Correlations". In: *The Astrophysical Journal* **826**:2, p. L30. DOI: 10.3847/2041-8205/826/2/L30.

Klein, K. G., Howes, G. G., and TenBarge, J. M. (2014). "The Violation of the Taylor Hypothesis in Measurements of Solar Wind Turbulence". In: *The Astrophysical Journal* **790**:2, p. L20. DOI: 10.1088/2041-8205/790/2/L20.

Klein, K. G., Alterman, B. L., Stevens, M. L., Vech, D., and Kasper, J. C. (2018). "Majority of Solar Wind Intervals Support Ion-Driven Instabilities". In: *Physical Review Letters* **120**:20, p. 205102. DOI: 10.1103/PhysRevLett.120.205102.

Klein, K. G., Howes, G. G., and TenBarge, J. M. (2017). "Diagnosing collisionless energy transfer using field–particle correlations: gyrokinetic turbulence". In: *Journal of Plasma Physics* **83**:4, p. 535830401. DOI: 10.1017/S0022377817000563.

Klein, K. G., Martinović, M., Stansby, D., and Horbury, T. S. (2019a). "Linear Stability in the Inner Heliosphere: Helios Re-evaluated". In: *The Astrophysical Journal* **887**:2, p. 234. DOI: 10.3847/1538-4357/ab5802.

Klein, K. G., Martinović, M., Stansby, D., and Horbury, T. S. (2019b). "Linear Stability in the Inner Heliosphere: Helios Re-evaluated". In: *The Astrophysical Journal* **887**:2, p. 234. DOI: 10.3847/1538-4357/ab5802.

Klein, K. G., Verniero, J. L., Alterman, B., Bale, S., Case, A., Kasper, J. C., Korreck, K., Larson, D., Lichko, E., Livi, R., McManus, M., Martinović, M., Rahmati, A., Stevens, M., and Whittlesey, P. (2021). "Inferred Linear Stability of Parker Solar Probe Observations Using One- and Two-component Proton Distributions". In: *The Astrophysical Journal* **909**:1, p. 7. DOI: 10.3847/1538-4357/abd7a0.

Klein, K. G. et al. (2023). "HelioSwarm: A Multipoint, Multiscale Mission to Characterize Turbulence". In: *Space Science Reviews* **219**:8, p. 74. DOI: 10.1007/s11214-023-01019-0.

Kolmogorov, A. N. (1941a). "Dissipation of energy in the locally isotropic turbulence". In: *Proceedings of the Royal Society of London. Series A - Mathematical and Physical Sciences* **434**:1890, pp. 15–17.

Kolmogorov, A. N. (1941b). "The local structure of turbulence in incompressible viscous fluid for very large reynolds' numbers". In: *Akademiia Nauk SSSR Doklady* **30**: pp. 301–305.

Kraichnan, R. H. (1965). "Inertial-range spectrum of hydromagnetic turbulence". In: *Physics of Fluids* **8**:7, pp. 1385–1387. DOI: 10.1063/1.1761412.

Kunz, M. W., Abel, I. G., Klein, K. G., and Schekochihin, A. A. (2018). "Astrophysical gyrokinetics: turbulence in pressure-anisotropic plasmas at ion scales and beyond". In: *Journal of Plasma Physics* **84**:2, p. 715840201. DOI: 10.1017/S0022377818000296.

Le Contel, O. et al. (2016). "The Search-Coil Magnetometer for MMS". In: *Space Science Reviews* **199**:1-4, pp. 257–282. DOI: 10.1007/s11214-014-0096-9.

Lee, E., Brachet, M. E., Pouquet, A., Mininni, P. D., and Rosenberg, D. (2010). "Lack of universality in decaying magnetohydrodynamic turbulence". In: *Physical Review E* **81**:1, p. 016318. DOI: 10.1103/PhysRevE.81.016318.

Lewis, H. C., Stawarz, J. E., Franci, L., Matteini, L., Klein, K., Salem, C. S., Burch, J. L., Ergun, R. E., Giles, B. L., Russell, C. T., and Lindqvist, P.-A. (2023). "Magnetospheric Multiscale measurements of turbulent electric fields in earth's magnetosheath: How do plasma conditions influence the balance of terms in generalized Ohm's law?" In: *Physics of Plasmas* **30**:8, p. 082901. DOI: 10.1063/5.0158067.

Lewis, H. C., Stawarz, J. E., Matteini, L., Franci, L., Klein, K. G., Wicks, R. T., Salem, C. S., Horbury, T. S., and Wang, J. H. (2024). "Turbulent Energy Conversion Associated With Kinetic Microinstabilities in Earth's Magnetosheath". In: *Geophysical Research Letters* **51**:24, e2024GL112038. DOI: 10.1029/2024GL112038.

Li, H., Jiang, W., Wang, C., Verscharen, D., Zeng, C., Russell, C. T., Giles, B., and Burch, J. L. (2020). "Evolution of the earth's magnetosheath turbulence: A statistical study based on MMS observations". In: *The Astrophysical Journal Letters* **898**:2, p. L43. DOI: 10.3847/2041-8213/aba531.

Liang, H., Barbhuiya, M. H., Cassak, P. A., Pezzi, O., Servidio, S., Valentini, F., and Zank, G. P. (2020). "Kinetic entropy-based measures of distribution function non-Maxwellianity: theory and simulations". In: *Journal of Plasma Physics* **86**:5, p. 825860502. DOI: 10.1017/S0022377820001270.

Liang, H., Cassak, P. A., Servidio, S., Shay, M. A., Drake, J. F., Swisdak, M., Argall, M. R., Dorelli, J. C., Scime, E. E., Matthaeus, W. H., Roytershteyn, V., and Delzanno, G. L. (2019). "Decomposition of plasma kinetic entropy into position and velocity space and the use of kinetic entropy in particle-in-cell simulations". In: *Physics of Plasmas* **26**:8, p. 082903. DOI: 10.1063/1.5098888.

Lindqvist, P. .-. et al. (2016). "The spin-plane double probe electric field instrument for MMS". In: *Space Science Reviews* **199**:1-4, pp. 137–165. DOI: 10.1007/s11214-014-0116-9.

Livadiotis, G., Desai, M. I., and Wilson, L. B. (2018). "Generation of Kappa Distributions in Solar Wind at 1 au". In: *The Astrophysical Journal* **853**:2, p. 142. DOI: 10.3847/1538-4357/aaa713.

Lopez, R. E. and Gonzalez, W. D. (2017). "Magnetospheric balance of solar wind dynamic pressure". In: *Geophysical Research Letters* **44**:7, pp. 2991–2999. DOI: 10.1002/2017GL072817.

Lyons, L. R. and Pridmore-Brown, D. C. (1990). "Force balance near an X line in a collisionless plasma". In: *Journal of Geophysical Research: Space Physics* **95**:A12, pp. 20903–20909. DOI: 10.1029/JA095iA12p20903.

Ma, Y., Cheng, W., Huang, S., Schmitt, F. G., Lin, X., and Huang, Y. (2024). "Hidden turbulence in van Gogh's *The Starry Night*". In: *Physics of Fluids* **36**:9, p. 095140. DOI: 10.1063/5.0213627.

Magyar, N., Van Doorsselaere, T., and Goossens, M. (2019). "The nature of elsässer variables in compressible MHD". In: *The Astrophysical Journal* **873**:1, p. 56. DOI: 10.3847/1538-4357/ab04a7.

Marino, R. and Sorriso-Valvo, L. (2023). "Scaling laws for the energy transfer in space plasma turbulence". In: *Physics Reports* **1006**: pp. 1–144. DOI: 10.1016/j.physrep.2022.12.001.

Markovskii, S. A., Vasquez, B. J., and Chandran, B. D. G. (2019). "Proton Temperature-anisotropy Instability Coexisting with Ambient Turbulence in the Solar-wind Plasma". In: *The Astrophysical Journal* **875**:2, p. 125. DOI: 10.3847/1538-4357/ab0f9d.

Marsch, E. and Tu, C.-Y. (1990). "On the radial evolution of MHD turbulence in the inner heliosphere". In: *Journal of Geophysical Research: Space Physics* **95**:A6, pp. 8211–8229. DOI: 10.1029/JA095iA06p08211.

Marsch, E. (2006). "Kinetic Physics of the Solar Corona and Solar Wind". In: *Living Reviews in Solar Physics* **3**: DOI: 10.12942/lrsp-2006-1.

Maruca, B. A., Chasapis, A., Gary, S. P., Bandyopadhyay, R., Chhiber, R., Parashar, T. N., Matthaeus, W. H., Shay, M. A., Burch, J. L., Moore, T. E., Pollock, C. J., Giles, B. J., Paterson, W. R., Dorelli, J., Gershman, D. J., Torbert, R. B., Russell, C. T., and Strangeway, R. J. (2018). "*MMS* Observations of Beta-dependent Constraints on Ion Temperature Anisotropy in Earth's Magnetosheath". In: *The Astrophysical Journal* **866**:1, p. 25. DOI: 10.3847/1538-4357/aaddfb.

Maruca, B. A., Kasper, J. C., and Gary, S. P. (2012). "Instability-Driven Limits on Helium Temperature Anisotropy in the Solar Wind: Observations and Linear Vlasov Analysis". In: *The Astrophysical Journal* **748**:2, p. 137. DOI: 10.1088/0004-637X/748/2/137.

Maruca, B. A., Qudsi, R. A., Alterman, B. L., Walsh, B. M., Korreck, K. E., Verscharen, D., Bandyopadhyay, R., Chhiber, R., Chasapis, A., Parashar, T. N., Matthaeus, W. H., and Goldstein, M. L. (2023). "The Trans-Heliospheric Survey: Radial trends in plasma parameters across the heliosphere". In: *Astronomy & Astrophysics* **675**: A196. DOI: 10.1051/0004-6361/202345951.

Matteini, L., Alexandrova, O., Chen, C. H. K., and Lacombe, C. (2016). "Electric and magnetic spectra from MHD to electron scales in the magnetosheath". In: *Monthly Notices of the Royal Astronomical Society* **466**:1, pp. 945–951. DOI: 10.1093/mnras/stw3163.

Matteini, L., Hellinger, P., Goldstein, B. E., Landi, S., Velli, M., and Neugebauer, M. (2013). "Signatures of kinetic instabilities in the solar wind". In: *Journal of Geophysical Research: Space Physics* **118**:6, pp. 2771–2782. DOI: 10.1002/jgra.50320.

Matthaeus, W. H., Goldstein, M. L., and King, J. H. (1986). "An interplanetary magnetic field ensemble at 1 AU". In: *Journal of Geophysical Research* **91**:A1, p. 59. DOI: 10.1029/JA091iA01p00059.

Matthaeus, W. H., Goldstein, M., and Roberts, D. (1991). "Evidence for the presence of quasi-two-dimensional nearly incompressible fluctuations in the solar wind". In: *Journal of Geophysical Research* **95**: DOI: 10.1029/JA095iA12p20673.

Matthaeus, W. H., Oughton, S., Osman, K. T., Servidio, S., Wan, M., Gary, S. P., Shay, M. A., Valentini, F., Roytershteyn, V., Karimabadi, H., and Chapman, S. C. (2014). "Nonlinear and Linear Timescales Near Kinetic Scales in Solar Wind Turbulence". In: *The Astrophysical Journal* **790**:2, p. 155. DOI: 10.1088/0004-637X/790/2/155.

Matthaeus, W. H., Servidio, S., and Dmitruk, P. (2008). "Comment on "Kinetic Simulations of Magnetized Turbulence in Astrophysical Plasmas"". In: *Physical Review Letters* **101**:14, p. 149501. DOI: 10.1103/PhysRevLett.101.149501.

Matthaeus, W. H., Servidio, S., Dmitruk, P., Carbone, V., Oughton, S., Wan, M., and Osman, K. T. (2012). "Local Anisotropy, Higher Order Statistics, and Turbulence Spectra". In: *The Astrophysical Journal* **750**:2, p. 103. DOI: 10.1088/0004-637X/750/2/103.

Matthaeus, W. H., Wan, M., Servidio, S., Greco, A., Osman, K. T., Oughton, S., and Dmitruk, P. (2015). "Intermittency, nonlinear dynamics and dissipation in the solar wind and astrophysical plasmas". In: *Philosophical Transactions of the Royal Society A: Mathematical, Physical and Engineering Sciences* **373**:2041, p. 20140154. DOI: 10.1098/rsta.2014.0154.

Matthaeus, W. H., Yang, Y., Wan, M., Parashar, T. N., Bandyopadhyay, R., Chasapis, A., Pezzi, O., and Valentini, F. (2020). "Pathways to dissipation in weakly collisional plasmas". In: *The Astrophysical Journal* **891**:1, p. 101. DOI: 10.3847/1538-4357/ab6d6a.

Matthaeus, W. H. and Goldstein, M. L. (1982). "Measurement of the rugged invariants of magnetohydrodynamic turbulence in the solar wind". In: *Journal of Geophysical Research: Space Physics* **87**:A8, pp. 6011–6028. DOI: 10.1029/JA087iA08p06011.

McManus, M. D., Klein, K. G., Bale, S. D., Bowen, T. A., Huang, J., Larson, D., Livi, R., Rahmati, A., Romeo, O., Verniero, J., and Whittlesey, P. (2024). "Proton- and Alpha-driven Instabilities in an Ion Cyclotron Wave Event". In: *The Astrophysical Journal* **961**:1, p. 142. DOI: 10.3847/1538-4357/ad05ba.

Montgomery, M. D., Asbridge, J. R., and Bame, S. J. (1970). "Vela 4 plasma observations near the Earth's bow shock". In: *Journal of Geophysical Research* **75**:7, pp. 1217–1231. DOI: 10.1029/JA075i007p01217.

Montgomery, M. D., Brown, M. R., and Matthaeus, W. H. (1987). "Density fluctuation spectra in magnetohydrodynamic turbulence". In: *Journal of Geophysical Research* **92**:A1, p. 282. DOI: 10.1029/JA092iA01p00282.

Narita, Y. and Gary, S. P. (2010). "Inertial-range spectrum of whistler turbulence". In: *Annales Geophysicae* **28**:2, pp. 597–601. DOI: 10.5194/angeo-28-597-2010.

Navier, C. L. M. H. (1822). "Memoire sur les lois du mouvement des uides". In: *Mem. Acad. Sci. Inst. France.* **6**:389.

Neugebauer, M. and Snyder, C. W. (1962). "Solar Plasma Experiment". In: *Science* **138**:3545, pp. 1095–1097. DOI: 10.1126/science.138.3545.1095.b.

Opie, S., Verscharen, D., Chen, C. H. K., Owen, C. J., and Isenberg, P. A. (2023). "The effect of variations in the magnetic field direction from turbulence on kinetic-scale instabilities". In: *Astronomy & Astrophysics* **672**: p. L4. DOI: 10.1051/0004-6361/202345965.

Osman, K. T., Matthaeus, W. H., Greco, A., and Servidio, S. (2011). "Evidence for Inhomogeneous Heating in the Solar Wind". In: *The Astrophysical Journal* **727**:1, p. L11. DOI: 10.1088/2041-8205/727/1/L11.

Owens, M. J. and Forsyth, R. J. (2013). "The Heliospheric Magnetic Field". In: *Living Reviews in Solar Physics* **10**: DOI: 10.12942/lrsp-2013-5.

Papen, M. von, Saur, J., and Alexandrova, O. (2014). "Turbulent magnetic field fluctuations in Saturn's magnetosphere". In: *Journal of Geophysical Research: Space Physics* **119**:4, pp. 2797–2818. DOI: 10.1002/2013JA019542.

Papini, E., Franci, L., Landi, S., Verdini, A., Matteini, L., and Hellinger, P. (2019). "Can hall magnetohydrodynamics explain plasma turbulence at sub-ion scales?" In: *The Astrophysical Journal* **870**:1, p. 52. DOI: 10.3847/1538-4357/aaf003.

Parashar, T. N. and Matthaeus, W. H. (2016). "Propinquity of Current and Vortex Structures: Effects on Collisionless Plasma Heating". In: *The Astrophysical Journal* **832**:1, p. 57. DOI: 10.3847/0004-637X/832/1/57.

Parashar, T. N., Chasapis, A., Bandyopadhyay, R., Chhiber, R., Matthaeus, W. H., Maruca, B., Shay, M. A., Burch, J. L., Moore, T. E., Giles, B. L., Gershman, D. J., Pollock, C. J., Torbert, R. B., Russell, C. T., Strangeway, R. J., and Roytershteyn, V. (2018). "Kinetic Range Spectral Features of Cross Helicity Using the Magnetospheric Multiscale Spacecraft". In: *Physical Review Letters* **121**:26, p. 265101. DOI: 10.1103/PhysRevLett.121.265101.

Parashar, T. N. and Gary, S. P. (2019). "Dissipation of Kinetic Alfvénic Turbulence as a Function of Ion and Electron Temperature Ratios". In: *The Astrophysical Journal* **882**:1, p. 29. DOI: 10.3847/1538-4357/ab2fc8.

Parker, E. N. (1958). "Dynamics of the interplanetary gas and magnetic fields." In: *The Astrophysical Journal* **128**: p. 664. DOI: 10.1086/146579.

Paschmann, G. and Daly, P. W. (1998). "Analysis methods for multi-spacecraft data. ISSI scientific reports series SR-001, ESA/ISSI, vol. 1. ISBN 1608-280X, 1998". In: *ISSI Scientific Reports Series* **1**:

Pecora, F., Yang, Y., Matthaeus, W. H., Chasapis, A., Klein, K. G., Stevens, M., Servidio, S., Greco, A., Gershman, D. J., Giles, B. L., and Burch, J. L. (2023). "Three-Dimensional Energy Transfer in Space Plasma Turbulence from Multipoint Measurement". In: *Physical Review Letters* **131**:22, p. 225201. DOI: 10.1103/PhysRevLett.131.225201.

Perri, S. et al. (2020). "On the deviation from Maxwellian of the ion velocity distribution functions in the turbulent magnetosheath". In: *Journal of Plasma Physics* **86**:1, p. 905860108. DOI: 10.1017/S0022377820000021.

Perri, S., Servidio, S., Vaivads, A., and Valentini, F. (2017). "Numerical Study on the Validity of the Taylor Hypothesis in Space Plasmas". In: *The Astrophysical Journal Supplement Series* **231**:1, p. 4. DOI: 10.3847/1538-4365/aa755a.

Pezzi, O., Liang, H., Juno, J. L., Cassak, P. A., Vásconez, C. L., Sorriso-Valvo, L., Perrone, D., Servidio, S., Roytershteyn, V., TenBarge, J. M., and Matthaeus, W. H. (2021a). "Dissipation measures in weakly collisional plasmas". In: *Monthly Notices of the Royal Astronomical Society* **505**: pp. 4857–4873. DOI: 10.1093/mnras/stab1516.

Pezzi, O., Pecora, F., Le Roux, J., Engelbrecht, N. E., Greco, A., Servidio, S., Malova, H. V., Khabarova, O. V., Malandraki, O., Bruno, R., Matthaeus, W. H., Li, G., Zelenyi, L. M., Kislov, R. A., Obridko, V. N., and Kuznetsov, V. D. (2021b). "Current Sheets, Plasmoids and Flux Ropes in the Heliosphere: Part II: Theoretical Aspects". In: *Space Science Reviews* **217**:3, p. 39. DOI: 10.1007/s11214-021-00799-7.

Pezzi, O., Yang, Y., Valentini, F., Servidio, S., Chasapis, A., Matthaeus, W. H., and Veltri, P. (2019). "Energy conversion in turbulent weakly collisional plasmas: Eulerian hybrid Vlasov-Maxwell simulations". In: *Physics of Plasmas* **26**:7, p. 072301. DOI: 10.1063/1.5100125.

Phan, T. D. et al. (2018). "Electron magnetic reconnection without ion coupling in Earth's turbulent magnetosheath". In: *Nature* **557**:7704, pp. 202–206. DOI: 10.1038/s41586-018-0091-5.

Plank, J. and Gingell, I. L. (2023). "Intermittency at Earth's bow shock: Measures of turbulence in quasi-parallel and quasi-perpendicular shocks". In: *Physics of Plasmas* **30**:8, p. 082906. DOI: 10.1063/5.0160439.

Politano, H. and Pouquet, A. (1998a). "von Kármán–Howarth equation for magnetohydrodynamics and its consequences on third-order longitudinal structure and correlation functions". In: *Physical Review E* **57**:1, R21–R24. DOI: 10.1103/PhysRevE.57.R21.

Politano, H. and Pouquet, A. (1998b). "Dynamical length scales for turbulent magnetized flows". In: *Geophysical Research Letters* **25**:3, pp. 273–276. DOI: 10.1029/97GL03642.

Pollock, C. et al. (2016). "Fast plasma investigation for magnetospheric multiscale". In: *Space Science Reviews* **199**:1-4, pp. 331–406. DOI: 10.1007/s11214-016-0245-4.

Qudsi, R. A., Bandyopadhyay, R., Maruca, B. A., Parashar, T. N., Matthaeus, W. H., Chasapis, A., Gary, S. P., Giles, B. L., Gershman, D. J., Pollock, C. J., Strangeway, R. J., Torbert, R. B., Moore, T. E., and Burch, J. L. (2020). "Intermittency and Ion Temperature–Anisotropy Instabilities: Simulation and Magnetosheath Observation". In: *The Astrophysical Journal* **895**:2, p. 83. DOI: 10.3847/1538-4357/ab89ad.

Rakhmanova, L., Khokhlachev, A., Riazantseva, M., Yermolaev, Y., and Zastenker, G. (2024). "Modification of the turbulence properties at the bow shock: statistical results". In: *Frontiers in Astronomy and Space Sciences* **11**: p. 1379664. DOI: 10.3389/fspas.2024.1379664.

Rakhmanova, L., Riazantseva, M., and Zastenker, G. (2021). "Plasma and magnetic field turbulence in the earth's magnetosheath at ion scales". In: *Frontiers in Astronomy and Space Sciences* **7**: DOI: 10.3389/fspas.2020.616635.

Retinò, A., Sundkvist, D., Vaivads, A., Mozer, F., André, M., and Owen, C. J. (2007). "In situ evidence of magnetic reconnection in turbulent plasma". In: *Nature Physics* **3**:4, pp. 235–238. DOI: 10.1038/nphys574.

Retinò, A. et al. (2022). "Particle energization in space plasmas: towards a multi-point, multi-scale plasma observatory". In: *Experimental Astronomy* **54**:2-3, pp. 427–471. DOI: 10.1007/s10686-021-09797-7.

Richardson, L. (1922). "Weather prediction by numerical process." In: *Quarterly Journal of the Royal Meteorological Society* **48**:203, pp. 282–284. DOI: https://doi.org/10.1002/qj.49704820311.

Robert, P., Dunlop, M. W., Roux, A., and Chanteur, G. (1998a). "Accuracy of current density determination". In: *ISSI Scientific Reports Series* **1**: pp. 395–418.

Robert, P., Roux, A., Harvey, C. C., Dunlop, M. W., Daly, P. W., and Glassmeier, K.-H. (1998b). "Tetrahedron Geometric Factors". In: *ISSI Scientific Reports Series* **1**: pp. 323–348.

Roberts, O. W., Narita, Y., Nakamura, R., Vörös, Z., and Verscharen, D. (2022). "The kinetic Alfvén-like nature of turbulent fluctuations in the Earth's magnetosheath: MMS measurement of the electron Alfvén ratio". In: *Physics of Plasmas* **29**:1, p. 012308. DOI: 10.1063/5.0068828.

Roberts, O. W., Alexandrova, O., Kajdič, P., Turc, L., Perrone, D., Escoubet, C. P., and Walsh, A. (2017). "Variability of the Magnetic Field Power Spectrum in the Solar Wind at Electron Scales". In: *The Astrophysical Journal* **850**:2, p. 120. DOI: 10.3847/1538-4357/aa93e5.

Roy, S., Bandyopadhyay, R., Yang, Y., Parashar, T. N., Matthaeus, W. H., Adhikari, S., Roytershteyn, V., Chasapis, A., Li, H., Gershman, D. J., Giles, B. L., and Burch, J. L. (2022). "Turbulent Energy Transfer and Proton–Electron Heating in Collisionless Plasmas". In: *The Astrophysical Journal* **941**:2, p. 137. DOI: 10.3847/1538-4357/aca479.

Russell, C. T. et al. (2016). "The magnetospheric multiscale magnetometers". In: *Space Science Reviews* **199**:1-4, pp. 189–256. DOI: 10.1007/s11214-014-0057-3.

Sabine, E. (1851). "V. On periodical laws discoverable in the mean effects of the larger magnetic disturbances". In: *Philosophical Transactions of the Royal Society of London* **141**: pp. 123–139. DOI: 10.1098/rstl.1851.0007.

Sabine, E. (1852). "VIII. On periodical laws discoverable in the mean effects of the larger magnetic disturbance.—No. II". In: *Philosophical Transactions of the Royal Society of London* **142**: pp. 103–124. DOI: 10.1098/rstl.1852.0009.

Sahraoui, F., Belmont, G., and Goldstein, M. L. (2012). "New Insight into Short-Wavelength Solar Wind Fluctuations from Vlasov Theory". In: *The Astrophysical Journal* **748**:2, p. 100. DOI: 10.1088/0004-637X/748/2/100.

Sahraoui, F., Huang, S. Y., Belmont, G., Goldstein, M. L., Rétino, A., Robert, P., and De Patoul, J. (2013). "Scaling of the Electron Dissipation Range of Solar Wind Turbulence". In: *The Astrophysical Journal* **777**:1, p. 15. DOI: 10.1088/0004-637X/777/1/15.

Sahraoui, F., Hadid, L., and Huang, S. (2020). "Magnetohydrodynamic and kinetic scale turbulence in the near-Earth space plasmas: a (short) biased review". In: *Reviews of Modern Plasma Physics* **4**:1, p. 4. DOI: 10.1007/s41614-020-0040-2.

Salem, C. S., Howes, G. G., Sundkvist, D., Bale, S. D., Chaston, C. C., Chen, C. H. K., and Mozer, F. S. (2012). "Identification of Kinetic Alfvén Wave Turbulence in the Solar

Wind". In: *The Astrophysical Journal* **745**:1, p. L9. DOI: 10.1088/2041-8205/745/1/L9.

Santos-Lima, R., Gouveia Dal Pino, E. M. de, and Lazarian, A. (2012). "The role of turbulent magnetic reconnection in the formation of rotationally supported protostellar disks". In: *The Astrophysical Journal* **747**:1, p. 21. DOI: 10.1088/0004-637X/747/1/21.

Saur, J., Politano, H., Pouquet, A., and Matthaeus, W. H. (2002). "Evidence for weak MHD turbulence in the middle magnetosphere of Jupiter". In: *Astronomy & Astrophysics* **386**: pp. 699–708. DOI: 10.1051/0004-6361:20020305.

Schekochihin, A. A., Cowley, S. C., Dorland, W., Hammett, G. W., Howes, G. G., Plunk, G. G., Quataert, E., and Tatsuno, T. (2008). "Gyrokinetic turbulence: a nonlinear route to dissipation through phase space". In: *Plasma Physics and Controlled Fusion* **50**:12, p. 124024. DOI: 10.1088/0741-3335/50/12/124024.

Schekochihin, A. A., Cowley, S. C., Dorland, W., Hammett, G. W., Howes, G. G., Quataert, E., and Tatsuno, T. (2009). "Astrophysical Gyrokinetics: Kinetic and Fluid Turbulent Cascades in Magnetized Weakly Collisional Plasmas". In: *The Astrophysical Journal Supplement Series* **182**:1, pp. 310–377. DOI: 10.1088/0067-0049/182/1/310.

Schekochihin, A. A. (2022). "MHD turbulence: a biased review". In: *Journal of Plasma Physics* **88**:5, p. 155880501. DOI: 10.1017/S0022377822000721.

Schekochihin, A. A. and Cowley, S. C. (2007). "Turbulence and Magnetic Fields in Astrophysical Plasmas". In: *Magnetohydrodynamics*. Ed. by R. Moreau. Vol. 80. Dordrecht: Springer Netherlands, pp. 85–115. DOI: 10.1007/978-1-4020-4833-3_6.

Schwartz, S. J., Goodrich, K. A., Wilson, L. B., Turner, D. L., Trattner, K. J., Kucharek, H., Gingell, I., Fuselier, S. A., Cohen, I. J., Madanian, H., Ergun, R. E., Gershman, D. J., and Strangeway, R. J. (2022). "Energy Partition at Collisionless Supercritical Quasi-

Perpendicular Shocks". In: *Journal of Geophysical Research: Space Physics* **127**:10, e2022JA030637. DOI: 10.1029/2022JA030637.

Servidio, S., Chasapis, A., Matthaeus, W. H., Perrone, D., Valentini, F., Parashar, T. N., Veltri, P., Gershman, D., Russell, C. T., Giles, B., Fuselier, S. A., Phan, T. D., and Burch, J. (2017). "Magnetospheric multiscale observation of plasma velocity-space cascade: Hermite representation and theory". In: *Physical Review Letters* **119**:20, p. 205101. DOI: 10.1103/PhysRevLett.119.205101.

Servidio, S., Valentini, F., Califano, F., and Veltri, P. (2012). "Local Kinetic Effects in Two-Dimensional Plasma Turbulence". In: *Physical Review Letters* **108**:4, p. 045001. DOI: 10.1103/PhysRevLett.108.045001.

Shestov, S. V., Voitenko, Y. M., and Zhukov, A. N. (2022). "Initiation of Alfvénic turbulence by Alfvén wave collisions: A numerical study". In: *Atti dell'Accademia Pontaniana* **661**: A93. DOI: 10.1051/0004-6361/202142362.

Shevyrev, N. N., Zastenker, G. N., Eiges, P. E., and Richardson, J. D. (2006). "Low frequency waves observed by Interball-1 in foreshock and magnetosheath". In: *Advances in Space Research* **37**: pp. 1516–1521. DOI: 10.1016/j.asr.2005.07.072.

Shue, J.-H., Song, P., Russell, C. T., Steinberg, J. T., Chao, J. K., Zastenker, G., Vaisberg, O. L., Kokubun, S., Singer, H. J., Detman, T. R., and Kawano, H. (1998). "Magnetopause location under extreme solar wind conditions". In: *Journal of Geophysical Research: Space Physics* **103**:A8, pp. 17691–17700. DOI: 10.1029/98JA01103.

Shuster, J. R. et al. (2019). "MMS measurements of the vlasov equation: Probing the electron pressure divergence within thin current sheets". In: *Geophysical Research Letters* **46**:14, pp. 7862–7872. DOI: 10.1029/2019GL083549.

Shuster, J. R. et al. (2023). "Temporal, Spatial, and Velocity-Space Variations of Electron Phase Space Density Measurements at the Magnetopause". In: *Journal of Geophysical Research: Space Physics* **128**:4, e2022JA030949. DOI: 10.1029/2022JA030949.

Stasiewicz, K. (2023). "Origin of flat-top electron distributions at the Earth's bow shock". In: *Monthly Notices of the Royal Astronomical Society: Letters* **527**:1, pp. L71–L75. DOI: 10.1093/mnrasl/slad146.

Stawarz, J. E., Eastwood, J. P., Phan, T. D., Gingell, I. L., Pyakurel, P. S., Shay, M. A., Robertson, S. L., Russell, C. T., and Le Contel, O. (2022). "Turbulence-driven magnetic reconnection and the magnetic correlation length: Observations from Magnetospheric Multiscale in Earth's magnetosheath". In: *Physics of Plasmas* **29**:1, p. 012302. DOI: 10.1063/5.0071106.

Stawarz, J. E., Eastwood, J. P., Phan, T. D., Gingell, I. L., Shay, M. A., Burch, J. L., Ergun, R. E., Giles, B. L., Gershman, D. J., Le Contel, O., Lindqvist, P. .-., Russell, C. T., Strangeway, R. J., Torbert, R. B., Argall, M. R., Fischer, D., Magnes, W., and Franci, L. (2019). "Properties of the turbulence associated with electron-only magnetic reconnection in earth's magnetosheath". In: *The Astrophysical Journal Letters* **877**:2, p. L37. DOI: 10.3847/2041-8213/ab21c8.

Stawarz, J. E., Matteini, L., Parashar, T. N., Franci, L., Eastwood, J. P., Gonzalez, C. A., Gingell, I. L., Burch, J. L., Ergun, R. E., Ahmadi, N., Giles, B. L., Gershman, D. J., Le Contel, O., Lindqvist, P.-A., Russell, C. T., Strangeway, R. J., and Torbert, R. B. (2021). "Comparative analysis of the various generalized ohm's law terms in magnetosheath turbulence as observed by magnetospheric multiscale". In: *Journal of Geophysical Research: Space Physics* **126**:1, 2020JA028447. DOI: https://doi.org/10.1029/2020JA028447.

Stawarz, J. E., Muñoz, P. A., Bessho, N., Bandyopadhyay, R., Nakamura, T. K. M., Eriksson, S., Graham, D. B., Büchner, J., Chasapis, A., Drake, J. F., Shay, M. A., Ergun, R. E., Hasegawa, H., Khotyaintsev, Y. V., Swisdak, M., and Wilder, F. D. (2024). "The Interplay Between Collisionless Magnetic Reconnection and Turbulence". In: *Space Science Reviews* **220**:8, p. 90. DOI: 10.1007/s11214-024-01124-8.

Stawarz, J. E. et al. (2016). "Observations of turbulence in a Kelvin-Helmholtz event on 8 September 2015 by the Magnetospheric Multiscale mission". In: *Journal of Geophysical Research (Space Physics)* **121**:11, pp. 11, 021–11, 034. DOI: 10.1002/2016JA023458.

Stawarz, J. E., Vasquez, B. J., Smith, C. W., Forman, M. A., and Klewicki, J. (2011). "Third Moments and the Role of Anisotropy from Velocity Shear in the Solar Wind". In: *The Astrophysical Journal* **736**:1, p. 44. DOI: 10.1088/0004-637X/736/1/44.

Stawarz, J. E. and Genestreti, K. J. (2023). "Preface to Special Topic: Plasma Physics from the Magnetospheric Multiscale Mission". In: *Physics of Plasmas* **30**:4, p. 040401. DOI: 10.1063/5.0148163.

Stawarz, J. E., Pouquet, A., and Brachet, M.-E. (2012). "Long-time properties of magnetohydrodynamic turbulence and the role of symmetries". In: *Physical Review E* **86**:3, p. 036307. DOI: 10.1103/PhysRevE.86.036307.

Stepanova, M., Borovsky, J. E., Retino, A., Uritsky, V., Vörös, Z., and Zimbardo, G. (2022). "Editorial: The Role of Turbulence in the Solar Wind, Magnetosphere, Ionosphere Dynamics". In: *Frontiers in Astronomy and Space Sciences* **8**: p. 763190. DOI: 10.3389/fspas.2021.763190.

Stewart, B. (1861). "XXII. On the great magnetic disturbance which extended from August 28 to September 7, 1859, as recorded by photography at the Kew Observatory". In: *Philosophical Transactions of the Royal Society of London* **151**: pp. 423–430. DOI: 10.1098/rstl.1861.0023.

Stokes, G. G. (1845). "On the theories of the inertial friction of fluids in motion". In: *Trans. Cambridge. Philos. Soc.* **8**:287.

Sundkvist, D., Retinò, A., Vaivads, A., and Bale, S. D. (2007). "Dissipation in Turbulent Plasma due to Reconnection in Thin Current Sheets". In: *Physical Review Letters* **99**:2, p. 025004. DOI: 10.1103/PhysRevLett.99.025004.

Svenningsson, I., Yordanova, E., Cozzani, G., Khotyaintsev, Y. V., and André, M. (2022). "Kinetic Generation of Whistler Waves in the Turbulent Magnetosheath". In: *Geophysical Research Letters* **49**:15. DOI: 10.1029/2022GL099065.

Swift, J. (1734). *On poetry: a rapsody.* On poetry: a rapsody. Printed at Dublin, re-printed at London, and sold by J. Huggonson.

Swisdak, M. (2016). "Quantifying gyrotropy in magnetic reconnection". In: *Geophysical Research Letters* **43**:1, pp. 43–49. DOI: 10.1002/2015GL066980.

Taylor, G. I. (1938). "The spectrum of turbulence". In: *Proceedings of the Royal Society of London. Series A - Mathematical and Physical Sciences* **164**:919, pp. 476–490. DOI: 10.1098/rspa.1938.0032.

Terry, P. W. (2018). "Theory of critical balance in plasma turbulence". In: *Physics of Plasmas* **25**:9, p. 092301. DOI: 10.1063/1.5041754.

Toledo-Redondo, S., Lavraud, B., Fuselier, S. A., André, M., Khotyaintsev, Y. V., Nakamura, R., Escoubet, C. P., Li, W. Y., Torkar, K., Cipriani, F., Barrie, A. C., Giles, B., Moore, T. E., Gershman, D., Lindqvist, P.-A., Ergun, R. E., Russell, C. T., and Burch, J. L. (2019). "Electrostatic Spacecraft Potential Structure and Wake Formation Effects for Characterization of Cold Ion Beams in the Earth's Magnetosphere". In: *Journal of Geophysical Research: Space Physics* **124**:12, pp. 10048–10062. DOI: 10.1029/2019JA027145.

Torbert, R. B. et al. (2016a). "Estimates of terms in Ohm's law during an encounter with an electron diffusion region". In: *Geophysical Research Letters* **43**:12, pp. 5918–5925. DOI: 10.1002/2016GL069553.

Torbert, R. B. et al. (2016b). "The FIELDS instrument suite on MMS: Scientific objectives, measurements, and data products". In: *Space Science Reviews* **199**:1-4, pp. 105–135. DOI: 10.1007/s11214-014-0109-8.

Torkar, K., Nakamura, R., Tajmar, M., Scharlemann, C., Jeszenszky, H., Laky, G., Fremuth, G., Escoubet, C. P., and Svenes, K. (2016). "Active Spacecraft Potential Control Investigation". In: *Space Science Reviews* **199**:1-4, pp. 515–544. DOI: 10.1007/s11214-014-0049-3.

Treumann, R. A. and Baumjohann, W. (1997). *Advanced Space Plasma Physics*. Imperial College Press. DOI: 10.1142/p020.

Vasavada, A. R. and Showman, A. P. (2005). "Jovian atmospheric dynamics: an update after *Galileo* and *Cassini*". In: *Reports on Progress in Physics* **68**:8, pp. 1935–1996. DOI: 10.1088/0034-4885/68/8/R06.

Vasyliunas, V. M. (1975). "Theoretical models of magnetic field line merging". In: *Reviews of Geophysics* **13**:1, pp. 303–336. DOI: 10.1029/RG013i001p00303.

Verdini, A. and Velli, M. (2007). "Alfven Waves and Turbulence in the Solar Atmosphere and Solar Wind". In: *The Astrophysical Journal* **662**:1, pp. 669–676. DOI: 10.1086/510710.

Verniero, J. L., Howes, G. G., Stewart, D. E., and Klein, K. G. (2021). "Determining Threshold Instrumental Resolutions for Resolving the Velocity-Space Signature of Ion Landau Damping". In: *Journal of Geophysical Research: Space Physics* **126**:5, e2020JA028361. DOI: 10.1029/2020JA028361.

Verscharen, D., Klein, K. G., Chandran, B. D. G., Stevens, M. L., Salem, C. S., and Bale, S. D. (2018). "ALPS: the Arbitrary Linear Plasma Solver". In: *Journal of Plasma Physics* **84**:4, p. 905840403. DOI: 10.1017/S0022377818000739.

Verscharen, D., Chandran, B. D. G., Boella, E., Halekas, J., Innocenti, M. E., Jagarlamudi, V. K., Micera, A., Pierrard, V., Štverák, Š., Vasko, I. Y., Velli, M., and Whittlesey, P. L. (2022). "Electron-Driven Instabilities in the Solar Wind". In: *Frontiers in Astronomy and Space Sciences* **9**: p. 951628. DOI: 10.3389/fspas.2022.951628.

Verscharen, D., Klein, K. G., and Maruca, B. A. (2019). "The multi-scale nature of the solar wind". In: *Living Reviews in Solar Physics* **16**:1, p. 5. DOI: 10.1007/s41116-019-0021-0.

Vlasov, A. A. (1945). "On the kinetic theory of an assembly of particles with collective interaction". In: *Russian Physics Journal* **9**: pp. 25–40.

Von Hann, J. and DeCourcy Ward, r. (1903). *Handbook of Climatology*. Macmillan.

Vörös, Z., Yordanova, E., Khotyaintsev, Y. V., Varsani, A., and Narita, Y. (2019). "Energy Conversion at Kinetic Scales in the Turbulent Magnetosheath". In: *Frontiers in Astronomy and Space Sciences* **6**: p. 60. DOI: 10.3389/fspas.2019.00060.

Walters, J., Klein, K. G., Lichko, E., Stevens, M. L., Verscharen, D., and Chandran, B. D. G. (2023). "The Effects of Nonequilibrium Velocity Distributions on Alfvén Ion-cyclotron Waves in the Solar Wind". In: *The Astrophysical Journal* **955**:2, p. 97. DOI: 10.3847/1538-4357/acf1fa.

Wan, M., Matthaeus, W. H., Karimabadi, H., Roytershteyn, V., Shay, M., Wu, P., Daughton, W., Loring, B., and Chapman, S. C. (2012). "Intermittent Dissipation at Kinetic Scales in Collisionless Plasma Turbulence". In: *Physical Review Letters* **109**:19, p. 195001. DOI: 10.1103/PhysRevLett.109.195001.

Wan, M., Matthaeus, W. H., Roytershteyn, V., Karimabadi, H., Parashar, T., Wu, P., and Shay, M. (2015). "Intermittent Dissipation and Heating in 3D Kinetic Plasma Turbulence". In: *Physical Review Letters* **114**:17, p. 175002. DOI: 10.1103/PhysRevLett.114.175002.

Wan, M., Servidio, S., Oughton, S., and Matthaeus, W. H. (2009). "The third-order law for increments in magnetohydrodynamic turbulence with constant shear". In: *Physics of Plasmas* **16**:9, p. 090703. DOI: 10.1063/1.3240333.

Wang, S., Chen, L.-J., Bessho, N., Hesse, M., Wilson, L. B., Giles, B., Moore, T. E., Russell, C. T., Torbert, R. B., and Burch, J. L. (2019). "Observational Evidence of Magnetic Reconnection in the Terrestrial Bow Shock Transition Region". In: *Geophysical Research Letters* **46**:2, pp. 562–570. DOI: 10.1029/2018GL080944.

Welch, P. (1967). "The use of fast Fourier transform for the estimation of power spectra: A method based on time averaging over short, modified periodograms". In: *IEEE Transactions on Audio and Electroacoustics* **15**:2, pp. 70–73. DOI: 10.1109/TAU.1967.1161901.

Wicks, R. T., Roberts, D. A., Mallet, A., Schekochihin, A. A., Horbury, T. S., and Chen, C. H. K. (2013). "Correlations at Large Scales and the Onset of Turbulence in the Fast Solar Wind". In: *The Astrophysical Journal* **778**:2, p. 177. DOI: 10.1088/0004-637X/778/2/177.

Wu, P., Perri, S., Osman, K., Wan, M., Matthaeus, W. H., Shay, M. A., Goldstein, M. L., Karimabadi, H., and Chapman, S. (2013). "Intermittent Heating in Solar Wind and Kinetic Simulations". In: *The Astrophysical Journal* **763**:2, p. L30. DOI: 10.1088/2041-8205/763/2/L30.

Xu, D. and Chen, T. (2012). "Constraints on electron temperature anisotropies in sheath regions of interplanetary shocks". In: *Planetary and Space Science* **62**:1, pp. 100–103. DOI: 10.1016/j.pss.2011.12.015.

Yaglom, A. M. (1949). "On the local structure of the temperature field in a turbulent flow". In: *Doklady* **69**:6, p. 743.

Yang, Y., Matthaeus, W. H., Parashar, T. N., Wu, P., Wan, M., Shi, Y., Chen, S., Roytershteyn, V., and Daughton, W. (2017a). "Energy transfer channels and turbulence cascade in Vlasov-Maxwell turbulence". In: *Physical Review E* **95**:6, p. 061201. DOI: 10.1103/PhysRevE.95.061201.

Yang, Y., Matthaeus, W. H., Oughton, S., Bandyopadhyay, R., Pecora, F., Parashar, T. N., Roytershteyn, V., Chasapis, A., and Shay, M. A. (2024). "Effective viscosity,

resistivity, and Reynolds number in weakly collisional plasma turbulence". In: *Monthly Notices of the Royal Astronomical Society* **528**:4, pp. 6119–6128. DOI: 10.1093/mnras/stae355.

Yang, Y., Matthaeus, W. H., Parashar, T. N., Haggerty, C. C., Roytershteyn, V., Daughton, W., Wan, M., Shi, Y., and Chen, S. (2017b). "Energy transfer, pressure tensor, and heating of kinetic plasma". In: *Physics of Plasmas* **24**:7, p. 072306. DOI: 10.1063/1.4990421.

Yang, Y., Matthaeus, W. H., Roy, S., Roytershteyn, V., Parashar, T. N., Bandyopadhyay, R., and Wan, M. (2022). "Pressure–Strain Interaction as the Energy Dissipation Estimate in Collisionless Plasma". In: *The Astrophysical Journal* **929**:2, p. 142. DOI: 10.3847/1538-4357/ac5d3e.

Yang, Y., Wan, M., Matthaeus, W. H., Sorriso-Valvo, L., Parashar, T. N., Lu, Q., Shi, Y., and Chen, S. (2019). "Scale dependence of energy transfer in turbulent plasma". In: *Monthly Notices of the Royal Astronomical Society* **482**:4, pp. 4933–4940. DOI: 10.1093/mnras/sty2977.

Yordanova, E., Vörös, Z., Raptis, S., and Karlsson, T. (2020). "Current sheet statistics in the magnetosheath". In: *Frontiers in Astronomy and Space Sciences* **7**: p. 2. DOI: 10.3389/fspas.2020.00002.

Yordanova, E., Vörös, Z., Sorriso-Valvo, L., Dimmock, A. P., and Kilpua, E. (2021). "A Possible Link between Turbulence and Plasma Heating". In: *The Astrophysical Journal* **921**:1, p. 65. DOI: 10.3847/1538-4357/ac1942.

Zenitani, S., Hesse, M., Klimas, A., Black, C., and Kuznetsova, M. (2011a). "The inner structure of collisionless magnetic reconnection: The electron-frame dissipation measure and Hall fields". In: *Physics of Plasmas* **18**:12, p. 122108. DOI: 10.1063/1.3662430.

Zenitani, S., Hesse, M., Klimas, A., and Kuznetsova, M. (2011b). "New Measure of the Dissipation Region in Collisionless Magnetic Reconnection". In: *Physical Review Letters* **106**:19, p. 195003. DOI: 10.1103/PhysRevLett.106.195003.

Zhang, H., Zong, Q., Connor, H., Delamere, P., Facskó, G., Han, D., Hasegawa, H., Kallio, E., Kis, Á., Le, G., Lembège, B., Lin, Y., Liu, T., Oksavik, K., Omidi, N., Otto, A., Ren, J., Shi, Q., Sibeck, D., and Yao, S. (2022). "Dayside Transient Phenomena and Their Impact on the Magnetosphere and Ionosphere". In: *Space Science Reviews* **218**:5, p. 40. DOI: 10.1007/s11214-021-00865-0.

Zhang, X., Angelopoulos, V., Artemyev, A. V., and Liu, J. (2018). "Whistler and Electron Firehose Instability Control of Electron Distributions in and Around Dipolarizing Flux Bundles". In: *Geophysical Research Letters* **45**:18, pp. 9380–9389. DOI: 10.1029/2018GL079613.

Zhao, L.-L., Zank, G. P., Nakanotani, M., and Adhikari, L. (2023). "Observations of Waves and Structures by Frequency–Wavenumber Spectrum in Solar Wind Turbulence". In: *The Astrophysical Journal* **944**:1, p. 98. DOI: 10.3847/1538-4357/acb33b.

Zhou, G., He, H., and Wan, W. (2020). "Effects of solar activity on taylor scale and correlation scale in solar wind magnetic fluctuations". In: *The Astrophysical Journal* **899**: p. L32. DOI: 10.3847/2041-8213/abaaa9.

Zimbardo, G., Greco, A., Sorriso-Valvo, L., Perri, S., Vörös, Z., Aburjania, G., Chargazia, K., and Alexandrova, O. (2010). "Magnetic Turbulence in the Geospace Environment". In: *Space Science Reviews* **156**:1-4, pp. 89–134. DOI: 10.1007/s11214-010-9692-5.

Appendix A

Derivations

This appendix contains detailed derivations of the momentum equation, generalised Ohm's law, and the energy equation, to expand on Chapter 2. The derivations are based on those presented in Gurnett and Bhattacharjee (2005).

A.1 The Momentum Equation

The Vlasov equation for species s describes how the velocity distribution function (VDF) evolves in phase space in response to electromagnetic fields. The expression is given by

$$\frac{df_s}{dt} \equiv \frac{\partial f_s}{\partial t} + \mathbf{v} \cdot \nabla_{\mathbf{x}} f_s + \frac{q_s}{m_s} (\mathbf{E} + \mathbf{v} \times \mathbf{B}) \cdot \nabla_{\mathbf{v}} f_s = 0, \tag{A.1}$$

where f_s is the velocity distribution function with dimensions $(\mathbf{x}, \mathbf{v}, t)$ corresponding to three spatial, three velocity space, and one time dimension, $\nabla_{\mathbf{x}}$ represents a physical-space derivative, $\nabla_{\mathbf{v}}$ represents a velocity space derivative, $\mathbf{E}$ is the electric field vector, $\mathbf{v}$ is the phase space velocity variable, and $\mathbf{B}$ is the magnetic field vector.

To obtain the momentum equation, we take the first velocity moment of the Vlasov equation. We start by multiplying (A.1) by the velocity space momentum variable $m_s\mathbf{v}$

and integrating over all of velocity space (V),

$$m_s \int_V \mathbf{v} \left[\frac{\partial f_s}{\partial t} + \mathbf{v} \cdot \nabla_{\mathbf{x}} f_s + q_s \left(\mathbf{E} + \mathbf{v} \times \mathbf{B} \right) \cdot \nabla_{\mathbf{v}} f_s \right] d^3 v = 0. \tag{A.2}$$

We will treat all the integrals in the above equation separately, starting with the first term on the Left-Hand Side (LHS). This integral can be readily evaluated using the density and bulk velocity $n_s \mathbf{v}_s = \int \mathbf{v} f_s d^3 v$,

$$m_s \int_V \mathbf{v} \frac{\partial f_s}{\partial t} d^3 v = \frac{\partial}{\partial t} \left(m_s \int_V \mathbf{v} f_s \, d^3 v \right) = \frac{\partial}{\partial t} \left(m_s n_s \mathbf{v}_s \right). \tag{A.3}$$

The second integral on the LHS of (A.2) is more involved. Rearranging as

$$m_s \int_V \mathbf{v} \left(\mathbf{v} \cdot \nabla_{\mathbf{x}} f_s \right) \, d^3 v = \nabla_{\mathbf{x}} \cdot \left[m_s \int_V \mathbf{v}\mathbf{v} f_s \, d^3 v \right], \tag{A.4}$$

and substituting the tensor identity

$$\mathbf{v}\mathbf{v} = \left(\mathbf{v} - \mathbf{v}_s \right) \left(\mathbf{v} - \mathbf{v}_s \right) + \mathbf{v}_s \mathbf{v} + \mathbf{v}\mathbf{v}_s - \mathbf{v}_s \mathbf{v}_s, \tag{A.5}$$

where $\mathbf{v}_s$ is the average velocity, gives

$$\nabla_{\mathbf{x}} \cdot \left[m_s \int_V \mathbf{v}\mathbf{v} f_s \, d^3 v \right] = \nabla_{\mathbf{x}} \cdot \left[m_s \int_V \left(\mathbf{v} - \mathbf{v}_s \right) \left(\mathbf{v} - \mathbf{v}_s \right) f_s \, d^3 v + m_s n_s \mathbf{v}_s \mathbf{v}_s \right], \tag{A.6}$$

since $\int \mathbf{v}_s \mathbf{v} f_s \, d^3 v = 0$. Using the definition of the pressure tensor

$$\mathbf{P}_s = m_s \int \left(\mathbf{v} - \mathbf{v}_s \right) \left(\mathbf{v} - \mathbf{v}_s \right) f_s \, d^3 v, \tag{A.7}$$

we can simplify (A.6) to

$$\nabla_{\mathbf{x}} \cdot \left[m_s \int_V \left(\mathbf{v} - \mathbf{v}_s \right) \left(\mathbf{v} - \mathbf{v}_s \right) f_s \, d^3 v + m_s n_s \mathbf{v}_s \mathbf{v}_s \right] = \nabla_{\mathbf{x}} \cdot \left[\mathbf{P}_s + m_s n_s \mathbf{v}_s \mathbf{v}_s \right]. \tag{A.8}$$

The third integral on the LHS of (A.2) can be simplified using

$$\mathbf{F} \cdot \nabla_{\mathbf{v}} f_s = \nabla_{\mathbf{v}} \cdot (\mathbf{F} f_s)\,, \tag{A.9}$$

since the Lorentz force $\mathbf{F} = q_s\,(\mathbf{E} + \mathbf{v} \times \mathbf{B})$ does not have a velocity divergence, so it can be brought inside the term. The term becomes

$$\int_V \mathbf{v}\,(\mathbf{F} \cdot \nabla_{\mathbf{v}} f_s)\; d^3v = \int_V \mathbf{v}\,[\nabla_{\mathbf{v}} \cdot (\mathbf{F} f_s)]\; d^3v. \tag{A.10}$$

The Right-Hand Side (RHS) of this equation can be expressed in terms of its vector components,

$$\int_V (v_x\,\hat{x} + v_y\,\hat{y} + v_z\,\hat{z}) \left[\frac{\partial}{\partial v_x} F_x f_s + \frac{\partial}{\partial v_y} F_y f_s + \frac{\partial}{\partial v_z} F_z f_s\right] d^3v, \tag{A.11}$$

which is an expression containing 9 individual integrals. We group these integrals into

$$\int_V v_x\,\hat{x} \frac{\partial}{\partial v_x}\,(F_x f_s)\; d^3v + \int_V v_y\,\hat{y} \frac{\partial}{\partial v_y}\,(F_y f_s)\; d^3v + \int_V v_z\,\hat{z} \frac{\partial}{\partial v_z}\,(F_z f_s)\; d^3v, \tag{A.12}$$

and

$$\begin{aligned} &\int_V v_x\,\hat{x} \frac{\partial}{\partial v_y}\,(F_y f_s)\; d^3v + \int_V v_x\,\hat{x} \frac{\partial}{\partial v_z}\,(F_z f_s)\; d^3v + \int_V v_y\,\hat{y} \frac{\partial}{\partial v_x}\,(F_x f_s)\; d^3v \\ &+ \int_V v_y\,\hat{y} \frac{\partial}{\partial v_z}\,(F_z f_s)\; d^3v + \int_V v_z\,\hat{z} \frac{\partial}{\partial v_x}\,(F_x f_s)\; d^3v + \int_V v_z\,\hat{z} \frac{\partial}{\partial v_y}\,(F_y f_s)\; d^3v. \end{aligned} \tag{A.13}$$

The three integrals in (A.12) are all of the form

$$\int_{-\infty}^{\infty}\int_{-\infty}^{\infty} dv_i\,dv_j \int_{-\infty}^{\infty} dv_k\,v_k \frac{\partial}{\partial v_k}\,(F_k f_s)\,, \tag{A.14}$$

where i, j, and k represent the components of the vectors. Integrating by parts gives

$$\int_{-\infty}^{\infty} dv_k\,v_k \frac{\partial}{\partial v_k}\,(F_k f_s) = [v_k\,F_k\,f_s]_{-\infty}^{\infty} - \int_{-\infty}^{\infty} F_k f_s\,dv_k, \tag{A.15}$$

where the $[v_k\,F_k\,f_s]_{-\infty}^{\infty}$ term is zero provided $f_s(v \to \infty) \to 0$ sufficiently rapidly. The six

integrals in (A.13) are of the form

$$\int_V v_j \frac{\partial}{\partial v_k} \left(F_k f_s\right)\, d^3v = \int_{-\infty}^{\infty}\int_{-\infty}^{\infty} dv_i\, dv_j\, v_k \int_{-\infty}^{\infty} \frac{\partial}{\partial v_k} \left(F_k f_s\right)\, dv_k, \tag{A.16}$$

which can be integrated directly as

$$\int_{-\infty}^{\infty} \frac{\partial}{\partial v_k} \left(F_k f_s\right)\, dv_k = \left[F_k\, f_s\right]_{-\infty}^{\infty} = 0, \tag{A.17}$$

where, as above, it is assumed that phase space density goes to zero sufficiently quickly at infinite velocity. The nine integrals thus become

$$\int_V \mathbf{v}\left[\nabla_{\mathbf{v}} \cdot \left(\mathbf{F} f_s\right)\right]\, d^3v = -\int_V \mathbf{F} f_s\, d^3v. \tag{A.18}$$

Using the Lorentz force $\mathbf{F} = q_s\left(\mathbf{E} + \mathbf{v} \times \mathbf{B}\right)$ and integrating, we arrive at the expression

$$\begin{aligned}\int_V \mathbf{v}\left(\mathbf{F} \cdot \nabla_{\mathbf{v}} f_s\right)\, d^3v &= -q_s \int_V \left(\mathbf{E} + \mathbf{v} \times \mathbf{B}\right) f_s\, d^3v \\ &= -q_s n_s \left(\mathbf{E} + \mathbf{v}_s \times \mathbf{B}\right).\end{aligned} \tag{A.19}$$

Together, the integrals in (A.2) become

$$\frac{\partial}{\partial t}\left(m_s n_s \mathbf{v}_s\right) + \nabla_{\mathbf{x}} \cdot \left[\mathbf{P}_s + m_s n_s \mathbf{v}_s \mathbf{v}_s\right] - q_s n_s \left(\mathbf{E} + \mathbf{v}_s \times \mathbf{B}\right) = 0. \tag{A.20}$$

Rearranging the terms, we obtain the standard form of the momentum equation

$$\boxed{\frac{\partial}{\partial t}\left(m_s n_s \mathbf{v}_s\right) + \nabla \cdot \left(m_s n_s \mathbf{v}_s \mathbf{v}_s\right) = q_s n_s \left(\mathbf{E} + \mathbf{v}_s \times \mathbf{B}\right) - \nabla \cdot \mathbf{P}_s,} \tag{A.21}$$

where ∇ represents $\nabla_{\mathbf{x}}$.

A.2 The Generalised Ohm's Law

Generalised Ohm's law is obtained by taking the difference between the ion and electron momentum equations and rearranging in terms of the current and pressure.

We start with the ion momentum equation

$$\frac{\partial}{\partial t}\left(m_i n_i \mathbf{v}_i\right) + \nabla \cdot \left(m_i n_i \mathbf{v}_i \mathbf{v}_i\right) = n_i e\left[\mathbf{E} + \mathbf{v}_i \times \mathbf{B}\right] - \nabla \cdot \mathbf{P}_i. \tag{A.22}$$

and the electron momentum equation

$$\frac{\partial}{\partial t}\left(m_e n_e \mathbf{v}_e\right) + \nabla \cdot \left(m_e n_e \mathbf{v}_e \mathbf{v}_e\right) = -n_e e\left[\mathbf{E} + \mathbf{v}_e \times \mathbf{B}\right] - \nabla \cdot \mathbf{P}_e. \tag{A.23}$$

Noting that current density $\mathbf{j}$ is proportional to $\mathbf{v}_i - \mathbf{v}_e$, we multiply (A.22) by m_e and (A.23) by m_i to obtain an equation containing a $(\mathbf{v}_i - \mathbf{v}_e)$ term,

$$\begin{aligned}\frac{\partial}{\partial t}\left(m_e m_i \mathbf{v}_i - m_i m_e \mathbf{v}_e\right) + \nabla \cdot \left[m_e m_i \mathbf{v}_i \mathbf{v}_i - m_i m_e \mathbf{v}_e \mathbf{v}_e\right] &= n\left(m_e + m_i\right)\mathbf{E} \\ &+ ne\left(m_e \mathbf{v}_i - m_i \mathbf{v}_e\right) \times \mathbf{B} \\ &- m_e \nabla \cdot \mathbf{P}_i + m_i \nabla \cdot \mathbf{P}_e,\end{aligned} \tag{A.24}$$

where $n = n_e = n_i$ is the number density assuming quasineutrality. Substituting the mass density $\rho_m = n(m_e + m_i)$, equation (A.24) becomes

$$\begin{aligned}m_e m_i \left\{\frac{\partial}{\partial t}\left[n(\mathbf{v}_i - \mathbf{v}_e)\right] + \nabla \cdot \left[n(\mathbf{v}_i \mathbf{v}_i - \mathbf{v}_e \mathbf{v}_e)\right]\right\} &= e\rho_m \mathbf{E} + ne\left(m_e \mathbf{v}_i + m_i \mathbf{v}_e\right) \times \mathbf{B} \\ &- m_e \nabla \cdot \mathbf{P}_i + m_i \nabla \cdot \mathbf{P}_e.\end{aligned} \tag{A.25}$$

We now simplify each group of terms on the RHS of (A.25), starting with the $\mathbf{B}$ part of the electromagnetic fields terms. Using the convenient mathematical tool

$$m_e \mathbf{v}_i + m_i \mathbf{v}_e = m_e \mathbf{v}_i + m_i \mathbf{v}_e + \left(m_e \mathbf{v}_e - m_e \mathbf{v}_e\right) + \left(m_i \mathbf{v}_i - m_i \mathbf{v}_i\right), \tag{A.26}$$

and then employing the following rearrangements of the expressions for the single-fluid velocity $\mathbf{u}$ and current density $\mathbf{j}$

$$\left(m_e + m_i\right)\mathbf{u} = m_e \mathbf{v}_e + m_i \mathbf{v}_i, \tag{A.27}$$

$$(m_i - m_e)\frac{\mathbf{j}}{ne} = m_i\mathbf{v}_i - m_i\mathbf{v}_e - m_e\mathbf{v}_i + m_e\mathbf{v}_e, \tag{A.28}$$

equation (A.26) can be expressed as

$$m_e\mathbf{v}_i + m_i\mathbf{v}_e = (m_e + m_i)\,\mathbf{u} - (m_i - m_e)\frac{\mathbf{j}}{ne}.$$

This form allows us to express the electromagnetic fields terms from (A.25) as

$$\rho_m\mathbf{E} + ne\,(m_e\mathbf{v}_i + m_i\mathbf{v}_e) \times \mathbf{B} = e\rho_m\mathbf{E} + ne\left[(m_e + m_i)\,\mathbf{u} - (m_i - m_e)\frac{\mathbf{j}}{ne}\right] \times \mathbf{B}. \tag{A.29}$$

The pressure terms group is simplified by noting that the ion pressure term, $m_e\nabla\cdot\mathbf{P}_i$, is reduced by a factor of m_e/m_i compared to the electron pressure term, $m_i\nabla\cdot\mathbf{P}_e$, allowing us to neglect the ion pressure contribution.

Bringing all the simplified terms back into the full expression in (A.25), we have

$$\begin{aligned} m_e m_i\left\{\frac{\partial}{\partial t}\left[n(\mathbf{v}_i - \mathbf{v}_e)\right] + \nabla\cdot\left[n(\mathbf{v}_i\mathbf{v}_i - \mathbf{v}_e\mathbf{v}_e)\right]\right\} &= e\rho_m\mathbf{E} \\ &+ ne\left[(m_e + m_i)\mathbf{u} - (m_i - m_e)\frac{\mathbf{j}}{ne}\right] \times \mathbf{B} \\ &+\ m_i\nabla\cdot\mathbf{P}_e. \end{aligned} \tag{A.30}$$

Turning to the LHS of the above expression, we can simplify the $\partial/\partial t$ term using the current density $\mathbf{j} = ne(\mathbf{v}_i - \mathbf{v}_e)$, as

$$\frac{\partial}{\partial t}\left[n(\mathbf{v}_i - \mathbf{v}_e)\right] = \frac{1}{e}\frac{\partial\mathbf{j}}{\partial t}, \tag{A.31}$$

and the ∇ term by substituting $\mathbf{v}_e = \mathbf{v}_i - \mathbf{j}/ne$, as

$$\begin{aligned} \nabla\cdot\left[n(\mathbf{v}_i\mathbf{v}_i - \mathbf{v}_e\mathbf{v}_e)\right] &= \nabla\cdot\left[n(\mathbf{v}_i\mathbf{v}_i - \left(\mathbf{v}_i - \frac{\mathbf{j}}{ne}\right)\left(\mathbf{v}_i - \frac{\mathbf{j}}{ne}\right)\right] \\ &= n\nabla\cdot\left[\mathbf{v}_i\mathbf{v}_i - \mathbf{v}_i\mathbf{v}_i + \frac{\mathbf{v}_i\,\mathbf{j}}{ne} + \frac{\mathbf{j}\,\mathbf{v}_i}{ne} - \frac{\mathbf{jj}}{(ne)^2}\right], \end{aligned} \tag{A.32}$$

which can be simplified using $\mathbf{u} \approx \mathbf{v}_i$ for $m_e \ll m_i$ as

$$\frac{1}{e}\nabla \cdot \left[\mathbf{uj} + \mathbf{ju} - \frac{\mathbf{jj}}{ne}\right]. \tag{A.33}$$

This allows us to write the whole LHS as

$$m_e m_i \left\{ \frac{\partial}{\partial t}\left[n(\mathbf{v}_i - \mathbf{v}_e)\right] + \nabla \cdot \left[n(\mathbf{v}_i\mathbf{v}_i - \mathbf{v}_e\mathbf{v}_e)\right] \right\} = \frac{m_e m_i}{e}\left[\frac{\partial \mathbf{j}}{\partial t} + \nabla \cdot \left(\mathbf{uj} + \mathbf{ju} - \frac{\mathbf{jj}}{ne}\right)\right], \tag{A.34}$$

and the total equation as

$$\begin{aligned}\frac{m_e m_i}{e}\left[\frac{\partial \mathbf{j}}{\partial t} + \nabla \cdot \left(\mathbf{uj} + \mathbf{ju} - \frac{\mathbf{jj}}{ne}\right)\right] = e\rho_m \mathbf{E} + ne\left[(m_e + m_i)\mathbf{u} - (m_i - m_e)\frac{\mathbf{j}}{ne}\right] \times \mathbf{B} \\ +\ m_i \nabla \cdot \mathbf{P}_e.\end{aligned} \tag{A.35}$$

Dividing through by $e\rho_m = ne(m_e + m_i)$ we get

$$\begin{aligned}\frac{m_e m_i}{ne^2(m_e + m_i)}\left[\frac{\partial \mathbf{j}}{\partial t} + \nabla \cdot \left(\mathbf{uj} + \mathbf{ju} - \frac{\mathbf{jj}}{ne}\right)\right] = \mathbf{E} + \left[\mathbf{u} - \frac{m_i - m_e}{(m_e + m_i)}\frac{\mathbf{j}}{ne}\right] \times \mathbf{B} \\ +\ \frac{m_i}{ne(m_i + m_e)}\nabla \cdot \mathbf{P}_e.\end{aligned} \tag{A.36}$$

Finally, by employing the following cancellations using $m_e \ll m_i$

$$\frac{m_e m_i}{ne^2(m_e + m_i)} \approx \frac{m_e}{ne^2}, \tag{A.37}$$

$$\frac{-(m_i - m_e)}{ne(m_e + m_i)} \approx \frac{-1}{ne}, \tag{A.38}$$

$$\frac{m_i}{ne(m_i + m_e)} \approx \frac{1}{ne}, \tag{A.39}$$

and rearranging, we obtain the generalised Ohm's law,

$$\boxed{\mathbf{E} = -\mathbf{u} \times \mathbf{B} + \frac{1}{ne}\mathbf{j} \times \mathbf{B} - \frac{1}{ne}\nabla \cdot \mathbf{P}_e + \frac{m_e}{ne^2}\left[\nabla \cdot \left(\mathbf{uj} + \mathbf{ju} - \frac{\mathbf{jj}}{ne}\right) + \frac{\partial \mathbf{j}}{\partial t}\right].} \tag{A.40}$$

There are some corrections to the above expression which come from Taylor expansion around the finite electron mass. The corrections are not calculated or used in this thesis, so a derivation is not provided. As presented by Stawarz et al. (2021),

$$\mathbf{E}_{\delta m_e} = \sum_{\ell=1}^{\infty} \left(-\frac{m_e}{m_i}\right)^{\ell} \mathcal{M}_{\ell}, \tag{A.41}$$

where

$$\mathcal{M}_{\ell} = \frac{2}{ne}\mathbf{j}\times\mathbf{B} - \frac{1}{ne}\nabla\cdot\mathbf{P} + \frac{m_e}{ne^2}\left[\nabla\cdot\left(\mathbf{uj}+\mathbf{ju}-(1+2\ell)\frac{\mathbf{jj}}{ne}\right)+\frac{\partial\mathbf{j}}{\partial t}\right], \tag{A.42}$$

giving the full form of the generalised Ohm's law

$$\boxed{\begin{aligned}\mathbf{E} = \eta\,\mathbf{j} - \mathbf{u}\times\mathbf{B} + \frac{1}{ne}\mathbf{j}\times\mathbf{B} - \frac{1}{ne}\nabla\cdot\mathbf{P}_e + \frac{m_e}{ne^2}\left[\nabla\cdot\left(\mathbf{uj}+\mathbf{ju}-\frac{\mathbf{jj}}{ne}\right)+\frac{\partial\mathbf{j}}{\partial t}\right] \\ + \sum_{\ell=1}^{\infty}\left(-\frac{m_e}{m_i}\right)^{\ell}\left\{\frac{2}{ne}\mathbf{j}\times\mathbf{B} - \frac{1}{ne}\nabla\cdot\mathbf{P} + \frac{m_e}{ne^2}\left[\nabla\cdot\left(\mathbf{uj}+\mathbf{ju}-(1+2\ell)\frac{\mathbf{jj}}{ne}\right)+\frac{\partial\mathbf{j}}{\partial t}\right]\right\}.\end{aligned}} \tag{A.43}$$

A.3 The Energy Equation

To obtain the energy equation, we start with the Vlasov equation,

$$\frac{df_s}{dt} \equiv \frac{\partial f_s}{\partial t} + \mathbf{v}\cdot\nabla_{\mathbf{x}} f_s + \frac{q_s}{m_s}\left(\mathbf{E}+\mathbf{v}\times\mathbf{B}\right)\cdot\nabla_{\mathbf{v}} f_s = 0, \tag{A.44}$$

and take the second moment, i.e. multiply Equation A.44 by $m_s\mathbf{vv}/2$ and integrate over velocity space. For convenience, we make the decomposition $\mathbf{v} = \mathbf{v}_s + \mathbf{w}$, where $\mathbf{v}_s$ is the bulk velocity of species s and $\mathbf{w}$ is the internal velocity coordinate in phase space relative to the bulk velocity.

The second moment of A.44 consists of three terms,

$$\int_V \frac{1}{2} m_s \left(\mathbf{v}_s+\mathbf{w}\right)\left(\mathbf{v}_s+\mathbf{w}\right)\frac{\partial f_s}{\partial t}\,d^3v, \tag{A.45}$$

$$\int_V \frac{1}{2} m_s \left(\mathbf{v}_s + \mathbf{w}\right)\left(\mathbf{v}_s + \mathbf{w}\right) \cdot \left(\mathbf{v}_s + \mathbf{w}\right) \nabla_{\mathbf{x}} f_s \, d^3v, \tag{A.46}$$

$$\int_V \frac{1}{2} m_s \left(\mathbf{v}_s + \mathbf{w}\right)\left(\mathbf{v}_s + \mathbf{w}\right) \frac{q_s}{m_s} \left[\mathbf{E} + \left(\mathbf{v}_s + \mathbf{w}\right) \times \mathbf{B}\right] \cdot \nabla_{\mathbf{v}} f_s \, d^3v, \tag{A.47}$$

which sum to 0. Starting with the first integral, A.45, and considering only the trace of the velocity tensor **vv** (for simplicity – the full tensor result of this derivation is called the pressure tensor equation and is beyond the scope of what is required in this thesis),

$$\int_V \frac{1}{2} m_s \left(\mathbf{v}_s + \mathbf{w}\right) \cdot \left(\mathbf{v}_s + \mathbf{w}\right) \frac{\partial f_s}{\partial t} \, d^3v = \frac{\partial}{\partial t} \int_V \frac{1}{2} \left(v_s^2 + 2\mathbf{v}_s \cdot \mathbf{w} + w^2\right) f_s \, d^3v, \tag{A.48}$$

we can employ the definition of the density $n_s = \int f_s \, d^3v$ to get

$$\frac{\partial}{\partial t} \left[\frac{1}{2} m_s n_s v_s^2 + \int_V m_s \mathbf{v}_s \cdot \mathbf{w} f_s \, d^3v + \frac{1}{2} \int_V m_s w^2 f_s \, d^3v\right]. \tag{A.49}$$

The second term in this equation is of the form $\int \mathbf{w} f_s \, d^3v$, which goes to zero as there is by definition no bulk $\mathbf{w}$. We can simplify the third part by noting that $\mathbf{w} = \mathbf{v} - \mathbf{v}_s$ and employing the definition of the pressure tensor $\mathbf{P}_s = m_s \int \left(\mathbf{v} - \mathbf{v}_s\right)\left(\mathbf{v} - \mathbf{v}_s\right) f_s \, d^3v$ then taking the trace $\mathrm{Tr}[\mathbf{P}_s] = 3p_s$ assuming isotropic scalar pressure p_s, giving the final form of A.45,

$$\frac{\partial}{\partial t} \left[\frac{1}{2} m_s n_s v_s^2 + \frac{3p_s}{2}\right]. \tag{A.50}$$

Considering the second integral, A.46, we again take the trace of **vv** to get the expression

$$\int_V \frac{1}{2} m_s \left(v_s^2 + 2\mathbf{v}_s \cdot \mathbf{w} + w^2\right) \left(\mathbf{v}_s + \mathbf{w}\right) \nabla_{\mathbf{x}} f_s \, d^3v, \tag{A.51}$$

which, when rearranged, expands into a sum of six integrals,

$$\begin{aligned} \frac{1}{2} m_s \nabla_{\mathbf{x}} \cdot \Bigg[& \int_V v_s^2 \mathbf{v}_s f_s \, d^3v + 2 \int_V \left(\mathbf{v}_s \cdot \mathbf{w}\right) \mathbf{v}_s f_s \, d^3v + \int_V w^2 \mathbf{v}_s f_s \, d^3v \\ & + \int_V v_s^2 \mathbf{w} f_s \, d^3v + 2 \int_V \left(\mathbf{v}_s \cdot \mathbf{w}\right) \mathbf{w} f_s \, d^3v + \int_V w^2 \mathbf{w} f_s \, d^3v \Bigg]. \end{aligned} \tag{A.52}$$

Again, terms of the form $\int \mathbf{w} f_s \, d^3v$ go to zero, and we can use the definitions of n_s, $\mathbf{P}_s$,

p_s, and the heat flux vector $q_s = \frac{m_s}{2}\int_V v^2 \mathbf{v} f_s \, d^3v$ to arrive at the final expression for A.46,

$$\nabla_{\mathbf{x}} \cdot \left[\frac{1}{2} m_s n_s v_s^2 \mathbf{v}_s + \frac{3 p_s \mathbf{v}_s}{2} + \mathbf{v}_s \cdot \mathbf{P}_s + \mathbf{q}_s \right]. \tag{A.53}$$

The third integral, A.47, can be written as

$$\int_V \frac{q_s}{2} \left(\mathbf{v}_s + \mathbf{w}\right)^2 \left[\mathbf{E} + \left(\mathbf{v}_s + \mathbf{w}\right) \times \mathbf{B}\right] \cdot \nabla_{\mathbf{v}} f_s \, d^3v, \tag{A.54}$$

which can be integrated by parts to give

$$\frac{q_s}{2} \left[\left(\mathbf{v}_s + \mathbf{w}\right)^2 \left[\mathbf{E} + \left(\mathbf{v}_s + \mathbf{w}\right) \times \mathbf{B}\right] f_s\right]_0^{\infty} - \frac{q_s}{2} \int_V f_s \nabla_{\mathbf{v}} \left(\left(\mathbf{v}_s + \mathbf{w}\right)^2 \left[\mathbf{E} + \left(\mathbf{v}_s + \mathbf{w}\right) \times \mathbf{B}\right] \right) d^3v, \tag{A.55}$$

in which the first term goes to zero provided $f_s \to 0$ sufficiently quickly as $v \to \infty$. The second term can be rearranged as

$$-\frac{q_s}{2} \int_V f_s \left[\mathbf{E} + \left(\mathbf{v}_s + \mathbf{w}\right) \times \mathbf{B}\right] \cdot \nabla_{\mathbf{v}} \left[\left(\mathbf{v}_s + \mathbf{w}\right)^2\right] d^3v, \tag{A.56}$$

since the Lorentz force does not have a velocity space gradient. Noting that $\nabla_{\mathbf{v}} \mathbf{v}^2 = 2\mathbf{v}$, the expression can be simplified further to

$$-q_s \int_V f_s \left[\mathbf{E} + \left(\mathbf{v}_s + \mathbf{w}\right) \times \mathbf{B}\right] \cdot \left(\mathbf{v}_s + \mathbf{w}\right) d^3v, \tag{A.57}$$

which, using $\left(\mathbf{v} \times \mathbf{B}\right) \cdot \mathbf{v} = 0$, simplifies further to

$$-q_s \int_V f_s \left(\mathbf{E} \cdot \mathbf{v}_s + \mathbf{E} \cdot \mathbf{w}\right) d^3v. \tag{A.58}$$

Finally, using the definition of n_s and removing the second term because again $\int \mathbf{w} f_s \, d^3v = 0$, we arrive at the final form of A.47,

$$-q_s n_s \mathbf{E} \cdot \mathbf{v}_s \equiv -\mathbf{E} \cdot \mathbf{j}_s. \tag{A.59}$$

Putting the three evaluated integrals together, the energy equation is given by

$$\boxed{\frac{\partial}{\partial t}\left[\frac{1}{2}m_s n_s v_s^2 + \frac{3p_s}{2}\right] + \nabla_{\mathbf{x}} \cdot \left[\frac{1}{2}m_s n_s v_s^2 \mathbf{v}_s + \frac{3p_s \mathbf{v}_s}{2} + \mathbf{v}_s \cdot \mathbf{P}_s + \mathbf{q}_s\right] - \mathbf{E} \cdot \mathbf{j}_s = 0.} \quad \text{(A.60)}$$

Appendix B

Table of Intervals

B.1 Chapter 4

The following intervals are sourced from Stawarz et al. (2022). The total length of the data set is 32,013 seconds.

Number	Start Date	End Date	Duration (s)
1	2015-10-21/06:55:10	2015-10-21/07:03:45	515
2	2015-10-29/14:48:05	2015-10-29/14:53:55	350
3	2015-10-31/10:22:27	2015-10-31/10:26:07	220
4	2015-11-15/05:27:36	2015-11-15/05:32:10	274
5	2016-02-23/21:54:06	2016-02-23/21:58:36	270
6	2016-09-28/16:50:14	2016-09-28/17:00:14	600
7	2016-09-30/17:50:34	2016-09-30/18:01:50	676
8	2016-10-25/09:45:57	2016-10-25/09:50:07	250
9	2016-11-09/13:41:23	2016-11-09/13:45:13	230
10	2016-12-08/10:16:52	2016-12-08/10:21:02	250
11	2016-12-08/10:25:02	2016-12-08/10:28:52	230
12	2016-12-09/09:01:40	2016-12-09/09:07:00	320
13	2016-12-09/09:26:25	2016-12-09/09:34:57	512

Number	Start Date	End Date	Duration (s)
14	2016-12-11/15:20:15	2016-12-11/15:32:31	736
15	2016-12-31/13:27:04	2016-12-31/13:31:02	238
16	2017-01-27/00:38:53	2017-01-27/00:42:01	188
17	2017-01-27/00:52:47	2017-01-27/00:56:56	249
18	2017-01-27/00:57:23	2017-01-27/01:02:36	313
19	2017-01-28/05:29:14	2017-01-28/05:34:50	336
20	2017-01-28/09:05:25	2017-01-28/09:11:12	347
21	2017-01-31/04:19:34	2017-01-31/04:25:50	376
22	2017-01-31/04:27:04	2017-01-31/04:30:03	179
23	2017-01-31/04:31:26	2017-01-31/04:35:13	227
24	2017-09-28/06:31:34	2017-09-28/06:58:14	1600
25	2017-09-28/10:43:00	2017-09-28/10:53:30	630
26	2017-09-28/20:42:00	2017-09-28/20:51:21	561
27	2017-11-13/19:06:36	2017-11-13/19:10:51	255
28	2017-11-13/19:30:44	2017-11-13/19:38:42	478
29	2017-11-16/15:36:06	2017-11-16/15:44:09	483
30	2017-11-25/01:02:52	2017-11-25/01:05:52	180
31	2017-12-01/13:12:07	2017-12-01/13:23:38	691
32	2017-12-09/06:12:34	2017-12-09/06:18:22	348
33	2017-12-12/04:21:15	2017-12-12/04:28:41	446
34	2017-12-12/19:32:59	2017-12-12/19:41:03	484
35	2017-12-17/19:42:54	2017-12-17/19:50:12	438
36	2017-12-21/06:41:57	2017-12-21/07:03:42	1305
37	2017-12-24/01:22:35	2017-12-24/01:38:31	956
38	2017-12-26/05:46:16	2017-12-26/06:03:00	1004
39	2017-12-26/06:12:44	2017-12-26/06:52:14	2370
40	2018-02-10/00:55:04	2018-02-10/01:00:33	329
41	2018-02-18/12:52:44	2018-02-18/13:03:01	617

Number	Start Date	End Date	Duration (s)
42	2018-02-21/07:31:54	2018-02-21/07:36:02	248
43	2018-02-21/07:48:54	2018-02-21/08:00:43	709
44	2018-03-15/20:32:00	2018-03-15/20:38:42	402
45	2018-04-13/15:39:34	2018-04-13/15:43:51	257
46	2018-04-14/23:00:14	2018-04-14/23:06:15	361
47	2018-04-15/00:31:04	2018-04-15/00:35:42	278
48	2018-04-19/05:08:04	2018-04-19/05:41:50	2026
49	2018-04-23/07:50:14	2018-04-23/08:33:38	2604
50	2018-04-24/21:44:15	2018-04-24/21:52:31	496
51	2018-04-27/16:30:57	2018-04-27/16:35:20	263
52	2018-04-27/16:39:47	2018-04-27/16:44:11	264
53	2018-04-27/17:35:44	2018-04-27/17:41:51	367
54	2018-04-27/17:56:25	2018-04-27/18:03:49	444
55	2018-04-28/20:48:55	2018-04-28/20:53:40	285
56	2018-04-28/21:02:05	2018-04-28/21:09:20	435
57	2018-04-28/21:29:06	2018-04-28/21:34:20	314
58	2018-04-28/22:22:46	2018-04-28/22:29:40	414
59	2018-05-23/14:35:26	2018-05-23/14:41:41	375
60	2018-05-28/22:23:40	2018-05-28/22:30:30	410

B.2 Chapters 5 & 6

The following intervals also derive from Stawarz et al. (2022), with additions in between some intervals as well as up to the end of the 2019/2020 dayside MMS dayside campaign. Some of the longer intervals have been split up to aid with computational tractability. The total length of the data set is 87,974 seconds.

Number	Start Date	End Date	Duration (s)
1	2015-10-21/06:55:10	2015-10-21/07:03:45	515
2	2015-10-29/14:48:05	2015-10-29/14:53:55	350
3	2015-10-31/10:22:27	2015-10-31/10:26:07	220
4	2015-11-15/05:27:36	2015-11-15/05:32:10	274
5	2016-02-23/21:54:06	2016-02-23/21:58:36	270
6	2016-09-28/16:00:00	2016-09-28/16:08:52	532
7	2016-09-28/16:50:06	2016-09-28/16:59:00	534
8	2016-09-28/17:32:06	2016-09-28/17:37:32	326
9	2016-09-28/16:50:14	2016-09-28/17:00:14	600
10	2016-10-01/18:30:00	2016-10-01/18:40:00	600
11	2016-09-30/17:50:34	2016-09-30/18:01:50	676
12	2016-10-25/09:45:57	2016-10-25/09:50:07	250
13	2016-11-09/13:41:23	2016-11-09/13:45:13	230
14	2016-12-08/10:16:52	2016-12-08/10:21:02	250
15	2016-12-08/10:25:02	2016-12-08/10:28:52	230
16	2016-12-09/09:01:40	2016-12-09/09:07:00	320
17	2016-12-09/09:26:25	2016-12-09/09:34:57	512
18	2016-12-11/15:20:15	2016-12-11/15:32:31	736
19	2016-12-31/13:27:05	2016-12-31/13:31:01	236
20	2017-01-27/00:38:54	2017-01-27/00:42:00	186
21	2017-01-27/00:52:47	2017-01-27/00:56:56	249
22	2017-01-27/00:57:23	2017-01-27/01:02:36	313
23	2017-01-28/05:29:14	2017-01-28/05:34:50	336
24	2017-01-28/09:05:25	2017-01-28/09:11:12	347
25	2017-01-31/04:19:34	2017-01-31/04:25:50	376
26	2017-01-31/04:27:04	2017-01-31/04:30:03	179
27	2017-01-31/04:31:26	2017-01-31/04:35:13	227
28	2017-09-28/06:31:34	2017-09-28/06:58:14	1600

Number	Start Date	End Date	Duration (s)
29	2017-09-28/10:43:00	2017-09-28/10:53:30	630
30	2017-09-28/20:42:00	2017-09-28/20:51:21	561
31	2017-11-13/19:06:36	2017-11-13/19:10:51	255
32	2017-11-13/19:30:44	2017-11-13/19:38:42	478
33	2017-11-16/15:36:06	2017-11-16/15:44:09	483
34	2017-11-25/01:02:53	2017-11-25/01:05:51	178
35	2017-12-01/13:12:07	2017-12-01/13:23:38	691
36	2017-12-09/06:12:34	2017-12-09/06:18:22	348
37	2017-12-12/04:21:15	2017-12-12/04:28:41	446
38	2017-12-12/19:32:59	2017-12-12/19:41:03	484
39	2017-12-17/19:42:54	2017-12-17/19:50:12	438
40	2017-12-21/06:41:57	2017-12-21/07:03:42	1305
41	2017-12-24/01:22:35	2017-12-24/01:38:31	956
42	2017-12-26/05:46:16	2017-12-26/06:03:00	1004
43	2017-12-26/06:12:44	2017-12-26/06:22:14	570
44	2017-12-26/06:22:14	2017-12-26/06:32:14	600
45	2017-12-26/06:32:14	2017-12-26/06:42:14	600
46	2017-12-26/06:42:14	2017-12-26/06:52:14	600
47	2018-02-10/00:55:05	2018-02-10/01:00:32	327
48	2018-02-18/12:52:44	2018-02-18/13:03:01	617
49	2018-02-21/07:31:54	2018-02-21/07:36:02	248
50	2018-02-21/07:48:54	2018-02-21/08:00:43	709
51	2018-03-15/20:32:01	2018-03-15/20:38:41	400
52	2018-04-13/15:39:34	2018-04-13/15:43:51	257
53	2018-04-14/23:00:14	2018-04-14/23:06:15	361
54	2018-04-15/00:31:04	2018-04-15/00:35:42	278
55	2018-04-19/05:08:04	2018-04-19/05:41:50	2026
56	2018-04-23/07:50:14	2018-04-23/08:33:38	2604

Number	Start Date	End Date	Duration (s)
57	2018-04-24/21:44:15	2018-04-24/21:52:31	496
58	2018-04-27/16:30:57	2018-04-27/16:35:20	263
59	2018-04-27/16:39:47	2018-04-27/16:44:11	264
60	2018-04-27/17:35:44	2018-04-27/17:41:51	367
61	2018-04-27/17:56:25	2018-04-27/18:03:49	444
62	2018-04-28/20:48:55	2018-04-28/20:53:40	285
63	2018-04-28/21:02:05	2018-04-28/21:09:20	435
64	2018-04-28/21:29:06	2018-04-28/21:34:20	314
65	2018-04-28/22:22:46	2018-04-28/22:29:40	414
66	2018-05-23/14:35:26	2018-05-23/14:41:41	375
67	2018-05-24/00:13:54	2018-05-24/00:17:21	207
68	2018-05-24/05:49:54	2018-05-24/05:54:01	247
69	2018-05-28/22:23:40	2018-05-28/22:30:30	410
70	2018-10-16/14:22:14	2018-10-16/14:32:21	607
71	2018-10-16/14:38:34	2018-10-16/14:47:01	507
72	2018-10-17/03:36:44	2018-10-17/03:45:41	537
73	2018-10-17/04:13:34	2018-10-17/04:22:00	506
74	2018-10-19/03:33:00	2018-10-19/03:42:11	551
75	2018-10-22/07:21:04	2018-10-22/07:35:11	847
76	2018-10-25/03:08:00	2018-10-25/03:16:30	510
77	2018-10-27/09:13:14	2018-10-27/09:23:00	586
78	2018-10-27/09:23:01	2018-10-27/09:32:00	539
79	2018-10-27/09:38:00	2018-10-27/09:48:30	630
80	2018-10-28/11:23:00	2018-10-28/11:35:00	720
81	2018-10-28/11:35:01	2018-10-28/11:45:21	620
82	2018-10-30/09:27:00	2018-10-30/09:42:00	900
83	2018-10-31/15:16:00	2018-10-31/15:27:00	660
84	2018-10-31/16:04:00	2018-10-31/16:17:00	780

Number	Start Date	End Date	Duration (s)
85	2018-11-01/22:16:16	2018-11-01/22:28:58	762
86	2018-11-03/12:40:00	2018-11-03/12:50:00	600
87	2018-11-07/13:15:00	2018-11-07/13:27:31	751
88	2018-11-07/13:27:32	2018-11-07/13:37:31	599
89	2018-11-15/20:54:00	2018-11-15/21:00:00	360
90	2018-11-15/21:33:30	2018-11-15/21:40:31	421
91	2018-11-15/22:10:00	2018-11-15/22:15:00	300
92	2018-11-21/16:10:14	2018-11-21/16:25:00	886
93	2018-11-21/16:28:00	2018-11-21/16:40:00	720
94	2018-11-21/16:40:01	2018-11-21/16:50:00	599
95	2018-11-21/17:40:54	2018-11-21/17:53:00	726
96	2018-11-21/17:56:00	2018-11-21/18:00:00	240
97	2018-11-24/09:22:30	2018-11-24/09:37:00	870
98	2018-11-29/23:09:00	2018-11-29/23:14:00	300
99	2018-11-29/23:18:00	2018-11-29/23:27:00	540
100	2018-12-01/23:04:06	2018-12-01/23:12:20	494
101	2018-12-05/14:55:00	2018-12-05/15:05:00	600
102	2018-12-05/15:10:00	2018-12-05/15:20:00	600
103	2018-12-10/10:02:00	2018-12-10/10:13:00	660
104	2018-12-18/20:03:00	2018-12-18/20:13:00	600
105	2018-12-18/20:36:30	2018-12-18/20:40:42	252
106	2018-12-18/20:36:30	2018-12-18/20:40:42	252
107	2019-01-22/11:24:25	2019-01-22/11:35:00	635
108	2019-02-12/14:33:04	2019-02-12/14:44:00	656
109	2019-02-12/14:44:01	2019-02-12/14:55:00	659
110	2019-02-12/15:00:00	2019-02-12/15:12:59	779
111	2019-04-20/13:24:04	2019-04-20/13:27:31	207
112	2019-10-09/07:12:14	2019-10-09/07:18:00	346

Number	Start Date	End Date	Duration (s)
113	2019-10-10/09:02:44	2019-10-10/09:10:00	436
114	2019-10-10/15:00:00	2019-10-10/15:07:21	441
115	2019-10-16/12:54:24	2019-10-16/13:04:00	576
116	2019-10-16/13:04:01	2019-10-16/13:16:00	719
117	2019-11-05/22:04:54	2019-11-05/22:13:42	528
118	2019-11-19/21:45:00	2019-11-19/21:53:00	480
119	2019-11-25/13:20:00	2019-11-25/13:30:00	600
120	2019-11-25/13:30:01	2019-11-25/13:40:00	599
121	2019-11-26/20:18:04	2019-11-26/20:21:30	206
122	2019-12-03/19:06:00	2019-12-03/19:17:00	660
123	2019-12-03/19:17:01	2019-12-03/19:28:00	659
124	2019-12-07/09:33:44	2019-12-07/09:40:00	376
125	2019-12-07/09:40:01	2019-12-07/09:50:00	599
126	2019-12-07/09:50:01	2019-12-07/10:00:00	599
127	2019-12-07/10:00:01	2019-12-07/10:10:00	599
128	2019-12-07/10:10:01	2019-12-07/10:20:00	599
129	2019-12-07/10:20:01	2019-12-07/10:30:00	599
130	2019-12-17/20:30:00	2019-12-17/20:40:00	600
131	2019-12-24/01:33:04	2019-12-24/01:46:11	787
132	2019-12-28/08:30:00	2019-12-28/08:37:00	420
133	2019-12-28/08:46:30	2019-12-28/08:53:30	420
134	2019-12-28/08:55:01	2019-12-28/09:05:00	599
135	2019-12-28/09:05:01	2019-12-28/09:15:00	599
136	2019-12-31/23:46:00	2019-12-31/23:57:00	660
137	2020-01-14/05:08:00	2020-01-14/05:14:30	390
138	2020-01-14/05:23:00	2020-01-14/05:35:00	720
139	2020-01-14/05:35:01	2020-01-14/05:43:00	479
140	2020-01-14/05:43:01	2020-01-14/05:52:00	539

Number	Start Date	End Date	Duration (s)
141	2020-02-04/07:26:25	2020-02-04/07:36:00	575
142	2020-02-04/07:36:01	2020-02-04/07:46:00	599
143	2020-02-04/07:46:01	2020-02-04/07:56:00	599
144	2020-02-04/07:56:01	2020-02-04/08:06:00	599
145	2020-02-04/08:06:01	2020-02-04/08:17:00	659
146	2020-02-04/08:17:01	2020-02-04/08:30:00	779
147	2020-02-11/20:59:44	2020-02-11/21:09:00	556
148	2020-02-11/21:09:01	2020-02-11/21:19:00	599
149	2020-02-14/20:56:54	2020-02-14/21:08:21	687
150	2020-02-26/00:23:54	2020-02-26/00:30:00	366
151	2020-02-26/00:30:01	2020-02-26/00:40:00	599
152	2020-02-26/00:40:01	2020-02-26/00:50:00	599
153	2020-02-26/00:58:30	2020-02-26/01:10:00	690
154	2020-02-26/01:10:01	2020-02-26/01:20:00	599
155	2020-02-29/10:03:00	2020-02-29/10:10:00	420
156	2020-02-29/10:10:01	2020-02-29/10:20:00	599
157	2020-02-29/10:20:01	2020-02-29/10:30:00	599
158	2020-02-29/10:30:01	2020-02-29/10:40:00	599
159	2020-02-29/10:40:01	2020-02-29/10:50:00	599
160	2020-02-29/10:50:01	2020-02-29/10:55:00	299
161	2020-03-20/21:07:54	2020-03-20/21:15:00	426
162	2020-03-20/21:15:02	2020-03-20/21:25:00	598
163	2020-03-20/21:25:01	2020-03-20/21:33:00	479

Appendix C

Figure Permissions

Some figures included in this thesis have been sourced from other publications. In each case, where necessary permission has been obtained, listed below.

Figure(s)	Source	Licence
1.1	Wikimedia (24/03/2025)	Photo of Public Domain Artwork
1.2	Wikimedia (12/03/2025)	Photo of Public Domain Artwork
1.3	Colagrossi et al. (2021)	Creative Commons CC BY
1.4	NASA / Mary Pat Hrybyk-Keith	Public Domain
2.6	Sahraoui et al. (2020)	License Agreement 5965900896514
2.7	Greco et al. (2018)	License Agreement 5965830443790
3.1	Stawarz and Genestreti (2023)	License Agreement 5995940842897

Table C.1: Licenses for figure reuse.